

AD-A145 009

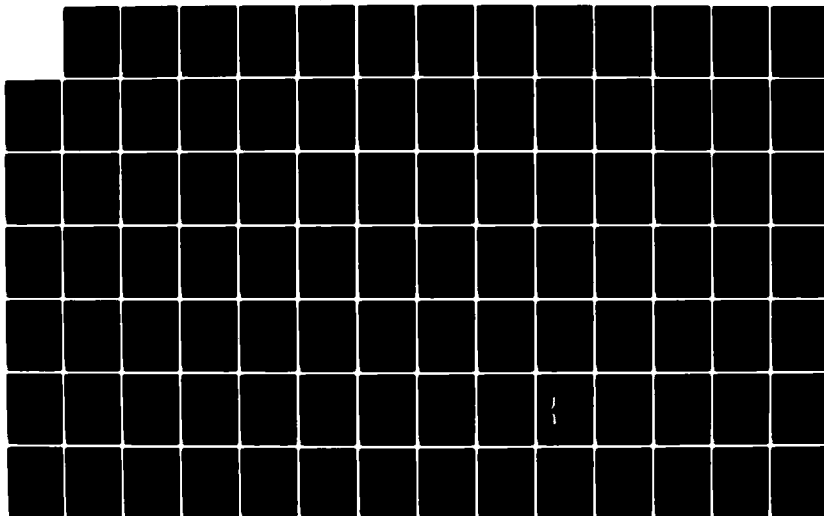
STUDIES OF SOLAR FLARES AND CORONAL LOOPS(U) CALIFORNIA
UNIV SAN DIEGO LA JOLLA CENTER FOR ASTROPHYSICS AND
SPACE SCIENCES R C CANFIELD 10 JUL 84 UCSD-SP-84-21
AFOSR-TR-84-0719 AFOSR-82-0092

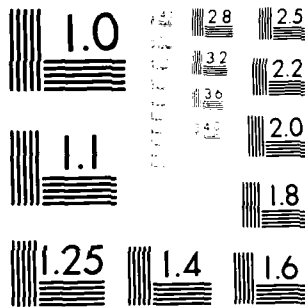
1/3

UNCLASSIFIED

F/G 3/2

NL





MICROCOPY RESOLUTION TEST CHART
NATIONAL BUREAU OF STANDARDS-1963-A

UNCLASSIFIED

SECURITY CLASSIFICATION OF THIS PAGE (When Data Entered)

AD-A145 009

REPORT DOCUMENTATION PAGE		READ INSTRUCTIONS BEFORE COMPLETING FORM
1. REPORT NUMBER SP-84-21 AFOSR-TR-84-0719	2. GOVT ACCESSION NO. AD-A145009	3. RECIPIENT'S CATALOG NUMBER
4. TITLE (and Subtitle) Studies of Solar Flares and Coronal Loops	5. TYPE OF REPORT & PERIOD COVERED Final Scientific Report 1 Feb. 1982 - 31 May 1984	
	6. PERFORMING ORG. REPORT NUMBER UCSD-SP-84-21	
7. AUTHOR(s) Richard C. Canfield	8. CONTRACT OR GRANT NUMBER(s) AFOSR 82-0092 (5)	
9. PERFORMING ORGANIZATION NAME AND ADDRESS Center for Astrophysics and Space Sciences, C-011 University of California, San Diego La Jolla, California 92093	10. PROGRAM ELEMENT, PROJECT, TASK AREA & WORK UNIT NUMBERS 61102F 2311/A1	
11. CONTROLLING OFFICE NAME AND ADDRESS AFOSR/NP Building 410 Bolling AFB, DC 20332	12. REPORT DATE 10 July 1984	
	13. NUMBER OF PAGES 240	
14. MONITORING AGENCY NAME & ADDRESS (if different from Controlling Office)	15. SECURITY CLASS. (of this report)	
	15a. DECLASSIFICATION/DOWNGRADING SCHEDULE	
16. DISTRIBUTION STATEMENT (of this Report) Approved for public release; distribution unlimited.		
17. DISTRIBUTION STATEMENT (of the abstract entered in Block 20, if different from Report) Approved for public release, distribution unlimited.		
18. SUPPLEMENTARY NOTES		
19. KEY WORDS (Continue on reverse side if necessary and identify by block number) Solar Flares Radiative Transfer Solar Corona Magnetohydrodynamic Stability		
20. ABSTRACT (Continue on reverse side if necessary and identify by block number) See next page		

DD FORM 1473 1 JAN 73 EDITION OF 1 NOV 65 IS OBSOLETE

UNCLASSIFIED SECURITY CLASSIFICATION OF THIS PAGE (When Data Entered)

DTIC FILE COPY

84 08 30 045

UNCLASSIFIED

SECURITY CLASSIFICATION OF THIS PAGE (When Data Entered)

ABSTRACT

The objectives of the research described in this report were to improve our understanding of solar flares and solar coronal loops. The specific approach to the flare objective was to analyze and interpret solar flare data, using theoretical methods developed as part of the research. The specific approach to the coronal loop objective was to investigate their thermal and magnetohydrodynamic stability, for various physical models.

The principal result of the flare research was to demonstrate that, in two well-observed flares, the mechanism of chromospheric evaporation accounts for the observed amount of flare X-ray plasma. The dominant energy transport mechanism is thermal conduction. Heating by energetic electrons is of secondary importance.

The principal results of the magnetohydrodynamic stability analyses were demonstrations of the role of radiative energy loss, compressibility, magnetic field line twist, foot-point magnetic field line tying, and radial plasma pressure gradient.



A-1

UNCLASSIFIED

CONTENTS

	Page
I. Research Objectives	4
II. Research Accomplishments	4
a. Solar Flare Observations and Interpretation	4
b. Theoretical Modeling of Flare Energy Transport	82
c. Solar Coronal Loop Magnetohydrodynamic Stability Theory ..	178
III. Professional Personnel	236
III. Publications	237
V. Spoken Papers	238
VI. Consultative and Advisory Functions	240

I. RESEARCH OBJECTIVES

The primary objective of this research was to improve our understanding of solar flares and solar coronal loops.

The scientific approach used during the grant period was to:

- (1) Analyze and interpret solar flare observations
- (2) Develop new theoretical methods of value in the analysis and interpretation of the solar flare observations,
- (3) Evaluate the thermal and magnetohydrodynamic stability of coronal loops, for various physical models.

II. RESEARCH ACCOMPLISHMENTS

a) Solar Flare Observations and Interpretation

In 1980 we obtained particularly good coordinated observations of both coronal and chromospheric aspects of flares, by means of NASA's Solar Maximum Mission (SMM) and Sacramento Peak Observatory. The two papers in this section constitute analysis of these data and interpretation in terms of the most important flare energy transport processes. The key element of the analysis was theoretical $H\alpha$ profiles, discussed in IIb (below).

The questions of common interest addressed in these papers are:

1. Can chromospheric evaporation (the heating of $T \sim 10^4\text{K}$ chromospheric material to $T \approx 10^7\text{K}$) account for the observed amount of flare X-ray plasma?
2. What physical process causes this chromospheric evaporation?
3. Is there evidence for substantial penetration of energetic particles into the chromosphere?

The conclusion of this research was that in these two flares chromospheric evaporation can account for the observed amount of X-ray emitting plasma. Heating by both nonthermal electrons and thermal conduction gives rise to chromospheric evaporation, but the latter dominates. Although evidence was found for penetration of nonthermal electrons into the flare chromosphere, it is not the dominant source of heating that leads to chromospheric evaporation.

Ap.J. in press, October 15, 1984.

SP-83-50 Rev.

A CONSISTENT PICTURE OF CORONAL AND CHROMOSPHERIC
PROCESSES IN A WELL-OBSERVED SOLAR FLARE

Todd A. Gunkler and Richard C. Canfield
Center for Astrophysics and Space Sciences
University of California, San Diego

Loren W. Acton
Lockheed Palo Alto Research Laboratory

Alan L. Kiplinger
Goddard Space Flight Center
and
Applied Research Corporation

Received: _____

ABSTRACT

We have analyzed the solar flare of 1522 UT 24 June 1980 using simultaneous observations in hard X-rays, soft X-rays, and H α line profiles. The X-ray observations were made with instruments aboard the Solar Maximum Mission satellite, and the H α profiles were taken with a CCD detector at Sacramento Peak Observatory. We used the theoretical profiles of Canfield, Gunkler, and Ricchiazzi (1984) to analyze the H α data. We studied various flare phenomena, including heating of the chromosphere by nonthermal electrons, enhanced coronal pressure, enhanced thermal conduction, chromospheric evaporation, and mass motion. We find that we can make a consistent picture of the flare in coronal and chromospheric processes.

We interpret the flare morphology in terms of a model where the energy release occurs at the site of the interaction of two large loop systems. The manifestations of the energy release were heating of the corona to $\sim 15 \times 10^6$ K and acceleration of nonthermal electrons, evidenced by both hard X-ray emission and H α profiles. The electrons produced penetrative heating and expansion of the flare chromosphere. The maximum flux of nonthermal electrons above 20 keV was estimated, from both H α and hard X-ray data, to be $\sim 10^{11}$ ergs cm $^{-2}$ s $^{-1}$. Electrons penetrated at both footpoints of one loop system, giving evidence for bidirectional beaming. H α and soft X-ray estimates of the

coronal pressure match well, with typical values of 400-1000 dynes cm^{-2} over $\text{H}\alpha$ footpoints.

The amounts of chromospheric evaporation by conduction and by nonthermal electrons were calculated from observed quantities. Both mechanisms can account for significant amounts of evaporation, but nonthermal electrons are at least 2-3 times less effective than conduction. The extent of evaporation was also calculated from the observed soft X-ray mass flux. Sufficient chromospheric evaporation was inferred by both methods to explain the observed increase in the coronal density.

Subject Headings: Sun: chromosphere -- Sun: corona --

Sun: flares -- Sun: X-rays

I. INTRODUCTION

a) Motivation

There are a number of important questions concerning the nature of the physical processes involved in solar flares. In particular: Are fast electrons accelerated in the corona and beamed into the chromosphere? What accounts for the increase in soft X-ray emission and higher coronal pressure? To what extent is the top of the chromosphere evaporated, hence providing coronal plasma? What are the role and extent of thermal conduction in flares? Where does the energy release take place, and what is its physical form? Using recent theoretical advances, these processes can now be studied through chromospheric, as well as coronal, observations. Nonthermal electrons, enhanced coronal pressure, and enhanced thermal conduction each have identifiable effects on the $H\alpha$ line profile. This allows us to test theories regarding the physics of solar flares. For example, it has been suggested (see, e.g., Chubb *et al.* 1966) that the hard X-ray emission during the impulsive phase of flares is thermal bremsstrahlung from a super-hot ($T_e \sim 10^8$ K) coronal plasma. This would result in greatly enhanced thermal conduction into the chromosphere. This is in contrast to the scenario in which chromospheric heating is by beams of nonthermal electrons (Brown 1971) and coronal temperatures are $10\text{-}30 \times 10^6$ K.

In addition, some authors (Dere and Cook 1979, Acton *et al.* 1982) have suggested that there may be a discrepancy between the coronal and the chromospheric or transition region pressures. This discrepancy, plus other measurements within a system generally assumed to be in pressure equilibrium, led Cheng, Feldman, and Doschek (1981) to question the importance of chromospheric evaporation. Our new techniques allow more accurate measurements of the chromospheric pressure, for comparison with estimates of the coronal pressure from soft X-ray data.

Finally, our ability to measure the flare parameters with our H α spatial resolution of 2.56" allows us to make intelligent guesses about the energization process. There are several opposing theories that can be tested. For example, in the model described by Sturrock (1974) and others, energy release takes place at the top of a single loop system, due to reconnection of open field lines. Another single-loop theory is that of Spicer (1977), where reconnection occurs between sheared field lines throughout the loop. These can be contrasted with the emerging flux theory (Heyvaerts, Priest, and Rust 1977), in which magnetic reconnection occurs at the interaction site between two magnetic loop systems. While the study of just one flare cannot rule out the possibility of different types of flares, it serves to guide and constrain flare modeling in the future.

b) Previous Work

In a previous paper (Acton *et al.* 1982, hereafter Paper I) we estimated the amount of chromospheric evaporation by comparing our observed H α profiles with the computed profiles of Dinh (1980). He constructed a grid of empirical atmospheres from the observation of a number of atomic lines during several flares, and computed H α line profiles for each atmosphere. Using the column depth of the transition region (the number of atoms in a cm² column above the chromosphere) for each atmosphere, we were able to assign a value of the evaporated mass to each of his profile types. These estimates of the amount of evaporated material were compared with the observed increase in the soft X-ray emission measure to show that we could see the change of state of the upper chromosphere during a flare.

Since completion of Paper I, we have improved on the work of Dinh by computing a large grid of flare atmospheres, treating the coronal pressure and the energy fluxes of nonthermal electrons and thermal conduction as parameters. Unlike Dinh's atmospheres, our atmospheres were computed assuming specific physical flare mechanisms, solving the equations of steady state energy balance, radiative transfer, statistical equilibrium, and hydrostatic equilibrium. This grid of models, with its more physical approach, offers significant improvement over the empirical models of Dinh.

In the following section, we give the methods of obtaining and analyzing the data. The morphology of the event is described in Section III. In Section IV, we use our methods to examine the coronal and chromospheric evidence for beams of nonthermal electrons, chromospheric evaporation, pressure balance, and mass motion. It will be shown that the observations strongly suggest a scenario in which two large magnetic loop systems interact to provide the flare energy.

II. METHOD

a) Observational

Simultaneous data were taken in X-rays and H α by instruments aboard the Solar Maximum Mission (SMM) spacecraft and ground-based instruments at Sacramento Peak Observatory (SPO). A summary of the instrumental characteristics is given in Table 1. The SPO data consist of 50x50 pixels within a small region on the solar surface. The H α profile for each pixel is obtained as the spectrograph slit is scanned across the field of view. Data outside the time interval 15:20 to 15:26 UT were affected by guiding difficulties caused by passing clouds. Profiles were observed outside this interval, but the spatial location and absolute intensity were difficult to determine accurately. Fortunately, the main flare effects occurred during the cloud-free period. Details of the SPO observational method can be found

in Paper I.

The Hard X-Ray Burst Spectrometer (HXRBS), described by Orwig, Frost, and Dennis (1980), is a large-area scintillation counter which measures the total solar flux in hard X-rays with excellent time resolution. The Hard X-Ray Imaging Spectrometer (HXIS, van Beek *et al.* 1980) has overlapping fine and coarse fields of view, which give images of the flare in both soft and hard X-rays. The Flat Crystal Spectrometer (FCS) of the X-Ray Polychromator (XRP, Acton *et al.* 1980) was operated in its polychromatic raster mode to provide soft X-ray images in six resonance lines sensitive to electron temperatures in the range $2 \times 10^6 \leq T_e \leq 50 \times 10^6$ K. Prior to 15:21:50 UT, a 4' x 4' region was scanned with 15" resolution. A 20" resolution quick-scan was then done to locate the brightest area, and from 15:22:36 UT to the end of the flare, a 2' x 2' region was scanned with 15" resolution. The Bent Crystal Spectrometer (BCS) of XRP provides soft X-ray spectra with good time resolution.

Co-alignment of the images from SMM and SPO, to an accuracy of "5", was done using sunspot images made by FCS, Big Bear Solar Observatory (BBSO) at $H\alpha + 2 \text{ \AA}$, and SPO at $H\alpha + 4.8 \text{ \AA}$. We used the known relationship between HXIS and FCS pointings for co-alignment of the hard X-ray images. Line-center spectroheliograms of the SPO data were compared to line-center BBSO pictures, with the known spatial scales of both images and typical $H\alpha$ features

(filaments, plages, etc.) being used to establish the co-registration.

b) Theoretical

The primary theoretical advance since Paper I has been the development of a large grid of theoretical $H\alpha$ profiles by Canfield, Gunkler, and Ricchiazzi (1984, hereafter CGR). These profiles, computed for static flare model atmospheres, show the effects of varying the coronal pressure and the fluxes of heat and nonthermal electrons on the columnar distribution of temperature and density. Three general results emerged from this study: only sufficiently high fluxes of nonthermal electrons produce pronounced Stark $H\alpha$ wings; only sufficiently high values of the coronal pressure remove the central reversal of the $H\alpha$ profiles; and the extent of chromospheric evaporation is determined primarily by the value of the conductive flux.

We can give quantitative estimates of several physical parameters by comparing the observed $H\alpha$ profiles to the grid of calculated profiles. We estimate the pressure by visually comparing the central reversals of observed profiles to those of theoretical profiles, such as those shown in Figure 1a. This plot shows the effect of varying the pressure while holding all other parameters fixed. The value of the pressure can be estimated to within a factor of $\sim 2-3$ by this method. Once the pressure has been

determined, a set of profiles with this pressure and a range of values of F_{20} (the energy flux of electrons above 20 keV) is used to determine the nonthermal electron flux. Examples of these theoretical profiles are shown in Figure 1b. Again, observed profiles are visually compared to the theoretical grid, paying attention this time to the angle of the profile wings. This naturally requires that the observed profiles be plotted with the same proportion between the vertical and horizontal scales as the theoretical profiles. The accuracy of F_{20} measurements is also a factor of $\sim 2-3$.

We can also use the work of Hummer and Rybicki (1968) to provide qualitative velocity information. Their work shows that profiles with bright red peaks indicate differentially expanding atmospheres, while profiles with bright blue peaks indicate that the atmosphere is being compressed. The magnitude of the velocities near the top of the chromosphere (where the $H\alpha$ profile core is formed) can be estimated by the Doppler shift of line center.

Coronal measurements of the parameters come primarily from the soft X-ray data. The run of emission measure ($\sim n_e^2 V$, where n_e = coronal electron density, V = volume of the soft X-ray plasma) with temperature T_e is calculated in the fashion described in Paper I. This differential emission measure can be used to get the (total thermal energy)x(density), which is

$\sim 3n_e^2 kT_e V$. To get coronal pressures and densities from these, a volume must be estimated. We assume that the flare plasma is contained in magnetic loops with their footpoints in the photosphere. We can estimate the cross-sectional area of the loops by measuring the area of chromospheric brightenings, and the loop lengths are great enough to be resolved by the imaging detectors.

The peak power of nonthermal electrons is calculated from the flux and spectrum of hard X-rays, as measured by the HXRBS instrument. It is assumed that the hard X-ray radiation is generated by thick-target nonthermal bremsstrahlung. We divide this total power by an estimate of the beam area to get a value of P_{20} . This estimate comes from the number of H α pixels that show the signature of electron beam heating.

III. FLARE MORPHOLOGY

This flare took place in NOAA active region 2522, at S29 W15. The central distance was 0.56, *Solar-Geophysical Data* (1980) assigned an H α importance of SB, and the X-ray importance was M1. The major flare H α features are sketched and labeled in Figure 2a, along with the SPO and PCS fields of view and the photospheric magnetic neutral lines from Kitt Peak National Observatory magnetograms. Note that parts of the flare are outside the SPO field of view. The H α flare can be divided into four main regions of interest.

The north (N) region and east (E) region are compact brightenings with the same magnetic polarity, while the west (W) and central (C) regions form a long, thin strand in a region of opposite polarity. We divide the strand into two regions on the basis of off-band Big Bear Solar Observatory (BBSO) pictures, magnetic connections suggested in $H\alpha$, and profile differences observed by SPO. In particular, large postflare loops unambiguously show the connection between the east and central regions, and preflare fibrils and the photospheric magnetic field configuration strongly suggest that field lines connect the north and west regions. A fifth region, just east of the north kernel, appears later in the flare, but never gets very bright.

There is evidence that the flare was set off by the interaction of the two large loop systems, which we sketch in Figure 2b. The bulk of the soft X-ray emission is from the region where the loops come close to each other, over the eastern end of the $H\alpha$ strand. We will call this region the "interaction site". The soft X-ray emitting material was observed to spread out east and west from this site, as the loop systems filled with flare plasma. Other evidence for interaction between the loops, particularly chromospheric heating by nonthermal electrons at the footpoints, will be presented later. The N-W loops (those connecting the north and west $H\alpha$ regions) were outside the HXIS fine field of view, thus limiting the X-ray spatial resolution

there to 15", the FCS resolution. Most of the E-C loop system was within the fine field of view, however, so we were able to define the coronal loop geometry to a resolution of 8". The location of the loop seen in EXIS was the same as that of the postflare H α loops connecting the east and central regions, observed 30 minutes after the impulsive phase. A surge was observed in H α just east of the interaction site, possibly within the E-C loops, even before the impulsive phase. The maximum velocity of the H α -absorbing material, seen at the beginning of the impulsive phase, was measured at 120 km s⁻¹. The maximum velocity seen by the BCS was ~300 km s⁻¹. (The velocities quoted in this paper will always be line-of-sight). These results will be presented in detail later, during the discussion of chromospheric evaporation.

IV. PHYSICAL INTERPRETATION

a) Nonthermal Electrons

The hard X-ray burst began at 15:21:50 UT, as shown in the top light curve of Figure 3. Significantly, it is in our first observation after this time that we first notice enhancements of the H α profile wings in a number of pixels. As mentioned before, Stark wings are the signature of penetration of fast electrons into the chromosphere. These extensive wings last until ~15:24 UT, roughly the end of the impulsive phase. The hard X-ray emission after that time is likely to be the tail of the thermal

X-ray emission from the coronal plasma. The H α wings are seen most strongly in the north region, with a number of pixels in the west and central regions also affected. It should be noted that the hard X-ray resolution from HXIS (32") and the microwave resolution from VLA data (28", Kundu *et al.* 1984) in this area were too low for identification of electron beaming locations. An example of the temporal development of the profile from a pixel in the north region during the flare is shown in the left column of Figure 4, showing enhanced wings during the impulsive phase. The greater enhancement of the red wing is a well-known phenomenon (see, e.g., Svestka 1976), but its physical origin is controversial. We defer further discussion of the red asymmetry to a future paper, and only the blue wing will be used in this current study when measuring wing enhancements.

The power of electrons with energy above 20 keV was calculated from the HXRBS data, under the collisional thick-target assumption. The peak power, at 15:22:50 UT, was 5.0×10^{28} ergs per second, with a number flux of 1.4×10^{36} electrons per second. The spectral index was at its minimum value of 5.5 at this time, compared with ~ 6.5 during the rest of the impulsive phase. The power can be converted to a flux by estimating the beam area from the number of H α pixels showing extensive blue wing enhancements. Assuming that the part of the long strand outside the SPO field of view had similar

characteristics to the part we saw, we estimate that between 6 and 15 pixels received beamed electrons at maximum. An assumed area of 10 pixels gives us a flux of $F_{20} = 1.45 \times 10^{11}$ ergs cm^{-2} s^{-1} . In comparison, the value of F_{20} estimated from the $H\alpha$ profiles is roughly 10^{11} ergs cm^{-2} s^{-1} , which agrees with the HXRBS data to within our margin of error.

Many of the $H\alpha$ pixels in the north, west, and central regions show the signature of differential chromospheric expansion, brighter red $H\alpha$ peaks than blue. The north pixel profiles in Figure 4 near 15:23:17 UT show this feature clearly. Only a very small number of pixels show a compression signature, and then only for a brief time during the impulsive phase. The expansion is consistent with the idea that the chromosphere at this site is being heated by nonthermal particles. Had the primary flare effect been just enhanced thermal conduction, no such expansion would have been expected. Conduction is relatively ineffective in the chromosphere, where the temperature and the temperature gradient are very low compared to the transition region and low corona. The main effect of turning on enhanced thermal conduction is to evaporate off the top of the chromosphere, leaving the rest unperturbed. Beamed electrons can heat the entire flare chromosphere, leading to broad $H\alpha$ lines and expansion. The signature of expansion, like the extensive wings, disappears at

the end of the hard X-ray burst.

It should be mentioned that a number of published flare simulations with nonthermal electron heating indicate a compression of the residual chromosphere, rather than expansion. This is due to the evaporation of the top of the chromosphere, and the dramatic pressure increase that results. However, most of these calculations only model ~ 10 s of the flare, and many turn off the nonthermal electrons after just a few seconds (e.g., Somov, Spektor, and Syrovatskii 1977). The 15 s temporal resolution of our H α data largely precludes observations on these time scales. Kostyuk and Pikel'ner (1975), on the other hand, modeled the heating of the solar chromosphere with a nonthermal electron beam of 100 s duration, which is more applicable to this flare. They found a differentially expanding chromosphere, like we observed, after 40 s. Prior to that time, however, their velocity signal was mixed, making it difficult to predict the H α response.

Some recent flare simulations are more sophisticated, particularly with regard to radiative transfer effects and the ability to resolve steep gradients by regridding schemes. Some calculations based on the work of Fisher, Canfield, and McClymont (1984) indicate that chromospheric compression should exist only for 10-15 s for the high fluxes of nonthermal electrons observed in this flare, and should not exist at all for much lower fluxes ($F_{20} \leq 10^{10}$ ergs cm $^{-2}$ s $^{-1}$). An expansion phase would follow

the compression phase. Indeed, after only a few seconds, the magnitude of the compression velocity would be below what we can see with our H α profiles (~ 5 - 10 km s $^{-1}$). Given our time resolution, it is not surprising that we see so little compression. Hopefully, future observational work will address this question more completely.

It should be noted that there was no evidence for unidirectional beaming of the nonthermal electrons. Indeed, the chromospheric response at the footpoints shows that roughly equal numbers of electrons traveled in each direction within the N-W loop system. Any differences in the fluxes between the north region and the strand can plausibly be explained by the greater area of the strand (Figure 2b). The east region did not show any signature of electron beam heating, but this is understandable in view of the amount of material fast electrons would have to traverse coming from the loop interaction site. The east region is separated from the rest of the flare by more than an arc-minute. It is at the end of a system of long loops, estimated at 75,000 km in length (assuming semi-circular loops). It brightens 45-60 seconds after the first brightenings in the strand (see Figure 3). The lack of observable Stark wings in the H α profiles guarantees that the nonthermal electron flux is at least a factor of 10 below its value in the other regions. Given the loop density of 3×10^{10} cm $^{-3}$, as calculated from the soft X-ray emission

measure and a volume estimate from $H\alpha$, the total column number in the loop is over $2 \times 10^{20} \text{ cm}^{-2}$. The stopping depth for monoenergetic electrons of energy E (in keV) is $\sim 10^{17} \times E^2$. Thus, only those few electrons with energy greater than 45 keV would reach the chromosphere. It would have been very informative if hard X-ray emission had been detectable coming from this loop. Unfortunately, although the loop is easily seen by HXIS in its low energy channels, the counting statistics in the 22-30 keV channels are too low for unambiguous identification as nonthermal emission.

b) Enhanced Coronal Pressure

At least 2 minutes before the impulsive phase, a statistically significant rise in the soft X-ray flux is seen. This subsides temporarily, but begins to rise again ~ 20 -30 s before the hard X-rays begin. In addition, the total $H\alpha$ flux from a number of pixels near the loop interaction site begins to increase ~ 1 minute prior to the impulsive phase (see Figure 3). The $H\alpha$ increase is probably due to a small enhancement of the overlying coronal pressure. As stated previously, values of the pressure can be estimated from the depth of the $H\alpha$ central reversal. The pressure increases dramatically during the impulsive phase, with the enhancement over the $H\alpha$ strand leading the enhancement over the north region by ~ 1 minute. This increase is easily seen in the time sequence of profiles in Figure 4. Note

particularly the strand pixel. Prior to the flare, $H\alpha$ is an absorption line. By 15:22:17 UT, it is in emission, and the central reversal has disappeared by 15:22:47 UT. There is also an expansion signature, like that discussed earlier for the north pixel profiles. The lack of central reversal is seen in a few strand pixels from very near the impulsive onset, and is a common feature to all the strand within a minute. This signature of high pressure lasts for minutes, certainly well past our $H\alpha$ data cutoff at 15:26 UT. Notice the contrast in the depth of the central reversal between the strand pixel and the north pixel during the impulsive phase. The reversal fills in much more slowly in the north pixel, remaining until 15:24:17 UT.

Using the theoretical grid of profiles, such as those shown in Figure 1, we estimate the maximum pressure over the strand to be roughly $400-1000 \text{ dynes cm}^{-2}$. The pressure over the north region also reaches these values at the end of the impulsive phase. These pressures can also be calculated from the soft X-ray data once the loop volume has been estimated. An upper limit on the north-south extent of the loop footpoints can be established by the fact that only one row of $H\alpha$ pixels is affected. This gives a maximum north-south extent of $2.56''$. The strand is long enough to cross an entire $15''$ FCS pixel. Assigning a rough figure of $15''$ to the length of a loop inside an FCS pixel gives a volume of $2.56 \times 15'' \times 15''$, or $2.2 \times 10^{26} \text{ cm}^3$. Combined with the emission

measure and (thermal energy)x(density) measurements, this gives a lower limit on the pressure over the strand of ~ 200 dynes cm^{-2} . The lower limit on the coronal density in this loop system can be computed from the same volume estimate to be $\sim 10^{11}$ cm^{-3} . The true pressure would be larger if the filling factor for the $H\alpha$ pixels were less than 1, so the coronal and chromospheric pressure estimates match fairly well.

The east region also shows the signature of enhanced coronal pressure, after some delay. Brief increases in pressure values are seen starting at 40 s after the hard X-ray onset, but long-lasting pressure effects are not seen until 2-3 minutes into the impulsive phase. The maximum pressure, as measured by both $H\alpha$ and soft X-ray data at $\sim 15:25$ UT, was ~ 100 dynes cm^{-2} . An increase in the coronal density was observed, as well as an increase in the temperature, but it is not possible to determine whether the material was evaporated from the east region or was transported from the central region through the long loops. We speculate that coronal plasma is initially heated over the west and central $H\alpha$ regions, and a thermal conduction front or hydrodynamic shock transports energy through magnetic loops to other regions.

It is instructive to calculate typical velocities and get the time scales for pressure equilibrium to be established in the loops. The sound speed in the corona is given by $125\sqrt{(T_e/10^6)}$ km s^{-1} . Taking the temperature to be 15×10^6 K,

we get $c_s \approx 500 \text{ km s}^{-1}$. Combining this with the loop lengths that we have estimated, we expect pressure differences between the east and central regions to exist for over two minutes, and between the north and west regions for ~ 1 minute. This is exactly the behavior observed in $H\alpha$. Although the velocities of conduction fronts and hydrodynamic shocks are difficult to calculate accurately without knowing the exact plasma conditions, typical Mach values for each are 2 or 3. This is consistent with the propagation time for the disturbance that caused the chromospheric response in the east region. However, fast electrons may have also played a role in this, even though they did not penetrate the chromosphere there in significant numbers.

In the decay phase of the flare, a drop in the coronal pressure was noted in both soft X-ray and $H\alpha$ data as the plasma cooled. By 15:45 UT, roughly half an hour after the impulsive phase, the plasma in the long E-C loop system had cooled to the point that it was absorbing $H\alpha$. These postflare loops persisted for at least an hour, as shown by BBSO $H\alpha$ movies. No obvious postflare loops were seen connecting the north and west regions.

c) Chromospheric Evaporation by Thermal Conduction and Nonthermal Electrons

The temperature of the coronal plasma at the loop interaction site increased to $\sim 15 \times 10^6 \text{ K}$ at the time of the

flare. This value comes from the peak of the high temperature part of the differential emission measure curve. A temperature increase leads to enhanced thermal conduction, which may evaporate enough of the chromosphere to provide the observed increases in the coronal density and pressure. To calculate the density enhancement due to evaporation, we must estimate the change in the transition region column depth. The rate of evaporation can be estimated by assuming that all the conductive flux goes into heating and expanding the evaporated material, ignoring radiation. Thus, the conductive flux would be equal to the enthalpy flux. Using a loop scaling law to relate the conductive flux to the apex temperature, An *et al.* (1983) and Antiochos and Sturrock (1978) have derived the following:

$$\kappa_0 T_A^{7/2} / (L/2) = 5k T_A \dot{N}_{tr} .$$

Thus,

$$\dot{N}_{tr} = dN_{tr}/dt = \kappa_0 T_A^{5/2} / [5k(L/2)] \quad (1)$$

and the total number of evaporated atoms will be

$$N_{tr} = \dot{N}_{tr} \Delta t . \quad (2)$$

(T_A = apex temperature, L = total loop length, N_{tr} = transition region column depth in cm^{-2} , $\kappa_0 \approx 10^{-6}$, $k = 1.38 \times 10^{-16}$, Δt = time from flare start to time of maximum loop density). The length of the N-W loops is $\sim 30,000$ km, and the maximum density was reached

2 minutes after flare start. For these parameters, we get:

$$\dot{N}_{tr} = 8.42 \times 10^{17} \text{ cm}^{-2} \text{ s}^{-1}$$

and $N_{tr} = \dot{N}_{tr} \times 120\text{s} = 1.01 \times 10^{20} \text{ cm}^{-2},$

giving a density of

$$n = N_{tr}/(L/2) = 6.7 \times 10^{10} \text{ cm}^{-3}.$$

This should be compared with the observed density in these loops of 10^{11} cm^{-3} . Radiative losses can be shown to be only a few percent of the conductive flux, but the above calculations are very sensitive to the coronal temperature. Since we used a relatively low temperature, perhaps the amount of evaporation given above should be considered a lower limit.

We can also estimate the evaporation due to the nonthermal electrons. McClymont, Canfield, and Fisher (1984) have derived the following formula for the transition region column depth, assuming that evaporation continues until nonthermal electron heating is balanced by radiation at 10^5 K :

$$N_{tr} = [C(\delta)F_c / (P_A + MgN_{tr})]^{2/\delta} \quad (3)$$

where $C(\delta) = [kT_5(\delta-2)B(\delta/2, 1/3)/(3f_5)] N_c^{(\delta/2 - 1)}$.

(P_A is the apex gas pressure, $M=1.56m_H$, g is solar gravity, F_c is the electron energy flux above a sharp cutoff, $T_5=10^5 \text{ K}$, δ is the

spectral index of the electron number spectrum, B is the complete beta function, f_5 (the radiative loss coefficient at 10^5 K) = 7×10^{-22} ergs $\text{cm}^3 \text{s}^{-1}$, N_c (the stopping depth for electrons at the cutoff energy) = $9.16 \times 10^{16} (E_c/1 \text{ keV})^2$. If $N_{tr} < N_c$, then this formula gives an upper limit.

This can be solved easily by successive approximations, usually with less than 10 iterations. For this flare we assume an energy cutoff of 20 keV, and get an upper limit on the amount of evaporation by choosing a lower limit for the apex pressure of $100 \text{ dynes cm}^{-2}$. Using the observed quantities $\delta = 6.5$, $F_{20} = 10^{11}$ ergs $\text{cm}^{-2} \text{s}^{-1}$, and $L = 3 \times 10^9$ cm, we get:

$$N_{tr} \leq 4.1 \times 10^{19} \text{ cm}^{-2}$$

and $n \leq 2.7 \times 10^{10} \text{ cm}^{-3}$.

The correct density is probably within a factor of 2-3 of this upper limit.

We see that evaporation by fast electrons can be significant, but is less important than evaporation by thermal conduction. Equations (1) through (3) can be used to show that in smaller, hotter flares, the difference between the two can be more than an order of magnitude. Since this is a relatively large, cool flare, we would expect thermal conduction to usually dominate the evaporation process.

In Paper I, we had estimated the amount of evaporation by comparing observed $H\alpha$ profiles to those of empirical flare models. This was based on a relationship inferred from the work of Dinh (1980) between the $H\alpha$ central reversal and the column depth of the transition region. However, Dinh had assumed that the apex gas pressure ($P_A \approx 2n_0 kT_A$) was negligible compared to the gravitational pressure (MgN_{tr}). In fact, the gas pressure term often dominates the total pressure. Thus, we feel that the chromospheric evaporation argument advanced in the present paper is on a sounder physical basis than that of Paper I.

d) Evaporation Estimate from X-Ray Blue Shifts

Another way to address the chromospheric evaporation question is through observed mass flux of the hot plasma. Velocities are determined from the BCS Ca XIX spectra. A Gaussian, centered on the rest position of the line, is fit to the red side, and the mean wavelength shift of the blue excess gives the velocity. This velocity, the total blue excess flux, and the flux inside the Gaussian are plotted in Figure 5. Velocities before 15:22:24 UT are uncertain due to poor count statistics. The velocity of the blue-shifted material during the impulsive phase is 200-300 km s⁻¹. During this time, the observed Ca XIX line profile is extremely nonGaussian and blue asymmetric. The red wing is enhanced as well, probably due to turbulence. The velocity drops after the impulsive phase, but it is significant

to note that there are still velocities of $\sim 150 \text{ km s}^{-1}$ at least 2 minutes after the majority of the nonthermal electron heating. We have already shown that pressure equilibrium can be established in the N-W loops, where most of the evaporation is taking place, in ~ 1 minute. Thus, we believe that evaporation is still taking place after the end of the impulsive phase, driven by thermal conduction from the hot plasma created earlier.

With the typical loop lengths in this flare of $\sim 30,000 \text{ km}$, and the velocities given above, the movement of a given parcel of material cannot exist for more than ~ 1 minute. Thus, we sum the emission measures of the blue-shifted component minute by minute through the period of significant blue shift. This gives a total emission measure of $\sim 3 \times 10^{49} \text{ cm}^{-3}$ for the upward-moving material. This matches the emission measure of the stationary material, measured by FCS to be $\sim 10^{50} \text{ cm}^{-3}$, to within the factor of 5-10 uncertainty for this method. Thus, in agreement with Feldman *et al.* (1980) and Antonucci *et al.* (1982), the BCS results are consistent with the evaporation picture in which chromospheric material is heated to coronal temperatures and expands upward into the overlying loops, providing the observed density enhancement there.

V. CONCLUSIONS

The data for this flare, both coronal and chromospheric, point towards a release of energy due to the interaction of two loop systems. Although we cannot determine whether magnetic reconnection took place between the loops, or whether each loop separately underwent instability, the simultaneity of energy release in the loops is strongly indicative of some interaction. The initial, and strongest, soft X-ray flux increase takes place at the interaction site. Enhanced pressure and chromospheric evaporation are seen at the footpoints of both sets of loops, and the corona and chromosphere are approximately in pressure balance. Chromospheric evaporation can provide the observed coronal density enhancement, with thermal conduction dominating over nonthermal electrons in the evaporation process. Strong evidence is seen in the wings of H α for the penetration of fast electrons into the chromosphere, and the nonthermal bremsstrahlung radiation expected from the electron energy flux inferred from H α matches the observed power in hard X-rays. There is no need for a $\sim 10^8$ K plasma component to provide additional hard X-rays. Electrons were apparently beamed in both directions within one loop system, and no evidence for unidirectional particle beaming was seen anywhere in the flare. Flare energy was transported to remote regions, away from the interaction site, by fast particles and either thermal conduction or hydrodynamic

flows. As is often the case in solar flares (Svestka 1976), a moderate amount of energy release took place before the existence of a large flux of impulsive nonthermal electrons.

Two interesting possibilities for future work arose from the study of this flare. Our limited $H\alpha$ time resolution prevented us from studying the temporal development of chromospheric compression and expansion in more detail. Fortunately, advances in the observational instrumentation at SPO will allow us to obtain spectra every few seconds. This should permit us to see the first stages of chromospheric heating and find the time dependence of any observed velocities. Also, this higher time resolution will make it possible to look for the signature of impulsive heating. A second question arose concerning the mechanism of the enhanced red wing of $H\alpha$. This effect can be seen in a number of the flares we observed during May and June 1980. We will explore the time development, morphology, and theory of this phenomenon in a future paper.

The authors wish to thank a number of individuals whose contributions were invaluable to the study of this flare. Dr. Harold Zirin provided $H\alpha$ movies, the EXIS team provided X-ray images and analysis, Dr. John W. Harvey of Kitt Peak National Observatory provided magnetograms, and Mr. Horst Mauter and Mr. Philip Wiborg were particularly helpful at SPO.

The UCSD work was supported by the United States Air Force Office of Scientific Research under grant 82-0092, and by the National Aeronautics and Space Administration under grant NSG-7406. The Lockheed work was supported by NASA under Contract NAS 5-23758 and by the Lockheed Independent Research Program. The SMM-XRP experiment has been developed jointly between Lockheed, Mullard Space Science Laboratory and the Rutherford-Appleton Laboratory. The Goddard work was supported by NASA under Contract NAS 5-26439.

REFERENCES

- Acton, L. W. *et al.* 1980, *Solar Phys.*, **65**, 53.
- Acton, L. W., Canfield, R. C., Gunkler, T. A., Hudson, H. S.,
Kiplinger, A. L., and Leibacher, J. W. 1982, *Ap. J.*,
263, 409.
- An, C. H., Canfield, R. C., Fisher, G. H., and McClymont, A. N.
1983, *Ap. J.*, **267**, 421.
- Antiochos, S. K., and Sturrock, P. A. 1978, *Ap. J.*, **220**,
1137.
- Antonucci, E. *et al.* 1982, *Solar Phys.*, **78**, 107.
- Brown, J. C. 1971, *Solar Phys.*, **18**, 489.
- Canfield, R. C., Gunkler, T. A., and Ricchiazzi, P. J. 1984,
Ap. J., **282**, 296.
- Cheng, C.-C., Feldman, U., and Doschek, G. A. 1981, *Astr. Ap.*,
97, 210.
- Chubb, T. A., Kreplin, R. W., Friedman, H. 1966, *J. G. R.*,
71, 3611.
- Craig, I. J. D., McClymont, A. N., and Underwood, J. E. 1978,
Astr. Ap., **70**, 1.

Dere, K. P., and Cook, J. W. 1979, *Ap. J.*, 229, 772.

Dinh, Q.-V. 1980, *Pub. Astr. Soc. Japan*, 32, 515.

Feldman, U., Doschek, G. A., Kreplin, R. W., and Mariska, J. T.
1980, *Ap. J.*, 1241, 1175.

Fisher, G. H., Canfield, R. C., McClymont, A. N. 1984, *Ap. J.*
(*Letters*), 281, L79.

Heyvaerts, J., Priest, E. R., Rust, D. M. 1977, *Ap. J.*,
216, 123.

Hummer, D. G., and Rybicki, G. 1968, *Resonance Lines in Astrophysics*,
Boulder: NCAR.

Kostyuk, N. D., and Pikel'ner, S. R. 1975, *Soviet Astr.*, 18,
590.

Kundu, M. R., Machado, M. E., Erskine, F. T., Rovira, M. G., and
Schmahl, E. J. 1984, *Astr. Ap.*, 132, 241.

McClymont, A. N., Canfield, R. C., and Fisher, G. H. 1984, *Ap. J.*,
submitted.

Orwig, L. E., Frost, K. J., and Dennis, B. R. 1980, *Solar Phys.*,
65, 25.

Ricchiazzi, P. J., and Canfield, R. C. 1983, *Ap. J.*, 272,
739.

Solar-Geophysical Data: 1980, No. 431, Part 1 (Boulder: NOAA Environmental and Information Service).

SOMOV, B. V., SPEKTOR, A. R., and SYROVATSKII, S. I. 1977, *Izv. Akad. Nauk. SSSR, Phys. Sec., Ser. fiz.*, **41**, 273.

Spicer, D. S. 1977, *Solar Phys.*, **53**, 305.

Sturrock, P. A. 1974, *Flare-Related Magnetic Field Dynamics*, Boulder: HAO, p. 187.

Svestka, Z. 1976, *Solar Flares* Dordrecht: Reidel, pp. 10, 118.

van Beek, H. F., Hoyng, P., Lafleur, B., and Simnett, G. M. 1980, *Solar Phys.*, **65**, 39.

Fig. 1.-- The effects of various physical processes on theoretical $H\alpha$ profiles (from CGR).

(a) As the coronal pressure (P_0) is increased, the central reversal disappears. The conductive flux at 10^5 K (F_5) and the energy flux of nonthermal electrons (F_{20}) are held fixed.

(b) As the flux of nonthermal electrons above 20 keV is increased, the $H\alpha$ profile develops extensive Stark wings. The amount of central reversal is not greatly affected. The conductive flux and coronal pressure are held fixed.

Fig. 2a.-- Sketch of the $H\alpha$ flare along with the SPO and FCS fields of view and the photospheric magnetic neutral lines (dashed lines). The bright $H\alpha$ regions are outlined and labeled, and a dark filament is drawn for reference. The squares in the lower right-hand corner of each field of view show the respective pixel sizes.

Fig. 2b.-- Hypothesized coronal loop structure, showing two large arcades of loops. The loops connecting the east and central $H\alpha$ regions were seen as postflare $H\alpha$ loops. The loops connecting the north and west regions were seen as preflare fibrils. Note that the

north $H\alpha$ region was displaced upward to make the field lines clearer.

Fig. 3.— Light curves for hard X-rays (top panel), soft X-rays (middle panel), and $H\alpha$ excess relative to preflare (averages of pixels in the north (N), strand (S), and east (E) regions, bottom panel).

Fig. 4.— $H\alpha$ profiles from the SPO observations. Each column is a time sequence of profiles from a single pixel. The left column is a pixel from the north $H\alpha$ region, and the right column is a pixel in the strand, near the west-central interface. The spectral range is $H\alpha \pm 4.8 \text{ \AA}$, and the distance between tick marks represents half the quiet sun continuum intensity. Each profile extends from the left vertical line to the small vertical dash at the right. A straight line connects the right end of each profile to the $I/I_c = 1.0$ point for that profile. Times during the impulsive phase are underlined.

Fig. 5.— The unshifted Gaussian soft X-ray flux in the Ca XIX line (thin curve), the excess to this Gaussian on the blue side of the line (thick curve), and the velocity of the blue-shifted material (broken curve).

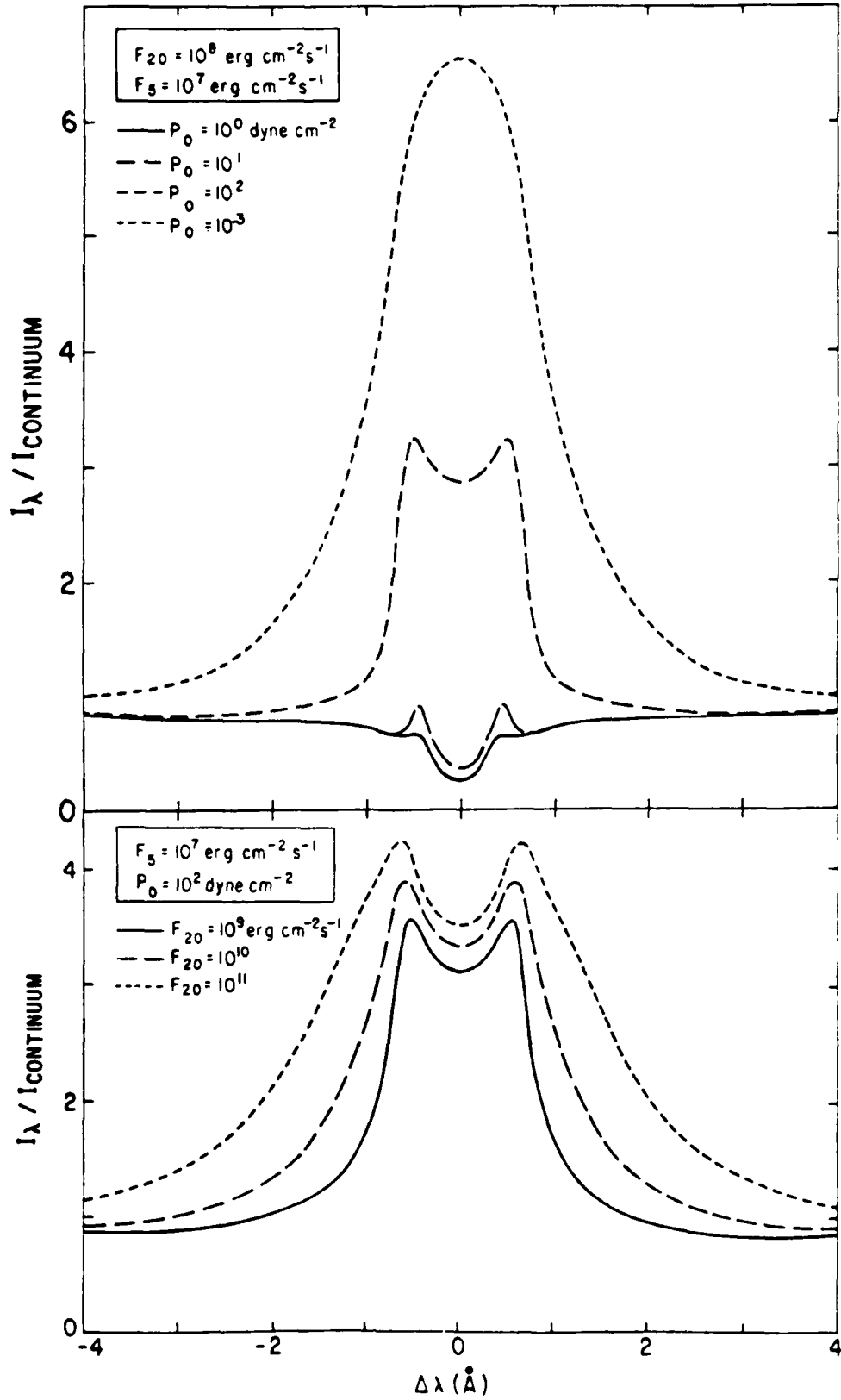


figure 1.

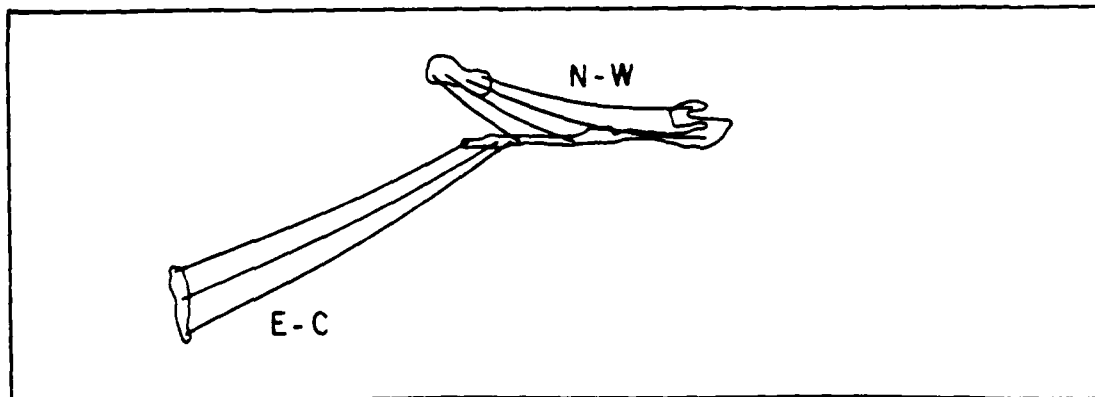
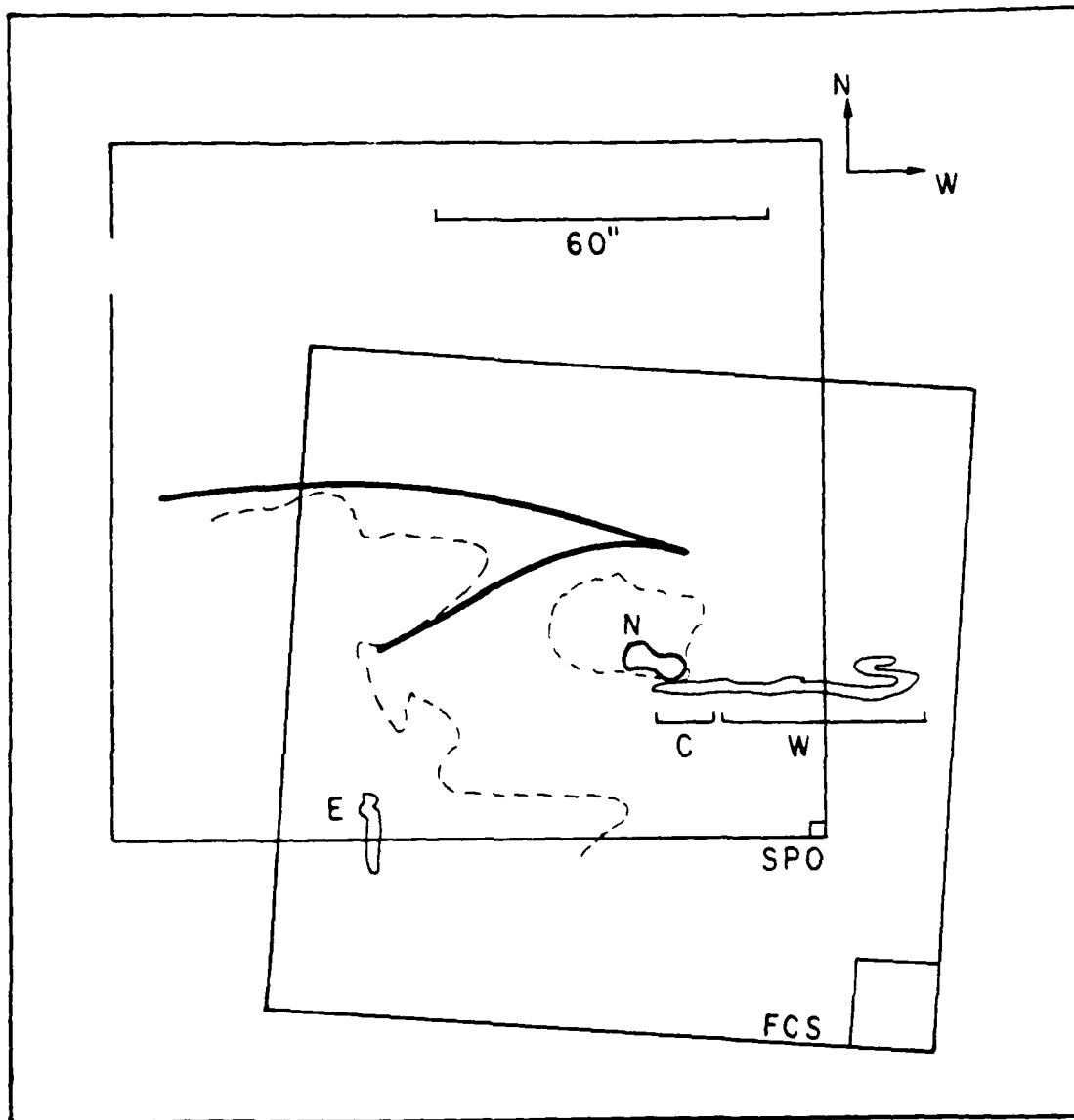


Figure 2.

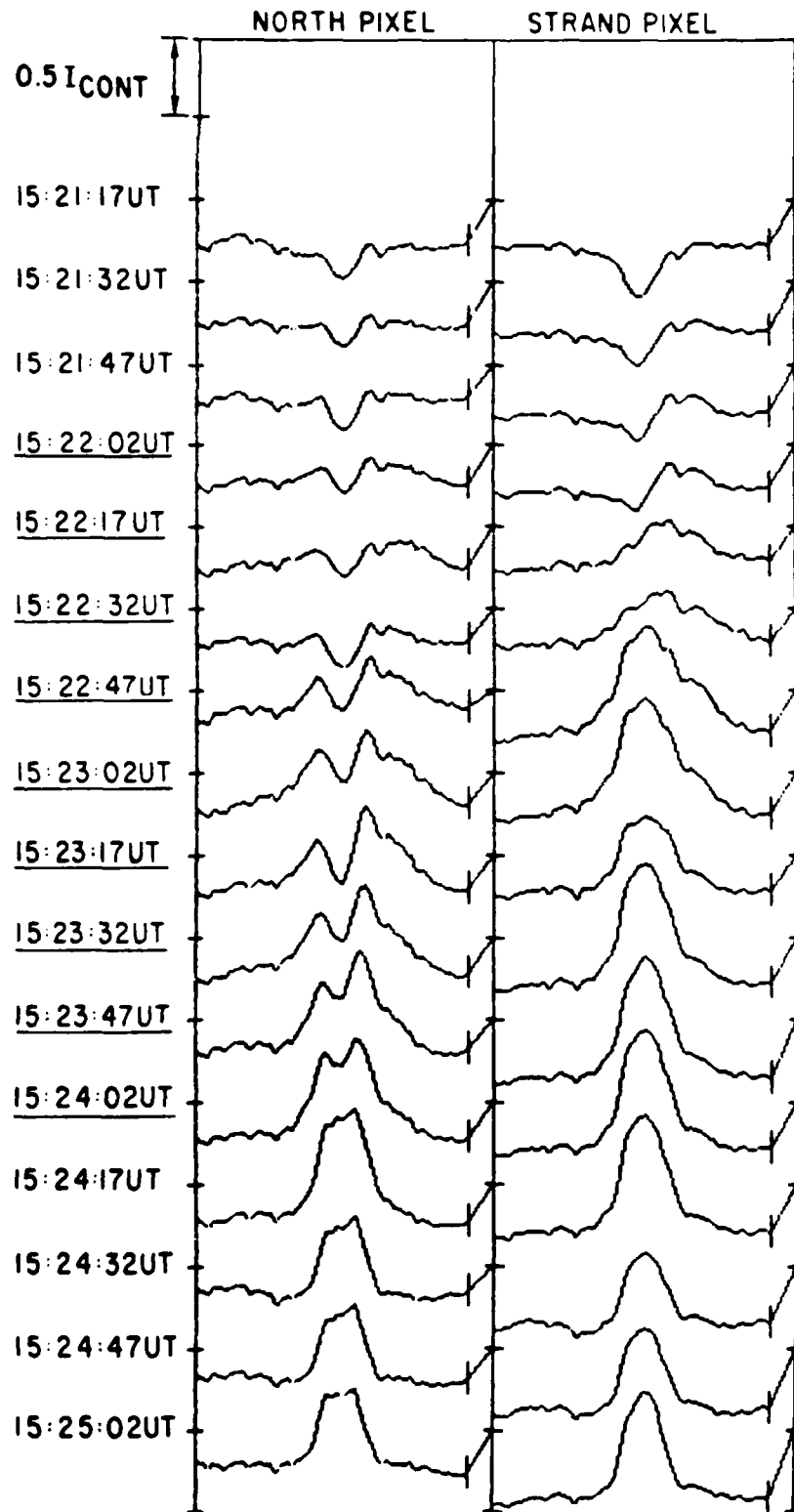


Figure 3.

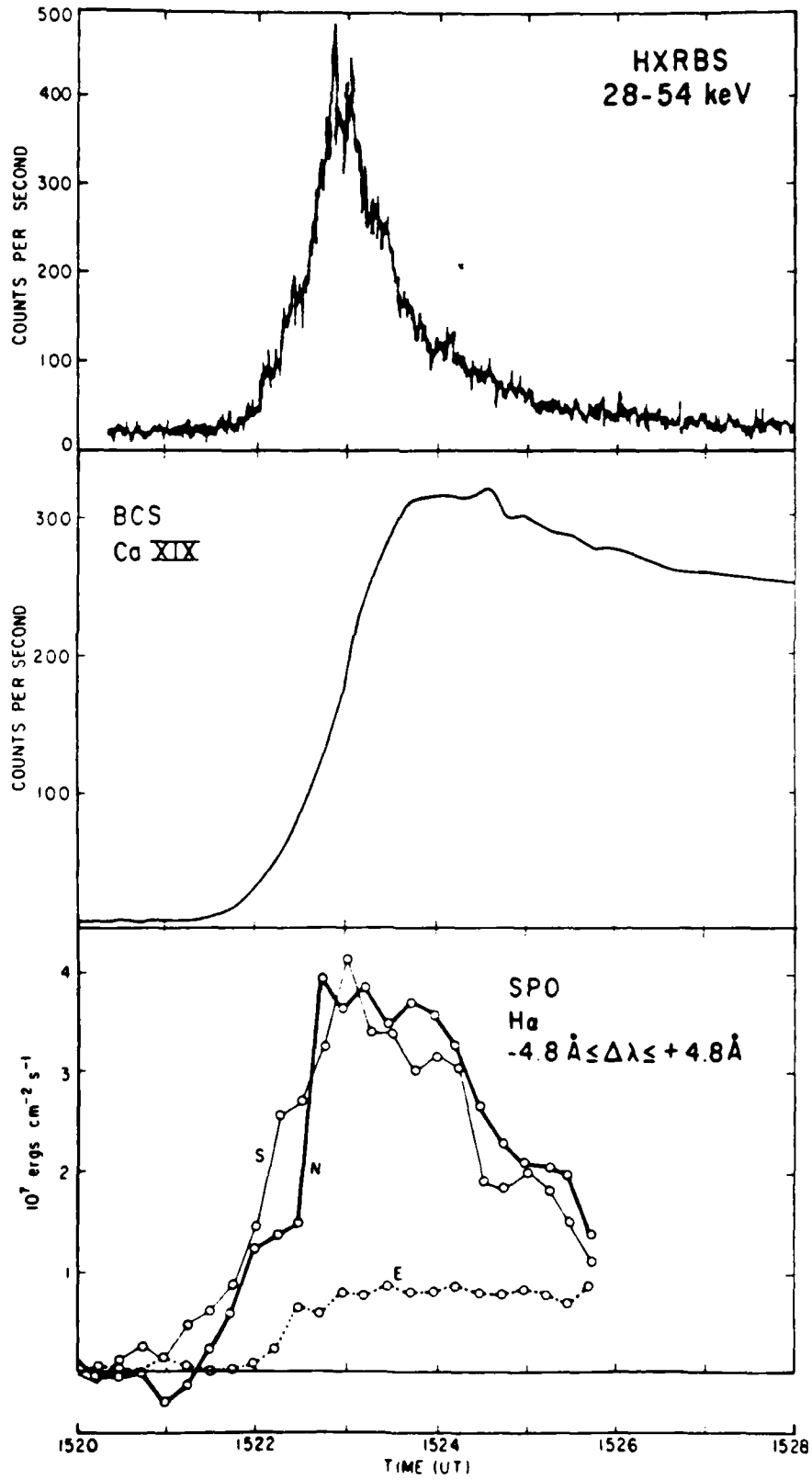


Figure 4.

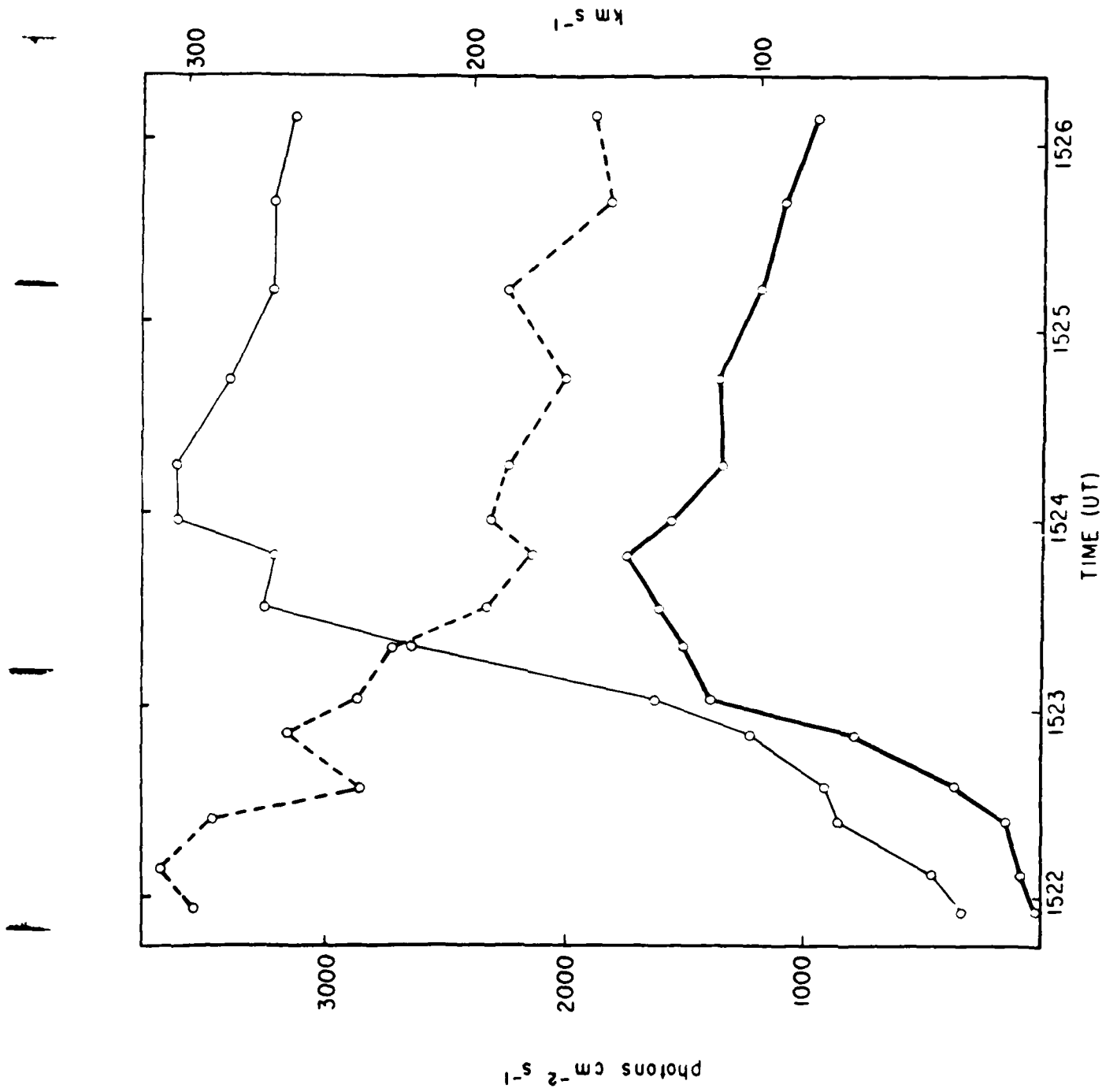


Figure 5.

AUTHORS' ADDRESSES

Loren W. Acton

52/12, Bldg. 255

Lockheed Palo Alto Research Laboratory

3251 Hanover St.

Palo Alto, CA 94304

Richard C. Canfield and Todd A. Gunkler

Mail Code C-011

University of California, San Diego

La Jolla, CA 92093

Alan L. Kiplinger

Code 602.6

Laboratory for Astronomy and Solar Physics

NASA - Goddard Space Flight Center

Greenbelt, MD 20771

Submitted to Ap. J. July 1984

SG&RC7MA

SP-84-08 Rev.

ENERGETIC ELECTRON HEATING
AND CHROMOSPHERIC EVAPORATION
DURING A WELL-OBSERVED COMPACT FLARE

Richard C. Canfield and Todd A. Gunkler¹

Center for Astrophysics and Space Sciences
University of California, San Diego

Received 1984 April 23; _____

Subject Headings: Sun:Flares - Line Profiles

¹: Now at Delta College

ABSTRACT

From the Solar Maximum Mission (SMM) and Sacramento Peak Observatory (SPO) we observed the compact solar flare of 7 May, 1980, previously studied by Acton *et al.* (1982) and Simnett (1983), with spatial, spectral and temporal resolution in both X-rays and H α profiles, throughout the impulsive phase. We have compared the observed flare H α profiles to theoretical H α profiles based on physical models of chromospheric flare processes and model parameters inferred from the X-ray observations.

We find that:

(1) The observed H α profiles show the theoretically predicted enhanced-wing signature of nonthermal electrons, well correlated in space and time with hard X-ray emission, for values of electron energy flux in agreement with the thick-target interpretation of the observed hard X-ray emission;

(2) Coronal pressure values inferred from the observed central reversals of the kernel H α profiles agree well with the values inferred from the analysis of soft X-ray data, at the end of the impulsive phase (the approximate time of maximum thermal X-ray emission measure);

(3) The dominant chromospheric evaporation mechanism is thermal conduction. This process successfully accounts for the measured coronal pressure at the time of maximum emission measure. Chromospheric evaporation driven by thick-target nonthermal electron heating is insufficient.

Subject headings: line profiles -- Sun: chromosphere -- Sun: flares

I. INTRODUCTION

There is no doubt that energetic electrons (with characteristic energy much greater than that of the 1-2 keV thermal flare electrons) exist during solar flares; well-known observational consequences include nonthermal hard X-rays and microwave radiation and the presence of the electrons themselves in interplanetary space. The physical mechanisms and morphology of the acceleration and transport of these electrons are topics of considerable interest in current solar flare research. It is believed that these electrons are accelerated in the corona and produce hard X-ray radiation by nonthermal bremsstrahlung as they are stopped at the feet of coronal loops (the so-called thick-target model, Brown 1971). Hard X-ray imaging observations (at energies greater than about 20 keV) tend to support this picture in flares in which the hard X-ray emission is impulsive (Duijveman and Hoyng 1983; Ohki *et al.* 1983). Substantial hard X-ray emission appears to come from 2 or more points, which can be identified with the feet of coronal loops, relatively low in the atmosphere, when limb events have been observed (Ohki *et al.* 1983)

From the point of view of particle transport theory, it is important to know whether the primary mechanism for stopping these fast particles is collisional, *i.e.*, Coulomb collisions with the ambient solar atmosphere, or whether noncollisional (say wave-particle) effects significantly modify the particle transport. Hard X-ray *direct imaging* observations, which presently claim spatial resolution of 7-8" (5000-6000 km at the sun), are not adequate to spatially resolve the distribution of emission if the stopping occurs in the chromosphere, whose density scale height is an order of magnitude smaller than the

instrumental resolution. Up to the present time, the most quantitative observational test of the collisional thick-target hypothesis is 2-spacecraft observation of nonimaged X-rays (Kane *et al.* 1983). These measurements of X-rays above 100 keV, simultaneously from 2 spacecraft, of flares partially occulted (by the solar limb) from one of the spacecraft, agree approximately with the predicted altitude dependence of collisional thick-target emission (Brown and McClymont 1975).

An independent test of the collisional thick-target model is to look for the heating effects of the collisions in chromospheric line profiles. An improved application of this approach is enabled by recent physical models of chromospheric energy balance during solar flares. Ricchiazzi and Canfield (1983) solved the equations of static energy balance, hydrostatic equilibrium, radiative transfer and atomic statistical equilibrium in a 1-dimensional theoretical model chromosphere. To make the problem computationally more tractable, and conceptually more simple, they neglected dynamic effects, on the grounds that such effects are of second-order importance for at least some, but certainly not all, of the chromospheric phenomena of interest. Their models show the effects of collisional heating by energetic nonthermal electrons, classical thermal conduction, and enhanced coronal pressure. Using these model atmospheres, as well as impulsive model atmospheres that apply only for the first few seconds of impulsive bursts, before significant chromospheric mass motions can develop, Canfield, Gunkler, and Ricchiazzi (1984), henceforth CGR, determined the theoretical H α spectral signatures of these processes. Hence, we can examine observations of profiles of the H α line during impulsive hard X-ray flares to see whether or not they show the predicted H α profile response to any

of these processes, we then see if the chromospheric response is consistent with the thermal and nonthermal X-ray observations and the collisional thick-target model.

In this paper we extend our previous analysis of chromospheric evaporation in the flare of 7 May, 1980 (Acton *et al.* 1982, henceforth Paper I) in which we showed, using empirical flare chromospheric models, that chromospheric evaporation can account for the thermal X-ray plasma of this flare. Recent work by Kiplinger *et al.* (1983) confirms that the hard X-ray emission of this flare was highly impulsive and nonthermal, leading us to believe that there might be nonthermal electron heating effects in the chromosphere. Hard X-ray images of this flare are available (Paper I and Simnett, 1983), so we have observational constraints on where these effects should appear. In this paper we also return to the issue of chromospheric evaporation, but for the interpretation we use physical model atmospheres, not empirical ones. We conclude that the imbalance between chromospheric and coronal pressures found in Paper I is due to a problem with the empirical models; pressure imbalance is not implied when the observations are interpreted using the physical models.

II. NONTHERMAL ELECTRON HEATING

We begin by discussing the way the H α profile should respond to thick-target nonthermal electron heating, using previous theoretical modeling. We show that broad Stark wings are the *theoretically* expected response, above moderately high values of the input nonthermal-electron energy flux. Then, in § b), we examine the observed spatial and temporal behavior of H α profiles and hard X-

rays during the impulsive phase, concluding that broad H α wings are closely related *observationally* to hard X-rays. Finally, § c), we show that the observed *width* of impulsive phase H α wings supports the thick-target nonthermal electron heating picture.

a) Theoretical H α Profiles

In CGR we modeled the effects of nonthermal electron heating on the profile of the H α line in 2 static approximations. We showed that in both the hydrostatic and impulsive models, only high values of the input flux of nonthermal electrons produce H α profiles with obvious broad Stark wings. The nonthermal electron flux is measured by F_{20} , the energy flux above 20 keV at the point of injection. We measure the column number density (the number of hydrogen nuclei per unit area) from this point, assumed to be the loop apex. The absence of such wings precludes heating with values of $F_{20} \geq 10^{10}$ ergs cm $^{-2}$ s $^{-1}$. The calculations show Stark wings both in the impulsive approximation, which applies for the first few seconds, and in the hydrostatic approximation, which applies after chromospheric mass motions have died out (after at least several tens of seconds). Approximately isotropic mass motions directly observed in chromospheric line profiles during flares are not large enough to account for H α wings as broad as those observed (see Canfield 1982, and below). We therefore expect that the presence of such wings is the signature of nonthermal electron heating throughout the temporal development of flares.

Figure 1 shows theoretically predicted H α profiles, from CGR, for various values of F_{20} . The upper panel shows profiles in the impulsive approximation,

for 4 different values of F_{20} , and a fixed value, F_5 , of the conductive flux at 10^5 K. The lower panel shows profiles in the hydrostatic approximation, for 3 different values of F_{20} , and fixed values of F_5 and the coronal apex pressure, P_0 . These calculations lead us to believe that if nonthermal electrons of sufficient intensity are present in the chromosphere during flares, we should expect broad H α wings at points in space and time associated with sufficiently intense hard X-rays. The figure shows that H α will have broad wings, with flare excesses at the level of 10% or more, extending into the extreme wing region (beyond $\pm 3 \text{ \AA}$).

b) Impulsive-Phase Observations

The key X-ray observations for this study of nonthermal electron heating are the SMM hard X-ray observations of the Hard X-Ray Burst Spectrometer (HXRBS, Orwig, Frost, and Dennis 1980) and the Hard X-Ray Imaging Spectrometer (HXIS, van Beek *et al.* 1980). The HXRBS is a large-area proportional counter sensitive to spatially unresolved solar X-radiation in the energy range 28-470 keV, with an instrumental time resolution of 128 ms. The HXIS is an array of mini-proportional counters that provides simultaneous spatial and spectral information in spatial pixels of 8" half-width in six energy bands from 3.5 to 30 keV.

Our impulsive-phase H α line profile observations were obtained using a charge-coupled device (CCD) array of 100 by 100 pixels in the focal plane of the Echelle Spectrograph of the Vacuum Tower Telescope (Dunn 1969, 1971) at SPO. The flare was observed with 2" x 2.67" spectroheliogram image pixels; each is

observed for 0.25 s at 25.6 s intervals. For each image pixel there are 50 spectral pixels of width $204 \text{ m}\text{\AA}$ over a 10 \AA window centered on $\text{H}\alpha$. Further details of the $\text{H}\alpha$ data acquisition are given in the Appendix of Paper I.

The temporal relationship between the SPO $\text{H}\alpha$ and HXRBS X-ray measurements is shown in Figure 2. The impulsive hard X-ray phase of this flare consisted of 2 periods of multiple impulsive bursts. The first extended from 145603 to 145612 UT and the second from 145624 to 145647. The times of $\text{H}\alpha$ profile measurement, shown by open circles, include 145616, between the 2 burst periods, and 145642, during the second burst period.

The spatial relationship between the SPO $\text{H}\alpha$ pixels and HXIS X-ray pixels is shown in Figure 3. The two large contiguous squares, one above the other, which together appear to frame each panel, are the 2 HXIS pixels in which somewhat over half of the 16-30 keV X-rays were detected. As in Paper I, we consider the impulsive phase as a whole, to accumulate higher photon counts. The alignment of $\text{H}\alpha$ and HXIS pixels is that of Paper I, in which it was shown that $38 \pm 3\%$ of the impulsive phase 16-30 keV photons came from the southern (lower) HXIS pixel, $15 \pm 2\%$ from the northern, and the balance predominantly at the level of roughly 6-8% from surrounding pixels. The 2 HXIS pixels shown in Figure 3 are pixels 5 and 8 of Paper I. A spatially deconvolved image, removing the effect of a triangular point response function of $8''$ full-width half-maximum, has been published by Simnett (1983); these same two pixels are his pixels 197 and 196, respectively.

We now focus our attention on those SPO $\text{H}\alpha$ pixels that show substantial $\text{H}\alpha$ wing enhancement. The $\text{H}\alpha$ line profiles of all such pixels are shown in Figure 3,

along with a few other less-disturbed pixels for comparison. The profiles of each pixel are plotted within the small rectangle that represents the pixel (both location and dimensions) in the spectroheliogram. This information is given at five indicated times spanning the impulsive hard X-ray burst period. Each H α pixel contains not only the profile observed at the given time, but also (lighter dotted curve) the profile observed in that pixel at 145525.38 s before the start of the first impulsive hard X-ray burst period. The H α flare kernels are indicated by the shaded pixels in Figure 3; they were defined as all pixels whose peak H α power (measured by integrating over $-5 \leq \Delta\lambda \leq +5\text{\AA}$) reached or exceeded half that of the brightest pixel. This, of course, need not have anything directly to do with nonthermal electron heating or the presence of wings. At 145616 UT North kernel pixel (40,42) shows relatively little wing development, while pixel (37,45), outside the South kernel, shows about the same core intensity but much more extensive wings.

Neglecting, for the moment, the matter of wing development, one might ask what we find to be the relationship between the relative power output of the 2 kernels in H α and hard X-rays. The observed ratio of impulsive south kernel to north kernel brightness in 16-30 keV X-rays (see above) is in the range 2.1-3.2, based on the count statistics derived in Paper I. The impulsive phase south-to-north ratio in H α , at the time of simultaneous impulsive X-ray emission and H α observation (145642 UT), is 2.9. Hence, the observed power ratios in the two different emissions agree to within observational uncertainty. In view of the sensitivity of H α power to pressure (see Figure 4), we feel that this agreement is of little direct relevance to the nonthermal electron heating of the chromosphere.

It is interesting to note that the relationship between H α kernel size and wing development is the same as that found by Neidig (1981); the larger kernel shows stronger wing development. Neidig interpreted this in terms of an asymmetric loop, in which electrons mirror above the chromosphere at the end at which the magnetic field lines are more strongly convergent, but enter the chromosphere and are stopped at the other end, producing H α wings there. In this flare we see supporting evidence for this picture, from both the H α wing and hard X-ray emission. The magnetic field morphology that one would infer from the relationship between footpoint locations and their proximity to sunspots supports this picture. We expect field lines to diverge away from the weaker North H α kernel, which is located closer to the nearby sunspot.

c) Comparison of Physical Models and Observation

Both the timing and the relative energetics of the relationship between hard X-ray emission and spectrally integrated H α emission suggests that fast electron heating is closely related to the creation of H α photons. However, what do we see when we make a direct comparison of the observed profiles to the theoretical profiles? One must bear in mind that both image motion and small sky transparency variations may affect the H α data. Image motion is certainly the more important of these two effects, and our H α data show evidence of either image motion combined with steep intensity gradients or real brightness variation on time scales much less than 1 second, during the impulsive phase (*cf.* Paper I). For this reason, one must always consider the effect of simply shifting the whole spectrum up or down at all wavelengths, in order to approximate the

effect of spatial displacement of the pixel of interest on the background continuum intensity.

Finally, when we compare the observed and theoretical $H\alpha$ profiles, we must also bear in mind that the theoretical profiles are symmetric, whereas in some cases the observed profiles are quite asymmetric. It has been known for a considerable period of time that the $H\alpha$ line in flares shows a bright red wing (Svestka 1976). Neither the relationship of this asymmetry to the X-ray flare nor the theoretical mechanism of its origin is well understood, although a recent paper by Ichimoto and Kurokawa (1984) concludes that it is a consequence of downward motion driven by impulsive heating due to either an energetic electron beam or thermal conduction.

Do observed $H\alpha$ profiles show broad wings that have a direct temporal relationship to impulsive hard X-ray emission? Referring to Figure 1, we see that at 145551 UT, 14 s before the start of impulsive X-ray emission, the $H\alpha$ profiles show no blue-wing emission that extends more than about $1-2 \text{ \AA}$ from line center. We ignore the red wing emission, since it may be enhanced by hydrodynamic motions, as discussed above. At 145616, between the 2 impulsive burst periods, pixel (37,45) shows excess blue emission all the way to $\Delta\lambda = -5 \text{ \AA}$, and the emission in pixels (37,44) and (42,42) extends blueward more than 3 \AA . If we adopt as a working criterion of wing enhancement an excess that extends farther to the blue than about 3 \AA , even taking into account any possible image motion effects by shifting the entire spectrum up or down, we find that 3 pixels show broad blue wings at 145616, 8 at 145642, 5 at 154707, 2 at 145733, and only 1 (40,42) during the next 3 spectroheliograms. After that time, no profiles show

such blue-wing enhancement. Hence, the temporal behavior of the wing enhancement beyond -3 \AA from line center closely matches the temporal behavior of impulsive hard X-rays. The blue wings are broadest, and more pixels show broad blue wings, at the time (145642) that coincides most nearly with hard X-ray emission.

The impulsive-phase energetics must also be examined; we find that they, too, tend to support the collisional thick-target model. The analysis of the SXRBS data of Paper I split the flare into 2.56 s time intervals. In the interval encompassing the 145642 spectroheliogram, using the power-law thick-target model, we found a power $P_{20} = 7 \times 10^{28} \text{ erg s}^{-1}$ in electrons above 20 keV and a photon spectral index $\gamma = 4.8$. If we estimate the flare area based on the number of pixels that show broad blue wings at this time (3), and assume them to be fully and uniformly filled, we conclude that the electron impact area was $2.3 \times 10^{17} \text{ cm}^2$. Combining the power and area estimates implies a value of $F_{20} = 3 \times 10^{11} \text{ ergs cm}^{-2} \text{ s}^{-1}$. This value is certainly sufficiently large that we would expect to see a broad-wing nonthermal electron signature, out to the $\pm 5 \text{ \AA}$ edge of our spectral field of view. Figure 3 shows that this is what is observed in these pixels at this time.

Combining timing and energetics, we see that in both respects there is a close relationship between the value of F_{20} inferred from P_{20} and the flare kernel area, on one hand, and the presence of H α wings, on the other. Given that $F_{20} = 3 \times 10^{11} \text{ ergs cm}^{-2} \text{ s}^{-1}$ at 145642 UT, we infer from the hard X-ray light curve given in Figure 2 that F_{20} significantly exceeds $10^{10} \text{ ergs cm}^{-2} \text{ s}^{-1}$ during the 3 times of H α profile observations underlined in Figure 3. These are the times at which at least several pixels show extensive H α wings. During the

post-impulsive period for which only 1 pixel shows extensive wings, we infer from Figure 2 that $F_{20} \sim 10^{10}$ ergs cm^{-2} s^{-1} . Hence, whenever $F_{20} \geq 10^{10}$ ergs cm^{-2} s^{-1} , the number of pixels showing broad H α wings appears to track hard X-ray emission quite directly. Our calculations in CGR show that the column depth at which the specific H α wing emission reaches a peak is in the lower chromosphere (column depth $N \approx 10^{21}$ cm^{-2}), where the radiative cooling time is short ($t_R \ll 1$ s). Thus the close temporal correlation is to be expected, if the dominant heating mechanism is direct collisions with nonthermal electrons.

It is interesting that this approaches the upper limit imposed by return current considerations (Kindel and Kennel 1971, Duijveman *et al.* 1981). Duijveman *et al.* (1982) show that if $T_e < T_i$, return current stability requires that the ambient electron density n_e exceeds $F_e/0.5v_e$, where F_e is the beam electron flux and v_e is the ambient electron thermal velocity. The data permit only a rough analysis, since we cannot be sure to what extent $T_e \neq T_i$, or how far the electron spectrum extends below 20 keV. However, 30 keV as the mean electron energy, 20 keV as the mean electron energy, 20 keV as their low-energy cut off, and 3×10^7 K as the ambient temperature, we find that $n_e > 6 \times 10^9$ cm^{-3} is required for stability. The soft X-ray observations of Paper I imply a preflare electron density of about 10^{11} cm^{-3} . Hence, only if $T_e/T_i \gg 1$ and the low-energy cutoff energy is much less than 20 keV do return-current stability considerations appear as a potential inconsistency.

In summary, the temporal, spectral, and spatial characteristics of the combined H α and hard X-ray data set support the hypothesis that nonthermal electrons are heating the flare chromosphere during the impulsive phase of this

flare, in numbers consistent with the thick target hard X-ray model.

III. PRESSURE BALANCE

A puzzling inconsistency arose in Paper I; the analysis carried out there implied a lack of pressure balance between the top of the chromosphere and the corona, even several hydrodynamic scale times after the impulsive phase. The X-ray coronal pressure was found to be 5-9 times greater than the upper chromospheric pressure around the time of maximum X-ray emission pressure. In Paper I we speculated that part of the problem arose from the use of $H\alpha$ profiles based on empirical model atmospheres. As we see below, if we use the CGR physical models to interpret the observed $H\alpha$ profiles, instead of empirical models, no such pressure imbalance is implied.

a) Coronal Pressure from X-Rays

The pressure in the soft X-ray emitting corona is based on temperature and density estimates. In Paper I, the characteristic coronal temperature was obtained from the SMM X-Ray Polychromator (XRP) data by the satellite-to-resonance-line technique, using the observed lines of Ca XIX and Fe XXV (Culhane *et al.* 1981). These temperatures were 10^7 and 6×10^6 K at 145712 and 145944 UT respectively. Also using the XRP data, the density was estimated from the total soft X-ray emission measure (all material at $T > 2 \times 10^6$ K) and the estimated X-ray source volume. The density so inferred was $2 \times 10^{11} \text{ cm}^{-3}$, with an uncertainty of about a factor of 2. Inferred pressures were thus $\sim 400 \text{ dyne cm}^{-2}$ at 1457 UT, near the end of the impulsive phase, and $\sim 250 \text{ dyne cm}^{-2}$ 3

minutes later, spanning the period of maximum emission measure.

Independent estimates of the coronal pressure have been made by Simnett (1983). Using the X-ray continuum spectra in the range 3.5-30 keV observed from HXIS, he derived values of temperature and emission measure in six time intervals during the flare. His method is based on a 2-temperature model of the X-ray plasma, and the spectra predicted by the model are fitted to the data. For the cool component, Simnett derives $T = 6.6 \times 10^6$ K during 145649-145729 UT, $T = 6.5 \times 10^6$ K during 145729-145854 UT, and $T = 6.4 \times 10^6$ K during 145854-150031 UT. For the hot component, he derives 21, 22 and 23×10^6 K respectively, during these same 3 intervals. On the basis of the HXIS image at flare maximum, Simnett derives a volume virtually identical to that of Paper I, but emission measures roughly 3 times larger. His derived densities for the cool component are 5.8, 5.9, and $4.6 \times 10^{11} \text{ cm}^{-3}$, during the 3 time intervals of interest. The corresponding pressure values are thus 1.3, 1.3 and 1.0×10^3 dyne cm^{-2} respectively. For the hot component, one can do no better than use the same volume, obtaining densities 9.8, 6.7 and $3.2 \times 10^{10} \text{ cm}^{-3}$, and pressures 5.7, 4.0 and 2.0×10^2 dynes cm^{-2} , respectively.

When we make a comparison, we see that the HXIS and XRP measures of coronal pressure during the period 1457-1500 UT, immediately following the impulsive phase, agree to within a factor of 3-4. The difference between the XRP and HXIS values accrues mainly from different inferred values of the emission

measure.

b) Coronal Pressure from H α

By comparing theoretical H α profiles to our observations, we can infer the coronal pressure. In CGR we showed that in hydrostatic equilibrium, the amplitude of the central reversal is a measure of the coronal pressure, P_0 . Figure 4 shows that as P_0 is increased, the central reversal (measured by the ratio I_0/I_{\max}) increases, reaching 1 between 10^2 and 10^3 dynes cm^{-2} . CGR showed that the primary reason for this pressure dependence, at high values of pressure, is collisional creation of H α photons in the region near unit line-center H α optical depth. We note that although we do not know what value of F_5 to associate with the observations, values of $F_5 > 10^7$ ergs $\text{cm}^{-2} \text{s}^{-1}$ (which we would expect from the measured value of the coronal temperature, the inferred loop length, and the coronal scaling laws of Craig, McClymont, and Underwood (1978)), would lead primarily to a reduction in the intensity of H α , but not an increase in the central reversal. For given P_0 , but higher F_5 , the radiation at line center would come from an even denser region than it does in Figure 4, i.e., we would expect a reduction in total intensity and even less central reversal.

In order to credibly compare the H α profiles of Figure 4 to the observations, we must be convinced of the plausibility of various assumptions. In particular, there must have been sufficient time after the major period of heating (which we identify as the impulsive phase, 1456-57 UT) for the mass motions necessary to establish equilibrium to take place. On the basis of the

observed temperatures at 1457 UT (see above), and the length of a loop connecting the north and south kernels (length $\approx 11,000$ km), the sound transit time throughout the loop is about 30 s. Hence, by 145730 UT, we can plausibly compare the hydrostatic profiles to the data.

The H α observations during the post-impulsive period of maximum X-ray emission measure show only weakly reversed and unreversed profiles in the flare kernels, which we identify as the footpoints of the arches that contain the soft X-ray plasma. In the south kernel, the central reversal is weak throughout this period. In the north kernel, it is even weaker. When we compare the amplitude of the reversal with the theoretical profiles in Figure 4, we conclude that in both the south and north kernels, the implied coronal pressure is in the range 100-1000 dynes cm $^{-2}$.

It is noteworthy that none of the observed H α profiles are as intense as the theoretical $P_0 = 10^3$ dynes cm $^{-2}$ profile in Figure 4. It must be kept in mind that in creating the model flare chromosphere on which the theoretical flare H α profiles are based, the set of values of F_{20} , F_5 and P_0 are not required to be consistent with any particular coronal structure. We believe that the major reason for the lower intensity of the of the observed profiles is that, for the specified value of P_0 , a physically consistent value of F_5 should be larger than the value $F_5 = 10^7$ ergs cm $^{-2}$ s $^{-1}$ illustrated in Figure 4. Craig, McClymont and Underwood (1978) show that the flux at the base of a purely conducting loop is

$$F_{\text{base}} = 7.5 \times 10^{-7} \beta^{1/2} T_0^{7/2} / L, \quad (1)$$

where $\beta \approx 1$ for nonisothermic heating functions, T_0 is the coronal (loop apex) temperature, and L is the loop half-length, all in CGS units. For the purely conducting model to be reasonable, we cannot apply it at temperatures less than a value T_{base} , below which radiation begins to become significant. Clearly $T_{\text{base}} \gg 10^5$ K, where F_5 measures the conductive flux. To relate F_5 to F_{base} we must take into account the effect of radiation at temperatures between 10^5 K and T_{base} . Fisher (1984) has shown that if one adopts a radiative loss function inversely proportional to temperature in this range (which is a reasonably good approximation to the functional dependence of the effective radiative cooling function, see McClymont and Canfield 1983), the balance between conductive flux divergence and radiation that determines the transition region temperature structure leads to

$$F_c(T) = 0.18 T^{1/4} F_5, \quad (2)$$

where $F_c(T)$ is the conductive flux at a temperature T within the transition region. Since the conducting coronal part of the loop is nearly isothermal, we equate the base and apex temperatures. Combining (1) and (2), we have

$$F_5 = 4.2 \times 10^{-6} T_0^{13/4} / L. \quad (3)$$

If we use the observed range of coronal temperatures, and the loop dimension inferred from the observations, we obtain $8 \times 10^7 \leq F_5 \leq 6 \times 10^9$ ergs $\text{cm}^{-2} \text{s}^{-1}$. [As an aside, we note that such transition-region flux values, though

large, do not exceed the saturated-flux limit (roughly one-sixth the energy carried by free-streaming electrons), because the transition region densities implied by the observed coronal pressure values are so high. For a coronal pressure of 10^3 dyne cm^{-2} , the saturated flux limit at 10^5 K is 1.3×10^{10} erg cm^{-2} s^{-1} .] In CGR we showed that such values of F_5 are in the range that sensitively affects the total H α intensity, for coronal pressures in the range $10^2 \leq P_0 \leq 10^3$ dynes cm^{-2} in the flare kernels. Hence, from the CGR models, we would expect observed intensities to be less than those shown in the theoretical models of Figure 4.

c) Comparison

We can now compare X-ray and H α estimates of the coronal pressures. From the X-ray spectra in Paper I we derived $P_0 = 250-400$ dynes cm^{-2} during the immediate postimpulsive time period of maximum emission measure (1457-1500 UT). Simnett (1983) derived $1.0-1.3 \times 10^3$ dynes cm^{-2} during this same period. From the H α spectra, we infer $10^2 < P_0 < 10^3$ dynes cm^{-2} in the flare kernels. Hence we conclude that within their apparent uncertainty, the two approaches give values that agree.

The speculation in Paper I that the apparent pressure imbalance found there might be due to the use of the empirical models of Dinh (1980) now seems confirmed. The problem seems to be that Dinh assumes that the coronal (apex) gas pressure is negligible in comparison to the gravitational pressure at the top of the chromosphere. The CGR models show that this is not true for values of P_0 in the range implied by our observations of this flare.

The order-of-magnitude agreement of these 2 measures of coronal pressure has implications for the volume filling factor in the coronal part of the flare loop plasma. The H α profile method does not make any assumption about coronal volume filling factor; it is only necessary that the observed flare profiles reflect the conditions at the footpoints of the coronal loops, in equilibrium. On the other hand, the X-ray pressure does depend on the assumption that the soft X-ray emitting volume is fully filled, so the derived pressure $P_0 \propto V^{-1/2}$. The order-of-magnitude agreement of the H α and soft X-ray pressure estimates supports the assertion that the soft X-ray volume filling factor is greater than approximately 10^{-2} .

IV. CHROMOSPHERIC EVAPORATION

We use the term *chromospheric evaporation* to describe the process in which enhanced heating is sufficient to drive the temperature of chromospheric material up to $T \approx 10^5$ K, above which the plasma is thermally unstable. As a result, its temperature jumps dramatically, typically to $T \gg 10^6$ K, where it is effectively stabilized by thermal conduction (Field 1965). Observed flare X-ray spectral lines are blue-shifted (Feldman *et al.* 190, Antonucci *et al.* 1982) by amounts corresponding to up-flow velocities of under the coronal sound speed. These motions are commonly (though not universally) ascribed to the transient pressure excess associated with evaporated chromospheric material (for a review, see Doschek *et al.* 1984). Two basic issues arise below. First, can chromospheric evaporation account for the amount of high-temperature material

($T \approx 10^6$ K) in the thermal X-ray flare plasma? Second, is chromospheric evaporation driven primarily through thermal conduction from the hot flare corona or through direct collisional heating of the chromosphere by nonthermal electrons?

In this paper we approach these questions differently from Paper I. There, the amount of material evaporated from the chromosphere was estimated from the observed $H\alpha$ profiles by comparing them with a grid of *empirical model chromospheres* created by Dinh (1980). These models do not distinguish between 2 different contributors to the pressure at the top of the chromosphere, specifically the coronal loop apex (confinement) pressure and gravitational pressure. On the other hand, the *physical model chromospheres* of CGR do make this distinction and hence permit us to take a different approach to estimating the amount of evaporation through interpretation of the $H\alpha$ line profile observations. In this paper we address these questions by estimating the extent to which the 2 different evaporation mechanisms, acting alone, displace the flare transition region to column numbers N_1 that are greater than the preflare value N_0 , and then compare N_1 for the 2 mechanisms to the value required to

explain the observations.

a) Evaporation by Nonthermal Electrons

In Paper I we estimated the column depth of evaporation through direct collisional heating by the thick-target fast electrons associated with the observed hard X-ray emission. We used an expression, derived by Lin and Hudson (1976), based on the physical assumption that at the flare transition region collisional heating is balanced by radiation, bearing in mind that the peak ability of the solar plasma to radiate is at $T \sim 10^5$ K. The estimate of the column density of the evaporated material given in Paper I should be revised for 2 reasons. Most importantly, the Lin and Hudson (1976) expression neglects the *dominant* contributor to the transition region pressure in closed loops, i.e. the loop apex pressure. Second, in § II above we showed that the H α wings imply a nonthermal electron impact area about a factor of 2 greater than that used in Paper I (there we used only the south kernel area). Hence, we now derive a revised estimate of the amount of evaporation by direct collisional heating.

McClymont, Canfield and Fisher (1984) take into account loop apex pressure in their consideration of direct collisional heating by nonthermal electrons. They use the analytical scattering approach of Brown (1973), assuming heating by Coulomb collisions only, in a vertical column of fully ionized plasma in which the power-law distribution of electron energies has a lower cutoff energy E_c that corresponds to stopping above the flare transition region. They show that transition region energy balance between radiation and collisional heating can be expressed as

$$[(P_0 + \bar{m}gN_1)/kT^*] f_5 = [(\delta-2) B(\delta/2, 1/3)]/[6 N_c^{1-\delta/2}] F_c N_1^{-\delta/2}. \quad (4)$$

The left-hand side is the specific (per H nucleus) radiative loss rate; the right-hand side is the specific collisional heating rate. The density at the flare transition region is given by $(P_0 + \bar{m}gN_1)/kT^*$, where $\bar{m}gN_1$ is the gravitational contribution, and T^* is taken to be the temperature of the un-ionized preflare chromosphere, in the case where the time scale is so short that material has insufficient time to change its density, or $2T_5$ in the hydrostatic case, where $T_5 = 10^5$ K and full ionization is assumed. The constant f_5 is the peak value of the specific radiative cooling function, at $T = 10^5$ K, 7×10^{-22} erg $\text{cm}^3 \text{s}^{-1}$. On the right-hand side, δ ($\delta = \gamma + 1$ for a thick target) is the spectral index of the nonthermal electron power law, $B(x, y)$ is the complete beta function, N_c is the stopping column number of electrons with the cutoff energy E_c , and F_c is the energy flux of nonthermal electrons above energy E_c (F_{20} , if $E_c = 20$ keV), at $N = 0$. If we define a coefficient $C(\delta)$ by

$$C(\delta) \equiv [kT^*(\delta-2) B(\delta/2, 1/3)]/[6 f_5 N_c^{1-\delta/2}],$$

then the column depth of chromospheric evaporation by direct collisional heating by flare electrons is the solution of the equation

$$N_1 = [C(\delta) F_c / (P_0 + \bar{m}gN_1)]^{2/\delta}, \quad (5)$$

which can conveniently be solved numerically by the method of successive approximations. If the solution of (5) is a value $N_1 < N_c$, then the value of N_1

is an upper limit.

For this flare, we can determine the depth of direct collisional evaporation from the inferred values of the parameters of equation (5): $F_{20} = 3 \times 10^{11}$ ergs $\text{cm}^{-2} \text{s}^{-1}$, and $\delta = 5.8$. By 1457 UT, the end of the impulsive phase, one can plausibly argue that there has been sufficient time to set up approximate pressure balance in this small loop (the hydrodynamic time scale ~ 15 s). If we adopt $P_0 \approx 70$ dynes cm^{-2} , the preflare value from Paper I, we then obtain $N \approx 7 \times 10^{19} \text{ cm}^{-2}$. This is certainly based on a lower limit to the pressure; a more appropriate value is 400 dynes cm^{-2} , which leads to $N \approx 4 \times 10^{19} \text{ cm}^{-2}$. Since $N_C \approx 4 \times 10^{19} \text{ cm}^{-2}$ for $E_C = 20$ keV, our result is insensitive to E_C unless $E_C \gg 20$ keV, in which case this N value is an upper limit. In any case, direct collisional evaporation cannot plausibly be argued to extend to column depths $N \approx 7 \times 10^{19} \text{ cm}^{-2}$, whatever the value of E_C .

As an aside, were we to (inconsistently) neglect P_0 , as done in Paper I, we would obtain $N \approx 1.3 \times 10^{20} \text{ cm}^{-2}$. If we were to (inconsistently) use the impulsive model at 1457 UT, adopting $T^* = 6000$ K as the temperature of the preflare chromosphere at the column depth of the flare transition region, we would obtain $N < 2 \times 10^{19} \text{ cm}^{-2}$. Below we will compare these values of N_1 to those

appropriate to conductive heating.

b) Conduction-Driven Evaporation

Heat deposited in the coronal part of a high-temperature loop is efficiently transported toward the chromospheric foot points by thermal conduction. In time-dependent numerical simulations of energy transport in loops whose flare heating was due solely to energetic electrons, Fisher, Canfield, and McClymont (1984) showed that only for the first second or so is evaporation dominated by direct collisional heating. In the case they considered, *i.e.*, a constant collisional heating rate, a quasisteady equilibrium was established in which conduction drove chromospheric evaporation as described by An *et al.* (1983):

$$F_1 = 5 k T_1 \frac{dN_1}{dt} + \int_{N_1}^{N_2} R dN, \quad (6)$$

where R is the radiative loss rate per H nucleus. Here the subscripts 1 and 2 refer respectively to the coronal and chromospheric boundaries of the flare transition region; dN_1/dt is the rate of addition of material to the corona, *i.e.*, the rate of chromospheric evaporation. Identifying F_1 with the base of a purely-conducting coronal loop, and neglecting radiation, we combine equations (1) and (6) to obtain

$$\frac{dN_1}{dt} = \kappa_0 T_0^{5/2} / (5 k L). \quad (7)$$

Our simulations of conduction-driven evaporation in Kopp *et al.* (1984) show that for $F_1 \sim 10^9$ ergs $\text{cm}^{-2} \text{s}^{-1}$, the radiation term of equation (6) is comparable to

the enthalpy term. Hence, we estimate that equation (7) is accurate to a factor of 2 or better, since P_1 is probably substantially higher in the flare of interest here, and therefore transition-region radiation is probably even less significant.

To determine the amount of conduction-driven evaporation at 1457 UT, we need only know the evolution of temperature during the impulsive phase. This information is available from Simnett (1983). As before, we identify the flare loop with his hot component. Simnett derives temperatures that start at 36×10^6 K at 145600-145606 UT, and gradually fall thereafter, reaching 21×10^6 K in the interval 145649-145729. Weighting by $T_o^{5/2}$ over the 60 s interval before the time of interest at the end of the impulsive phase (1457 UT), we see that conductive-driven evaporation will have reached a column depth of approximately $N_1 \sim 8 \times 10^{20}$, with an uncertainty of a factor of 2.

c) Comparison with Observations

In order to ascertain whether either fast electron heating or thermal conduction could account for the measured evaporation in this flare, we note that the X-ray observations require $n_e V$ to be approximately 3×10^{37} (Paper I) to 7×10^{37} (Simnett). Given a cross-sectional area of 6.3×10^{16} cm² (Paper I), the required values of evaporated column density (at each footpoint) are 2.4 - 5.6×10^{20} cm⁻². We have seen above that fast electron heating can account for at most 7×10^{19} cm⁻², while conduction can account for as much as 8×10^{20} cm⁻². We therefore conclude that of these two alternatives, only conductively-

driven chromospheric evaporation accounts for the thermal X-ray plasma observed in this flare, at the time of maximum emission measure.

V. CONCLUSIONS

The primary conclusion of this paper is that there is consistent evidence for heating of the chromosphere by nonthermal energetic electrons during the impulsive phase of this flare, although it is not heating by these electrons that produces the bulk of the soft X-ray plasma through chromospheric evaporation. It appears that there is satisfactory order-of-magnitude agreement between the observed H α wing development and the theoretical H α wings expected from the spectrum of nonthermal electrons inferred from observed hard X-rays. From the point of view of transport theory, it appears that collisional stopping of the energetic electrons provides a satisfactory theoretical interpretation of the observations. However, it seems that thermal conduction, not heating by energetic electrons, is the preferred mechanism for production of the thermal X-ray plasma maximum emission measure, just after the end of the impulsive hard X-ray phase.

The authors wish to thank Horst Mauter and Philip Wiborg for their help in obtaining the H α observations, and George Fisher, Sandy McClymont, John Brown, and George Simnett for helpful discussions on the interpretation of the data. This work was supported by the United States Air Force Office of Scientific Research under grant 82-0092, and by the National Science Foundation, under grant AST 83-20306.

REFERENCES

- Acton, L. W., Canfield, R. C., Gunkler, T. A., Hudson, H. S., Kiplinger, A. L., and Leibacher, J. W. 1982, *Ap. J.*, 263, 409.
- An, C.-H., Canfield, R. C., Fisher, G. H., and McClymont, A. N. 1983, *Ap. J.*, 267, 421.
- Antonucci, E. et al. 1882, *Solar Phys.*, 78, 107.
- Brown, J. C. 1971, *Solar Phys.*, 18, 489.
- Brown, J. C. 1973, *Solar Phys.*, 31, 143.
- Brown, J. C., and McClymont, A. N. 1975, *Solar Phys.*, 41, 135.
- Canfield, R. C. 1982, *Solar Phys.*, 75, 263.
- Canfield, R. C., Gunkler, T. A., and Ricchiazzi, P. J. 1984, *Ap. J.*, in press.
- Craig, I. J. D., McClymont, A. N., and Underwood, J.H. 1978, *Astron. Astrophys.*, 70, 1.
- Culhane, J. L. et al. 1981, *Ap.J. (Letters)*, 244, L141.
- Dinh, Q.-V. 1980, *Publ. Astron. Soc. Japan*, 32, 515.
- Doschek, G. A. et al. 1984, in *Solar Flares*, ed. M. Kundu and B. Woodgate, in preparation.
- Duijveman, A., and Hoyng, P. 1983, *Solar Phys.*, 86, 279.
- Duijveman, A., Hoyng, P., and Ionson, J. 1981, *Ap. J.*, 245, 721.
- Duijveman, A., Hoyng, P., and Machado, M. E. 1982, *Solar Phys.*, 81, 137.
- Dunn, R. B. 1971, *The Menzel Symposium on Solar Physics, Atomic Spectra, and Gaseous Nebulae*, ed. K. B. Gebbie (NBS Spec. Pub. 353; Washington, U.S. Govt. Printing Office), p. 71.
- Dunn, R. B. 1979, *Sky and Tel.*, 38, 1.
- Feldman, U., Doschek, G. A., Kreplin, R. W., and Mariska, J. T. 1980, *Ap. J.*, 142, 531.

- Field, G. W. 19965, *Ap. J.*, 142, 531.
- Fisher, G. H. 1984, private communication.
- Ichimoto, K., and Kurokawa, K. 1984, *Solar Phys.*, submitted.
- Kane, S. R., Fenimore, E. E., Klebesadel, R. W., and Laros, J. G. 1982, *Ap. J. (Letters)*, 254, L53.
- Kindel, J. M., and Kennel, C. F. 1971, *J. Geophys. Res.*, 76, 3055.
- Kiplinger, A. L., Dennis, B. R., Emslie, A. G., Frost, K. J., and Orwig, L. E. 1983, *Ap. J. (Letters)*, 265, L99.
- Kopp, R. et al. 1984, in *Solar Flares*, ed. M. Kundu and B. Woodgate (Washington: U.S. Government Printing Office), in preparation.
- Lin, R. P. and Hudson, H. S. 1976, *Solar Phys.*, 50, 153.
- McClymont, A. N. and Canfield, R. C. 1983, *Ap. J.*, 265, 497.
- McClymont, A. N., Canfield, R. C. and Fisher, G. H. 1984, in preparation.
- Neidig, D. F. 1981, *Solar Phys.*, 70, 129.
- Ohki, K., Takakura, T., Tsuneta, S., and Nitta, N. 1983, *Solar Phys.*, 86, 301.
- Orwig, L. E., Frost, K. J., and Dennis, B. R. 1980, *Solar Phys.*, 65, 25.
- Ricchiuzzi, P. J., and Canfield, R. C. 1983, *Ap. J.*, 272, 739.
- Simnett, G. M. 1983, *Solar Phys.*, 86, 289.
- Svestka, Z. 1976, *Solar Flares*, D. Reidel Publ. Co., Dordrecht, Holland, p. 7.
- van Beek, H. F., Hoyng, P., Lafleur, B., and Simnett, G. M. 1980, *Solar Phys.*, 65, 39-52.

FIGURE CAPTIONS

Fig. 1.--Theoretically predicted $H\alpha$ profile signatures of nonthermal electron heating, from CGR. Top: Impulsive approximation. Bottom: Hydrostatic approximation. The unit of intensity, $I_{\text{continuum}}$, is that of the quiet sun in the vicinity of $H\alpha$.

Fig. 2.--Temporal development of hard X-ray counts and $H\alpha$ energy output of the flare of 7 May, 1980 from Paper I. The hard X-ray data sum all counts at energies above 30 keV. The $H\alpha$ data sum all power within 5 \AA of preflare line center, subtracting the average value during a preflare reference period. For the $H\alpha$ data, circles indicate values and times of observations. The heavy solid curve indicates the integrated $H\alpha \pm 5 \text{ \AA}$ energy output (left scale). Percentage contributions of the south and north kernels (see Figure 3) are indicated by the light solid and dashed lines respectively (right scale).

Fig. 3.-- $H\alpha$ profile observations at times spanning the impulsive hard X-ray phase. The 2 large contiguous squares that appear to frame each panel indicate 2 relevant $8'' \times 8''$ HXIS pixels; the smaller rectangles indicate relevant $2'' \times 2.67''$ $H\alpha$ pixels. The location of the $H\alpha$ pixel in the spectroheliogram is indicated by its (row, column) index (i, j). In each $H\alpha$ pixel 2 spectra are plotted in units of I_c , the observed quiet sun continuum intensity near the flare site. The heavier spectrum is that at the indicated time; the lighter spectrum is that of 145525 UT, before the

impulsive phase. The values of (i,j) are the (row,column) indices of the pixels in the $H\alpha$ spectroheliogram. The shaded pixels are the north and south kernel pixels of Paper I. Times underlined are those for which $F_{20} > 10^{10}$ ergs cm^{-2} s^{-1} .

Fig. 4.--Theoretically predicted $H\alpha$ profiles for 4 values of the coronal pressure, P_0 , and fixed values of nonthermal electron energy flux F_{20} and conductive flux at 10^5 K, F_5 .

Fig. 5.-- $H\alpha$ profile observations at times spanning the post-impulsive period of maximum emission measure (1457-1500 UT). Same format as Figure 3.

EFFECT OF NONTHERMAL ELECTRONS

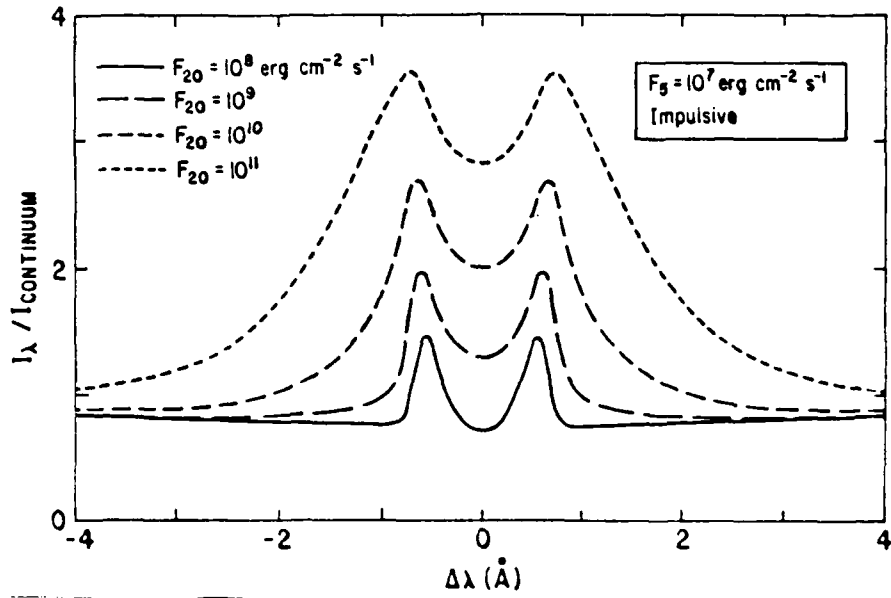
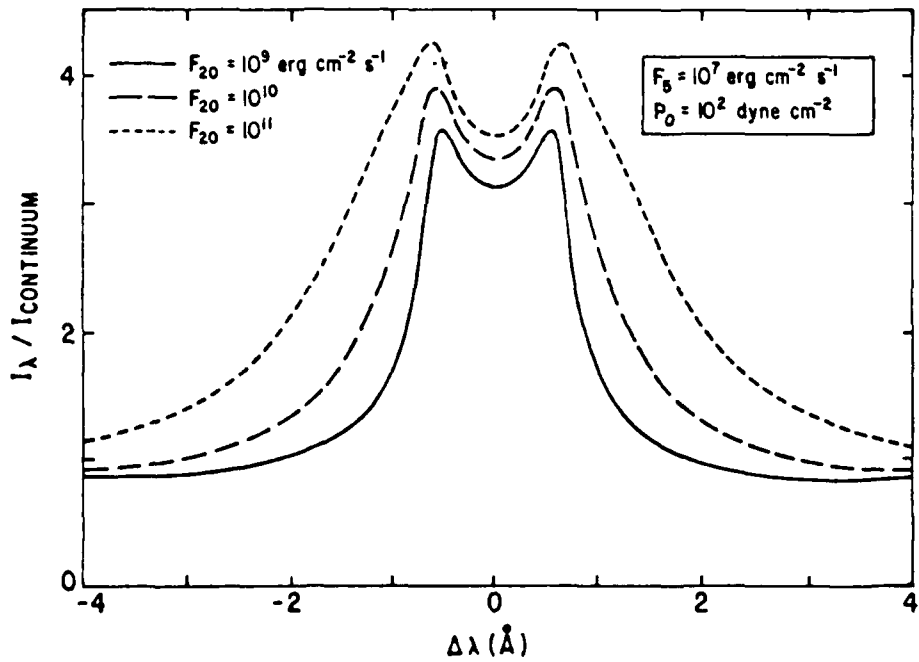
EFFECT OF NONTHERMAL ELECTRONS
(NOMINAL CORONAL PRESSURE)

Figure 1

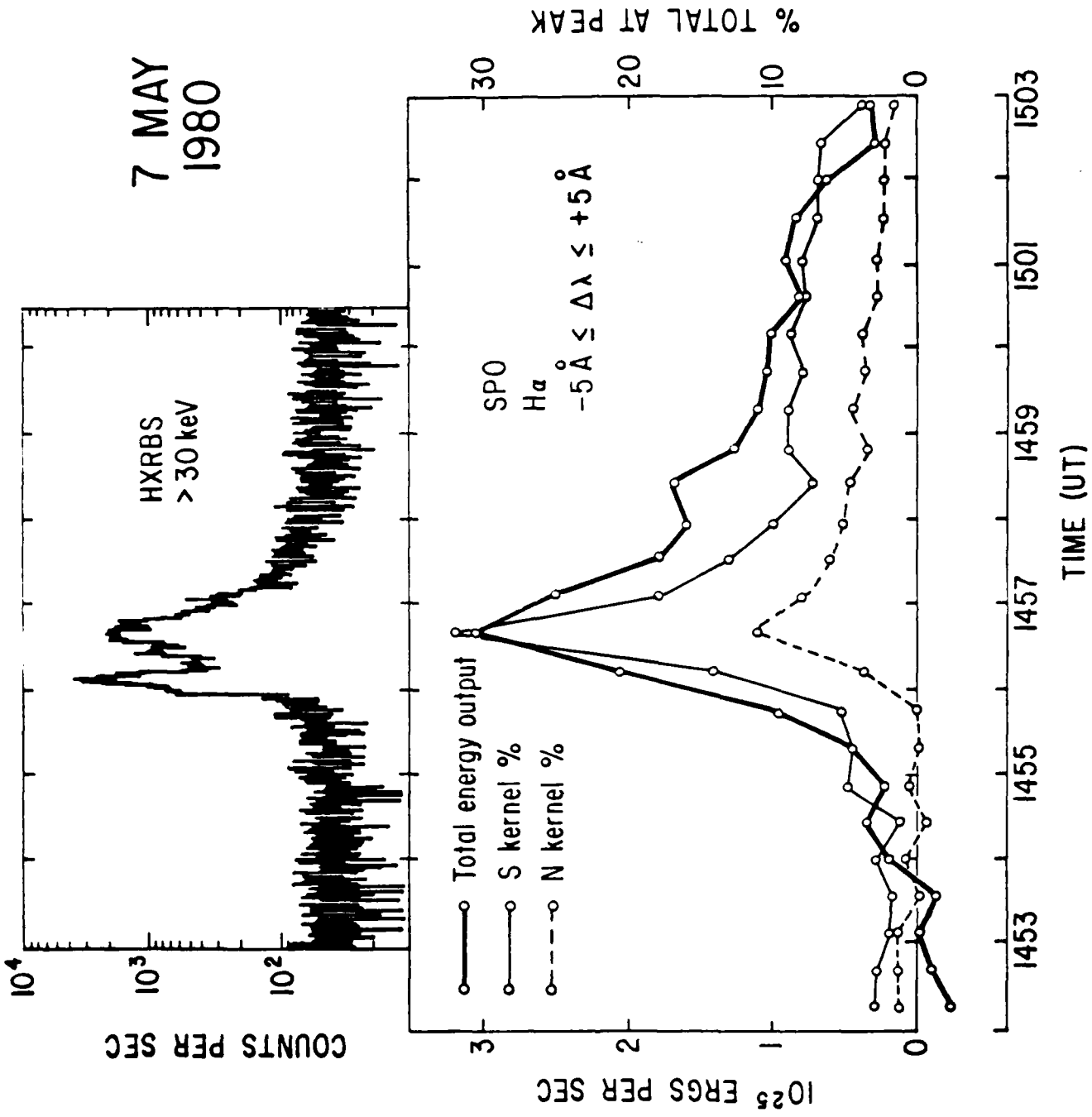
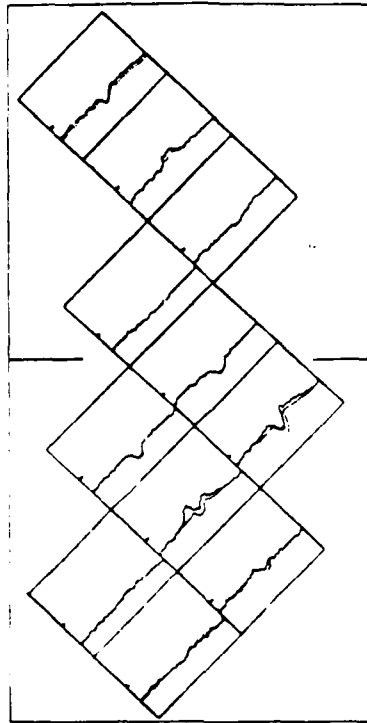
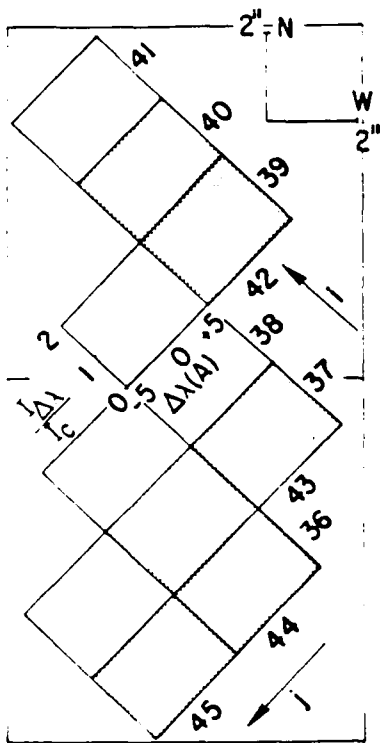
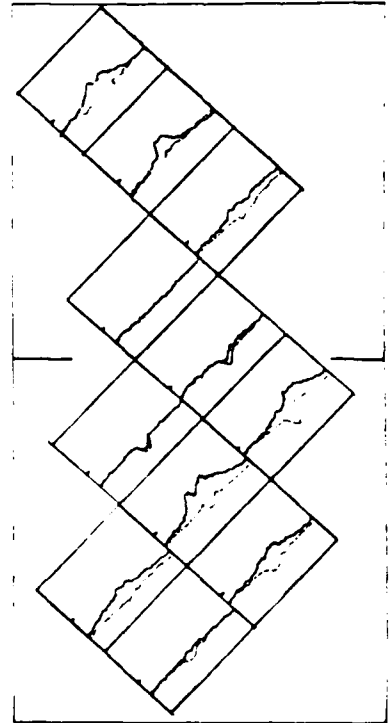


Figure 2

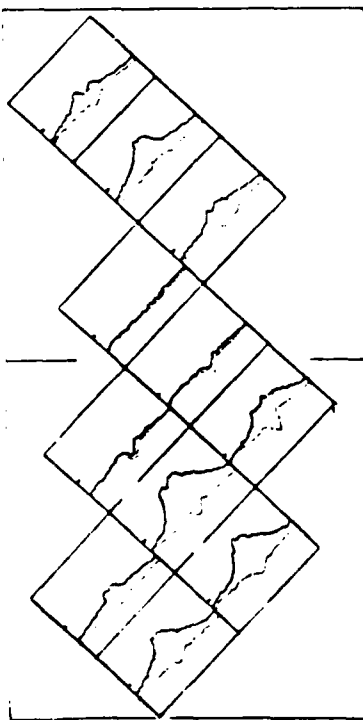
IMPULSIVE PHASE



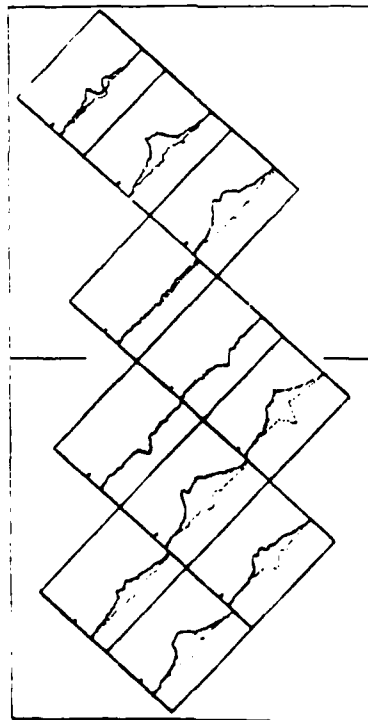
14:55:51 UT



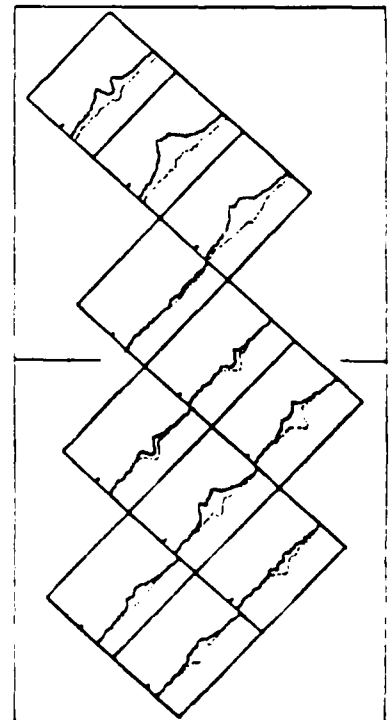
14:56:16 UT



14:56:42 UT



14:57:07 UT



14:57:33 UT

Figure 3

EFFECT OF CORONAL PRESSURE (LOW NONTHERMAL ELECTRON FLUX)

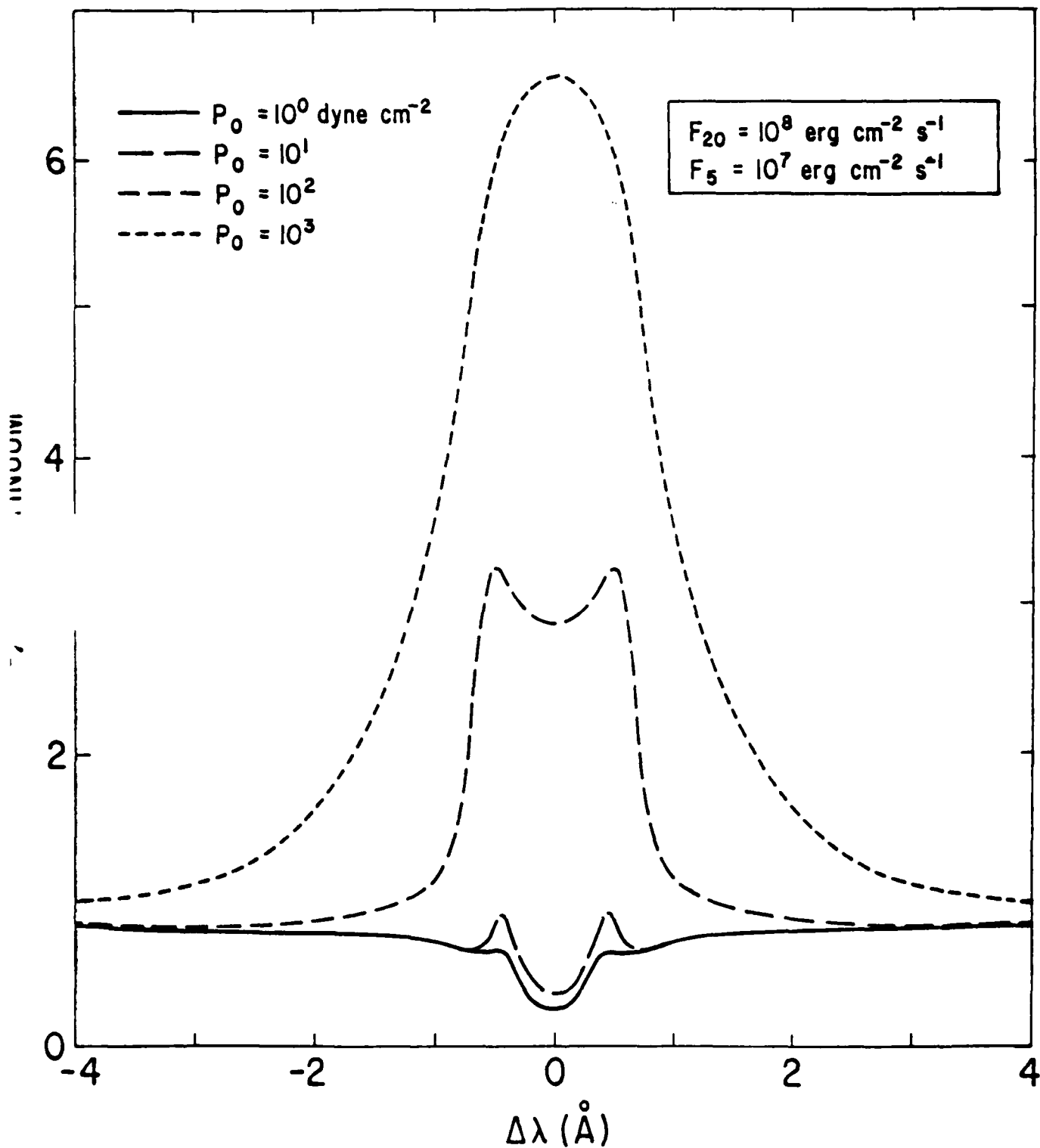
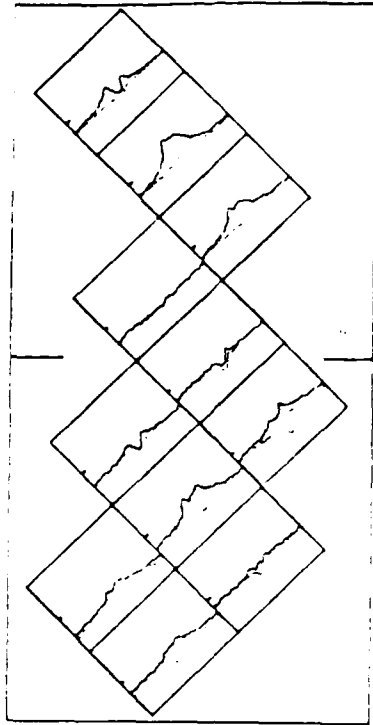
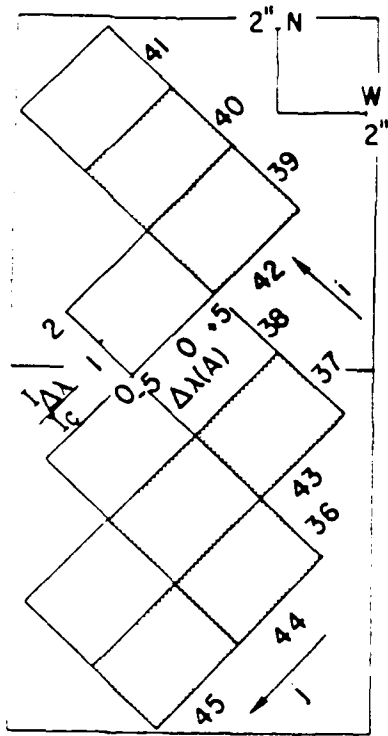
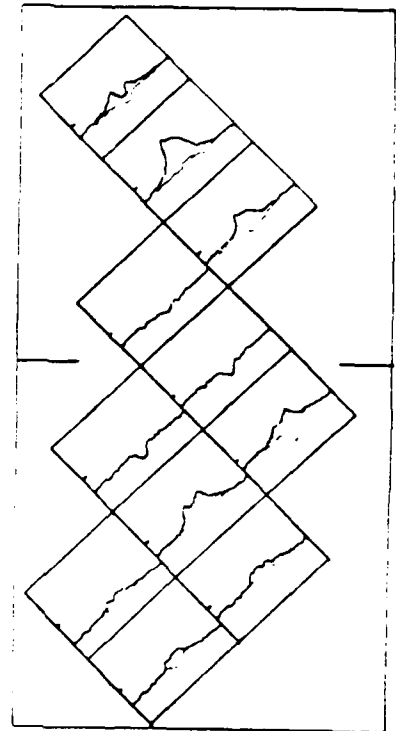


Figure 4

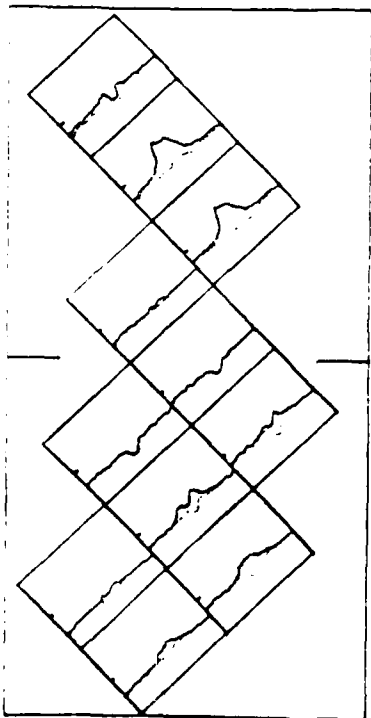
POST-IMPULSIVE PHASE



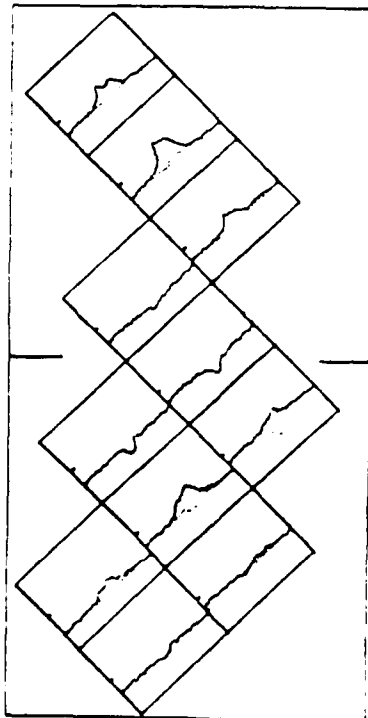
14:57:33 UT



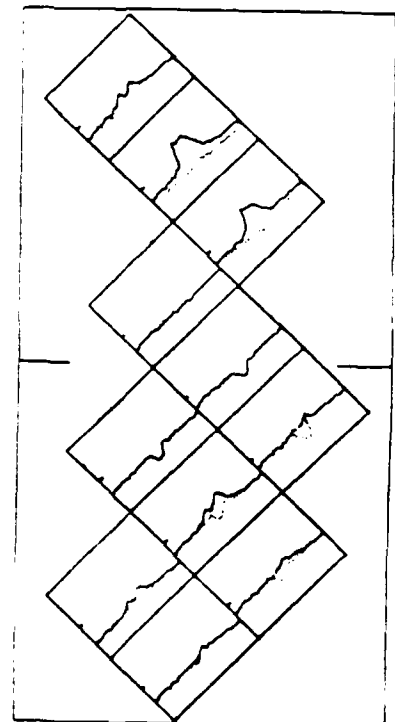
14:57:58 UT



14:58:24 UT



14:58:50 UT



14:59:15 UT

Figure 5

AUTHORS' MAILING ADDRESSES

RICHARD C. CANFIELD

Center for Astrophysics and Space Sciences, C-011

University of California, San Diego

La Jolla, CA 92093

TODD A. GUNKLER

Delta College

University Center, MI 48710

b) Theoretical Modeling of Flare Energy Transport

In order to analyze and interpret our flare observations, we have developed methods for efficient and realistic treatments of radiative transfer. We have then used these methods to construct physically self-consistent model flare atmospheres. Finally, we have calculated $H\alpha$ spectral line profiles for various model flare atmospheres, and thereby demonstrated how the $H\alpha$ line profile responds to energetic electrons, thermal conduction and coronal pressure.

The flare model atmospheres show that the chromosphere responds quite differently to these three different processes. The amount of evaporated material depends on all three processes considered. However, only thermal conduction can account for sufficient chromospheric evaporation in small flares. Only energetic electrons can give heating of the residual flare chromosphere.

Similarly, the $H\alpha$ line profile responds quite differently to these three different processes. The most important effects, from the point of view of the interpretation of our observations, are:

1. Only high values of the flux of energetic electrons produce $H\alpha$ profiles with obvious wide Stark wings;
2. Only high values of coronal pressure can cause flare $H\alpha$ emission profiles that are not centrally reversed (a relative minimum at line center).

These $H\alpha$ signatures are the key to the analysis of the data in the previous section (IIa).

Published in "Methods in Radiative
Transfer", W. Kalkofen, ed. (Cambridge
Univ. Press) p.101-129 (1984)

PROBABILISTIC RADIATIVE TRANSFER

SP-82-36

Richard C. Canfield, A. N. McClymont, and R. C. Puetter
Center for Astrophysics and Space Sciences C-011,
University of California San Diego, La Jolla, California 92093, U.S.A.

Abstract. We have developed a computationally efficient method for highly nonlinear problems in which radiative transfer is an important aspect of the heating and cooling of the medium. In this paper we summarize all essential aspects of the method. We derive an approximate probabilistic radiative transfer equation for one-dimensional plane-parallel atmospheres of finite or semi-infinite extent, for both spectral lines and bound-free continua. We also discuss boundary conditions, accuracy, escape probabilities, and practical aspects of complete linearization, which is a key element of the method. Our method is accurate to a few tens of percent for a wide variety of realistic problems in which frequency redistribution of scattered photons dominates the transfer and escape of radiation.

1 INTRODUCTION

Probabilistic methods of radiative transfer have two basic features that make them desirable—ease of understanding and computational speed. Their ease of understanding comes through analytical, rather than numerical, treatment of frequency integration. This approach recognizes that in many radiative transfer problems, the detailed atomic physics can be decoupled conceptually from the description of the effects of photon propagation. The computational speed of the unique method discussed in this paper accrues from three factors: (1) analytic frequency integration reduces the number of equations to be solved numerically; (2) the radiative transfer equation is cast in first-order differential form; (3) no elaborate auxiliary equations are required.

Analytical frequency integration has substantial computational benefits. The usual approach of *frequency-dependent* radiative transfer, i.e. the simultaneous numerical solution of the radiative transfer equation at many discrete frequencies within a spectral line or continuum, is reduced to solution of a *frequency-integrated* equation at a single reference frequency. In practice, this reduces the number of radiative transfer equations per spectral feature (line or continuum) by an order of magnitude or more. Typically the computing time required to solve the system of equations in a complete linearization approach scales as the number of equations to a power of between two and three on parallel-processing computers, or three on scalar processors. Hence,

Published in "Methods in Radiative
Transfer", W. Kalkofen, ed. (Cambridge
Univ. Press) p.101-129 (1984)

PROBABILISTIC RADIATIVE TRANSFER

SP-82-36

Richard C. Canfield, A. N. McClymont, and R. C. Puetter
Center for Astrophysics and Space Sciences C-011,
University of California San Diego, La Jolla, California 92093, U.S.A.

Abstract. We have developed a computationally efficient method for highly nonlinear problems in which radiative transfer is an important aspect of the heating and cooling of the medium. In this paper we summarize all essential aspects of the method. We derive an approximate probabilistic radiative transfer equation for one-dimensional plane-parallel atmospheres of finite or semi-infinite extent, for both spectral lines and bound-free continua. We also discuss boundary conditions, accuracy, escape probabilities, and practical aspects of complete linearization, which is a key element of the method. Our method is accurate to a few tens of percent for a wide variety of realistic problems in which frequency redistribution of scattered photons dominates the transfer and escape of radiation.

1 INTRODUCTION

Probabilistic methods of radiative transfer have two basic features that make them desirable—ease of understanding and computational speed. Their ease of understanding comes through analytical, rather than numerical, treatment of frequency integration. This approach recognizes that in many radiative transfer problems, the detailed atomic physics can be decoupled conceptually from the description of the effects of photon propagation. The computational speed of the unique method discussed in this paper accrues from three factors: (1) analytic frequency integration reduces the number of equations to be solved numerically; (2) the radiative transfer equation is cast in first-order differential form; (3) no elaborate auxiliary equations are required.

Analytical frequency integration has substantial computational benefits. The usual approach of *frequency-dependent* radiative transfer, i.e. the simultaneous numerical solution of the radiative transfer equation at many discrete frequencies within a spectral line or continuum, is reduced to solution of a *frequency-integrated* equation at a single reference frequency. In practice, this reduces the number of radiative transfer equations per spectral feature (line or continuum) by an order of magnitude or more. Typically the computing time required to solve the system of equations in a complete linearization approach scales as the number of equations to a power of between two and three on parallel-processing computers, or three on scalar processors. Hence,

the analytic frequency integration translates into a speed gain of at least two orders of magnitude on parallel processors, or three on scalar machines.

Because our equation is a first order differential equation, rather than an integral equation, it relates only adjacent spatial points, rather than all points in the atmosphere. Hence, it has the same advantage over integral methods as the well-known Feautrier (1964) method used in frequency-dependent radiative transfer; one has to solve only band matrices, not full matrices, to obtain a simultaneous numerical solution of the full set of equations. This leads to a further speed gain, by a factor on the order of the number of equations in the numerical grid, relative to integral equation techniques.

Many interesting applications of radiative transfer theory involve systems of equations of various types, rather than just a single equation that describes, say, radiative transfer in an idealized atom with only a single radiative transition. Two quite different approaches have commonly been taken to the solution of such systems. For example, let us consider the usual steady-state multilevel-atom radiative transfer problem. One approach to solving this system of equations is to solve for the source function in equivalent two-level atom form. The numerical technique that is commonly used is successive substitution (see, for example, Athay 1972). The second approach uses the equations in primitive form, which has the advantage of avoiding the elaborate and time-consuming evaluation of the auxiliary equations of the equivalent two-level atom form. The primitive equations are usually solved by complete linearization, using a Newton-Raphson procedure. This method was pioneered by Auer & Mihalas (1969), and is described in a very readable fashion in Mihalas' (1978) book.

The assumptions made to obtain the advantages of probabilistic radiative transfer are common to all techniques that use a frequency-integrated radiative transfer equation and escape probabilities alone, without further refinement. These assumptions break down above certain limits on the gradients of properties of the medium. Although our experience thus far indicates that these limits are not reached in many problems of astrophysical interest, they obviously must be kept in mind. Also, at present, probabilistic methods have not been fully developed for treating overlapping spectral features (say, the overlapping continua of H^- and atomic hydrogen) or partial frequency coherence of scattered photons. The reasons for these various limitations will become clear in appropriate sections below.

A key advance in radiative transfer theory was the derivation of a differential frequency-integrated radiative transfer equation. Such an equation was derived by Frisch & Frisch (1975), hereafter FF, in two-level atom form. Their equation was subsequently cast into primitive form by Canfield *et al.* (1981 a), henceforth CPR, and subsequently generalized by Puetter *et al.* (1982), henceforth PHRC.

The approach to radiative transfer described in this paper has recently been applied to a wide range of solar and astrophysical problems at UCSD. Applications have included coupled radiative transfer and gas dynamics (McClymont & Canfield 1983 a,b, Canfield *et al.* 1983, An *et al.* 1983), coupled static energy balance and multi-element radiative transfer (Ricchiazzi 1982, Ricchiazzi & Canfield 1983), and steady-state multilevel-atom radiative transfer for interlocked lines and continua (Canfield *et al.* 1981 b, Puetter & LeVan 1982).

Our methods are a synthesis of the numerical approach of Auer & Mihalas (1969) and the analytical approach of Ivanov (1973). We have tried to write this paper for a reader who is familiar with stellar atmospheres theory at the level of, say, Mihalas' (1978) book. We have not elaborated on finite difference methods, since many suitable descriptions are readily available (*e.g.* Richtmyer & Morton 1967, Ames 1969, Potter 1973), and limited space precludes a complete description here.

The methods discussed here are oriented toward both spectral lines and continua, in plane-parallel atmospheres. We begin, in Section 2, by discussing the atomic population equations and cooling rates. After introducing the radiative transfer equation in its usual monochromatic (frequency-dependent) form in Section 3 we take two different approaches to probabilistic (frequency-integrated) radiative transfer in Sections 4 and 5. In the latter we split the radiation field into two oppositely-directed streams, while in the former we do not. The interrelated questions of boundary conditions and accuracy are discussed in Sections 6 and 7. The fundamental topic of escape probabilities for various types of absorption and emission coefficient profiles is treated in Section 8. Finally, in Section 9, we discuss numerical methods, with emphasis on techniques for complete linearization, which strongly motivate our entire approach.

2 ATOMIC POPULATION EQUATIONS AND COOLING RATES

Before discussing probabilistic radiative transfer methods we will first discuss the atomic population equations and the expression for the radiative cooling rate, since these equations in a large measure determine the particular radiative transfer quantities that shall interest us in later sections. The atomic population equations can be written

$$\partial n_i / \partial t = -n_i \sum_{j \neq i} R_{ij} + \sum_{j \neq i} n_j R_{ji} \quad (2.1)$$

where for $i > j$

$$R_i \equiv C_i + A_i + B_i J^{s_{im}} \quad (2.2)$$

and for $i < j$

$$R_{ij} \equiv C_{ij} + B_{ij} J^{abs} \quad (2.3)$$

We define

$$J^{stim} \equiv \int_0^{\infty} d\nu J_{ij} \Psi_{ij} \quad (2.4)$$

and

$$J^{abs} \equiv \int_0^{\infty} d\nu J_{ji} \Phi_{ji} \quad (2.5)$$

In the above equations, A_{ij} , B_{ij} for $i > j$, and B_{ji} for $i < j$ are the Einstein coefficients for spontaneous emission, stimulated emission, and absorption respectively for transitions from level i to j , C_{ij} is the collisional rate coefficient from level i to j , Ψ_{ij} and Φ_{ji} are respectively the normalized emission and absorption coefficient profiles ($\int_0^{\infty} d\nu \Psi_{ij} = \int_0^{\infty} d\nu \Phi_{ji} = 1$), and J_{ij} is the monochromatic mean intensity at frequency ν .

We will typically assume that $\Psi_{ij} = \Phi_{ji}$ for spectral lines and ignore stimulated process in the bound-free continua. This assumption will be important to our results below and is discussed further in Section 3. Note also that the values of the Einstein B's employed here are defined per unit mean intensity, and not per unit energy density, which is another common form.

Often it will be desirable to separate J_{ij} into a *diffuse component*, J_{ij}^d , arising from the local emission in the gas, and an *incident component*, J_{ij}^{inc} , arising outside the atmosphere. Hence the total mean intensity is written

$$J_{ij}(\tau) = J_{ij}^d(\tau) + J_{ij}^{inc}(\tau) \quad (2.6)$$

We distinguish these components of the total mean intensity by italics.

An important alternative form of equations (2.1–2.5) is obtained by rearranging the radiative rates into *net radiative downward rates*. When this is done equation (2.1) remains identical but, if $i > j$

$$R_{ij} = C_{ij} + A_{ij} \rho_{ij} \quad (2.7)$$

where

$$\rho_{ij} = (n_i A_{ij} + n_i B_{ij} J^{stim} - n_j B_{ji} J^{abs}) / n_i A_{ij} \quad (2.8)$$

and if $i < j$

$$R_{ij} = C_{ij} \quad (2.9)$$

The quantity ρ has been given various names. It has been termed the net radiative bracket by Thomas & Athay (1961) and the *flux divergence coefficient* by Canfield & Puetter (1981). At times we will indicate, using subscripts, the specific transition to which ρ applies.

Assuming that we can define an *effective mean intensity* J such that

$$J \equiv J^{\text{stim}} = J^{\text{abs}} \quad (2.10)$$

we find for the transition between the upper level, u , and the lower level, l

$$\rho_{ul} = 1 - J/S_0 \quad (2.11)$$

where

$$S_0 \equiv n_u A_{ul} / (n_u B_{lu} - n_l B_{ul}) \quad (2.12)$$

The other important consideration for our probabilistic radiative transfer scheme is the expression for the cooling rate. It follows from equation (2.8) that the *flux divergence* (radiative cooling rate) per unit volume Q_{ul} in transition $u-l$ is

$$Q_{ul} = h\nu_{ul} n_u A_{ul} \rho_{ul} \quad (2.13)$$

for lines, and

$$Q_{cl} = h\nu_{cl} n_c A_{cl} \rho_{cl}^E \quad (2.14)$$

for bound-free continua, where

$$\rho_{cl}^E \equiv 1 - (J \langle \nu/\nu_0 \rangle_a) / (S_0 \langle \nu/\nu_0 \rangle_e) \quad (2.15)$$

The factors that account for the difference between the absorption-weighted and emission-weighted average frequencies respectively are

$$\langle \nu/\nu_0 \rangle_a \equiv \int_0^\infty d\nu (\nu/\nu_0) \Phi_\nu \quad (2.16)$$

and

$$\langle \nu/\nu_0 \rangle_e \equiv \int_0^\infty d\nu (\nu/\nu_0) \Psi_\nu \quad (2.17)$$

The distinction between the *photon flux divergence coefficient* ρ , which is used to calculate radiative rates in equation (2.8), and the *energy flux divergence coefficient*, ρ^E , which is used to calculate the cooling rates, is necessary for bound-free continua because of their large frequency bandwidth. For lines we have to a good approximation $\langle \nu/\nu_0 \rangle_a = \langle \nu/\nu_0 \rangle_e = 1$, so the distinction is unnecessary.

3 THE RADIATIVE TRANSFER EQUATION

For plane parallel atmospheres, the equation of radiative transfer at frequency ν can be written

$$\mu \partial I_\nu(\mu) / \partial x = -\kappa_\nu I_\nu(\mu) + j_\nu \quad (3.1)$$

or

$$\mu \partial I_\nu(\mu) / \partial \tau = -\phi_\nu [I_\nu(\mu) - S_\nu] \quad (3.2)$$

where

$$S_\nu \equiv j_\nu / \kappa_\nu \quad (3.3)$$

and

$$d\tau \equiv \kappa_\nu dx \quad (3.4)$$

where x is the distance into the atmosphere, μ is the cosine of the angle between the direction of radiation propagation and the inward normal to the atmosphere, $I_\nu(\mu)$ is the specific intensity of radiation at the frequency ν and propagating in direction μ , κ_ν is the opacity per unit length at frequency ν , j_ν is the emissivity per unit volume at frequency ν , τ is the line center optical depth (optical depth at the ionization edge for bound-free continua), ϕ_ν is the absorption coefficient profile scaled to unity at line center ionization edge), and S_ν is the source function.

For spectral lines the volume emissivity is

$$j_\nu = h\nu n_u A_{ul} \Psi_\nu \frac{1}{4\pi} \quad (3.5)$$

and the linear opacity is

$$\kappa_\nu = n_l B_{lu} \phi_\nu - n_u B_{ul} \Psi_\nu \frac{h\nu}{4\pi} \quad (3.6)$$

and thus

$$S_\nu = \frac{n_u A_{ul} \Psi_\nu}{(n_l B_{lu} \phi_\nu - n_u B_{ul} \Psi_\nu)} \quad (3.7)$$

where we have counted the stimulated emissions as negative absorptions. Employing the relationships between the Einstein coefficients for spectral lines

$$A_{ul} / B_{ul} = 2h\nu_0^3 / c^2 \quad (3.8)$$

and

$$B_{lu} / B_{ul} = g_u / g_l \quad (3.9)$$

we can write equation (3.7) as

$$S_\nu = (2h\nu_0^3/c^2) (g_u n_l / g_l n_u - \Psi_\nu / \Phi_\nu)^{-1} \Psi_\nu / \Phi_\nu. \quad (3.10)$$

If $\Psi_\nu = \Phi_\nu$, then

$$S_\nu = S_0, \quad (3.11)$$

where

$$S_0 = (2h\nu_0^3/c^2) (g_u n_l / g_l n_u - 1)^{-1}. \quad (3.12)$$

Here ν_0 is the line center frequency and g_u and g_l are the statistical weights of the upper and lower levels. Replacing Ψ_ν / Φ_ν by 1 is adequate for many spectral lines. This approximation may become inadequate, however, for an accurate treatment of cooling by weakly interlocked resonance lines (like hydrogen Ly α), since wing scattering in these lines is coherent and the majority of line photons result from scattered radiation.

For bound-free continua, κ_ν is simply given by

$$\kappa_\nu = n_l \sigma_\nu(\nu) \quad (3.13)$$

where n_l is the level population of the lower level and $\sigma_\nu(\nu)$ is the cross-section for radiative transitions at frequency ν between level l and the continuum, c . Thus the photoionization rate can be written (Mihalas 1978, p. 130)

$$n_l B_c J = 4\pi n_l \int_0^\infty d\nu J_\nu \sigma_\nu(\nu) / h\nu \quad (3.14)$$

Assuming that

$$\sigma_\nu(\nu) = \sigma_\nu(\nu_0) \phi_\nu, \quad (3.15)$$

where

$$\phi_\nu = (\nu/\nu_0)^{-s}, \quad (3.16)$$

which, after normalization, becomes

$$\Phi_\nu = [(s-1)/\nu_0] \phi_\nu, \quad (3.17)$$

we find

$$n_l B_c J = [4\pi n_l \sigma_\nu(\nu_0) / h\nu_0] \int_0^\infty d\nu J_\nu \Phi_\nu / h\nu. \quad (3.18)$$

Here we have defined, by analogy to spectral lines, the absorption rate coefficient, B_c , as

$$B_c \equiv 4\pi \sigma_c(\nu_0) / h(s-1) \quad (3.19)$$

and the effective mean intensity, J , as

$$J \equiv h\nu_0 \int_0^\infty d\nu J_\nu \Phi_\nu / h\nu_0 \quad (3.20)$$

By detailed balance we can obtain an expression for the spontaneous recombination rate coefficient $A_c(\nu) = A_{c1} \Psi(\nu)$, where

$$A_{c1} \equiv (8\pi g_c / g_c c^2) \sigma_c(\nu_0) \nu_0^3 e^{-\alpha} E_{s-2}(\alpha) \quad (3.21)$$

$$\Psi(\nu) \equiv (\nu/\nu_0)^{3-s} e^{-\alpha(\nu/\nu_0)^2} \nu E_{s-2}(\alpha) \quad (3.22)$$

$$\alpha \equiv h\nu_0 / kT \quad (3.23)$$

and

$$g_c \equiv (2\pi mkT/h^2)^{3/2} 2U n_e \quad (3.24)$$

(as shown by Osterbrock 1974, Appendix 1). Here ν_0 is the ionization edge frequency, U is the statistical weight of the ion, m is the mass of the electron, $E_n(x)$ is the exponential integral of order n

$$E_n(x) = \int_0^\infty dt t^{-n} e^{-xt} \quad (3.25)$$

and T is the electron temperature.

Thus the source function for bound-free continua, ignoring stimulated recombination, can be written

$$S_\nu = J_\nu / \kappa_\nu = h\nu n_c A_{c1} \Psi_\nu / n_i B_c \Phi_\nu \quad (3.26)$$

or

$$S_\nu = (2h\nu_0^3/c^2) (g_c n_i / g_i n_c)^{-1} (\nu/\nu_0)^3 e^{-\alpha(\nu/\nu_0)^2} \quad (3.27)$$

or

$$S_\nu = S_0 (\nu/\nu_0) \Psi_\nu / \Phi_\nu \quad (3.28)$$

where

$$S_0 = (2h\nu_0^3/c^2) (g_c n_i / g_i n_c)^{-1} (s-1) e^{-\alpha} E_{s-2}(\alpha) \quad (3.29)$$

4 ONE-STREAM PROBABILISTIC RADIATIVE TRANSFER

The formal solution to equation (3.2) in the absence of incident radiation, and assuming Φ_ν and Ψ_ν do not vary with optical depth, is

$$I_\nu^-(\mu, \tau_\nu) = \int_0^{\tau_\nu} dt/\mu S_\nu e^{-(\tau_\nu - t)/\mu} \quad ; \mu > 0 \quad (4.1)$$

$$I_\nu^+(\mu, \tau_\nu) = -\int_{\tau_\nu}^{\infty} dt/\mu S_\nu e^{-t/\mu} e^{-(\tau_\nu - t)/\mu} \quad ; \mu < 0 \quad (4.2)$$

where I_ν^- and I_ν^+ are the radiation fields propagating into and out of the atmosphere respectively. In the equations above, τ_ν is the optical depth at frequency ν , which is given by

$$\tau_\nu = \tau \phi_\nu \quad (4.3)$$

where τ is the line center (photoionization edge, for bound-free continua) optical depth and T_ν is the total depth of the slab at frequency ν (note T_ν is infinite for semi-infinite atmospheres).

To derive the expression for the mean intensity

$$J_\nu(\tau_\nu) \equiv \langle I_\nu \rangle \int d\Omega I_\nu(\mu) \quad (4.4)$$

or

$$J_\nu(\tau_\nu) = (1/2) \int_{-1}^1 d\mu I_\nu^-(\mu, \tau_\nu) + (1/2) \int_1^{\infty} d\mu I_\nu^+(\mu, \tau_\nu) \quad (4.5)$$

we use equations (4.1) and (4.2) to obtain

$$J_\nu(\tau_\nu) = - (1/2) \int_{-1}^1 d\mu \int_0^{\tau_\nu} dt/\mu S_\nu e^{-(\tau_\nu - t)/\mu} + (1/2) \int_1^{\infty} d\mu \int_{\tau_\nu}^{\infty} dt/\mu S_\nu e^{-t/\mu} e^{-(\tau_\nu - t)/\mu} \quad (4.6)$$

or using equation (3.25)

$$J_\nu(\tau_\nu) = (1/2) \int_0^{\tau_\nu} dt S_\nu E_1(t - \tau_\nu) + (1/2) \int_0^{\tau_\nu} dt S_\nu E_1(\tau_\nu - t) \quad (4.7)$$

or

$$J_\nu(\tau_\nu) = (1/2) \int_0^{\tau_\nu} dt S_\nu E_1(t - \tau_\nu) \quad (4.8)$$

To get an expression for the *effective mean intensity*, which since we assume $\Psi_\nu = \Phi_\nu$ is

$$J(\tau) = \int_0^\infty d\nu J_\nu \Phi_\nu \quad (4.9)$$

we use equation (4.8) to obtain

$$J(\tau) = (1/2) \int_0^\infty d\nu \Phi_\nu \int_0^\tau dt \phi_\nu S_\nu E_1(|t-\tau| \phi_\nu) \quad (4.10)$$

Since for both lines and continua we are assuming we can write

$$S_\nu \equiv S_\nu \Psi_\nu = \Phi_\nu \quad (4.11)$$

we find

$$J(\tau) = (1/2) \int_0^\tau dt S_\nu(t) \int_0^\infty d\nu \phi_\nu \Psi_\nu E_1(|t-\tau| \phi_\nu) \quad (4.12)$$

If we define

$$K_1(\tau) \equiv (1/2) \int_0^\infty d\nu \phi_\nu \Psi_\nu E_1(|\tau| \phi_\nu) \quad (4.13)$$

then

$$J(\tau) = \int_0^\tau dt S_\nu(t) K_1(t-\tau) \quad (4.14)$$

where τ and t now measure line center (ionization edge) optical depths and we have chosen to write the kernel function in equation (4.14) as K_1 in keeping with common notation. However, note that many authors define K_1 in slightly different ways. For example, this definition is 1/2 that given by Ivanov (1973). Other common modifications to these formulas and definitions result from using mean optical depth rather than line center (ionization edge) optical depth.

The fundamental assumptions of equation (4.14) are: (1) the atmosphere is *plane parallel* and (2) the propagation of photons from one point to another depends only on their optical depth difference, and not upon the conditions at the individual points (through the assumption that Φ_ν and Ψ_ν do not depend upon τ). The second assumption is a good approximation as long as there is sufficiently little variation of the atmospheric parameters within a photon mean free path. We return to this point in the discussion of escape probabilities below.

The value for the frequency integrated mean intensity given in equation (4.14) is, of course, only the diffuse component of the total intensity. The incident component must be added to this value to obtain the total value of $J(\tau)$:

$$J(\tau) = J(\tau) + J^{inc}(\tau) \quad (4.15)$$

where

$$J(\tau) = \int_0^T dt S_0(t) K_1(t-\tau) \quad (4.16)$$

$$J^{inc}(\tau) = (1-\epsilon) \int_0^\infty d\nu \Phi_\nu \int_0^1 d\mu (1-\mu) e^{-\tau/\mu} e^{-\nu\tau} + (1-\epsilon) \int_0^\infty d\nu \Phi_\nu \int_0^1 d\mu (1-\mu) e^{-\tau/\mu} e^{-\nu(T-\tau)} \quad (4.17)$$

Here we see that we need be concerned with calculating only the diffuse component of the radiation field, since the incident contribution can be expressed in closed form. Thus, in deriving our probabilistic radiative transfer equation, we shall work from equation (4.14) assuming that J^{inc} is zero. First we shall apply the operator

$$\int_0^\tau d\tau' S_0(\tau') \partial / \partial \tau' \quad (4.18)$$

to both sides of equation (4.14) and obtain

$$\int_0^\tau d\tau' S_0(\tau') \partial J(\tau) / \partial \tau' = \int_0^\tau d\tau' S_0(\tau') \partial / \partial \tau' \int_0^T dt S_0(t) K_1(t-\tau) \quad (4.19)$$

which can be written

$$\int_0^\tau d\tau' S_0(\tau') \partial J(\tau) / \partial \tau' = \int_0^\tau d\tau' S_0(\tau') \partial / \partial \tau' \int_0^T dt S_0(t) K_1(t-\tau) + \int_0^\tau d\tau' S_0(\tau') \partial / \partial \tau' \int_0^T dt S_0(t) K_1(t-\tau) \quad (4.20)$$

One can show that the first term of the right hand side of equation (4.20) is identically zero since $K_1(t-\tau) = K_1(\tau-t)$. In the second term, since $0 < \tau < \sigma < t < T$ and the integrand vanishes for $\tau-t \gg 1$, we can write $S(\tau) \cong S(t) \cong S(\sigma)$. If S is slowly varying, i.e. $(d \ln S_0 / d \ln \tau) \ll 1$, we obtain

$$\int_0^\tau d\tau' S_0(\tau') \partial J(\tau) / \partial \tau' \cong S_0^2(\sigma) \int_0^\tau d\tau' \partial / \partial \tau' \int_0^T dt K_1(t-\tau) \quad (4.21)$$

From the definition of the single flight escape probability p_e (see Section 8), and the relationship between $E_1(x)$ and $E_2(x)$ (see, e.g. Abramowitz & Stegun 1964)

$$\int_0^x dt K_1(t) = p_e(0) - p_e(x) = 1 - p_e(x) \quad (4.22)$$

Thus we also have the relation

$$\int_x^T dt K_1(t-x) = p_e(x-T) - p_e(T-x) \quad (4.23)$$

and hence

$$\int_0^x dt \partial_t \partial_\tau \int_x^T dt K_1(t-x) = p_e(0) - p_e(T) - p_e(x) - p_e(T-x) \quad (4.24)$$

Substituting equation (4.24) into equation (4.21), applying the operator

$$S_0^{-1}(\tau) \partial_t \partial_\tau \quad (4.25)$$

to the result, and then replacing x with τ we have

$$\begin{aligned} \partial J \partial_\tau &= 2 [p_e(0) - p_e(T) - p_e(\tau) - p_e(T-\tau)] \partial S_0^{-1} \partial_\tau \\ &\quad - S_0^{-1} \partial_\tau [p_e(\tau) - p_e(T-\tau)] \end{aligned} \quad (4.26)$$

This equation can be expressed in a number of forms. Since $p_e(0) = 1$,

$$\partial J \partial_\tau = [1 - 2p_e^*(\tau)] \partial S_0^{-1} \partial_\tau - S_0^{-1} \partial_\tau p_e^* \partial_\tau \quad (4.27)$$

or

$$\partial(S_0 - J) \partial_\tau = \partial(\rho S_0^{-1}) \partial_\tau = 2(\rho_e^*) \partial_\tau [(\rho_e^*)^{-1} S_0] \quad (4.28)$$

or

$$\partial_\tau \partial_\tau = \partial \rho_e^* \partial_\tau + (2\rho_e^* - \rho) \partial \ln S_0^{-1} \partial_\tau \quad (4.29)$$

where

$$\rho = 1 - J/S_0 \quad (4.30)$$

and

$$\rho_e^*(\tau) = p_e(\tau) + p_e(T-\tau) - p_e(T) \quad (4.31)$$

It is important to remember that since the probabilistic differential equations given above were derived for the diffuse radiation fields, the values of ρ given by these equa-

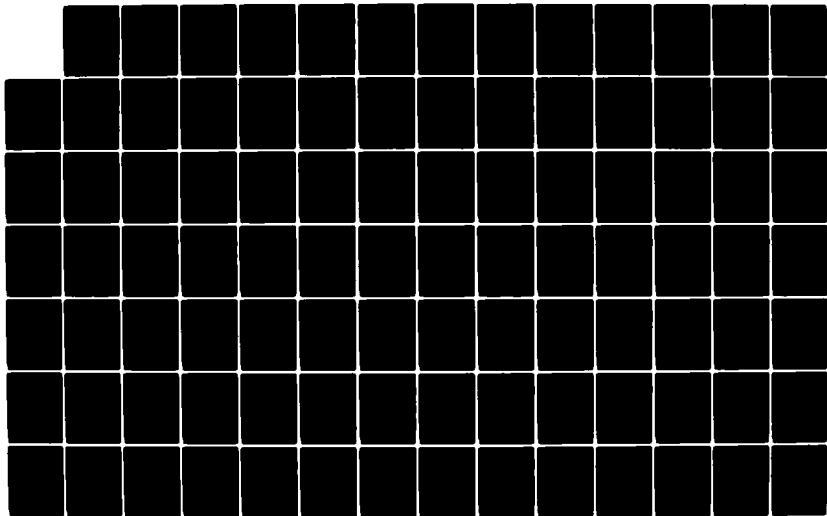
AD-A145 009

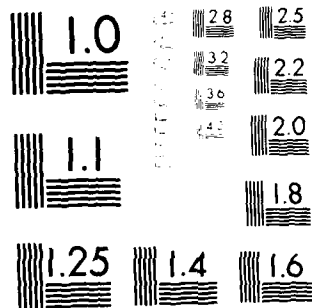
STUDIES OF SOLAR FLARES AND CORONAL LOOPS(U) CALIFORNIA
UNIV SAN DIEGO LA JOLLA CENTER FOR ASTROPHYSICS AND
SPACE SCIENCES R C CANFIELD 10 JUL 84 UCSD-SP-84-21
AFOSR-TR-84-0719 AFOSR-82-0092 F/G 3/2

23

UNCLASSIFIED

NL





MICROCOPY RESOLUTION TEST CHART
 NATIONAL BUREAU OF STANDARDS-1963-A

tions are the values for the diffuse radiation fields. The contributions of the incident radiation fields must be added to these values.

One can also write the probabilistic radiative transfer equation (for steady state problems) in equivalent two-level atom form:

$$S_2 \partial/\partial\tau (p_0^* + \epsilon) - (2p_0^* + \epsilon) \partial S_2/\partial\tau = \partial/\partial\tau (\epsilon B) \quad (4.32)$$

where we have written the source function in the well-known two-level atom form (cf. Mihalas 1978, p. 376; Jefferies 1968, p. 181):

$$S_2 = (J + \epsilon B) / (1 + \epsilon) \quad (4.33)$$

The sole approximation of the derivation of our probabilistic radiative transfer equation from (4.14) is that S_2 varies slowly compared to K_1 . Since $K_1(\tau)$ varies like the derivative of $p_0(\tau)$, it is necessary that the absolute value of $d \ln S_2 / d \ln \tau \ll 1$ for the approximation to be valid (unless the value of τ is very small).

The various forms of the probabilistic radiative transfer equation (4.27) through (4.29) and (4.32) are useful for different applications. Since the obvious intent of our approach is to develop a radiative transfer equation that is useful as part of an extensive set of equations, (4.27) through (4.29) are much more useful, they do not require the evaluation of ϵ and B , which is very time-consuming. For simple problems in which ϵ and B are fixed, equation (4.32) is the obvious choice.

5 TWO-STREAM PROBABILISTIC RADIATIVE TRANSFER

The equations developed in Section 4 treat the radiation field in a 'one-stream' approach. For finite slab atmospheres a two-stream approach to the radiation field has the advantage that it allows specification of the mean intensity at each of the atmosphere boundaries (*i.e.* the diffuse radiation field propagating into the slab is identically zero at each boundary). Since the results of this approach are important to understanding the boundary condition problem presented in the next section, we will now develop these equations.

Equation (4.7) shows that the mean intensity J_ν can be written in two parts, which we shall call J_ν^+ and J_ν^- , corresponding to I_ν^+ and I_ν^- . By integrating these quantities over frequency we obtain the expressions for the diffuse contribution to both J^+ and J^- (cf. 4.14):

$$J^-(\tau) = \int_0^\tau dt S_2(t) K_1(t-\tau) \quad (5.1)$$

$$J^+(\tau) = \int_\tau^1 dt S_0(t) K_1(t-\tau) \quad (5.2)$$

where τ is again the line center (photoionization edge) optical depth and K_1 is given by equation (4.13). We now proceed in a manner nearly identical to Section 4 and apply the operator

$$\int_0^{\infty} d\tau S_0(\tau) \partial/\partial\tau \quad (5.3)$$

to equation (5.1) to obtain

$$\int_0^{\infty} d\tau S_0(\tau) \partial J^-(\tau) \partial\tau = \int_0^{\infty} d\tau S_0(\tau) \partial \partial\tau \int_0^{\infty} dt S_0(t) K_1(t-\tau) \quad (5.4)$$

or

$$\begin{aligned} \int_0^{\infty} d\tau S_0(\tau) \partial J^-(\tau) \partial\tau &= \int_0^{\infty} d\tau S_0(\tau) \partial \partial\tau \int_0^{\infty} dt S_0(t) K_1(t-\tau) \\ &- \int_0^{\infty} d\tau S_0(\tau) \partial \partial\tau \int_0^{\infty} dt S_0(t) K_1(t-\tau) \end{aligned} \quad (5.5)$$

Again, just as in Section 4, the symmetry of K_1 causes the first right-hand term to vanish, with the result

$$\int_0^{\infty} d\tau S_0(\tau) \partial J^-(\tau) \partial\tau = \int_0^{\infty} d\tau S_0(\tau) \partial \partial\tau \int_0^{\infty} dt S_0(t) K_1(t-\tau) \quad (5.6)$$

Assuming that S_0 varies slowly in comparison to $K_1(t-\tau)$, we find

$$\int_0^{\infty} d\tau S_0(\tau) \partial J^-(\tau) \partial\tau \approx \int_0^{\infty} d\tau S_0(\tau) \partial \partial\tau S_0(\tau) \int_0^{\infty} dt K_1(t-\tau). \quad (5.7)$$

Using equation (4.23) we obtain

$$\int_0^{\infty} d\tau S_0(\tau) \partial J^-(\tau) \partial\tau = \int_0^{\infty} d\tau S_0(\tau) \partial \partial\tau S_0(\tau) [p_0(\sigma-\tau) - p_0(0)] \quad (5.8)$$

or since $p_0(0) = 1/2$

$$\begin{aligned} \int_0^{\infty} d\tau S_0(\tau) \partial J^-(\tau) \partial\tau &= - (1/2) \int_0^{\infty} d\tau S_0(\tau) \partial S_0(\tau) \partial\tau \\ &+ \int_0^{\infty} d\tau S_0(\tau) \partial/\partial\tau [S_0(\tau) p_0(\sigma-\tau)] \end{aligned} \quad (5.9)$$

If we now further assume that S_0 varies slowly on the scale of ρ_0 then we can write

$$\int_0^T dt S_0(t) \partial J^+(t) / \partial t \approx - (1/4) \int_0^T dt \partial S_0^2(t) / \partial t + S_0^2(0) \int_0^T dt \partial \rho_0(t) / \partial t \quad (5.10)$$

This last assumption is apparently more restrictive than assuming S_0 varies slowly in comparison to K_1 . However, the resulting equations are very similar. After evaluating the right hand side of equation (5.10) we apply the operator

$$S_0^{-1}(t) \partial / \partial t \quad (5.11)$$

and by replacing t with τ we immediately gain the result

$$\partial J^+(t) / \partial t = [\rho_0(0) - 2\rho_0(t)] \partial S_0(t) / \partial t - S_0(t) \partial \rho_0(t) / \partial t \quad (5.12)$$

Applying the operator

$$\int_0^T dt S_0^{-1}(t) \partial / \partial t \quad (5.13)$$

to equation (5.12) and using a similar line of reasoning we obtain

$$\partial J^+(t) / \partial t = [\rho_0(0) - 2\rho_0(T-t)] \partial S_0(t) / \partial t - S_0(t) \partial \rho_0(T-t) / \partial t \quad (5.14)$$

The above equations for J^+ and J^- , when added together, give the result:

$$\partial J(t) / \partial t = \partial [J^+(t) + J^-(t)] = 2 [\rho_0(0) - \rho_0(t) - \rho_0(T-t)] \partial S_0(t) / \partial t - S_0(t) \partial [\rho_0(t) + \rho_0(T-t)] \quad (5.15)$$

This result is nearly identical to equation (4.26). The only difference between the two equations is the appearance of the term $2\rho_0(T) \partial S_0(t) / \partial t$ in equation (4.26), which vanishes for large T . Nonetheless, we feel that equation (4.26) is slightly preferable to equation (5.15) since we did not need to assume that S_0 vary slowly in comparison to ρ_0 to derive this equation. We can, however, easily make both sets of equations the same by defining

$$\rho_0^+ = \rho_0(t) - \rho_0(T) \quad (5.16)$$

$$\rho_0^- = \rho_0(T-t) - \rho_0(T) \quad (5.17)$$

to obtain

$$\partial J^+(t) / \partial t = [1 - 2\rho_0^+(t)] \partial S_0(t) / \partial t - S_0(t) \partial \rho_0^+(t) \quad (5.18)$$

$$\partial J^-(t) / \partial t = [1 - 2\rho_0^-(t)] \partial S_0(t) / \partial t - S_0(t) \partial \rho_0^-(t) \quad (5.19)$$

The other forms of the two-stream radiative transfer equation can also be obtained by defining ρ^+ and ρ^- in the appropriate manner:

$$\rho^+ = \frac{1}{2} - J^+/S_0 \quad (5.20)$$

$$\rho^- = \frac{1}{2} - J^-/S_0 \quad (5.21)$$

and thus obtain

$$\partial(S_0 - J^+)/\partial\tau = \partial(\rho^+ S_0)/\partial\tau = 2(\rho_0^+) \partial/\partial\tau [(\rho_0^+)^{-1} S_0] \quad (5.22)$$

$$\partial(S_0 - J^-)/\partial\tau = \partial(\rho^- S_0)/\partial\tau = 2(\rho_0^-) \partial/\partial\tau [(\rho_0^-)^{-1} S_0] \quad (5.23)$$

and

$$\partial\rho^+/\partial\tau = \partial\rho_0^+/\partial\tau - (2\rho_0^+ - \rho^+) \partial \ln S_0 / \partial\tau \quad (5.24)$$

$$\partial\rho^-/\partial\tau = \partial\rho_0^-/\partial\tau - (2\rho_0^- - \rho^-) \partial \ln S_0 / \partial\tau \quad (5.25)$$

The two-stream approach, while apparently quite similar to the one-stream approach, has one very significant advantage: it allows two boundary conditions. This advantage will be discussed further in Section 6 below.

6. BOUNDARY CONDITIONS

We now turn to the question of boundary conditions, for both the one-stream and two-stream approaches, and for both semi-infinite and finite plane-parallel atmospheres.

For semi-infinite atmospheres, for which one-stream radiative transfer is of well-known accuracy, the boundary condition reflects the fact that the probability of photon escape approaches zero deep in the atmosphere. Hence, both the effective intensity and the line center source function approach the effective Planck function:

$$J(\tau=\infty) = S_0(\tau=\infty) = B(\tau=\infty) \quad (6.1)$$

where

$$B = \int_0^\infty d\nu B_\nu \Phi_\nu \quad (6.2)$$

In effect, this boundary condition is adequate because it follows trivially from the equivalent boundary condition for a semi-infinite atmosphere in the two-stream approach:

$$J^+(\tau=\infty) = J^-(\tau=\infty) = B(\tau=\infty)/2 \quad (6.3)$$

Clearly these boundary conditions can be implemented accurately in a numerical calculation, in which a finite number of grid points are used to represent a semi-infinite atmosphere, only by ensuring that the optical depth of the deepest point in the model atmosphere is sufficiently large.

The question of appropriate boundary conditions for a one-stream approach to finite atmospheres has recently been discussed by PHRC and Hummer & Rybicki (1982). Both of these papers treat time-independent atmospheres using an effective two-level atom approach in which the values of ϵ and B are held fixed, and the boundary conditions discussed in them are most useful for such problems (see Section 7 below). Also, several of these expressions are of limited usefulness either because they are only approximate or they only establish upper and lower limits. Hence, we will not discuss them further here. The exception is the global energy balance condition suggested by Hummer & Rybicki. This condition, which can be written

$$\int_0^{\tau} d\tau \rho S = \int_0^{\tau} d\tau \rho_e S \quad (6.4)$$

requires that the excess of the number of emissions over the number of absorptions be equal to the number of escaping photons, integrated over the atmosphere. Hubbard & Puetter (1983) have successfully used this boundary condition for a multilevel atom radiative transfer problem in a finite atmosphere.

For finite atmospheres it may be better to use two-stream radiative transfer, because exact and fixed boundary conditions are available, *i.e.* there is no *diffuse* radiation coming into either side:

$$J(\tau=0) = J(\tau=T) = 0 \quad (6.5)$$

On the other hand, one could also use a one-stream approach

$$J(\tau_0) = \int_0^{\tau} dt S(t) K_1(\tau-t) \quad (6.6)$$

where τ_0 is the optical depth at the point where the boundary condition is imposed. However, this has the significant disadvantage that the value of $J(\tau_0)$ changes from iteration to iteration. Hubbard & Puetter (1983) found the global energy balance condition, equation (6.4), superior to equation (6.6).

7 ACCURACY OF THE SOLUTIONS

The accuracy of probabilistic radiative transfer methods depends on both the equation itself and on the boundary condition. In the case of semi-infinite atmospheres, both the one and two-stream boundary conditions can be approximated to arbitrarily high accuracy, and FF have adequately discussed the accuracy of the radiative transfer equation itself. They showed that the one-stream probabilistic radiative transfer equation gives results accurate to a few tens of percent unless the effective Planck function varies on an unrealistically small spatial scale. The FF discussion shows that probabilistic techniques will prove useful for a wide range of problems of physical interest. Our experience is that even models that appear to have very steep Planck-function gradients, such as the semi-empirical solar model chromospheres of Vernazza et al. (1981), yield source functions whose gradients do not violate the assumptions of one-stream probabilistic radiative transfer.

For finite atmospheres, the accuracy of the combination of one-stream probabilistic radiative transfer and the boundary conditions of PHRC and Hummer & Rybicki (1982) is a matter that must be established, since the boundary conditions are not exact. These authors have shown that their methods are typically accurate to 30% or better, in the cases they examined.

On the other hand, there is no question of accuracy of boundary conditions for finite atmospheres when two-stream radiative transfer is used; only the accuracy of the probabilistic radiative transfer equation itself need be determined.

8 PHOTON ESCAPE PROBABILITIES

From the sections above, it is clear that photon escape probabilities play a central role in probabilistic radiative transfer. Hence, in order to model nature accurately, we must employ escape probabilities that rest on a sound mathematical and physical foundation. Furthermore, having developed an efficient computational technique, we are interested in expressions for the photon escape probability that will not compromise computational speed. In this section we will develop simple and efficient expressions for the single flight photon escape probability for a variety of physical processes.

Our probabilistic radiative transfer equation assumes that the atmosphere is plane-parallel and that the kernel given in equation (4.13) can be represented adequately as a difference kernel, i.e. that the propagation of photons from one point to another depends only on their optical depth difference, and does not depend on other physical conditions at the points themselves. The escape probabilities are defined on the same assumptions. If one wants to treat atmospheres with significant velocity gradients, for example, it is then necessary to derive both an appropriate transfer equation

and appropriate escape probabilities. We will begin with a description of the static escape probabilities that we use, and return later in this section to the question of the range of their validity in atmospheres with bulk flow velocities.

The probability that a photon will escape the medium in a single flight is given by

$$p_e(\tau) \equiv \int_0^{\infty} d\nu \int_0^1 d\mu \Psi_\nu e^{-\tau\mu} \quad (8.1)$$

which can be written

$$p_e(\tau) = \int_0^{\infty} d\nu \Psi_\nu E_2(\tau\phi_\nu) \quad (8.2)$$

For spectral lines, if we assume that the line profile is symmetric, change the variable of integration to displacement from line center $x = (\nu - \nu_0) / \Delta\nu_D$, where $\Delta\nu_D$ is the Doppler width, and assume that the emission and absorption coefficient profiles are identical, this reduces to

$$p_e(\tau) = \int_0^{\infty} dx \Psi(x) E_2(\tau\phi(x)) \quad (8.3)$$

or

$$p_e(\tau) = M \int_0^{\infty} dx \phi(x) E_2(\tau\phi(x)) \quad (8.4)$$

where M is the normalization constant defined by

$$\Phi \equiv M \phi_0 \quad (8.5)$$

In order to achieve high computational speed, it is usually necessary to employ approximate expressions for the photon escape probabilities. However, these expressions can be made to have surprisingly good accuracy over a wide range of optical depths. This is usually done by using a simple analytical expression for the escape probability that incorporates exact asymptotic escape probabilities that have the proper behavior as the optical depth approaches infinity. Below, we will derive such exact asymptotic forms of the escape probability, which we denote by \bar{p}_e , for a variety of common absorption coefficient profiles.

Before we proceed, it is instructive to examine an approximate expression for \bar{p}_e which gives one some physical understanding for how the functional form of the escape probability arises. For purposes of illustration, we will derive an approximate asymptotic form for Doppler absorption profiles. Following the development of

Osterbrock (1962), we assume that only photons with optical depths less than unity escape the atmosphere. Under this assumption

$$\bar{p}_s(\tau) \approx \int_{x_1}^{\infty} dx \Phi(x) , \quad (8.6)$$

where

$$\tau \phi(x_1) \equiv 1 . \quad (8.7)$$

For a Doppler absorption coefficient profile,

$$\phi(x) = \pi^{-1/2} \delta(x) = \pi^{-1/2} \exp(-x^2) \quad (8.8)$$

As τ goes to infinity so does x_1 and we find

$$\bar{p}_s(\tau) \approx (\pi^{-1/2} x_1) \exp(-x_1^2) \quad (8.9)$$

This reduces to

$$\bar{p}_s(\tau) \approx (2\pi^{-1/2} \tau^{-1/2}) \exp(-\tau^{-1/2}) \quad (8.10)$$

As we shall see below, Osterbrock's approximation gives the correct functional form of \bar{p}_s for a Doppler absorption coefficient profile, though the numerical factor is in error by a factor of two. The reason this approximation is successful is that redistribution of photons in frequency, which it takes into account, is very important, and only photons emitted at nearly optically thin frequencies escape.

We will now turn to the derivation of the exact asymptotic expression. Following the lead of Ivanov (1973 § 2.6), in whose notation the probability that a photon escapes the atmosphere in a single flight is $K_2^{-1/2}$, we shall change the variable of integration in equation (8.4) to $z = 1/\delta(x)$, and thus obtain

$$p_s(\tau) = M \int_1^{\infty} dz z^{-1} x'(z) E_2(\tau/z) , \quad (8.11)$$

where $x'(z)$ is the derivative of x with respect to z . Letting $y = \tau/z$ we get

$$p_s(\tau) = M \int_0^{\tau} dy y^{-1} x'(\tau/y) E_2(y) , \quad (8.12)$$

which we rewrite as

$$p_s(\tau) = M x'(\tau) \int_0^{\tau} dy y^{-1} E_2(y) x'(\tau/y)/x'(\tau) . \quad (8.13)$$

We are now ready to derive the asymptotic form of p_e (i.e. we let $\tau \rightarrow \infty$ in eq. 8.13). For many functional forms of $\Phi(x)$ we have

$$\lim_{\tau \rightarrow \infty} [x'(\tau/y) / x'(\tau)] = y^{2\delta} \quad (8.14)$$

and hence the exact asymptotic form of p_e is

$$\bar{p}_e(\tau) = M x'(\tau) \int_0^{\infty} dy y^{2\delta-1} E_2(y) \quad (8.15)$$

By the definition of $E_2(x)$ we have

$$\bar{p}_e(\tau) = M x'(\tau) \int_0^{\infty} dy y^{2\delta-1} \int_0^{\infty} dt t^{-2} \exp(-ty) \quad (8.16)$$

or, reversing the order of integration,

$$\bar{p}_e(\tau) = M x'(\tau) \int_0^{\infty} dt t^{-2} \int_0^{\infty} dy y^{2\delta-1} \exp(-ty) \quad (8.17)$$

Again changing variables, this time letting $u = ty$, we find

$$\bar{p}_e(\tau) = M x'(\tau) \int_0^{\infty} dt t^{-2\delta+2} \int_0^{\infty} du u^{2\delta-1} \exp(-u) \quad (8.18)$$

Noting that the first integral is easily evaluated and the second is a gamma function, we finally obtain

$$\bar{p}_e(\tau) = M \Gamma(2\delta) x'(\tau) / (2\delta + 1) \quad (8.19)$$

Having derived the exact asymptotic form of p_e , we can also write the expression for the asymptotic expression for K_1 . Since

$$K_1(\tau) = -dp_e/d\tau \quad (8.20)$$

(see equation (4.13)), we immediately find

$$K_1(\tau \rightarrow \infty) = -M \Gamma(2\delta) x''(\tau) / (2\delta + 1) \quad (8.21)$$

Equation (8.19) gives the following exact asymptotic expression in the case of pure Doppler broadening:

$$\bar{p}_e(\tau) = (4\pi^{\delta} \tau \ln^{\delta} \tau)^{-1} \quad (8.22)$$

while for line absorption coefficient profiles varying like $\Phi(x) = \alpha^{-1} x^{-\beta}$ with $\beta > 1$, equation (8.21) gives the exact asymptotic result

$$\bar{p}_e(\tau) = \alpha^{1/\beta} M^{(\beta-1)/\beta} \Gamma[(\beta-1)/\beta] \tau^{-\beta-1/\beta} / (2\beta-1) . \quad (8.23)$$

From equation (8.23) we can calculate the asymptotic escape probability for a wide range of physical processes, as done by Puetter (1981) and Puetter & Hubbard (1982).

In the radiative and collisional *damping wings* of strongly interlocked resonance lines, which have a Lorentz profile, i.e. $\Phi(x) = a / \pi x^{-2}$, the asymptotically exact expression is

$$\bar{p}_e(\tau) = (1/3) (a / \pi^2 \tau)^{1/2} , \quad (8.24)$$

where $a = \Gamma^2 / (4\pi \Delta\nu_D)$, and Γ is the total damping width of the transition (Mihalas 1978, p. 278).

If *linear Stark* broadening (we assume a Holtsmark profile $\Phi(x) = \alpha_{\text{H}} x^{-5/2}$) dominates the absorption coefficient profile, we obtain the exact asymptotic escape probability for hydrogenic ions

$$\bar{p}_e(\tau) = (1/4) \alpha_{\text{H}}^{-2/5} \pi^{-3/2} \Gamma(3/5) \tau^{-3/5} , \quad (8.25)$$

where

$$\alpha_{\text{H}} = 6.9 \times 10^{-5} Z^{-3/2} (n_2 n_1)^3 \chi_1 T_4^{-3/4} n_{e2} . \quad (8.26)$$

In equation (8.26) n_2 and n_1 are the principal quantum number of the upper and lower levels, $\chi_1 = 0.5$ if $n_2 = n_1 + 1$ and $\chi_1 = 1.0$ otherwise, $T_4 = T_e / 10^4$ K, $n_{e2} = n_e / 10^{12} \text{ cm}^{-3}$ (we assume that $n_2 = n_e$), and Z is the charge on the ion.

$\text{Ly}\alpha$ and other weakly interlocked resonance lines cannot be treated, using the methods described in this paper, without further approximation, since we know that the emission and absorption coefficient profiles differ. This is because *wing* scattering is coherent in the atom's frame and $\text{Ly}\alpha$ emission is almost always dominated by scattering. Adams (1972) has shown that diffusion of photons in space and frequency is critically important to the escape of $\text{Ly}\alpha$, and has estimated an eventual escape probability that takes these processes into account. An upper limit to the single flight escape probability p_e is given by this eventual escape probability, i.e.

$$p_e(\tau) \leq 1 / (3\pi^2 \tau) . \quad (8.27)$$

To apply probabilistic radiative transfer to $\text{Ly}\alpha$ and similar lines, one can make either of two approximations. On one hand, one can assume that frequency redistribution is confined to the Doppler core, and the damping wings play no role, i.e. one can use a pure Doppler escape probability. Milkey and Mihalas (1973) showed, for a solar model

atmosphere, that this is a reasonably good approximation. On the other hand, one can adopt equation (8.27) as an equality, and use it as an effective single-flight escape probability. Although these two different approaches are based on much different physical mechanisms, they do not give dramatically different values of the Ly α escape probability.

If Stark broadening dominates wing photon emission in Ly α , but the damping wings dominate wing photon absorption, we find the asymptotically exact expression

$$\bar{p}_s(\tau) = (2/7) \tau^{3/2} \Gamma(3/4) \alpha^{-1/2} a^{-3/4} \tau^{-3/4} \quad (8.28)$$

In order to treat single flight escape in the bound-free continua we must take into account the difference between the emission coefficient profile and the absorption coefficient profile. An accurate treatment of the photon escape probability unfortunately requires numerical integration of equation (8.2). For many applications, however, approximate values for the photon escape probability are adequate. Furthermore, approximate expressions for p_s are more expedient computationally. For these reasons Canfield & Ricciuzzi (1981) derived the following approximate form for p_s in bound-free continua.

$$p_s(\tau) = (23)^{-1/2} \exp[-\tau^3 - \tau(3 - \beta)] \quad (8.29)$$

where

$$\beta = \max\{3 - \tau^{1/2}, 1\} \quad (8.30)$$

and α is defined in equation (3.23). This expression uses the fact that at low temperatures the Boltzmann factor cuts off sharply the contribution of electrons beyond the ionization edge. As long as α is significantly larger than 1 and β is not much larger than 1, equation (8.29) is a reasonably accurate approximation to p_s . Thus, equation (8.29) gives good values for the photon escape probabilities between $\tau = 0$ and reasonably large values of τ .

Having now evaluated the exact asymptotic escape probabilities under various circumstances, we need a procedure to join the various regimes, since in general the absorption coefficient profile will not be totally dominated by the Doppler, damping, or Stark component. Obviously an exact calculation is not in the spirit of the techniques discussed above since it would compromise computational speed. Fortunately, it is often adequate to express the absorption coefficient profile as the sum of various parts (a sum of the Doppler profile and a Lorentz profile is an expedient approximation to the exact Voigt profile, for example). This is the approximation we have used in applications (see, for example, Canfield & Puetter 1981 a,b, Canfield *et al.* 1981 b,

Puetter & LeVan 1982). One must take care, however, that the individual terms in the sum are well behaved outside of their region of dominance. The exact asymptotic expressions typically diverge as τ approaches zero; obviously steps must be taken, for example, to ensure that p_0 takes the value of $1/2$ at $\tau = 0$.

It is clear that static escape probabilities and our basic radiative transfer equation begin to break down significantly at certain identifiable limits on the gradients of Doppler width and bulk flow velocity. Useful guidelines are given by Hummer & Rybicki (1980), based on general expressions from Sobolev (1957). Hummer and Rybicki show that for a given value of the flow-velocity gradient $\gamma \equiv dv/d\tau$ (v in units of the thermal velocity), the expression for the static escape probability holds approximately for all values of line center optical depth less than a critical value τ_c which depends only on γ and the form of ϕ . For Doppler profiles $\tau_c = 3.1/\gamma(2\ln\gamma)^{1/2}$. For Lorentz profiles $\tau_c = 8/\gamma^2$.

9. NUMERICAL METHODS

Our approach to radiative transfer was developed for applications in which radiative transfer is but one of several aspects of the physical problem of interest. Hence, the method anticipates the simultaneous solution of a set of many coupled nonlinear equations, which may include time dependence. For solution on a digital computer, these continuous equations must be replaced by a finite set of equations on a discrete grid, which may be written as

$$\bar{F}(\bar{x}) = \bar{0}, \quad (9.1)$$

where each component x_i ($i=1,\dots,N$) of \bar{x} represents one of the physical variables at some point in space.

Some considerations are unique to time-dependent problems. Nonlinear time-dependent equations may be integrated using either *explicit* or *implicit* formulations of the finite difference equations (Richtmyer & Morton 1967, p. 17). In an explicit formulation, the variables to be determined at a future time occur only in the linear time derivatives. However, explicit formulations have the great disadvantage that numerical instability can limit the time step to an impractically small value. Any physically important diffusion mechanism (e.g. thermal conduction) or "stiff" process, whose time scale is short compared to the typical time scale of interest (e.g. atomic transition rates), limits the time step to the time scale of that phenomenon. (If the time scale depends on Δ scale length the relevant length is the spatial separation of points on the finite difference grid.)

To overcome this problem, we use a *fully implicit* formulation of the finite difference equations, in which the undetermined variables appear also in the nonlinear terms of the equations. This method is numerically stable for all time steps. The solution of steady state nonlinear equations is necessarily a fully implicit problem.

The system of nonlinear equations represented by (9.1) can be solved only by iteration. Two basic methods are recognized: complete linearization and successive substitution. While neither method is guaranteed to converge, a successive substitution scheme possessing a large radius of convergence can sometimes be devised on the basis of physical reasoning. Such a scheme may converge reliably but with agonizing slowness. The complete linearization, or Newton-Raphson, method, on the other hand, converges rapidly, provided the initial estimate of the solution is close enough to the true solution. The size of the zone of convergence around the solution point \bar{x} may be estimated by Kantorovich's convergence theorem (Henrici 1963).

In the complete linearization method, (9.1) is expanded about the current estimate \bar{x}^j of the solution \bar{x}

$$\bar{F}(\bar{x}^{j+1}) = (\partial \bar{F} / \partial \bar{x}) (\bar{x}^j - \bar{x}) + O(|\bar{x}^j - \bar{x}|^2) = \bar{F}(\bar{x}^j) = \bar{0} \quad (9.2)$$

Thus a first order (linearized) approximation \bar{x}^{j+1} to the solution \bar{x} is given by

$$\bar{x}^{j+1} = \bar{x}^j - (\partial \bar{F} / \partial \bar{x})^{-1} \bar{F}(\bar{x}^j) \quad (9.3)$$

Given an initial estimate $\bar{x}^{(0)}$ of the solution, (9.3) is applied iteratively for successive j , until some estimate of the remaining error $|\bar{x}^j - \bar{x}|$ is considered negligible. Our experience indicates that the radius of convergence can be large, so that convergence is obtained without difficulty. However, circumstances can arise in which the radius of convergence is extremely small (for which a physical reason is often apparent), in these cases we have been forced to use a successive substitution approach.

In the successive substitution method, each cycle of the iteration is broken down into a sequence of steps. First, a subset of the equations is chosen and solved (by Newton-Raphson iteration, if the equations are nonlinear) for a subset of the variables. Next, another subset of the equations is solved for another subset of variables; the most recent values of the remaining variables are used, i.e. the newly calculated variables of the first subset together with the "previous generation" of the other variables. This procedure is repeated until updated values of all the variables have been calculated, then another iteration cycle may begin. In contrast to the well-defined mathematical procedure of the Newton-Raphson iteration, the construction of a successful successive substitution scheme is an art. That is, the choice of subsets and the order in which they are solved relies on insight into the particular physics and mathematics of the problem.

In several applications we have found that a *hybrid* of complete linearization and successive substitution has computational advantages. Perhaps the simplest example of a hybrid method arises in connection with the optical depths, which are dependent variables in our frequency-integrated radiative transfer method. The optical depth equation for each transition can be included in the system of simultaneously solved equations, along with the radiative transfer equation. Ricchiazzi & Canfield (1983) devised an alternative method in which optical depths are removed from the set of linearized variables; in this stable, yet rapidly converging, hybrid scheme, consistent optical depths are computed from the remaining linearized variables after each iteration of the linearization cycle. This has the obvious benefit of nearly halving the length of the band matrix. These authors also found that the convergence properties of the hybrid method were not materially different from those of the full set of equations.

Another hybrid scheme that achieves a speed increase and reduces storage requirements was used successfully by Canfield et al. (1981 b) and Puetter & LeVan (1982). They not only removed the optical depths from the linearization, but they also solved the combined atomic population equations and radiative transfer equations at only one spatial grid point at a time, using the values at the grid point below it as boundary conditions. Our experience with this scheme indicates that convergence is not rapid initially, but that once convergence begins, it is essentially as rapid as complete linearization.

Regardless of the method of solution, it is advantageous to reduce the number of linearized variables to the *minimum* set (see, e.g., Mihalis 1978, Chapter 7). In the work of McClymont & Canfield (1983 a), the solution of the basic set of equations was speeded up by a factor of approximately three by using the hydrodynamic continuity equation and the atomic rate equations to express the linearized changes in density, position and atomic populations in terms of the remaining variables.

Substantial economies in computing time and space can be achieved by the use of *optimal spatial and temporal grids*. It is straightforward to maintain optimal temporal resolution simply by monitoring the changes in key physical variables from one time step to the next. Optimal spatial resolution takes a bit more effort. It is essential to maintain enough spatial grid resolution to *properly represent the smallest scales*, yet it is uneconomical to use a finer spatial grid than necessary. Certainly some problems can be treated with a uniform spatial grid in an appropriate variable, say optical depth. However, in a hydrodynamic calculation in which both radiative transfer and thermal conduction were important, and large thermal fluxes were present, McClymont & Canfield (1983 a) found it necessary to use an adaptive nonuniform Lagrangian grid in which grid points were automatically inserted and deleted to maintain optimum spatial resolution in the key variables. The use of this method has two slight drawbacks; first,

the finite difference formulae are more complicated than on the usual uniform grid, and secondly, the insertion or deletion of grid points inevitably excites small hydrodynamic oscillations. However, alternative methods using moving finite difference grids are not well developed at this time (see, e.g. Tscharnuter & Winkler 1979, Gelnas *et al.* 1980).

Whether the method of solution is complete linearization, successive substitution or a hybrid, attention to the physics described by the equations is essential. It is important that the equations, boundary conditions and finite difference formulation are all self-consistent. Two areas, in particular, must be considered carefully: the evaluation of the derivatives $\partial \bar{f} / \partial \bar{x}$ and the self-consistency of the solution at the end of an iteration cycle. Each of these points is discussed below.

In our initial attempts to apply the Newton-Raphson method, we evaluated the matrix of derivatives $\partial \bar{f} / \partial \bar{x}$ numerically, by perturbing each variable and evaluating the change in each equation. The resulting derivatives were found to vary wildly and convergence was not obtained. In certain regions, the equations are 'stiff', i.e. the solution is determined by the small net difference between two competing processes (e.g. ionization equilibrium is the result of competition between ionizations and recombinations). Under these circumstances, any errors or inconsistency between the derivatives of the competing processes, with respect to the variables on which they depend, drastically alters the apparent dependence of the important net difference on these variables. Hence, the iteration will never converge. This problem was overcome by deriving *analytic expressions for all derivatives* (a tedious process).

We have also found that convergence is more rapid when the variables $\bar{x}^{(i)}$ describe a *self-consistent and physically realizable situation* at the beginning of each iteration cycle. Therefore, after each iteration cycle, we perform what amounts to a successive substitution step. In the radiative hydrodynamic calculation (McClymont & Canfield 1983 a), for instance, we discard the linearized corrections to the density, atomic populations, and optical depths, and recompute these from the continuity, atomic rate and opacity equations, using the linearly corrected values of temperature, velocity, and mean intensities. This technique can also be viewed as reducing the dimensionality of the space to be searched for the solution. After solving (9.3), $\bar{x}^{(i+1)}$ lies in the full N-dimensional solution space; before beginning the next iteration it is projected back into a subspace of self-consistent solutions.

10 CONCLUSION AND OVERVIEW

We have described a computationally efficient technique for including the transfer of radiation, not just its escape, among the physical effects treated in a variety of complex nonlinear problems in the dynamics and equilibria of radiating gases. We have found that these techniques provide a method for including radiative transfer

effects in complex problems that otherwise would exclude it because of limitations on computing resources. We feel that many interesting problems currently under consideration in solar physics and astrophysics fall into this class, including the specific examples cited above and obvious extensions of these problems. We expect that these techniques will become more common and more refined in the future.

While the above techniques can already find use in a number of interesting problems, there are several aspects that might be improved and thereby result in even greater usefulness. At the time this paper was written, the accuracy of the two-stream approach had not yet been studied thoroughly, and the relative benefits of one-stream and two-stream radiative transfer were not yet clear. Another aspect that would benefit from further study is the incorporation of the ability to handle arbitrarily large gradients of both Doppler and bulk flow velocities into a frequency-integrated probabilistic radiative transfer scheme. A second important problem that one cannot attack with present probabilistic methods is partial frequency redistribution. If the treatment of these phenomena could be incorporated in a useful way, then the techniques of probabilistic radiative transfer would be able to attack an extremely large range of problems.

We wish to thank Gene Hubbard, Paul LeVan, and Paul Ricchiazzi, who have collaborated with us in developing and applying many of the techniques described above. We also wish to thank Wolfgang Kalkofen, who has made many suggestions that have enhanced the value of this manuscript. This research has been supported by grants ATM81-12866 from the National Science Foundation, NAGW-30 from the National Aeronautics and Space Administration, and AFOSR 82-0092 from the United States Air Force Office of Scientific Research, Air Force Systems Command. Computing facilities for the development of these methods have been provided by the National Center for Atmospheric Research, which is supported by the National Science Foundation.

REFERENCES

- Abramowitz, M., & Stegun, I.A. 1964, Handbook of Mathematical Functions, Washington, U.S. Government Printing Office.
- Ames, W.F. 1969, Numerical Methods for Partial Differential Equations, Thomas Nelson and Sons.
- Athay, R.G. 1972, Radiation Transport in Spectral Lines, Dordrecht, Reidel.
- Auer, L., & Mihalas, D. 1969, Ap.J., 158, 641.
- Avrett, E.H., & Hummer, D.G. 1965, MNRAS, 130, 4.
- Canfield, R.C., Fisher, G.H., & McClymont, A.N. 1983, Ap.J., 265, in press.
- Canfield, R.C., & Puetter, R.C. 1981, Ap.J., 243, 381.
- Canfield, R.C., Puetter, R.C., & Ricchiazzi, P.J. 1981 a, Ap.J., 248, 82.
- Canfield, R.C., Puetter, R.C., & Ricchiazzi, P.J. 1981 b, Ap.J., 249, 383.
- Canfield, R.C., & Ricchiazzi, P.J. 1980, Ap.J., 239, 1036.
- Feautrier, P. 1964, C.R.Acad.Sci. Paris, 258, 3189.
- Frisch, U., & Frisch, H. 1975, MNRAS, 173, 167.
- Gelinas, R.J., Doss, S.K., & Miller, K. 1981, JComp Phys., 40, 202.

- Henrici, P. 1963. *Discrete-variable Methods in Ordinary Differential Equations*. Wiley, New York.
- Hubbard, E.N., & Puetter, R.C. 1983, in preparation.
- Hummer, D.G., & Rybicki, G.B. 1981, *BAAS*, **12**, 798.
- Hummer, D.G., & Rybicki, G.B. 1982, *ApJ.*, **263**, 925.
- Ivanov, V.V. 1973. *Transfer of Radiation in Spectral Lines*. NBS. Spec. Publ. 385. U.S. Govt. Printing Off., Washington.
- Jefferies, J.T. 1968, *Spectral Line Formation*, Waltham, Blaisdell.
- McClymont, A.N., & Canfield, R.C. 1983 a,b. *ApJ.*, **265**, in press.
- Mihalas, D. 1978, *Stellar Atmospheres*, San Francisco, Freeman
- Milkey, R.W., & Mihalas, D. 1973, *ApJ.*, **185**, 709.
- Osterbrock, D.E. 1974, *Astrophysics of Gaseous Nebulae*, San Francisco, Freeman
- Potter, D. 1973, *Computational Physics*, London, Wiley.
- Puetter, R.C. 1981, *ApJ.*, **251**, 446.
- Puetter, R.C., Hubbard, E.N., Ricchiazzi, P.J., & Canfield, R.C. 1982, *ApJ.*, **258**, 46
- Puetter, R.C., & LeVan, P.D. 1982, *ApJ.*, **260**, 44
- Ricchiazzi, P.J. 1982, Ph. D. Thesis, University of California, San Diego
- Ricchiazzi, P.J., & Canfield, R.C. 1983, *ApJ.*, submitted
- Richtmyer, R.D., & Morton, K.W. 1967, *Difference Methods for Initial Value Problems*, 2nd ed., New York, Interscience.
- Sobolev, V.V. 1957, *Sov Astr.*, **1**, 678
- Thomas, R.N., & Athay, R.G. 1961, *Physics of the Solar Chromosphere*, New York, Interscience.
- Tscharnutter, W.M., & Winkler, K-H. 1979, *Computer Phys Comm.*, **18**, 171
- Vernazza, J.E., Avrett, E.H., & Loeser, R. 1981, *ApJ Suppl.*, **45**, 619

A STATIC MODEL OF CHROMOSPHERIC HEATING IN SOLAR FLARES

PAUL J. RICCHIAZZI¹ AND RICHARD C. CANFIELD

Center for Astrophysics and Space Sciences, University of California, San Diego

Received 1983 January 24, accepted 1983 March 8

ABSTRACT

We have modeled the response of the solar chromosphere to several flare processes: nonthermal electrons, thermal conduction, and coronal pressure. The equations of steady state energy balance, hydrostatic equilibrium, radiative transfer, and atomic statistical equilibrium are solved simultaneously by finite difference methods, using linearization and iteration. It is assumed that the atmospheric response is confined to one dimension by a strong vertical magnetic field. The radiative transfer equation is solved for the most important optically thick transitions of hydrogen, magnesium, and calcium. Radiative loss due to H^+ , the EUV and X-ray lines of heavier ions, and free-free bremsstrahlung is included in an optically thin manner.

Our theoretical atmospheres elucidate the role of various physical processes in establishing the structure of flare chromospheres. At low coronal pressures, conduction is more important than nonthermal electrons in establishing the position of the transition region. Only thermal conduction can account for sufficient chromospheric evaporation in compact flares. Of the mechanisms considered, only nonthermal electrons cause significant heating below the flare transition region. Collisional ionization by nonthermal electrons significantly enhances the ionized fraction in the lower chromosphere. This, combined with the heating effects of the nonthermal electrons, influences the temperature and density structure there. This relates to the controversy over the mechanism for temperature minimum heating during flares, and implies that semiempirical models of chromospheric structure during the impulsive phase must take into account nonthermal ionization.

Subject headings: hydromagnetics — radiative transfer — Sun: chromosphere — Sun: flares

1. INTRODUCTION

The thick target model for the generation of flare hard X-rays has been adopted by many authors as an explanation for the observed enhancements in chromospheric emission during flares (Lin and Hudson 1971; Sturrock 1968). This idea seems to be supported by the observed simultaneity of hard X-ray (HXR) bursts and the sudden brightenings of small $H\alpha$ kernels during the impulsive phase (de Jager 1967; Vorpahl and Zirin 1970; Vorpahl 1972). It has even been suggested that the bulk of the energy release in some flares goes into the acceleration of energetic electrons and that virtually all flare enhancements are powered by them (Lin and Hudson 1976). Opposing this point of view, several authors have suggested that thermal conduction alone is sufficient to explain all the chromospheric manifestations of solar flares (Svestka 1973; Machado and Emslie 1979; Shmeleva and Syrovatskii 1973).

In this paper we present a steady state calculation of the chromospheric response to nonthermal electrons, enhanced thermal conduction, and enhanced gas pressure from the corona. The results of this calculation will show how the chromospheric effects of these mecha-

nisms compare over a wide range of physical conditions. A natural outcome of this investigation will be an estimate of the relative importance of thermal electron conduction and nonthermal electron thick-target heating in the process of chromospheric evaporation. Observations of chromospheric spectral lines and continua, together with predictions of line profiles based on our theoretical flare chromospheres, can help set limits on the energy spectrum of nonthermal electrons present in the chromosphere during flares.

Two basic approaches have been used to understand and interpret the chromospheric response to flare energy release: *semiempirical* and *synthetic*.

The *semiempirical method* makes no assumption about the mode of energy transport in the flare. The temperature structure of the chromosphere and photosphere (which are assumed to be homogeneous, plane-parallel, and in hydrostatic equilibrium) is deduced by trial and error fitting of the computed spectral features to the observations.

In the *synthetic method*, which is applied in this paper, the generated model atmospheres are solutions to specific physical equations, such as those describing energy balance, pressure equilibrium, and, in the more sophisticated models, radiative transfer. If the physics of

¹ Now at Institute for Astronomy, University of Hawaii

b) Statistical Equilibrium Equations

In terms of the population fractions, x_i , the statistical equilibrium equations can be written

$$\sum_{j=i}^s x_j Z_{ji} = x_i \sum_{j=i}^s Z_{ij}, \quad i=1, s, \quad (5)$$

where the Z_{ij} are the sum of the radiative and collisional rate coefficients from state i to state j , and s is the total number of levels included in the model atom. A linearly independent set is obtained by replacing one of the equations by a particle conservation constraint,

$$\sum_{i=1}^s x_i = y(m), \quad (6)$$

where $y(m)$ is the relative number abundance of element m with respect to hydrogen

For bound-bound transitions the Z_{ij} are given by

$$Z_{ij} = C_{ij} + B_{ji} J \quad (\text{upward transitions}),$$

$$Z_{ji} = C_{ji} + B_{ij} J - A_{ji} \quad (\text{downward transitions}),$$

(7)

where B_{ij} , B_{ji} , and A_{ji} are respectively the Einstein probabilities of absorption, stimulated emission, and spontaneous emission, and C_{ij} and C_{ji} are the upward and downward collisional rate coefficients. In the bound-free case we ignore stimulated recombinations, so the Z_{ij} are given by

$$Z_{ij} = C_{ij} + R_{ij} \quad (\text{ionization}),$$

$$Z_{ji} = C_{ji} + R_{ji} \quad (\text{recombination}), \quad (8)$$

where R_{ij} and R_{ji} are the photoionization and photorecombination rates (cf. Jefferies 1968). R_{ij} is directly proportional to the bound-free continuum mean intensity integrated over the photoionization cross section.

The references for the various rates which enter into the atomic rate equations are as follows. The values for the radiative transition probabilities are given by Wiese, Smith, and Miles (1969). The photoionization coefficient is given by Mihalas (1978) for hydrogen, by Milkey and Mihalas (1974) for Mg II, and by Shine and Linsky (1974) for Ca II. Convenient forms for the collisional rates are

$$C_{ij} = n_e \Omega_{ij}(T) e^{-h\nu_{ij}/kT} \quad (\text{upward transitions}),$$

$$C_{ji} = n_e (g_j/g_i) \Omega_{ji}(T) \quad (\text{downward transitions}),$$

(9)

where Ω is the collision strength of the transition. The collision strengths are based on the results of Johnson (1972) for hydrogen, on Shine and Linsky (1974) for calcium, and on Milkey and Mihalas (1974) for magnesium.

An auxiliary statistical equilibrium equation not included in equation (5) is the charge conservation equation

$$x_e = x_i + x_m, \quad (10)$$

where $x_e = n_e/n_H$, x_i is the ionized fraction of hydrogen, and x_m is the metal (i.e., non-hydrogenic) contribution to the electron fraction. We have set $x_m = 8 \times 10^{-4}$ in all calculations in this paper.

In the statistical equilibrium equations, we have limited the calculation to the first and second bound level and the continuum of hydrogen, the $3s$ (ground state) and $3p$ bound levels and continuum of singly ionized magnesium, and the $4s$ (ground state), $3d$, and $4p$ bound levels and continuum of singly ionized calcium. The radiative transfer equation is solved for all transitions within each model atom.

The $4p$ and $3d$ states of Ca II and the $3p$ state of Mg II are actually composed of a small number of substates with nearly equal energies. In solving the statistical equilibrium equations, it is assumed that these substates are populated relative to each other according to their statistical weights. Shine and Linsky (1974) have investigated the effects of neglecting the separate rate equations for the fine structure levels of Ca II. They find that grouping the substates in this way introduces only a modest error.

c) Collisional Ionization by Nonthermal Electrons

Nonthermal electrons not only heat the chromosphere through Coulomb collisions; they also alter its state by direct collisional ionization (Hudson 1972; Lin and Hudson 1976). To appraise the importance of this effect we include explicit nonthermal ionization and excitation terms in the statistical equilibrium equations.

The calculation of the collisional ionization rate due to a nonthermal distribution of electrons is nontrivial because the imposed nonthermal distribution is altered by the production of energetic secondary electrons which also contribute to the ionization rate. This problem has been treated in detail by Dalgarno and Griffing (1958) for the case of a neutral hydrogen target. They found that, for an initial beam energy above 200 eV per electron, the mean number of ion pairs produced is simply equal to 3.78×10^9 erg⁻¹ times the total energy loss of the beam electrons. Our case differs slightly from theirs, since the chromosphere is not completely neutral. In the chromospheric case, the beam energy lost through collisions with ambient electrons will have no direct effect on the collisional ionization rate. We can allow for

this by relating the ionization rate, dn_i/dt , to the rate at which beam energy is lost to the neutral particles:

$$dn_i/dt = 3.78 \times 10^9 dF_n/dz = C_{ni}^{(1)} n_i, \quad (11)$$

where $C_{ni}^{(1)}$ is the collisional ionization rate from the first level. The quantity dF_n/dz is the rate at which collisions with neutral particles remove energy from the beam. It can be related to the total energy deposition rate of the beam electrons dF_e/dz by

$$dF_n/dz = dF_e/dz [(1-x)\Lambda'/\gamma], \quad (12)$$

where x is the ionized fraction, $\gamma = \Lambda x + \Lambda'(1-x)$, and Λ and Λ' are respectively the Coulomb logarithms for collisions with ambient electrons and neutral particles. Combining this with equation (11) and setting $n_i = (1-x)n_H$, we find

$$C_{ni} = 3.78 \times 10^9 dF_e/dz (\Lambda'/n_H \gamma). \quad (13)$$

In addition to causing ionization from the ground state, collisions with nonthermal electrons also directly excite line transitions and cause ionizations from other bound levels. To estimate the nonthermal collisional effects for these other transitions, we have included in the statistical equilibrium equations nonthermal collisional rates which do not include the contribution from secondary electrons. These rates are computed directly from an integration of the collision cross section and velocity over the energy distribution of primary electrons.

The electrons which penetrate into the chromosphere have energies in excess of 20 keV—much larger than the ionization energies of hydrogen or singly ionized magnesium or calcium. At these energies it is appropriate to use asymptotic high-energy approximations for the collisional cross sections. These are based on simple scaling laws and the Born approximation, and have the form

$$\sigma = \pi a^2 [p \ln(\epsilon) + q] (\epsilon - 1) / \epsilon^2, \quad (14)$$

where σ is the collisional cross section, ϵ is the ratio of electron energy to ionization/excitation energy, πa^2 is the area of the first Bohr orbit, and p and q are constants for each transition. Using this approximation for the collisional cross section, the nonthermal collisional rate (not including secondaries) can be written

$$C_{ni} = 2.63 \times 10^{20} \left[0.83 p \ln \left(\frac{E^*}{E_i} \right) + q \right] \frac{dF_e}{dz} \frac{E_i}{(\gamma n_H)}, \quad (15)$$

where E_i is the energy of the transition (Ricchiazzi 1982). The quantity E^* is the cutoff injection energy of

beam electrons at the column depth N , i.e., no electrons with energy less than E^* can penetrate to depth N . It can be written

$$E^* = (2\pi e^4 [2 + \beta/2] \gamma N / \mu_0)^{1/2}, \quad (16)$$

where $\beta = (\Lambda x + (1-x)(\Lambda'' - \Lambda'))/\gamma$ and μ_0 is the pitch angle cosine of the injected electrons. The definitions of the quantities Λ , Λ' , and Λ'' are given by Emslie (1978). The quantities p and q for the transitions of interest here are provided by Ricchiazzi (1982).

d) Hydrostatic Equilibrium

In our physical model of the flare chromosphere a strong vertical magnetic field is assumed to confine the redistribution of chromospheric material within a vertical column of constant cross section. The gas pressure at some point in this column is the sum of the total weight of the material above that point and the gas pressure at the top of the column. We can write the gas pressure P as

$$P = P_1 - mg \int_0^z n dz' = P_1 - mgN, \quad (17)$$

where P_1 is the gas pressure at the top of the column, m is the mean mass per nucleon (which we take to be 1.4 times the proton mass), g is the solar gravitational acceleration, z is the distance measured from the loop apex, and N is the column number density of nuclei. X-ray observations of postflare coronal loops imply coronal loop pressures between 1 and 10^3 dyn cm $^{-2}$ (Feldman, Cheng, and Doschek 1982; Underwood *et al.* 1978).

In terms of microscopic quantities, the gas pressure can also be written

$$P = n_H kT (1.1 + x_e) - \frac{1}{2} n_H m v_t^2, \quad (18)$$

where x_e is the electron density fraction n_e/n_H and v_t is the microturbulent velocity. The factor 1.1 is used to account for the number density contribution of helium and other metals. We used the $v_t(N)$ distribution of provided by VAL in their model F, in all our model calculations. The nonthermal pressure component in equation (18) provides a small and roughly constant fraction of the gas pressure throughout most of the preflare atmosphere (Model F). However, the much larger thermal pressures in the flare model atmospheres dominate over the nonthermal component.

e) Energy Balance

The condition of energy balance requires that the total heating rate be equal to the net radiative energy loss rate. In terms of the energy flux of nonthermal

electrons, F_{20} (for electrons with $E \geq 20$ keV), and the thermal conductive flux, F_c , this condition can be written

$$R = Q - (dF_c/dz + dF_{20}/dz)/n_H, \quad (19)$$

where R is the specific radiative loss rate (i.e., per hydrogen atom) and Q is the preflare specific heating rate. The latter quantity is evaluated by computing the total radiative loss rate of the preflare atmosphere. This same specific ambient (preflare) energy input is maintained at each column depth point in the flare atmosphere.

f) Radiative Energy Loss

The specific radiative loss rate in an optically thick transition is given by

$$R(j, l) = h\nu x_j \rho_l A_{jl}. \quad (20)$$

The quantities x and ρ are determined by a solution of the combined equations of radiative transfer and statistical equilibrium discussed previously. Our probabilistic radiative transfer equation can be expected to produce mean intensities and level populations that are within about 50% of those produced by the more complete frequency-dependent methods (Frisch and Frisch 1978). Ricchiazzi (1982) has shown that as long as $\rho > 0$ the radiative loss rate is known to about the same 50% accuracy because it depends only on a good estimate of the neutral fraction. Only in regions of the atmosphere where $\rho < 0$ and $-\rho$ is comparable to the destruction probability p_d is knowledge of the actual value of ρ critical.

Radiative loss from the optically thin transitions of the H^- ion, the EUV lines and continua of metal ions, and free-free bremsstrahlung all play an important role in the energy balance at some point in the solar transition region, chromosphere, and upper photosphere. The approximations used for these important radiative loss mechanisms are as follows. We have adopted the H^- radiative energy loss rate formula given by Henoux and Nakagawa (1977):

$$R_{H^-} = 1.5 \times 10^{-37} n_e x_1 T^{-3/2} e^{8762/T} [T^4 - (4170)^4]. \quad (21)$$

This expression is based on the assumption that H^- ionization is in LTE and that the emission is in an optically thin region. The validity of these assumptions is supported by a comparison of the H^- radiative loss rate using this equation with the H^- loss rates tabulated by VAL. Throughout the chromosphere of VAL model C the loss rate computed with equation (21) agrees with the more rigorous treatment of VAL to within 20%.

As an aside, we note that Allen (1974) presents a tabulation of the H^- absorption coefficient per unit neutral hydrogen pressure and unit electron density averaged over a blackbody radiation profile. Between 4000 K and 1.1×10^4 K this quantity is roughly proportional to the fourth power of the local temperature. Several authors have taken advantage of this result to write the H^- radiative loss as

$$R_{H^-} = 2.21 \times 10^{-30} n_e x_1 T. \quad (22)$$

This approximation yields radiative losses which are up to a factor of 5 times larger than the VAL results in regions of the chromosphere in which H^- radiative loss is important. Furthermore, this formula is clearly inappropriate to describe the H^- radiative loss at the temperature minimum where equation (21) and the results of VAL indicate that H^- heats the atmosphere.

Raymond (1981) has calculated the radiative loss rate of a low-density plasma composed of He, C, N, O, Ne, Si, S, Fe, and Ni. Raymond's calculations include the effects of forbidden and semiforbidden line transitions, dielectric recombination, and two-photon continua. The specific power radiated by these transitions is given by

$$R_{\text{metal}} = n_e \Phi(T). \quad (23)$$

For temperatures below 10^4 K, $\Phi(T)$ is given by

$$\Phi(T) = C_1 \exp(-C_2/T), \quad (24)$$

where $C_1 = 3.708 \times 10^{-22}$ and $C_2 = 67172$ K. C_1 and C_2 are chosen to match Raymond's $\Phi(T)$ at $T = 10^4$ K and $10^{4.1}$ K, which mimics the temperature dependence of the collisional excitation rate. The function $\Phi(T)$ is plotted, along with our low-temperature extrapolation, in Figure 1.

The bremsstrahlung radiative loss rate used in these calculations is nonstandard in that absorption of the photospheric radiation is included. While in the corona, the absorption rate due to this process is very small compared to the loss rate, this is not the case at the lower temperatures of the chromosphere.

Assuming a photospheric radiation field represented by a geometrically diluted Planck function with radiation temperature T_R , Ricchiazzi (1982) has shown that the bremsstrahlung radiative loss rate can be written

$$R_{\text{brem}} = 1.4 \times 10^{-27} T^{1/2} n_e x_e \times \{1 - [\Psi(1 + T_R/T) + \gamma][T_R/2T]\}, \quad (25)$$

where Ψ is the digamma function, and γ is Euler's constant. The standard result, with no absorption, is recovered by setting $T_R = 0$. When the local electron temperature equals T_R , absorptions reduce the net radia-

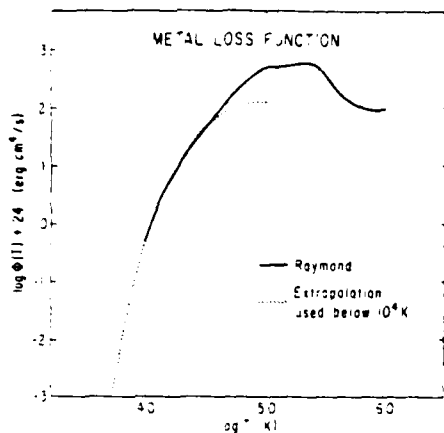


FIG. 1—Solid curve, the radiative energy loss function of metals excluding the contributions from hydrogen, magnesium, and calcium; dotted curve, the low-temperature extrapolation which is used below 10^4 K.

tive loss rate by a factor of 2. In these calculations, T_R has been set equal to 6^{00} K.

g) Thermal Conduction

The thermal conductive flux is (Spitzer 1962)

$$F_c = -\kappa_0 T^{5/2} dT/dz, \quad (26)$$

where the value of κ_0 is 1.5×10^{-6} . The contribution that protons or neutral hydrogen atoms make to the total heating rate is negligible.

The rate at which conduction heats the plasma is

$$dF_c/dz = -d(\kappa_0 T^{5/2} dT/dz)/dz. \quad (27)$$

Among the parameters which specify the coronal input into the lower atmosphere is the quantity F_3 , the conductive flux at $T = 10^3$ K. Withbroe (1978) has used the observed differential emission measure of a large flare to infer the conductive flux during the heating phase. He finds that the conductive flux at 10^3 K steadily drops from 3×10^9 ergs $\text{cm}^{-2} \text{s}^{-1}$, 15 minutes after flare maximum, to 6×10^7 , 3 hours and 38 minutes after maximum. Using these values as guidelines, we have explored the effects of varying F_3 in the range 10^6 to 10^8 ergs $\text{cm}^{-2} \text{s}^{-1}$.

h) Heating by Nonthermal Electrons

Emslie (1978) has derived a set of formulae for the energy deposition rate of a beam of charged particles penetrating into a cold hydrogen target. His treatment generalizes the results of Brown (1973) and Lin and Hudson (1976) to include interactions with neutral hy-

drogen atoms, which will dominate at low chromospheric temperatures.

In terms of the energy flux, F_{20} (for electrons above the reference energy, $E = 20$ keV), the specific heating rate is

$$-\left(\frac{1}{n_H}\right) \frac{dF_e}{dz} = \left(\frac{1}{2\mu_0}\right) \pi e^4 \gamma (\delta - 2) B \left(\frac{\delta}{2}, \frac{2}{4 + \beta}\right) \times \frac{F_{20}}{E^2} \left[\left(2 - \frac{\beta}{2}\right) \frac{\gamma \pi e^4 N}{\mu_0 E^2} \right]^{-\delta/2}, \quad (28)$$

where δ is the power law index of the nonthermal electron number flux and μ_0 is the pitch angle cosine of the injected electrons. The other quantities are given by Emslie (1978).

In the thick target model, the nonthermal electron power law index is related to the HXR power law index by $\delta = \gamma + 1$ (Lin and Hudson 1976). The range of electron spectra implied by the HXR observations is $3 < \delta < 8$, with $\delta = 5$ being most probable. In this paper a standard value of $\delta = 5$ will be assumed for most of the calculations. In order to explore typically inferred values of electron flux, we calculate a grid of theoretical atmosphere with $F_{20} = 10^9, 10^{10},$ and 10^{11} ergs $\text{cm}^{-2} \text{s}^{-1}$.

Since the nonthermal electrons transport charge to deeper layers, an upflowing reverse current, among the ambient electrons, must be generated to maintain charge neutrality (cf. Hoyng, Knight, and Spicer 1978). However, since a complete understanding of how the reverse current affects the heating rate is not yet available, we have neglected its effects in our calculation.

i) Method of Solution

We have used numerical methods based on the generalized Newton-Raphson (GNR) approach of Auer and Mihalas (1968) to simultaneously solve the finite-difference form of equations of radiative transfer, atomic level statistical equilibrium, pressure balance, and energy balance. Application of this procedure to the full set of equations proved to be numerically unstable unless the initial guess of the values of the dependent variables was very near the final solution. Hence an intermediate step was inserted in each GNR step. The successful procedure consisted of the following:

1. Construct a first-guess model atmosphere using a simple radiative loss formula.

2. Holding the temperature and optical depth scales fixed, determine the density, atomic populations, and flux divergence coefficients by integrating point-by-point upward from the fixed lower (subphotospheric) boundary.

3. Evaluate all optical depths and escape probabilities from the current values of the atomic populations.

4. Perform a single GNR step, correcting the full set of variables: temperature, density, level populations, flux divergence coefficients.

5. Same as step 2.

6. Repeat steps 3 through 5 until no escape probability changes by more than 10^{-4} and no temperature changes by one part in 10^3 .

Step 5 is required to stabilize the procedure. Between 10 and 15 iterations are typically required. Further details are given by Ricchiazzi (1982).

III. THEORETICAL ATMOSPHERES

The conductive heat flux, the flux of nonthermal electrons, and the coronal pressure each has a unique effect on the theoretical atmospheres. In this section we discuss the mechanisms that underlie these effects.

To streamline the exposition, the values of the most important parameters used to generate the theoretical atmospheres will be referred to in a shorthand notation consisting of three numbers separated by colons. The numbers represent values of $\log F_{20}$, $\log F_3$, and $\log P_0$, all in cgs units. For example, the atmosphere with nonthermal electron energy flux $F_{20} = 10^{10}$ ergs $\text{cm}^{-2} \text{s}^{-1}$, conductive flux $F_3 = 10^7$ ergs $\text{cm}^{-2} \text{s}^{-1}$, and coronal pressure $P_0 = 10^2$ dyn cm^{-2} , will be referred to as 10:7:2. In all atmospheres shown, δ and μ are held at fixed values $\delta = 5$ and $\mu_0 = 1$.

a) Upper Chromosphere and Transition Region

The effect that nonthermal electrons have on the temperature profile is shown in Figures 2a and 2b, for coronal pressures of 1 and 100 dyn cm^{-2} , respectively, and with a conductive flux of 10^7 ergs $\text{cm}^{-2} \text{s}^{-1}$. In the atmospheres shown in Figure 2a the position of the transition region is completely insensitive to the variation of the nonthermal electron flux. In these low-pressure atmospheres the heating rate at temperatures above 2×10^4 K is mainly due to thermal conduction. On the other hand, the transition regions of the higher pressure atmospheres plotted in Figure 2b are moderately sensitive to the value of F_{20} . For this value of the coronal pressure the importance of conduction for temperatures 10^4 K $< T < 10^5$ K, relative to electron beam heating is much reduced. Deeper down in the chromosphere, where the total gas pressures are nearly the same, and 1 and 100 cm^{-2} models are practically identical. The effect of varying the conductive flux is much different.

The effects of changing the value of F_3 are investigated in Figures 3a and 3b for $P_0 = 1$ and 100 dyn cm^{-2} , respectively. In the low-pressure case the temperature structure of the upper atmosphere is very sensitive to the value of F_3 . On the other hand, in the high-pressure atmosphere, the temperature structure is quite insensitive to F_3 until $F_3 \geq 10^{15}$ ergs $\text{cm}^{-2} \text{s}^{-1}$.

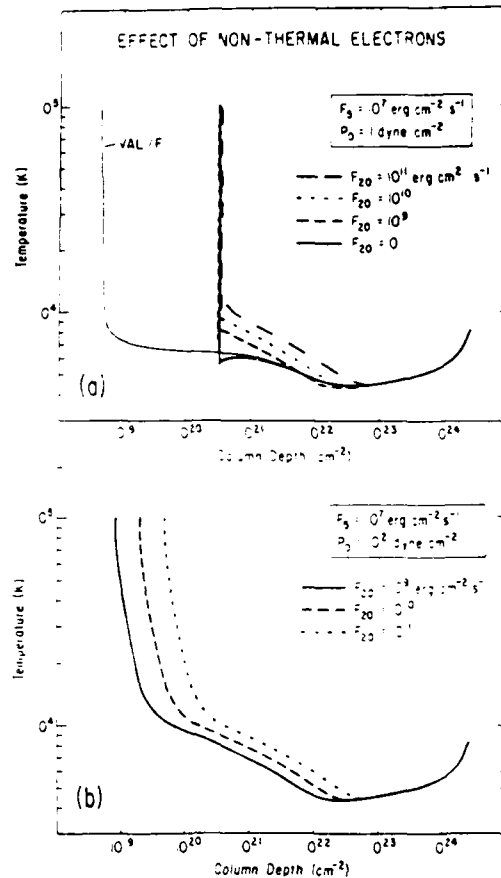


FIG. 2.—Effect of varying F_{20} , the energy flux of nonthermal electrons at $E > 20$ keV, for a fixed conductive flux of 10^7 ergs $\text{cm}^{-2} \text{s}^{-1}$, and fixed coronal pressures of (a) 1 dyn cm^{-2} and (b) 100 dyn cm^{-2} .

These comparisons of high and low coronal pressure atmospheres illustrate that the relative importance of thermal conduction depends on the value of the coronal pressure. To see how this comes about, consider an atmosphere in which conduction dominates the heating rate in the temperature range $T_0 < T < T_1$, where T_0 and T_1 are the temperatures at the base and top of the transition region. Since the temperature gradients are small in the residual chromosphere, one can assume the conductive flux is negligible for $T \leq T_0$. Ignoring optically thick radiators for the moment, the energy balance condition can be written

$$dF_c/dz = n^2 \Phi(T). \tag{29}$$

If one assumes $n = P/2kT$, this equation can be written

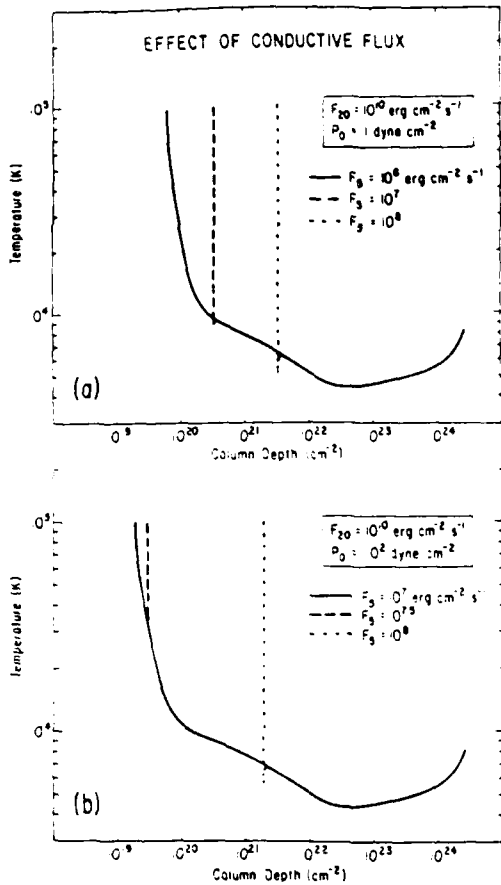


FIG. 3.—Effect of varying F_3 , the conductive flux at $T = 10^5$ K, for fixed values of P_0 and F_{20} . (a) $P_0 = 1$ dyn cm^{-2} ; (b) 100 dyn cm^{-2} .

tegrated to yield

$$F_3^2 - F_c^2(T) = P^2 \lambda(T), \quad (30)$$

where

$$\lambda(T) = (\kappa/2k^2) \int_T^{10^5} T^{1/2} \Phi(T) dT. \quad (31)$$

Now, using the fact that $F_c(T_0) = 0$, we find

$$P = F_3 [\lambda(T_0)]^{-1/2}. \quad (32)$$

Since $\Phi(T)$ is strongly peaked at $T = 10^5$ K, $\lambda(T)$ is nearly constant for $T \ll 10^5$ K. Thus, as long as the temperature at the base of the transition region is much smaller than 10^5 K, the pressure of the transition region is directly proportional to F_3 . Put another way, if F_3 is

kept fixed and P_0 is increased, the formation depth of the transition region must decrease such that $P = P_0 + mgV$ is constant. This effect should be manifested in atmospheres in which thermal conduction dominates down to relatively low temperatures.

In Table 1 we have summarized the physical characteristics of our theoretical atmospheres. Notice that the values of the total gas pressure at $T = 10^5$ K (the column marked P at $T = 10^5$ K) of the 10:8:0 and the 10:8:2 atmospheres are both about 220 dyn cm^{-2} , even though an additional 99 dyn cm^{-2} has been applied to the latter atmosphere. The smaller values of the transition-region column depth that are implied for the atmospheres with larger values of P_0 will increase the amount of nonthermal electron heating (because this heating rate is proportional to $N^{-6/2}$). Thus, increasing P_0 tends to increase the importance of heating by nonthermal electrons relative to conductive heating. This effect is also illustrated in Figure 4 for atmospheres 10:7:0 and 10:7:1. In this case the total pressure of the transition region stays constant at about 22 dyn cm^{-2} while P_0 is increased from 1 to 10 dyn cm^{-2} . As the coronal pressure is increased further, as in the 10:7:2 and 10:7:3 atmosphere, the upper parts are no longer conduction dominated. This relaxes the constant-pressure requirement. In atmosphere 10:7:3, for example, the total pressure at 10^5 K is much larger than in atmosphere 10:7:0 because the heating due to beam electrons can supply the energy for the augmented radiative loss rate. One can also verify the accuracy of equation (32) by noting that the transition region pressure of atmospheres 10:8:2 and 10:8:0 are almost precisely a factor of 10 larger than atmospheres 10:7:0 and 10:7:1.

An interesting feature of the conduction-dominated models is the small temperature dip that separates the transition region from the chromosphere. This feature can be seen at the bottom of the conduction-dominated regions of atmospheres 11:7:0, 10:7:0, 9:7:0, 0:7:0 in Figure 2a, 10:8:0 in Figure 3a, and 10:8:2 in Figure 3b. This feature has a simple physical explanation. At the base of the transition region the conductive flux makes a negligible contribution to the heating rate. Therefore, the heating rate at this column depth is the same as in an atmosphere with an equal value of F_{20} but a smaller value of F_3 . However, the cooling rate at that point is very different. Since almost all the material above the base point is ionized in the high conduction case, the optical depth in the transitions of hydrogen, magnesium, and calcium is greatly reduced. The temperature drops because these ions radiate more effectively. (Further discussion appears below.) At larger depths, the temperature quickly climbs back up to the value found in the low flux models. This rapid recovery is caused by a sudden increase of opacity with increased depth. At a column depth 3 to 4 times larger than the base point, the optical depth of these radiators attains practically the

TABLE I
CHARACTERISTICS OF THEORETICAL MODEL ATMOSPHERES

Model	Log V_r^a (cm^{-2})	H^b (km)	ΔH_{tr}^c (km)	P at 10^5 K (dyn cm^{-2})	T_{min} (K)	Log V_m^d (cm^{-2})
0:7:0	20.5	1041	0.26	22	4440	22.6
9:7:0	20.5	1113	0.29	21	4353	22.4
10:7:0	20.5	1205	0.26	22	4365	22.5
11:7:0	20.5	1400	203.00	23	4435	22.8
10:6:0	19.8	2670	1356	5	4372	22.5
10:8:0	21.5	756	0.03	216	4376	22.5
10:7:1	20.3	1237	0.25	23	4368	22.5
10:7:2	19.3	954	57	101	4400	22.4
10:7:3	18.9	567	3.5	1001	4329	22.6
9:7:2	18.9	887	25	101	4348	22.4
11:7:2	19.7	1076	135	103	4427	22.8
10:7:5.2	19.5	944	42	102	4362	22.6
10:8:2	21.3	743	0.03	225	4360	22.6
11:7:2, $\mu_j = 0.5$	19.5	1014	98	102	4392	22.6
11:7:2, $\delta = 3$	19.5	1258	209	102	4851	22.6
11:7:2, $\delta = 7$	19.7	979	86	103	4345	22.3
10:7:0 ^e	20.5	1234	0.26	22	4529	22.8
VAL-F	18.7	2130	11	0.3	4409	22.5

^aLog of the column depth at $T = 10^5$ K point
^bHeight above photosphere of $T = 10^5$ K point
^cThickness of region with temperature between 10^4 and 10^5 K
^dLog of the column depth at the temperature minimum point
^eCollisional ionization by nonthermal electrons doubled in this run

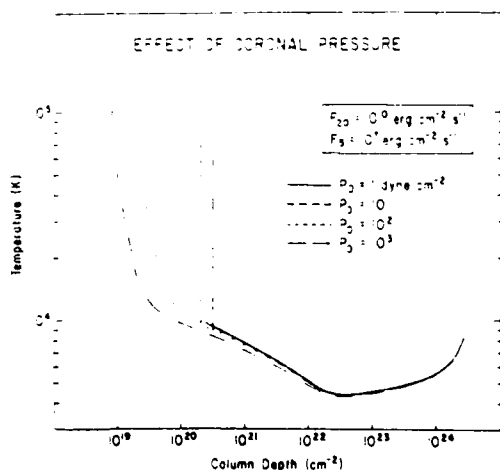


FIG. 4.—Effect of varying coronal pressure for fixed values of F_{20} and F_3 . Note that conductive heating is negligible in both the 10^2 and 10^3 dyn cm^{-2} atmospheres.

same value as they would have had in the low flux atmosphere.

A surprising result of these calculations is that radiative losses from the optically thick radiators are important only at the base of a conduction-dominated region. This result is illustrated in Figures 5, 6, and 7 for

models 10:6:0, 10:7:0, and 10:8:0, respectively. In the bottom panels of these figures we have plotted the temperature as a function of the optical depth in the Ly α transition. This choice of independent variable allows us to resolve features in the transition region more easily. In the next higher panel the net cooling rate per unit volume is shown. The top three panels show the relative contributions of the different heating and cooling mechanisms. These three figures illustrate how the importance of the thick radiators is modulated by the conductive flux imposed at the top of the model atmosphere. In model 10:6:0 the conductive heating never contributes more than a few percent to the total heating rate. Consequently the total contribution of hydrogen, magnesium, and calcium never exceeds 15% of the total radiative loss rate. On the other hand, conduction dominates the heating rate in the region $\tau_{\text{Ly}\alpha} < 10^2$ in the 10:7:0 model and $\tau_{\text{Ly}\alpha} < 10^4$ in the 10:8:0 model. In both these models the contribution of the optically thick radiators is large. At $T = 2 \times 10^4$ K, the temperature at which Ly α radiates most efficiently, all of the models are effectively thin in the Ly α transition. Furthermore, we find that the resonance lines of magnesium and calcium are effectively thin in the upper chromosphere. Therefore, the reason for the relatively small radiative loss from the optically thick radiators in the low conductive flux atmospheres is not merely a consequence of enhanced absorption. A thorough examination of how the relative importance of hydrogen is modulated by the

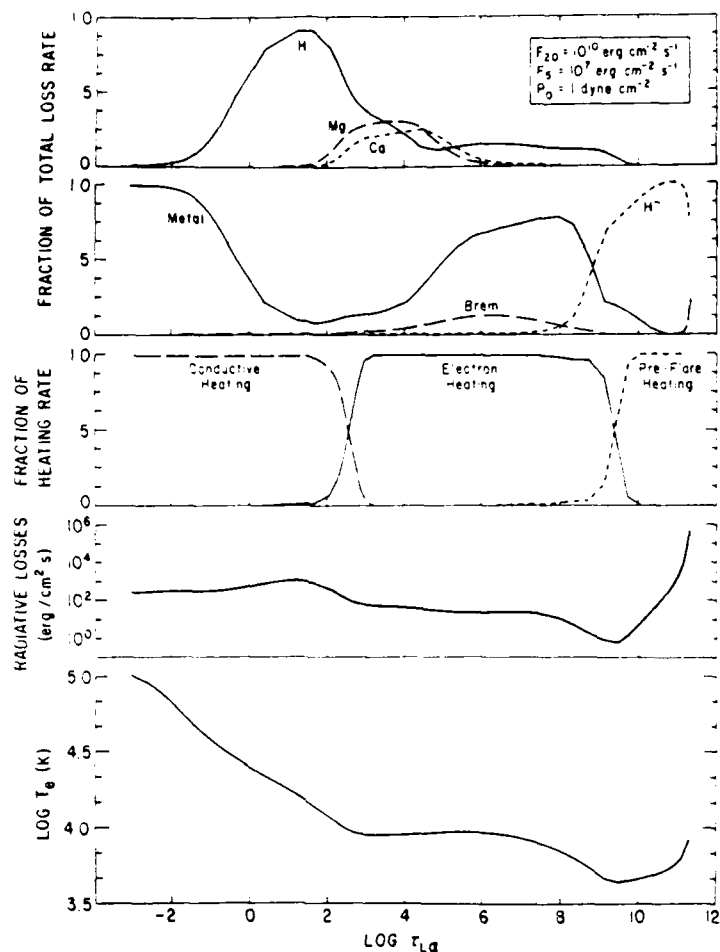


FIG. 5 — The distribution of heating and cooling mechanisms in the 10^6 - 10 atmosphere as a function of Ly α optical depth. The bottom two panels show the temperature and total radiative cooling rate. The relative importance of the different heating and cooling mechanisms is plotted in the top three panels.

conductive flux is given below. This analysis also applies to the modulation of magnesium and calcium.

As long as the flux divergence coefficient is not negative (which it is not for Ly α at 2×10^4 K), the radiative energy loss rate of an effectively thin radiator is well approximated by the energy of the transition multiplied by the collisional creation rate. Hence we can write the ratio of hydrogen to metal radiative loss rates as

$$\frac{R_H}{R_{\text{metal}}} = \frac{h\nu\Omega_{12}x_1 \exp(-h\nu/kT)}{\Phi(T)} = G(T)x_1, \quad (33)$$

where Ω_{12} is the collisional strength of the Ly α transition and $G(T)$ is a function of temperature only. Thus, the ratio of hydrogen to metal loss at 2×10^4 K varies

from atmosphere to atmosphere only through the variation of the neutral fraction. This analysis agrees with the numerical results. The neutral fraction is larger in the high conductive flux atmospheres because the Ly α source function is depressed by enhanced photon escape in the thinner transition regions of these atmospheres. Since the second level population is relatively smaller, the rate of photoionization in the Balmer continuum is reduced and a large neutral fraction results.

b) The Lower Chromosphere and Temperature Minimum Region

In the lower chromosphere the conductive heating rate is totally negligible. In addition the larger optical depth of this region reduces the importance of radiative loss from hydrogen, magnesium, and calcium. In this

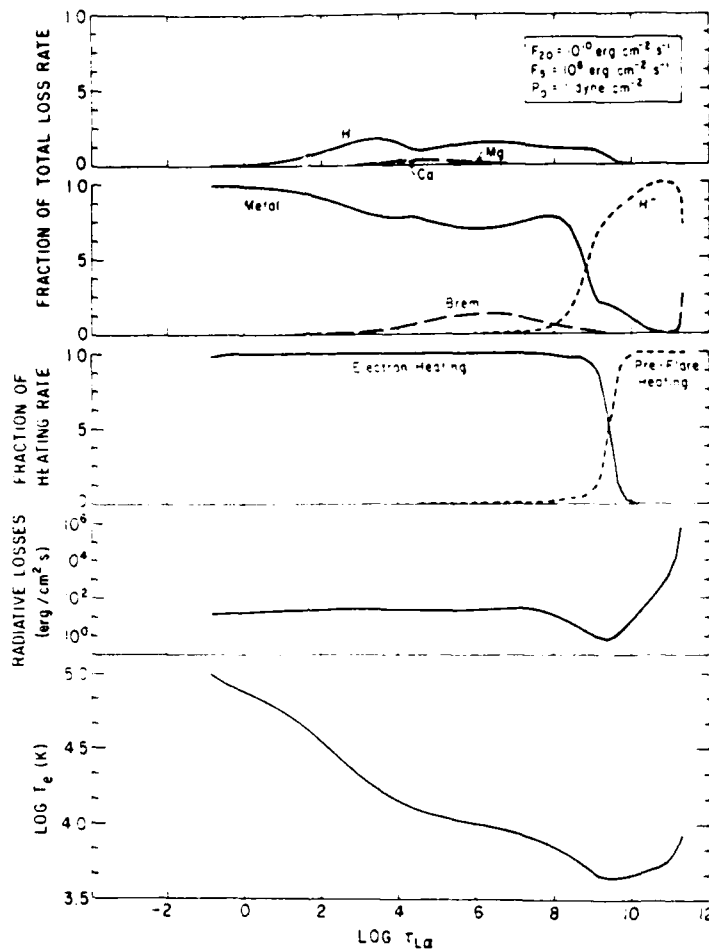


FIG. 6—Same quantities as in Fig. 5 for the 10:7:0 atmosphere with $F_9 = 10^9 \text{ ergs cm}^{-2} \text{ s}^{-1}$.

region the temperature structure is determined primarily by the balance of the optically thin radiative loss mechanisms (metals, bremsstrahlung, and H^-) versus heating by nonthermal electrons. Even though the radiative loss due to the optically thick radiators is not important here, a solution to the radiative transfer and statistical equilibrium equations for hydrogen is still required to find the electron density on which the optically thin radiative loss rates depend. It should also be emphasized that the metal loss rate used in these calculations does not include any contribution from hydrogen, magnesium, or calcium. A calculation based on the metal loss rate of a plasma of cosmic abundance (for example, as given by Raymond, Cox, and Smith 1976) will overestimate the total radiative loss rate in this region of the atmosphere.

The response of the lower chromosphere to heating by nonthermal electrons is shown in Figure 2. In

the column depth range 5×10^{20} to 10^{22} cm^{-2} , the temperature is enhanced by roughly 10% for each factor of 10 increase in the electron energy flux above $10^9 \text{ ergs cm}^{-2} \text{ s}^{-1}$. The temperature tends to its preflare value at larger column depths. As shown in Table 1, the minimum temperature for some of the electron-bombarded atmospheres is actually less than that of the preflare atmosphere. In the 9:7:0 atmosphere, for example, T_{min} is 47 K less than the VAL/F T_{min} . This result is even more puzzling when one notes that the total heating rate (and cooling rate) at this column depth is twice as large as the original preflare heating rate. Part of the explanation for this phenomenon is the increased density brought about by increased coronal pressures. Since the gas pressure of the preflare atmosphere at $N = 10^{22} \text{ cm}^{-2}$ is on the order of 10^3 dyn cm^{-2} , the imposition of a coronal pressure of this same order will increase the density and consequently increase the radia-

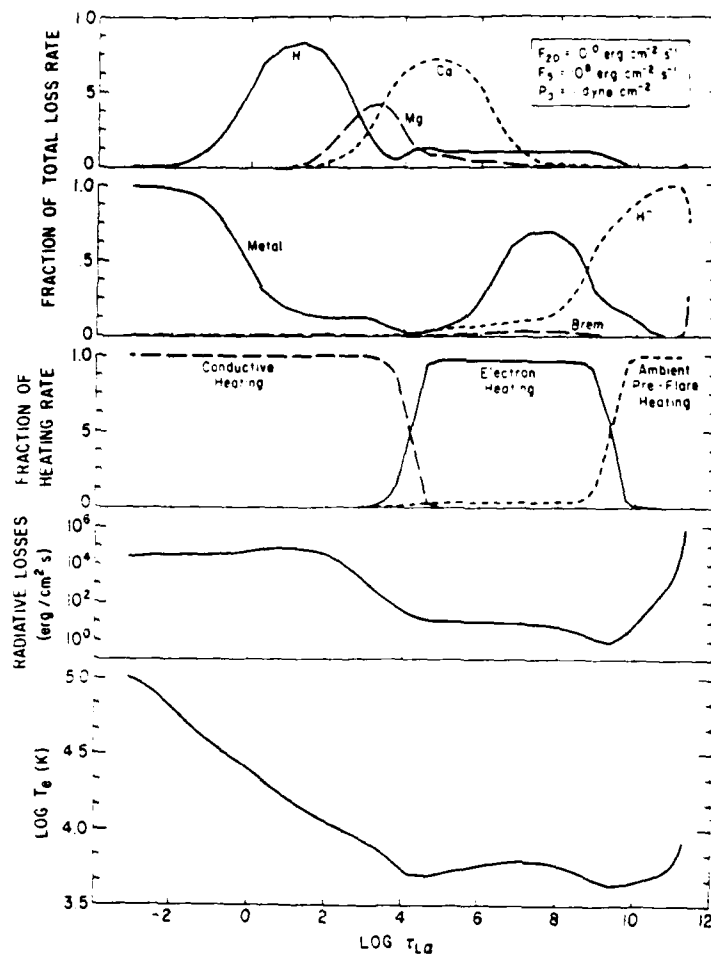


FIG. 7.—Same quantities as in Figs. 5 and 6 for the 10:8:0 atmosphere with $F_5 = 10^8$ ergs $\text{cm}^{-2} \text{s}^{-1}$

tive loss rate. This mechanism helps to explain the extremely low T_{\min} of model 10:7:3, but it fails to explain the small T_{\min} in the low-pressure atmospheres.

The increased radiative efficiency in these models can be explained by considering how the direct collisional ionization by nonthermal electrons affects the state of the gas near the temperature minimum. Throughout most of the quiet solar chromosphere, photoionization from the second level and photorecombination to the bound levels are the dominant rates that determine the hydrogen ionized fraction. In an atmosphere bombarded by nonthermal electrons the ionized fraction is increased directly as a result of enhanced collisional ionizations from the first level. Nonthermal electrons also increase the photoionizations in the Balmer continuum by increasing the second level population through nonthermal collisional excitations in the Ly α transition. Since

the radiative loss near the temperature minimum is dominated by H^- (e.g., Fig. 5, 6, or 7), the increase in the radiative loss rate is directly proportional to the increase in ionized fraction. Hence, the value of T_{\min} decreases in the flare atmospheres because the relative increase of the ionized fraction is greater than that of the total heating rate.

In Figure 8 we show two versions of model 10:7:0, one with nonthermal collisional ionization, one without. Note that when nonthermal collisions are left out, T_{\min} is hotter by 164 K. The maximum difference occurs slightly above the temperature minimum at $N = 2 \times 10^{22} \text{ cm}^{-2}$ where the atmosphere without nonthermal collisions is 10% hotter. At smaller column depths and larger temperatures the difference is smaller for two reasons. First, at higher temperatures the thermal collisional rates begin to dominate the nonthermal rates. Second, in

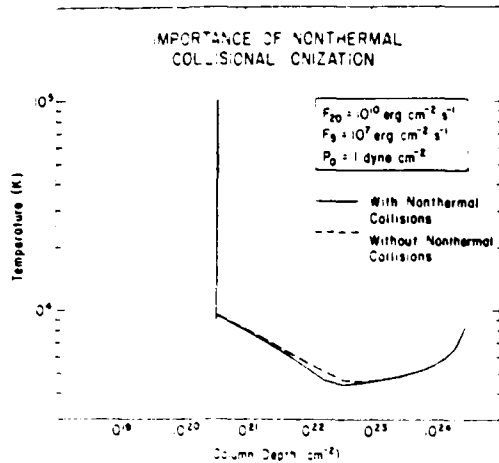


FIG. 8.—Effect of neglecting nonthermal collisional ionization in the 10^{-10} atmosphere.

the upper part of the atmosphere the ionized fraction approaches 1 in both models. Hence, the relative difference in the ionized fraction decreases.

c) Coronal Height Scale

By choosing to specify our theoretical atmospheres parametrically in terms of the quantities F_{20} , F_3 , and P_0 , we have avoided dealing with the coronal temperature structures that would be consistent with our model. To place our atmospheres in a more general physical context, below we estimate the coronal height scales that are implied for several values of the coronal pressure.

If the loop length is held fixed, the coronal pressure P_0 , and the depth of the transition region N_T are related by the condition of hydrostatic equilibrium. By making different choices of P_0 we are in effect choosing different coronal loop lengths. To illustrate this relationship, consider a flux tube of constant cross sectional area. We can use equation (17) to write

$$L = \int_0^{N_T} 2kT_c / (P_0 - mgN) dN, \quad (34)$$

where L is the arc length from the loop apex to the transition region. Making the assumption that T_c is constant in the corona, the integral can be evaluated as

$$L = (2kT_c / mg) \ln(1 + mgN_T / P_0). \quad (35)$$

Now inserting a typical coronal flare temperature of 10^7 K, using the values of N at $T = 10^5$ K for N_T from Table 1, and adding the height of the transition region to L , we find the loop length to be 1.3×10^6 , 3.6×10^5 , 6440, and 790 km for the 1, 10, 100, and 1000 dyn cm^{-2} atm, respectively. Including the effect of a cross sectional area which expands in the corona will tend to reduce these estimates.

The length estimate for the 1000 dyn cm^{-2} model implies that the entire loop structure must be contained within the preflare chromosphere. Clearly, this situation does not correspond to the traditional concepts of the flare structure, though there are no observations that rule out such small loop lengths. The compact flare events with coronal pressures as large as 1000 dyn cm^{-2} are typically observed in structures having lengths of order 10^4 km. This is consistent with a transition region which forms at roughly $3 \times 10^{20} \text{ cm}^{-2}$. If nonthermal electrons are assumed to dominate the heating rate at $T = 10^5$ K, the implied value of F_{20} can be found by setting the electron heating rate equal to the metal radiative cooling rate at this temperature and column depth. Using $\delta = 5$ and $\mu_0 = 1$ in equation (32), and writing $n_e = n_H = (mgN + P_0) / 2k(10^5 \text{ K})$ in the equation for R_{metal} , we find

$$F_{20} = 6.72 \times 10^{-41} N_T^{5/2} (6.41 \times 10^{-20} N_T + P_0). \quad (36)$$

Inserting $N_T = 3 \times 10^{20} \text{ cm}^{-2}$ and $P_0 = 1000 \text{ dyn cm}^{-2}$, we find $F_{20} = 10^{14} \text{ ergs cm}^{-2} \text{ s}^{-1}$. This value of F_{20} is much too large to be consistent with the HXR observations. On the other hand, if conduction drives the evaporation, then by equation (34) the total gas pressure in the transition region should be given by

$$P_0 + 6.41 \times 10^{-20} N_T = P = 2.2 \times 10^{-6} F_3, \quad (37)$$

where the coefficient of F_3 was estimated from Table 1. Inserting $N_T = 3 \times 10^{20} \text{ cm}^{-2}$ and $P_0 = 1000 \text{ dyn cm}^{-2}$, we find $F_3 = 4.5 \times 10^8 \text{ ergs cm}^{-2} \text{ s}^{-1}$. This value of F_3 is consistent with the conductive flux estimate made by Withbroe (1978). Hence, we conclude that plausible loop lengths follow only if the major process that drives chromospheric evaporation is thermal conduction.

IV. DISCUSSION

An important objective of this research is an improved understanding of how the chromosphere and transition region respond to the altered environment of a solar flare. Our grid of theoretical atmospheres can be used to understand the functional relationship between atmospheric temperature structures and the parameters F_{20} , δ , F_3 , and P_0 .

A number of researchers have produced static semiempirical models of solar flare temperature structures. These semiempirical atmospheres are potentially a good yardstick against which our theoretical atmospheres can be compared, in order to infer the nature of the physical processes that heat flare atmospheres. Unfortunately, the semiempirical atmospheres have a number of features that weaken the significance of this comparison. For example, most of the observations on which these model atmospheres are based are made at times long

after the impulsive phase, i.e., at a time when the electron heating rate is negligible. Another difficulty is that some of the model atmospheres are meant only to represent the average conditions in flares and are not based on observations of a single event, perhaps not even the same kind of event. It is also important to note that none of the semiempirical atmospheres include the effects of nonthermal ionization or coronal pressure. Despite their shortcomings, however, these models have much to say about the average atmospheric structure after the impulsive phase.

a) The Dinh Model

Dinh (1980) has constructed several semiempirical model atmospheres based on the cooling phase spectra of three chromospheric flares. Throughout the model the gas pressure is set equal to mgV . Unlike our models, no explicit allowance is made for the additional coronal pressure.

After a trial atmosphere is prescribed the emergent intensities of the Lyman continuum and H α line are calculated. Dinh finds that these spectral features are very sensitive to the choice of transition region thickness, Δh . In models with Δh as large as 50–80 km the amount of Lyman continuum radiation is much larger than observed in the three flares. The observed Lyman continuum (Lyc) flux could be matched with observed values only when Δh was kept less than or equal to 11 km. We have found a similar behavior for the Ly α and Ly ϵ fluxes produced by our atmospheres. Of course, in our case, Δh is not a free parameter. It is instead a computed result for particular choices of F_{20} , δ , F_3 , and P_1 . The flare observations compiled by Machado *et al.* (1981), henceforth MAVN, limit the Ly α flux to the range $10^{6.5} - 10^{7.5}$ ergs cm $^{-2}$ s $^{-1}$. Our calculated Ly α flux is within these observational limits only in those models that are conduction dominated at a temperature of 2×10^4 K (model 11:7:2, $\delta = 3$, is the one exception). Those atmospheres that are not conduction dominated produce too much Ly α flux. To understand why this is so, note that when the value of F_3 is increased, the total amount of material with temperatures near 2×10^4 K is decreased because of the larger temperature gradient. Even though the total gas pressure of the transition region is increased by the larger transition region depth, the reduction in emitting volume is sufficient to decrease the Ly α flux. As noted previously, a conduction-dominated atmosphere is a prerequisite to producing a Ly α radiative loss rate that is significant to the total radiative loss at $T = 2 \times 10^4$ K. Thus the effect of an increased thermal conductive flux is to increase the relative importance of Ly α loss at 2×10^4 K while at the same time decreasing the total flux of Ly α radiation.

This result seems to be at odds with the comparisons of the Ly α flux and conductive flux made by Machado and Emslie (1979) for seven *SkyLab* flares. They claim a

positive correlation between the fluxes, with the conductive flux always within a factor of 2 of the Ly α flux. However, this finding is open to question. The formula they used relating the differential emission measure to the conductive flux involves rough estimates of the flare area and transition region pressure. This could easily introduce a factor of 3 error in their conductive flux (Withbroe 1978). Since the highest and lowest conductive fluxes in their list differ by a factor of only 10, the correlation they claim is not well supported.

In the chromospheric region Dinh achieves the best agreement with the observed H α profiles of the 1B flare of 1974 June 30 with transition region depth $N_1 = 8.5 \times 10^{20}$ cm $^{-2}$, $T_{\text{chrom}} = 8300$ K, and $\Delta h = 3$ km. A feature of this model which is consistent with other semiempirical models is the temperature enhancement inferred in the residual chromosphere. In this region of his model the temperature gradients are much too small to produce any substantial conductive heating. A comparison to our atmospheres reveals that this same amount of temperature enhancement is closely matched by model 11:7:0. However, the fact that Dinh's observations were made 3 min after flare maximum suggests that heating by nonthermal electrons is not the cause of this inferred temperature enhancement.

b) The MAVN Models

The semiempirical model atmospheres of Machado *et al.* (1980), hereafter MAVN, are based on a large set of *SkyLab* data which includes observations of six flares during 1973. Their models are meant to represent the average conditions in these events. They claim that their models are consistent with the flare observations of the hydrogen Ly α , Ly β , H α lines, the Lyman and Balmer continua, the Ca II H, K and infrared triplet lines, the Mg II h and k lines, and the Si I $\lambda\lambda 1525$ and 1682 and C I $\lambda\lambda 1100$ and 1239 continua.

The MAVN models, like the other semiempirical models, do not explicitly include the effect of the coronal containment pressure. The gas pressures in the transition regions of their models are 8.6 dyn cm $^{-2}$ for F_1 and 95 dyn cm $^{-2}$ for F_2 . These values are consistent with the coronal pressure estimates of the large-volume flares to which their model applies.

Like Dinh, they find that a steep temperature rise in the transition region above 8500 K is necessary to reproduce the Lyman continuum intensity. The thickness of the transition region in their models are 4 km for F_1 and 1.2 km for F_2 . As in the Dinh model, temperature enhancements are inferred for the upper chromosphere. The elevated temperature in the chromosphere of either of their models is required for consistency with the observations of the Ly α wing and C I continua.

A feature of the MAVN F_2 model that is not present in Dinh's model is the temperature enhancement in the lower chromosphere. Since this model is claimed to

present the structure of the early stages of bright flares, this feature may be due to heating by nonthermal electrons. Machado, Emslie, and Brown (1978) have presented theoretical calculations of the temperature enhancement at the depth of the preflare temperature minimum (which they take to be $2 \times 10^{22} \text{ cm}^{-2}$). One of the implications of their calculation is that nonthermal electron heating can produce the types of enhancements found in the MAVN T_{min} region. In their calculation, the temperature is found as a solution to a simple energy balance formula in which radiative losses due to the H^- ion are equated to the heating by the ambient preflare process and the nonthermal electrons. In their Figure 3 they show that for $F_{20} = 10^{10} \text{ ergs cm}^{-2} \text{ s}^{-1}$ a temperature increase of 12% is expected (for $\delta = 5$). At $F_{20} = 10^{11} \text{ ergs cm}^{-2} \text{ s}^{-1}$ they would predict an increase of 50%. Both of the estimates are much larger than those of our calculation. At the same depth and the same value of δ we find temperature enhancements of only 3.3% and 18% for $F_{20} = 10^{10}$ and $10^{11} \text{ ergs cm}^{-2} \text{ s}^{-1}$, respectively. The crudeness of their H^- radiative loss formula accounts for this overestimate. In this formula they ignore the hydrogen contribution to the electron density on the grounds that the metal contribution, which is held fixed in their calculation, is dominant. Our calculations do not support this assumption. We find that collisional ionization of hydrogen by nonthermal and thermal electrons causes hydrogen to be the dominant contributor to the electron density at this column depth. As noted previously, this additional ionization increases the radiative loss rate and thereby decreases the net temperature enhancement. One can only conclude that the temperature enhancements inferred by MAVN at $N = 10^{22} \text{ cm}^{-2}$ cannot be explained by electron heating with reasonable values of F_{20} and δ .

c) The Lites and Cook Model

Lites and Cook (1979) analyzed spectra of the 1973 August 9 flare recorded by the ultraviolet spectrograph aboard *Skylab*. They derived a semiempirical model of the flaring chromosphere based on a solution to the radiative transfer equation for hydrogen Ly α , Ly β , and H α as well as some lines and continua of the ions C I, C II, C III, and C IV. Their model atmosphere was constructed by iteratively adjusting $T(N)$ until the synthetic carbon line profiles and continua matched the UV data at a time 1 minute after the flare maximum. The transition region of this model is set at a column depth of $1.3 \times 10^{20} \text{ cm}^{-2}$, where the gas pressure is 8 dyn cm^{-2} . Again, as in the Dinh and MAVN models, the coronal pressure contribution is not included explicitly. In this case, however, we are able to obtain an independent estimate of the coronal gas pressure by referring to other research on this well-studied flare. Underwood *et al.* (1978) have studied the concurrent X-ray and EUV data for this event. Based on their

estimates of the emission measure and flare volume (from the *Skylab* SXR images), they find coronal pressures in the range $1000\text{--}3000 \text{ dyn cm}^{-2}$ with temperatures of 1 or $2 \times 10^7 \text{ K}$ before and up to the time of the Lites and Cook observations. Since this flare was compact, there should have been plenty of time for this pressure to be felt at the transition region. Other researchers have estimated that the conductive flux at 10^9 K is about $6 \times 10^9 \text{ ergs cm}^{-2} \text{ s}^{-1}$ (Machado and Emslie 1979) and electron flux is approximately $10^9 \text{ ergs cm}^{-2} \text{ s}^{-1}$ (Canfield and Cook 1978) at this same time.

None of our energy balance models comes very close to matching this set of coronal input parameters. However, in view of the large difference between the coronal pressures inferred by Underwood *et al.* and the much lower transition region pressure in Lites and Cook's semiempirical atmosphere, it would be unwise to compare our results at column depths less than $3 \times 10^{22} \text{ cm}^{-2}$, where the high coronal pressure found by Underwood *et al.* should dominate over *mgV*. The only meaningful comparison would be at larger depths where the effects of the coronal pressure and, incidentally, the conductive flux, are negligible. At these depths Lites and Cook find greater temperature increases than in our atmospheres. But at these column depths and temperatures other considerations cloud the issue. If it is assumed that the high-energy electrons inferred by Canfield and Cook penetrate into the chromosphere, then the hydrogen ionized fraction should be altered by the additional nonthermal collisional rates. A plausible explanation for the larger temperature of the Lites and Cook temperature minimum region is their neglect of nonthermal ionization. Since their hydrogen ionized fraction is smaller than ours at a given temperature, they must invoke a larger value of T_{min} to explain the increased emission at the temperature minimum. On the other hand, the difference may also be explained by our neglect of other temperature-minimum heating mechanisms in our theoretical model.

V. SUMMARY AND CONCLUSIONS

We have presented an improved theoretical approach to static energy balance problems involving optically thick radiative transfer. Our use of a frequency integrated radiative transfer equation has allowed us to improve the treatment of the effects of several important chromospheric radiators, thereby providing a more realistic treatment of radiative cooling than has previously been used for this problem. With this technique, we have modeled the response of the solar chromosphere to both a long-lived flux of nonthermal solar flare electrons and a large heat flux from the overlying flare corona. In addition to the more realistic treatment of radiative cooling, our model also incorporates the effects of increased coronal pressure (presumably brought about by chromospheric evaporation into the coronal parts of the

flare loop) and nonthermal collisional ionization. Neither of these mechanisms has been explicitly included in previous synthetic or semiempirical models of the flare chromosphere. The theoretical atmospheres we have generated illustrate a number of interesting phenomena associated with these mechanisms.

The coronal pressure modulates the relative importance of heating by nonthermal electrons versus heating by thermal conduction. For a particular choice of the energy flux of nonthermal electrons, F_{20} , and the thermal conductive flux, F_3 , the relative importance of heating by nonthermal electrons is increased as the coronal pressure is increased. For the high coronal pressure that is characteristic of a compact flare, thermal conduction is important in the energy balance only for large values of F_3 . All else being equal, the increased radiative efficiency brought about by the higher pressure causes the transition region to form at much smaller column depth; hence less material exists at temperatures greater than 10^5 K. To reproduce the pressure and emission measure observed in compact flares without resorting to an unacceptably short loop length or large nonthermal electron flux, it is necessary to assume a thermal conductive flux greater than 10^8 ergs cm^{-2} s^{-1} .

In the low coronal pressure atmospheres it is found that the column depth at which the transition zone forms is determined primarily by the value of the conductive flux, at least for values of flux greater than 10^7 ergs cm^{-2} s^{-1} . Increasing the conductive flux increases the depth of formation and decreases the thickness of the transition zone. This correlation of formation depth with conductive flux agrees with the results of Machado and Emslie (1979). However, the thinner transition zone which is a result of higher conductive flux also has the effect of reducing the total Ly α flux, contradicting their suggestion that the Ly α and conductive fluxes are positively correlated.

Models with thick transition zones tend to produce too much Ly α flux. Only those models with a large imposed conductive flux and hence thin transition zones match the Ly α observations. This would seem to indicate that conductive fluxes at least as large as 10^7 ergs cm^{-2} s^{-1} exist at temperatures of 10^5 K only a few minutes after flare onset. This also suggests that conductive heating at a temperature of 2×10^4 K (the region of peak Ly α loss) is important in almost all phases of the flare evolution, and its effects must be included in all models of chromospheric flare heating.

Even though a larger value of the conductive flux has the effect of reducing the Ly α flux, it is only in the conductively dominated atmospheres that the radiative

cooling from Ly α or the lines of Mg II or Ca II is important. The thinner transition zones of these conductively dominated atmospheres produce reduced optical depths in the upper chromosphere and thereby increase the radiative efficiency of these optically thick radiators relative to the optically thin radiative energy loss from metals.

An increased conductive flux cannot be used to explain the enhanced chromospheric temperatures inferred by the semiempirical models, even though it is adequate to explain the larger depths of the transition zone. This refutes the suggestion made by some authors that thermal conduction alone is sufficient to produce all the observed flare enhancements at all atmospheric levels (e.g., Machado and Emslie 1979; Shmeleva and Syrovatskii 1973; Svestka 1973).

The large temperature enhancements inferred for the flare chromosphere by MAVN and Lites and Cook (1979) are not evident in our synthetic atmospheres. Other theoretical treatments of heating by nonthermal electrons have predicted larger temperature enhancements in the lower chromosphere (Machado, Emslie and Brown 1978) for moderate values of F_{20} and the electron power law index, δ . Due to the effects of nonthermal collisional ionization, our theoretical models do not show such temperature enhancements for equivalent values of F_{20} and δ . At a given temperature the ionized fraction and radiative energy loss rate are larger in our atmospheres. Hence, the energy balance condition requires lower equilibrium temperatures. This suggests that semiempirical models of flare chromospheres at the time of heating by nonthermal electrons should also include the effects of nonthermal collisions in the atomic statistical equilibrium equations.

The potential that our theoretical method holds has not been exhausted by the research presented in this paper. An important future application of our theoretical atmospheres will be the synthesis of spectral line profiles that can be directly compared to the observations. These line profiles will be a direct link between the observations and the physical processes in the flare. In a future paper we will present such line profiles.

We wish to thank George Fisher, Sandy McClymont, Rick Puetter, and Todd Gunkler for helpful discussions, and John Raymond for supplying his results for optically thin radiative loss rates due to metals. This work has been supported by the National Aeronautics and Space Administration, through grant NSG 7406, and by the Air Force Office of Scientific Research, Air Force Systems Command, through grant 82-0092.

REFERENCES

- Allen, C. W. 1974, *Astrophysical Quantities* (3d ed.), London: Athlone Press.
 Athav, R. G. 1972, *Radiation Transport in Spectral Lines* (Dordrecht: Reidel)
 Auer, L. and Mihalas, D. 1968, *Ap J.*, **225**, 311.
 Brown, J. C. 1973, *Solar Phys.*, **31**, 143.
 Brown, J. C., Canfield, R. C., and Robertson, M. N. 1978, *Solar Phys.*, **57**, 399 (BCR)

- Canfield, R. C., and Cook, J. W. 1978, *Ap J.*, **225**, 641.
 Canfield, R. C., McClymont, A. N., and Puetter, R. C. 1983, in *Methods in Radiative Transfer*, ed. W. Kalkofen (Cambridge: Cambridge University Press), in press.
 Canfield, R. C., Puetter, R. C., and Ricchiazzi, P. J. 1981, *Ap J.*, **248**, 82.
 Canfield, R. C., and Ricchiazzi, P. J. 1980, *Ap J.*, **239**, 1036.
 Dalgarno, A., and Griffing, G. W. 1958, *Proc. Roy. Soc. London*, **A248**, 415.
 de Jager, C. 1967, *Solar Phys.*, **2**, 327.
 Dinh, Q.-V. 1980, *Pub. Astron. Soc. Japan*, **32**, 515.
 Doughty, D. D., Fraser, D., and McEachran, R. P. 1966, *M. V. R. A. S.*, **132**, 255.
 Emslie, A. G. 1978, *Ap J.*, **224**, 241.
 Feldman, U., Cheng, C.-C., and Doschek, G. A. 1982, *Ap J.*, **255**, 320.
 Frisch, U., and Frisch, H. 1975, *M. V. R. A. S.*, **173**, 167.
 Henoux, J. C., and Nakagawa, Y. 1977, *Astr. Ap.*, **57**, 105.
 Hoyng, P., Knight, J. W., and Spicer, D. S. 1978, *Solar Phys.*, **58**, 139.
 Hudson, H. S. 1972, *Solar Phys.*, **24**, 414.
 Jefferies, J. T. 1968, *Spectral Line Formation* (Waltham: Blaisdell).
 Johnson, L. C. 1972, *Ap J.*, **174**, 227.
 Keddie, A. W. 1970, Ph.D. thesis, University of Glasgow.
 LaBonte, B. J. 1978, Thick Target Models of Impulsive Chromospheric Flares, unpublished.
 Lin, R. P., and Hudson, H. S. 1971, *Solar Phys.*, **17**, 412.
 _____ 1976, *Solar Phys.*, **50**, 153.
 Lites, B. W., and Cook, J. W. 1979, *Ap J.*, **228**, 598.
 Machado, M. E., Avrett, E. H., Vernazza, J. E., and Noves, R. W. 1981, *Ap J.*, **242**, 336 (MAVN).
 Machado, M. E., and Emslie, A. G. 1979, *Ap J.*, **232**, 903.
 Machado, M. E., Emslie, A. G., and Brown, J. C. 1978, *Solar Phys.*, **58**, 363.
 McClymont, A. N., and Canfield, R. C. 1983, *Ap J.*, **265**, 483.
 Mihalas, D. 1978, *Stellar Atmospheres* (San Francisco: Freeman).
 Milkey, R. W., and Mihalas, D. 1973, *Ap J.*, **185**, 709.
 _____ 1974, *Ap J.*, **192**, 769.
 Raymond, J. C. 1981, private communication.
 Raymond, J. C., Cox, D. P., and Smith, B. W. 1976, *Ap J.*, **204**, 290.
 Ricchiazzi, P. J. 1982, Ph.D. thesis, University of California, San Diego.
 Shine, R. A., and Linsky, J. L. 1974, *Solar Phys.*, **37**, 145.
 Shmeleva, O. P., and Syrovatskii, S. I. 1973, *Solar Phys.*, **33**, 341.
 Spitzer, L. 1962, *Physics of Fully Ionized Gases* (New York: Interscience).
 Stille, J. L., and Callaway, J. 1970, *Ap J.*, **160**, 245.
 Sturrock, P. A. 1968, in *Structure and Development of Solar Active Regions*, ed. K. O. Kiepenheuer (Dordrecht: Reidel), p. 471.
 Svestka, Z. 1973, *Solar Phys.*, **31**, 389.
 Underwood, J. H., Antiochos, S. K., Feldman, U., and Dere, K. P. 1978, *Ap J.*, **224**, 1017.
 Vernazza, J. E., Avrett, E. H., and Loeser, R. 1976, *Ap J. Suppl.*, **30**, 1.
 _____ 1981, *Ap J. Suppl.*, **45**, 61 (VAL).
 Vorpahl, J. 1972, *Solar Phys.*, **26**, 397.
 Vorpahl, J., and Zinn, H. 1970, *Solar Phys.*, **11**, 285.
 Weese, J., Smith, D. F., and Miles, D. 1969, *Atomic Transition Probabilities* (Washington: National Bureau of Standards).
 Withbroe, G. L. 1978, *Ap J.*, **225**, 641.

RICHARD C. CANFIELD: Center for Astrophysics and Space Sciences, C-011, University of California, San Diego, La Jolla, CA 92093

PAUL J. RICCHIAZZI: Institute for Astronomy, University of Hawaii, 2680 Woodlawn Drive, Honolulu, HI 96822

THE $H\alpha$ SPECTRAL SIGNATURES OF SOLAR FLARE
NONTHERMAL ELECTRONS, CONDUCTIVE FLUX,
AND CORONAL PRESSURE

by

Richard C. Canfield, Todd A. Gunkler
Center for Astrophysics and Space Sciences
University of California, San Diego

and

Paul J. Ricchiazzi^{*}
Institute for Astronomy
University of Hawaii

Received: _____

Subject Headings: Sun: Flares - Line Profiles.

^{*} Present Address: Mission Research Corporation, Santa Barbara,
CA.

ABSTRACT

We have calculated H α line profiles based primarily on the static model flare chromospheres of Ricchiazzi and Canfield (1983), which show the effects of enhanced fluxes of nonthermal electrons and heat, as well as enhanced pressure, on the temperature, density, and ionization structure of the chromosphere. Both hydrostatic and impulsive phase models are examined. Hydrostatic model atmospheres with substantial electron heating characteristically produce wide and bright H α profiles with a central reversal (measured by the ratio of central to peak intensity) that is insensitive to the electron heating rate. In the impulsive atmospheres, however, the central reversal does depend, to some degree, on the nonthermal electron heating rate. Enhanced thermal conduction reduces the width and total intensity of the profiles. High thermal conduction alone cannot account for flare H α enhancements. High coronal pressure dramatically increases the width and total intensity of the H α profiles, while reducing the central reversal.

We are able to identify two unique qualitative signatures among the mechanisms examined. First, only high values of the flux of energetic electrons (above about 10^{10} erg cm $^{-2}$ s $^{-1}$ above 20 keV) produce H α profiles with obvious broad (Stark) wings of non-Gaussian form; the absence of such wings precludes such heating. Second, only high values of coronal pressure (in

excess of 100 dyne cm^{-2}) produce strong $H\alpha$ emission profiles that are not centrally reversed.

I. INTRODUCTION

a) Motivation

During a solar flare, the chromosphere is heated above its pre-flare value by various mechanisms. Recent observations of hard X-ray emission from the footpoints of coronal loops strongly suggest that energetic electrons are being stopped there. In addition, measurements of elevated coronal temperatures suggest that thermal conduction could also play a role. Another process that affects the chromosphere is enhanced coronal pressure, which is a direct consequence of the observed increase in both coronal density and temperature. In a previous paper (Ricchiuzzi and Canfield 1983, henceforth Paper I), we have modeled the response of the chromosphere to these processes. In this paper we compute the $H\alpha$ profiles for various models, thus giving us their $H\alpha$ spectral signatures. Other flare processes, such as heating by energetic nonthermal protons (Lin and Hudson 1976, Emslie 1983) or soft X-ray irradiation (Henoux and Nakagawa 1977, Machado 1978) have been shown to be of much less importance in chromospheric heating (see, e.g., Canfield et al. 1980).

The $H\alpha$ line is chosen because it is an optically thick line

from the chromosphere. Because it is optically thick, its spectral profile gives us information about how flare effects are distributed in column depth. The chromospheric response is useful for discriminating between heating mechanisms; it has the characteristic that the initial energy deposition profile is not smeared by thermal conduction like it is in the corona. Although energy is spread out over a photon mean free path, this is small enough that the final temperature distribution is sensitive to the initial deposition profile. For our purposes the chromosphere is defined by its temperature structure. We call the chromosphere that region of the atmosphere above the temperature minimum, but below 10^5K .

During the Solar Maximum Mission (SMM) and the Solar Maximum Year, the extensive improvements in simultaneous multispectral imaging of flares included substantial improvements in $H\alpha$ spectroscopy. In particular, the advent of charge-coupled device (CCD) detectors led to spectroscopic observations of $H\alpha$ that have combined temporal and spatial resolution approaching previous filtergrams. As a consequence, there is available a new source of information on flare processes in addition to the morphological $H\alpha$ information commonly available before. Among such spectral observations are those of Acton et al. (1982) and Gunkler et al. (1984), whose observations also combine simultaneous $H\alpha$ and X-ray imaging and spectroscopy.

Their H α profiles show a wide variety of line profile types and suggestive, but ill-understood, relationships to the spatial and temporal structure of the X-ray emitting part of the flare. The motivation for this work is to provide a theoretical basis for interpretation of such observed H α profiles.

b) Previous Work on Theoretical H α Profiles

In the past, two different approaches have been taken to the theoretical interpretation of flare chromospheric line profiles. Authors who have adopted the semiempirical method have determined an ad hoc distribution of thermodynamic variables in a flare chromosphere that is adequate to explain the observed line profile, consistent with known atomic physics and radiative transfer. On the other hand, authors who have adopted the synthetic method have supposed specific physical processes. They have then modeled the effect of these processes on the distribution of thermodynamic variables in the flare chromosphere. Such model flare chromospheres can either be compared to semiempirical model chromospheres or, alternatively, be used to compute theoretical spectra for comparison with observations. We take the latter approach in this paper.

There have been only a few applications of the synthetic method to chromospheric flare spectra in the past decade, largely

due to the lack of availability of suitably realistic (yet expedient) methods for treating the highly nonlinear theoretical problem of energy and momentum transport in a partially opaque atmosphere. It has been difficult to treat both radiative and dynamic aspects of the problem simultaneously, because the problem must be treated numerically, and it is highly demanding of computational resources. The obvious importance of radiative energy loss in the radiation-dominated chromosphere has led most authors to treat the radiative aspects most completely, leaving the dynamic aspects until later. Such work was first done by Brown (1973), who modeled the chromospheric heating effects of steady-state beams of nonthermal electrons. He used a simple radiative cooling expression that assumed that the Lyman continuum dominated chromospheric radiative loss. Theoretical H α profiles of these model atmospheres were determined by Canfield (1974). These profiles were all strongly centrally-reversed, and had very weak wings. In contrast, the highest-quality observations, such as those of Zirin and Tanaka (1973), Schoolman and Ganz (1981) and Acton et al. (1982), show both centrally-reversed and nonreversed profiles, and in the most intense kernels, pronounced wings.

Nakagawa, Wu and Han (1973) modeled the effects of flare shocks on the chromosphere, using a kinematic approach for the gas dynamics and assuming the chromospheric gas was optically

thin. Canfield and Athay (1974) determined $H\alpha$ profiles for these model chromospheres at selected times during the shock propagation, and found that the theoretical profiles not only were always centrally reversed, but also showed much stronger asymmetry than typically observed.

Improved models of flare chromospheres heated by nonthermal electrons were obtained by Brown, Canfield and Robertson (1978), henceforth BCR. They, like Brown (1973), solved the problem of the balance between heating by nonthermal electrons and cooling by radiation, in order to obtain the static temperature and density structure. They used an approximate source function scaling-law approach to take optical depth effects into account in hydrogen cooling, which they assumed was dominated by $H\alpha$ and $L\alpha$. Other hydrogen lines and continua were neglected; all other atomic species were assumed to radiate in an optically thin manner, cut off rather arbitrarily at low temperatures. BCR then computed $H\alpha$ line profiles for their model atmospheres corresponding to various values of F_{20} , the input energy flux of electrons with initial energies above 20 keV. They found $H\alpha$ profiles with widths comparable to the observations for high values of F_{20} , but the profiles consistently had central reversals. Only by invoking inhomogeneous structure of the electron injection region and of flare chromospheric motions were they able to reconcile their synthetic line profiles with the

observations of Zirin and Tanaka (1973), for values of F_{20} suggested by the hard X-ray observations.

Kostyuk (1976) also found that all her electron-heated atmospheres (taking dynamics into account, but not radiative transfer) produced strongly reversed $H\alpha$ profiles. Like BCR, she achieved agreement with the unreversed profiles often observed only by hypothesizing the superposition of profiles that differed due to inhomogeneous electron streams, velocity gradients, etc. It is interesting to note that more recent work (cf. Canfield 1982, Acton et al. 1982) argues against the presence of such high broadening velocities. In these papers and in the present paper (below), mechanisms other than such inhomogeneities are seen to give rise to unreversed profiles.

Our recent determination of the structure of flare chromospheres (Paper I), which forms the basis of most of the $H\alpha$ line profiles of this paper, is a substantial improvement over BCR. First, both thermal conduction and high pressure imposed by the overlying flare corona are taken into account, in addition to heating by nonthermal electrons. Second, the treatment of radiation, which is all-important in such computations, includes radiative transfer effects in all the energetically dominant chromospheric radiators, not just hydrogen. Third, an improved probabilistic radiative transfer equation is used in place of source-function scaling laws.

II. MODEL ATMOSPHERES

This paper is based on static models of flare chromospheres that have been obtained for two limiting assumptions. For the majority of the atmospheres, taken from Paper I, it is assumed that the flare effects have obtained for a sufficiently long period of time that hydrostatic equilibrium is a good approximation. To complement these "hydrostatic" model atmospheres, we have computed a few new atmospheres under the assumption that the flare heating has just been turned on and, although there has been sufficient time to reach energy balance, the density structure has not yet had time to change significantly. The latter model atmospheres will be referred to specifically as "impulsive" in the discussion to follow. Both cases are, of course, limiting approximations for the actual time-dependent situation; the static simplifications are useful for understanding those phenomena that do not depend sensitively on mass motions. Both models are relevant to flares; in some flares the energy fluxes in both thermal and nonthermal electrons are thought to change on characteristic times of one second and less. In other flares, they change very slowly, with characteristic times of order one hundred seconds and more.

The methods used to obtain the hydrostatic model atmospheres are described in detail in Paper I; they will therefore be described only briefly here. These models were

obtained by numerically solving the equations of steady state energy balance, hydrostatic equilibrium, radiative transfer, and atomic statistical equilibrium. It was assumed that the atmospheric response is confined to one dimension by a strong vertical magnetic field. In order to obtain the radiative cooling rate in lines for which optical depth effects are significant, the probabilistic radiative transfer equation of Canfield, Puetter, and Ricchiazzi (1981) (see also Canfield, McClymont and Puetter 1983) was solved for each of the energetically most important transitions of hydrogen, magnesium and calcium. The probabilistic radiative loss rates computed here typically agree with more rigorous methods (Vernazza, Avrett, and Loeser 1981) to within a factor of two. Radiative losses due to H^- , the EUV and X-ray lines of heavier ions, and free-free bremsstrahlung were included in an optically thin manner. Because the heating mechanism of the ambient solar atmosphere is not well known, the ambient (nonflare) heating rate was assumed to retain the same distribution as the preflare atmosphere, Model F of Vernazza, Avrett, and Loeser (1981), which represents the bright elements of the chromospheric network. It was assumed that this heating was a function of column depth alone. For most of the chromosphere the flare heating rate by fast electrons far exceeds the ambient heating rate.

The method for obtaining the impulsive model atmospheres

differs from that for the hydrostatic model atmospheres only in that the equation of hydrostatic equilibrium is not included. These model atmospheres are thus in energy balance, but not pressure balance. Their density distribution is that of the preflare model atmosphere.

Under what circumstances are the two limiting static assumptions close approximations to the full time-dependent problem? We can answer this question by comparing the relevant characteristic times: the pressure equilibrium timescale t_p (density scale height/sound speed), the flare heating timescale t_h (mean thermal energy/flare heating rate), and the radiative cooling timescale t_r (mean thermal energy/net radiative cooling rate). Our assumption of energy balance will be a reasonable approximation if the flare effects have obtained for a time much greater than t_r and t_h . Hydrostatic equilibrium is possible only if the elapsed time is much greater than t_p . The impulsive models will be valid only if the elapsed time is much less than t_p but much greater than t_r or t_h . For the models discussed in this paper, the value of t_p is of order 10 s in the chromosphere and exceeds 60 s in the photosphere. The value of t_h is much less than that of t_p in the chromosphere, and much greater in the photosphere. The value of t_r exceeds t_p only around the temperature minimum. It is the chromosphere that is of primary interest to flare H α profiles, since H α has no significant

opacity near the temperature minimum, and the flare effects modeled are insignificant in the photosphere. In the chromosphere both the heating and cooling times are much less than a second, so the impulsive models can in effect be plausibly compared to the observations for the first few seconds; after tens of seconds only the hydrostatic models are plausible.

In the model chromospheres on which this paper is based, the flare corona is not included explicitly. Instead, the coronal flare inputs to the chromosphere are treated parametrically. We explore these parameters over ranges of values believed to be relevant to solar flares. The input parameters are:

Nonthermal electron flux (F_{20}): The flux of electrons above 20 keV is specified. The electrons are assumed to have a power-law spectrum given by $N(E) \propto E^{-\delta}$, where N is the number of beamed electrons of energy E per square centimeter per second, and δ is the spectral index. The cosine of the pitch angle of the nonthermal electrons is called μ , where $\mu = 1.0$ indicates that the electrons are going straight down into the chromosphere. The values used were $F_{20} = 10^8, 10^9, 10^{10},$ or 10^{11} erg cm⁻² s⁻¹; $\delta = 3, 5,$ or 7 ; and $\mu = 1.0$ or 0.5 .

Conductive flux (F_5): The thermal energy flux from the corona is specified where the temperature is 10^5 K. Values used ranged from 10^6 to 10^9 erg cm⁻² s⁻¹.

Coronal pressure (P_0): The gas pressure at the top of the loop, the site of postulated electron acceleration, where the column depth is zero, is specified in the hydrostatic models. Values used were 1, 10, 100, or 1000 dyne cm^{-2} . In the impulsive model atmospheres the coronal pressure is not a parameter; the density distribution is that of the preflare atmosphere.

III. H α LINE PROFILES

a) Radiative Transfer Methods

After computing the model atmospheres, the next step is to generate theoretical H α line profiles for each model. Taking the temperature and density structure as fixed, we solve our probabilistic radiative transfer equation for a 4-level plus continuum hydrogen atom, again assuming atomic excitation and ionization equilibrium. Complete redistribution within a pure Doppler absorption coefficient profile is adopted for the Lyman lines (following Milkey and Mihalas 1973). The absorption coefficient profile for all subordinate transitions has a Doppler core and wings due to both the linear Stark effect (we assume a Holtmark profile) and resonance broadening (hydrogen-hydrogen collisions, see Mihalas 1978).

The use of probabilistic radiative transfer for the computation of line profiles is uncommon in the current

literature, because it has developed into a useful working method only recently. It is clear on various grounds that it is well suited to the calculation of H α profiles for our flare model atmospheres. First, we have already shown that probabilistic radiative transfer gives total radiative loss rates that are good to about a factor of two (Canfield and Ricchiazzi 1980). The computed source functions will be yet more accurate, since radiative loss rates are more sensitive to small errors than source functions. Second, as we will show below, the major challenge in the computation of H α line profiles is not the radiative transfer in H α itself, but rather in the Lyman lines, owing to the importance of interlocking between the various hydrogen transitions. Methods of probabilistic radiative transfer for resonance lines have not yet been developed fully, owing to the breakdown of the assumption of complete frequency redistribution within the line profile in such lines under certain conditions. However, in flare atmospheres the high collisional transition rate due to the high density of the Lyman- α forming region tends to make this line's source function frequency independent farther into its wings, and hence make our calculation of H α line profiles better for flare atmospheres than for the quiet sun. Finally, we made a quantitative comparison of a flare profile based on probabilistic radiative transfer to one given in the most recent semiempirical flare modeling work, that of Dinh (1980). Dinh solved a frequency dependent radiative

transfer equation instead of our frequency-integrated form; he did not have to ignore the depth dependence of the absorption coefficient profile, and hence in this respect his method is superior to ours. For computational expedience, however, he assumed that the Lyman lines were in radiative detailed balance, an assumption that is inferior to our treatment. Comparison of our computed Dinh Model 3 H α profile to his shows satisfactory quantitative agreement. Our profile has a central intensity which is approximately 20% lower than his, due to a small central reversal that his profile shows only weakly. We anticipate that this is due to our different treatment of the Lyman lines, which have their biggest effect where the core of H α is formed. The half-width and intensities throughout the wings are virtually identical.

b) Dependence on Input Parameters

We now investigate the effects of the physical parameters of the model flare chromospheres on H α profiles, using the models, methods and parameters discussed above. Our approach is to adopt a nominal set of parameters, and then to vary each parameter, by itself, to see how it affects the H α profile. Obviously this does not necessarily imply any physical consistency of the values adopted; the temporal evolution of a flare loop, even if it can be described to a good approximation as a sequence of steady states, is associated with variations in

more than just one of our input parameters. The relationship between these parameters is a function of coronal plasma dynamics and particle acceleration, which is beyond the scope of this work (see, e.g., Ricchiazzi 1982, Ricchiazzi and Canfield 1983, Fisher et al. 1984).

Our primary objective in this section is to establish the relationship between the input parameters of the models and the H α profiles; we defer a complete physical discussion of such matters as the mechanisms and origins of the H α radiation until the following section.

We start with models computed in the hydrostatic approximation. The results are shown in Figures 1 through 7. The upper panel of each figure shows how the columnar temperature structure changes as the values of the parameters are changed, i.e. how the temperature structure reflects the physical process whose role is being varied. The lower panel shows the corresponding H α profiles. The values of H α spectral intensity are expressed in terms of the preflare solar continuum near H α , and the wavelength range shown is H α \pm 4 \AA . The nominal set of parameters is $P_{20} = 10^{10}$ erg cm $^{-2}$ s $^{-1}$, $P_5 = 10^7$ erg cm $^{-2}$ s $^{-1}$, $P_0 = 100$ dyne cm $^{-2}$, $\mu = 1$, $\delta = 5$.

Figures 1 and 2 show how the temperature structure and H α profile change as the nonthermal electron flux is varied. In

Figure 1 $P_0 = 1 \text{ dyne cm}^{-2}$, a low value, but P_0 has its nominal value (100 dyne cm^{-2}) in Figure 2. The low value is intended to represent pressure in large coronal loops in which material heated to coronal temperatures is distributed over a large volume; the nominal case is more typical of the later phases of compact flares with small coronal loop volumes.

The upper panel of Figure 1, the low pressure case, shows that the nonthermal electron heating penetrates well into the chromosphere; temperature increases even down to the preflare temperature minimum for high electron flux values. The lower panel shows pronounced sensitivity of both total emission and profile width to the value of F_{20} . However, each of the profiles shown in this figure has the same amplitude of central reversal, *i.e.* the same ratio of central intensity to peak intensity.

Figure 2 shows the effect of varying the nonthermal electron flux in the nominal pressure case. The temperature structure of the upper chromosphere is much different from that shown in Figure 1; this is due to the dominance of the source term in the energy budget by nonthermal electron heating, not thermal conduction. It remains true that throughout the chromosphere a higher temperature is reached at all column depths as F_{20} is increased, just as was the case at low pressures. The main point to be made regarding the $H\alpha$ profiles shown in the lower panel is that, just as in Figure 1, both the total emission and the profile

width are sensitive functions of F_{20} . Again, the amplitude of the central reversal is quite independent of F_{20} .

Figures 3 and 4 show the effect of changing the coronal pressure P_0 at two different values of nonthermal electron energy flux F_{20} . In Figure 3 the nominal value is used ($F_{20} = 10^{10}$ erg cm⁻² s⁻¹), as might be the case for a long-lived electron beam in a fairly strong flare. In Figure 4 we consider low values of F_{20} , which mimic the effects of long-lived weak nonthermal electron heating, as well as the effects of typical values of X-ray heating during the thermal phase of flares (Ricchiazzi 1982).

Figure 3 shows the effect of varying the coronal pressure at the nominal value of F_{20} . Increasing the coronal pressure has a very different effect than increasing the electron flux. The temperature structure in the lower chromosphere is not affected much, but the column depth of the transition region decreases as the pressure increases. As shown in Paper I, the pressure sensitivity of the temperature structure is easily understood. At high coronal pressures, owing to the increased value of density at a given temperature, the outer atmosphere is more able to radiate away the imposed energy flux at a given value of column number. As the lower panel of the figure shows, the coronal pressure not only affects the total emission and profile width, it also affects the amplitude of the central reversal. The

amplitude of the central reversal changes rapidly between 10 and 1000 dyne cm^{-2} . The reversal disappears entirely at the upper end of the range explored.

Figure 4 shows the effect of varying coronal pressure at a low value of F_{20} . The electron beam is very weak, the chromosphere is cooler and the transition region forms at lower column depth than in the high F_{20} case. Again we see that as P_0 is increased the central reversal goes away. The $H\alpha$ profiles have less width and lower intensity than those from the more strongly electron-heated atmospheres of Figure 3. The key feature to note is that extensive wings indicate nonthermal electron heating.

The effect of varying the amplitude of the conductive flux at 10^5 K, F_5 , is shown in Figures 5, 6, and 7, for low, nominal, and high coronal pressures respectively. These figures show both similarities and important differences. All three figures show that when the conductive flux is high enough, the top part of the chromosphere is evaporated to coronal temperatures, while the lower chromosphere is virtually untouched. However, it is important to realize that the critical value of F_5 , at which conduction begins to affect the transition region temperature structure and the $H\alpha$ line profile, varies with coronal pressure, and that the coronal pressure may or may not be important to the pressure of a conduction-dominated transition region. Heating by conduction will be unimportant to chromospheric structure until

it dominates over heating by nonthermal electrons in the energy balance at the point where $T = 10^5$ K. Lin and Hudson (1976) have given an expression for the column depth of the transition region when the heating is electron-beam dominated. In Paper I we have given the corresponding expression for the conduction-dominated case; we showed that in the latter case the column depth of the transition region (N_{tr}) adjusts so that the total pressure there is proportional to F_5 : $P_{tr} = P_0 + mgN_{tr} = 2.2 \times 10^{-6} F_5$ (m = mean mass of nuclei $\approx 1.4m_H$, g = solar gravity, cgs units). Note that the column depth of the transition region is insensitive to the value of P_0 until it dominates the total pressure. This is illustrated by the models with $F_5 = 10^8$ erg cm^{-2} s^{-1} in Figures 5 and 6. From the equation above, the total pressure in both cases will be $(2.2 \times 10^{-6}) \times 10^8 = 220$ dyne cm^{-2} . It can be easily shown that N_{tr} must only change by a factor of 1.8 to adjust for the extra 99 dyne cm^{-2} in the nominal pressure case. The $H\alpha$ profile becomes sensitive to F_5 only when the transition region becomes conduction dominated. Figure 5 shows that the core is affected first, and then the total intensity drops, as F_5 is increased. Figure 6 shows that the effect of increasing F_5 can be sudden, which is explored further in Figure 7.

Figure 7 shows a conduction-dominated case in which coronal pressure determines the transition region location. In this figure a conductive flux of 10^8 erg cm^{-2} s^{-1} is not enough to

evaporate the upper chromosphere, in contrast to the nominal pressure case in Figure 6. The models with $F_5 \leq 10^8 \text{ erg cm}^{-2} \text{ s}^{-1}$ are virtually identical. However, when the conductive flux is increased to $10^9 \text{ erg cm}^{-2} \text{ s}^{-1}$, the atmosphere becomes conduction-dominated and the above equation relating P_0 and F_5 again obtains. One can establish whether the transition region is electron-heating dominated or conduction dominated by comparing values of the transition-region column depth determined by each mechanism in the absence of the other [cf. Ricchiazzi and Canfield 1983, equations (36) and (37)]. When conduction dominates, the atmosphere is extremely sensitive to the value of F_5 . High values of conductive flux make the chromosphere very thin, which is accompanied by a substantial reduction in H α emission.

We now investigate atmospheric structure and H α profiles in the impulsive approximation discussed in Section II. Figures 8 and 9 show the effects of varying F_{20} and F_5 respectively; P_0 is not a free parameter. Both figures show effects that are similar to those in the hydrostatic cases.

The upper panel of Figure 8 shows that, as F_{20} is increased, the temperature increases throughout the chromosphere, and hence the region of significant heating extends to greater column depth. The temperature structures bear considerable resemblance to those of hydrostatic models with

intermediate values of coronal pressure. This is simply due to the fact that the density distributions for the preflare case resemble those of the hydrostatic models with intermediate coronal pressure. The lower panel of Figure 8 shows that the H α profiles change in total emission, width and central reversal as F_{20} is varied. The behavior of the width and total emission is qualitatively similar to the hydrostatic models; substantial wings and higher total emission still correspond to higher values of F_{20} . However, the behavior of the amplitude of the central reversal is somewhat different. It is no longer true that it is independent of F_{20} ; instead, as F_{20} increases, the amplitude of the central reversal decreases.

Figure 9 shows the effects of varying F_5 in the impulsive approximation. At the lowest value of F_5 conduction is not yet important in the energy balance at temperature 10^5 K. For higher values of F_5 , both the temperature structure and the H α profiles are sensitive to F_5 , for the same reasons alluded to above in the paragraphs on hydrostatic atmospheres.

Finally, we have explored the effect of varying the nonthermal electron spectral index and the electron pitch angle. Their effects are straightforward. Varying the spectral index smoothly varies the relative amount of heating in the upper chromosphere versus the lower chromosphere. The H α profile manifestation is as expected: Relatively more heating at high

values of column number (smaller spectral index δ) produces relatively more wing emission. Varying the pitch angle also varies the relative columnar distribution of heating in a smooth way. As expected, more heating at higher column depth (smaller pitch angle, larger μ) gives more wing emission.

c) Mechanism of Formation

What physical factors determine the form of the $H\alpha$ profile for each model flare atmosphere? Crudely speaking, in the region where continuum opacity is negligible, the emergent intensity as a function of wavelength displacement from line center is a mapping of the $H\alpha$ source function, S , as a function of $H\alpha$ optical depth. The intensity at line center depends on the value of S relatively high in the chromosphere, and the intensity in the wings depends on S in the lower parts of the chromosphere. The source function is a measure of the ratio between upper and lower level populations in the transition. This ratio is determined both by collisional processes, which depend only on the local temperature and density, and on radiation fields, which can be very non-local. If collisions dominate, the source function will be the Planck function, B . If radiation dominates, and if escape of photons from the region is significant, S departs from B .

A useful way to understand the profiles is to look at the

depth dependence of both B and the departure of S from B . A third useful quantity is the effective $H\alpha$ Planck function, \bar{B} , which includes the effect of interlocking with other transitions, *i.e.* the effect of indirect transitions between the second and third levels of the hydrogen atom. In analogy with the simple two-level atom formulation, \bar{B} is defined so that the source function is given by $S = (\int d\nu J_\nu \Phi_\nu + \bar{\epsilon} \bar{B}) / (1 + \bar{\epsilon})$, where J_ν is the mean intensity of the radiation field in $H\alpha$, Φ_ν is the $H\alpha$ absorption coefficient profile, and $\bar{\epsilon} / (1 + \bar{\epsilon})$ is the effective $H\alpha$ photon destruction probability per scattering (see, *e.g.*, Canfield and Puetter 1981). If S closely matches \bar{B} , it means that the level populations are controlled largely by interlocking with other transitions. If \bar{B} closely matches B , it means that all interlocked transitions are in local thermodynamic equilibrium.

To show why the $H\alpha$ profile depends sensitively on the temperature and density distribution of the flare chromosphere, we look in detail at three hydrostatic models that have the nominal values of the nonthermal electron energy flux and conductive flux and differ only in the value of coronal pressure. Figure 10 shows how pressure affects the line center optical depth dependence of S , B and \bar{B} ; pressure is lowest in the top panel and highest in the bottom. The first point to note is that S follows \bar{B} very closely in all three cases. This illustrates a very important fact: $H\alpha$ is just one of a strongly interlocked set of

transitions, and its source function depends on other lines. The second point to note is that, as pressure increases, \bar{B} approaches B more closely throughout all but the upper chromosphere. This reflects the increasing dominance of the interlocked transitions by collisional processes that push their source functions toward the Planck function. At small optical depths the interlocked transitions decouple from the Planck function due to photon escapes, so \bar{B} is insensitive to variations in B there.

To find out which interlocked lines are important we carried out an analysis comparing atomic transition rates between the $n = 2$ and $n = 3$ levels of hydrogen via all possible third levels, following the methods described by Jefferies (1968) and Canfield and Puetter (1981). We find that the principal interlocked transitions are Lyman α and Lyman β , with Paschen α contributing increasingly with higher pressure. Lyman α , in particular, is known to be highly sensitive to local values of temperature and density. The behavior of $H\alpha$ in flares is thus very different from that in the quiet sun, where the $H\alpha$ source function is determined by radiation in the Balmer and Paschen continua (Gebbie and Steinitz 1974). These continua are formed in the photosphere, and thus in nonflaring conditions $H\alpha$ is sensitive to chromospheric temperature and density only through changes in the optical depth scale.

What affects the variation of the $H\alpha$ source function in

these flare atmospheres? The optical thickness of the chromosphere is of considerable importance. For example, if its thickness is increased, $H\alpha$ tends to be formed in a higher temperature region. This effect can be seen by comparing the absolute values of S and its depth dependence in the low pressure and moderate pressure cases (top and middle panels) in Figure 10. Increasing the pressure adds more absorbing material to the outer atmosphere, so the Planck function becomes higher at a given value of $H\alpha$ line center optical depth for the moderate pressure case than for the low pressure case. This causes the $H\alpha$ source function to be higher as well.

Why should the amplitude of the central reversal be coronal pressure dependent? The important factor is the relationship of collisional and radiative transition rates. At the outer edge of an atmosphere, the number of upward transitions is lowered by the escape of photons into space; they are not scattered there, and do not contribute to maintaining a large ratio of upper and lower level population. This lowers the value of the source function near the outer edge, and causes the spectral line profile to have a central reversal. However, if the collisional rates are high, as is the case at high pressure, the loss of radiative upward transitions is less important, since collisions do the job, and S stays closer to the Planck function. This effect can be seen by comparing the moderate and high pressure cases in Figure 10. A

high pressure corona increases the density in the upper chromosphere, resulting in higher collisional transition rates, and a smaller departure of S from B. This results in a source function which continues to rise all the way out to the point where $\tau_{H\alpha} = 1$, thus giving an unreversed profile.

Where in the model atmospheres does the emergent $H\alpha$ radiation originate? For several different models, Figure 11 shows the depth dependence of the $H\alpha$ flux divergence, defined here as the derivative of the integrated flux ($H = \iint d\nu \mu I_\nu d\omega/4\pi$) with respect to the logarithm of the column number, N. Since we plot $dH/d(\log N)$ vs. $\log N$, the flux from any given column depth range can be integrated by eye, noting that the vertical scale is logarithmic. The flux divergence distribution is given by the solid curve, the temperature by the dashed curve. Note that continuum absorption cuts off the $H\alpha$ flux divergence at $(\log N) \approx 24.5$ in the photosphere. Figure 11 (a) shows the distribution for a quiet sun model, Model C of Vernazza, Avrett, and Loeser (1981). The quiet chromosphere is very thin in $H\alpha$, so the vast majority of the total emission (though obviously not line center emission, for example) comes from the photosphere. If we heat the atmosphere with beamed nonthermal electrons (i.e., increase F_{20}), the chromosphere becomes increasingly thicker in $H\alpha$ due to the increase in the second level population. This increases the chromospheric emission, as shown in Figures 11 (b)

and (c). The photospheric $H\alpha$ flux divergence is actually slightly decreased, since the escape of photons from there is inhibited by the thicker chromosphere. Figures 11 (d) and (e) show the effect of increasing the conductive flux (F_5), which pushes the transition region down toward higher column depth. Although stripping off the top of the chromosphere allows more radiation to escape from the residual chromosphere and photosphere, the emerging $H\alpha$ flux in the high F_5 case is lower because of the high emissivity of the layer that was evaporated. Comparison of Figures 11 (d) and (f) shows that increasing the coronal pressure (P_0) simply adds more chromospheric material, thus adding to the total emission. As a general rule, the total $H\alpha$ flux is strongly related to the $H\alpha$ optical thickness of the region where the continuum optical depth is less than unity. Finally, although the $H\alpha$ flux divergence in the conductively heated transition regions of some of the model atmospheres is very large, especially in Figure 11 (e), these regions are so thin that their contributions to the emergent $H\alpha$ flux are negligible.

Finally, what processes dominate the formation of the $H\alpha$ wings? For all P_{20} and our nominal parameters, we find that Stark redistribution is the dominant escape mechanism in the wings of $H\alpha$ throughout the chromosphere. Resonance broadening is important only at and below the temperature minimum, where flare effects are small.

d) Interpretation of Dependence on Input Parameters

On the basis of our understanding of the formation of H α in the flare model atmospheres, it is now possible to interpret many aspects of the input-parameter dependence of the line profile characteristics seen above.

(i) Heating by Nonthermal Electrons

In the range $10^8 \leq F_{20} \leq 10^{11}$ erg cm $^{-2}$ s $^{-1}$, shown in Figures 1, 2, and 8, increasing F_{20} produces more H α emission. The analysis in the preceding section indicates that this is due primarily to enhanced production of H α photons per hydrogen nucleus. In the hydrostatic case, the amplitude of the central reversal is essentially independent of F_{20} because the ratio of collisional to radiative rates at the point of unit line center H α optical depth does not change significantly, due to the hydrostatic adjustment. In the impulsive models, however, the amount of central reversal decreases as F_{20} increases, because the density at the unit optical depth point increases (the density at each column depth remains the same as the preflare atmosphere). The unique signature of substantial nonthermal electron heating is formation of extensive Stark wings; they are strongest at $\mu = 1$ and small values of δ , since they reflect heating of the deep chromosphere.

(ii) Heating by Thermal Conduction

Thermal conduction has no effect on chromospheric structure until it begins to dominate the heating term in the energy balance at $T = 10^5$ K, which depends on the value of the coronal pressure. Figures 5, 6 and 7 explore the range $10^6 \leq F_5 \leq 10^9$ erg cm⁻² s⁻¹. When thermal conduction first becomes important, only the core of H α is affected, because only the upper atmosphere is "evaporated" to coronal temperatures; whereas the lower atmosphere is virtually unperturbed. As F_5 increases further, the entire H α profile is affected, dramatically reducing the total amount of H α emission. The total number of atoms in the chromosphere decreases, and the number of H α emitting atoms decreases even more dramatically, since the remaining chromosphere has a low characteristic temperature.

(iii) The Role of Coronal Pressure

In the range $1 \leq P_0 \leq 1000$ dyne cm⁻², explored in Figures 3 and 4, the effect of increasing the value of the coronal pressure is both to enhance the total amount of emergent H α radiation and to reduce the H α central reversal. The reason is straightforward; the pressure at any given temperature, and hence the density, is increased down to the point where $mgN \sim P_0$. This results in the production of more H α photons, as a result of interlocking with the density-sensitive Lyman lines. The higher density also enhances the production of H α photons in the outer chromosphere

by making collisions even more effective at photon generation in the interlocked transitions, which fills in the central reversal of H α .

IV. DISCUSSION

We now have available a variety of theoretical H α profiles, corresponding to the specific physical processes thought to be of dominant importance in the energetics of flare chromospheres. How can they be used in the interpretation of observed line profiles? First, they may be compared directly to the observations, which we leave for a future paper (Gunkler et al. 1984). In addition, one must ask whether the calculations reveal any unique qualitative spectral signatures. In fact, the calculations show that in some cases such signatures indeed exist. In others, however, there is considerable ambiguity, which can be resolved only by further constraints on the values of one or more parameters, or a specific relationship between two or more of the parameters.

Our results show two unambiguous qualitative line profile signatures. First, only sufficient dominance of flare heating by nonthermal energetic electrons ($P_{20} \geq 10^{10}$ erg cm⁻² s⁻¹) produces broad Stark emission wings of obviously non-Gaussian form; neither thermal conduction nor high coronal pressure alone do so. Low values of P_{20} are inevitably associated with the

absence of obviously non-Gaussian emission wings. Second, only high coronal pressure produces strong unreversed emission profiles. Neither high nonthermal electron flux nor high conductive flux alone does so. Conversely, $H\alpha$ profiles with substantial central reversals are invariably associated with relatively low values of coronal pressure ($P_0 < 10^2$ dyne cm^{-2}).

Other profile characteristics are ambiguous and cannot immediately be related to a unique physical process without additional information. High total $H\alpha$ emission certainly indicates flare heating, but one cannot quantitatively fix the values of all three of the most important parameters (F_{20} , F_5 , and P_0) on the basis of total intensity alone. Conversely, low $H\alpha$ emission alone does not necessarily imply low flare heating; we have seen that even in the presence of high nonthermal electron heating, the total $H\alpha$ intensity can be made low by a high value of the conductive flux. Also, one must bear in mind that there is an intrinsic uncertainty in the atmospheric temperature values owing to a factor of two uncertainty in the total radiative losses, and hence (roughly speaking) a factor of two uncertainty in the total $H\alpha$ emission would not be surprising. Finally, although the amplitude of the central reversal is useful qualitatively, it cannot be used to quantitatively establish the values of the important parameters without additional constraints or relationships. It depends on both pressure and conductive flux in some ranges of conductive flux, and depends on which of the two

static approximations (hydrostatic or impulsive) is used.

ACKNOWLEDGEMENTS

This research has been supported by the Air Force Office of Scientific Research, Air Force Systems Command, through grant 82-0092.

REFERENCES

- Acton, L. W. *et al.* 1982, *Ap. J.*, 263, 409
- Brown, J. C. 1973, *Sol. Phys.*, 31, 143.
- Brown, J. C., Canfield, R. C., and Robertson, M. H. 1978, *Sol. Phys.*, 57, 399.
- Canfield, R. C. 1974, *Sol. Phys.*, 34, 339.
- Canfield, R. C., and Athay, R. G. 1974, *Sol. Phys.*, 34, 193.
- Canfield, R. C., and Ricchiazzi, P. J. 1980, *Ap. J.*, 239, 1036.
- Canfield, R. C. *et al.*, 1980, in *Solar Flares*, ed. P. A. Sturrock (Boulder: Colorado Associated University Press), p. 231.
- Canfield, R. C., and Puetter, R. C. 1981, *Ap. J.*, 243, 381.
- Canfield, R. C., Puetter, R. C., and Ricchiazzi, P. J. 1981, *Ap. J.*, 248, 82.
- Canfield, R. C. 1982, *Sol. Phys.*, 75, 263.
- Canfield, R. C., McClymont, A. N., and Puetter, R. C. 1983, in *Methods in Radiative Transfer*, ed. N. Kalkofen (Cambridge University Press), in press.
- Dinh, Q.-V. 1980, *Publ. Astron. Soc. Japan*, 32, 515.
- Emslie, A. G. 1983, *Sol. Phys.*, 86, 133.
- Fisher, G. H., Canfield, R. C., and McClymont, A. N. 1984, *Ap. J.* (submitted).
- Gebbie, K. B., and Steinitz, R. 1974, *Ap. J.*, 188, 399.
- Gunkler, T. A., Acton, L. W., Canfield, R. C., Kiplinger A. L. 1984, in preparation.

- Henoux, J.-C., and Nakagawa, Y. 1977, *Astron. Astrophys.*, **57**,
105.
- Jefferies, J. T. 1968, *Spectral Line Formation* (Waltham: Blaisdel).
- Kostyuk, N. D. 1976, *Sov. Astron.*, **20**, 206.
- Lin, R. P., and Hudson, H. S. 1976, *Sol. Phys.*, **50**, 153.
- Machado, M. E. 1978, *Sol. Phys.*, **60**, 341.
- Mihalas, D. 1978, *Stellar Atmospheres* (2nd ed.; San Francisco: W.H.
Freeman and Co.).
- Milkey, R. W., and Mihalas, D. 1973, *Ap. J.*, **185**, 709.
- Nakagawa, Y., Wu., S. T, and Han, S.M. 1973, *Sol. Phys.*, **30**,
111.
- Ricchiazzi, P. J. 1982, Ph.D. Thesis, University of California,
San Diego.
- Ricchiazzi, P. J., and Canfield, R. C. 1983, *Ap. J.*, **272**,
739.
- Schoolman, S. A., and Ganz, E. D. 1981, *Sol. Phys.*, **70**, 363.
- Vernazza, J. E., Avrett, E. H., and Loeser, R. 1981, *Ap. J. Suppl.*,
45, 619.
- Zirin, H., and Tanaka, K. 1973, *Sol. Phys.*, **32**, 173.

FIGURE CAPTIONS

Fig. 1.-- The effect of varying the energy flux of nonthermal electrons above 20 keV, F_{20} , at low coronal pressure. Hydrostatic approximation. Top: model atmospheres. Column depth is the number of hydrogen nuclei measured from the acceleration site in the corona. Bottom: $H\alpha$ profiles. Intensity is measured in units of the preflare continuum near $H\alpha$.

Fig. 2.-- The effect of varying the energy flux of nonthermal electrons above 20 keV, F_{20} , at nominal coronal pressure. Hydrostatic approximation. Top: model atmospheres. Bottom: $H\alpha$ profiles.

Fig. 3.-- The effect of varying the coronal pressure, P_0 , at nominal nonthermal electron flux. Hydrostatic approximation. Top: Model atmospheres. Bottom: $H\alpha$ profiles.

Fig. 4.-- The effect of varying the coronal pressure, P_0 , at low electron energy flux. Hydrostatic approximation. Top: Model atmospheres. Bottom: $H\alpha$ profiles.

Fig. 5.-- The effect of varying the conductive flux, F_5 , at low coronal pressure. Hydrostatic approximation. Top: Model atmospheres. Bottom: $H\alpha$ profiles.

Fig. 6.-- The effect of varying the conductive flux, F_5 , at nominal coronal pressure. Hydrostatic approximation. Top: Model atmospheres. Bottom: $H\alpha$ profiles.

Fig. 7.-- The effect of varying the conductive flux, F_5 , at very high coronal pressure. Hydrostatic approximation. Top: Model atmospheres. Bottom: $H\alpha$ profiles.

Fig. 8.-- The effect of varying F_{20} , the energy flux of nonthermal electrons above 20 keV. Impulsive approximation. Top: model atmospheres. Bottom: $H\alpha$ profiles.

Fig. 9.-- The effect of varying the conductive flux F_5 . Impulsive approximation. Top: Model atmospheres. Bottom: $H\alpha$ profiles.

Fig. 10.--The effect of varying the coronal pressure P_0 on the source function (S), Planck function (B), and effective Planck function (\bar{B}), as a function of $H\alpha$ line center optical depth. Top: low pressure, $P_0 = 10$ dyne cm^{-2} . Middle: nominal pressure, $P_0 = 100$ dyne cm^{-2} . Bottom: high pressure, $P_0 = 1000$ dyne cm^{-2} .

Fig. 11.--The dependence of the columnar distribution of net $H\alpha$ emission on atmospheric parameters. Hydrostatic approximation. The solid curve shows the $H\alpha$ flux divergence

(left scale) and the dashed curve shows the temperature (right scale). Note that the ordinate is logarithmic.

Panel (a): Average quiet sun model VAL/C.

Panel (b): Low electron heating, low coronal pressure.

Panel (c): High electron heating, low coronal pressure.

Panel (d): Low coronal pressure.

Panel (e): High conductive flux, low coronal pressure.

Panel (f): Nominal atmospheric parameters.

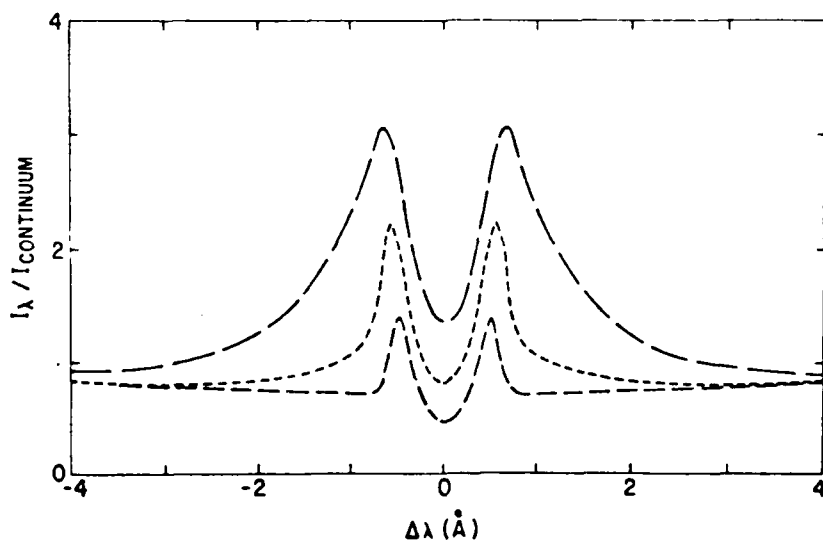
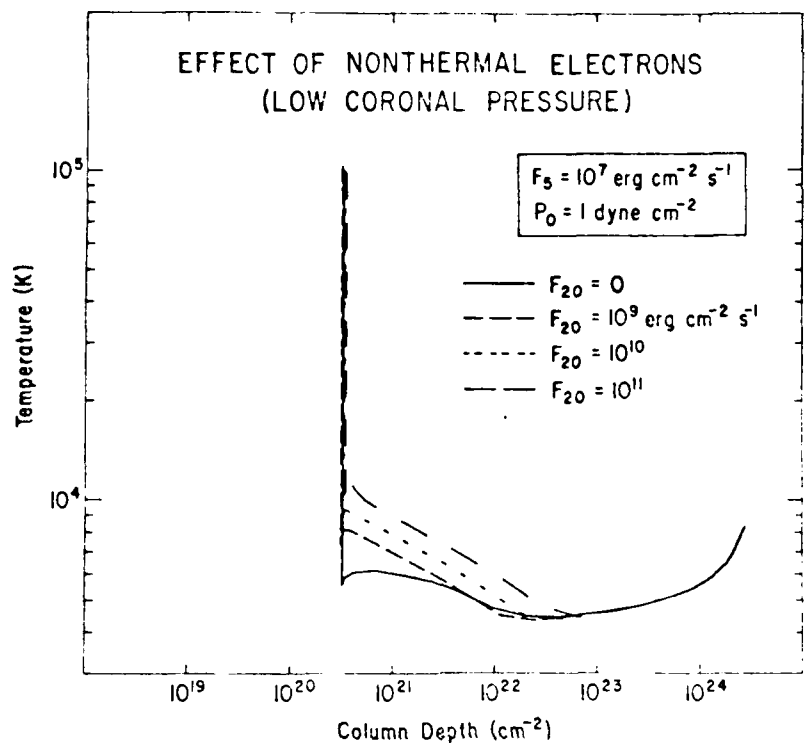


Figure 1

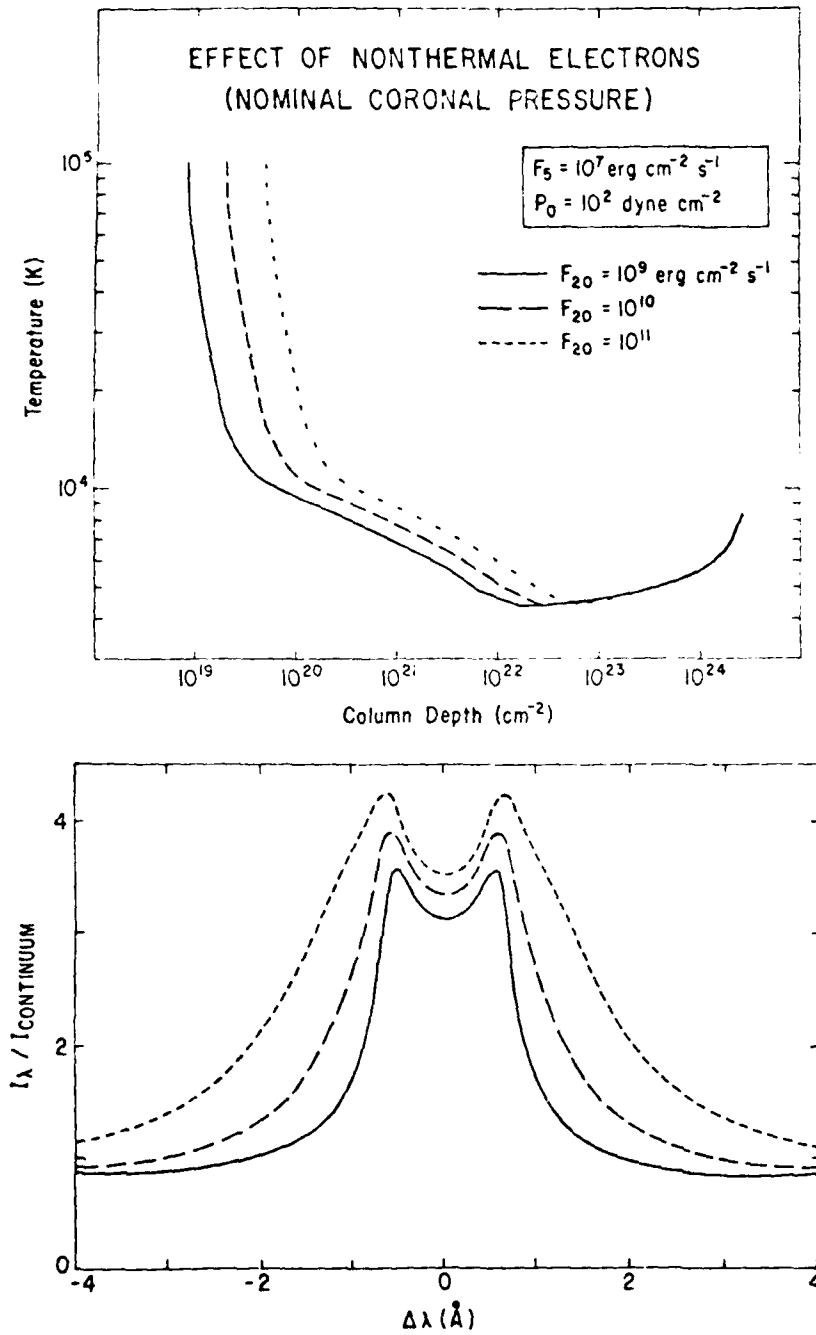


Figure 2

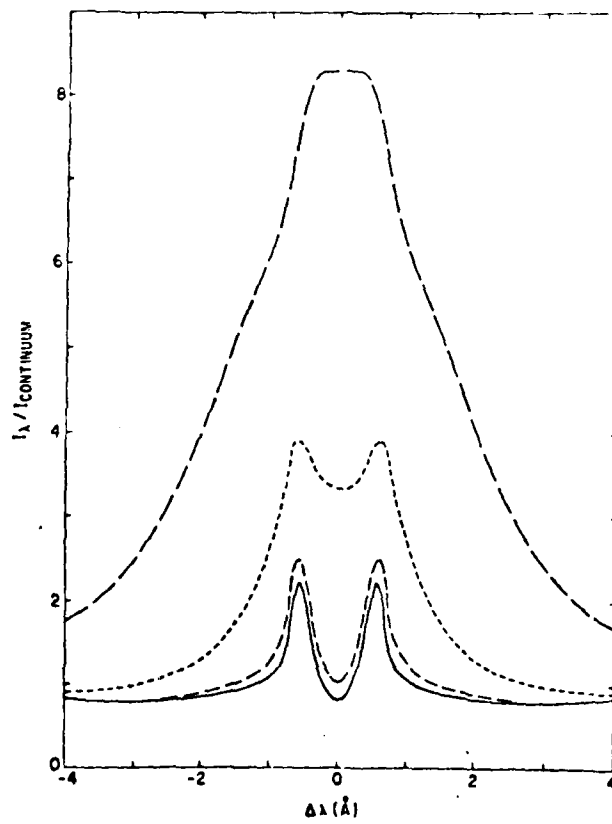
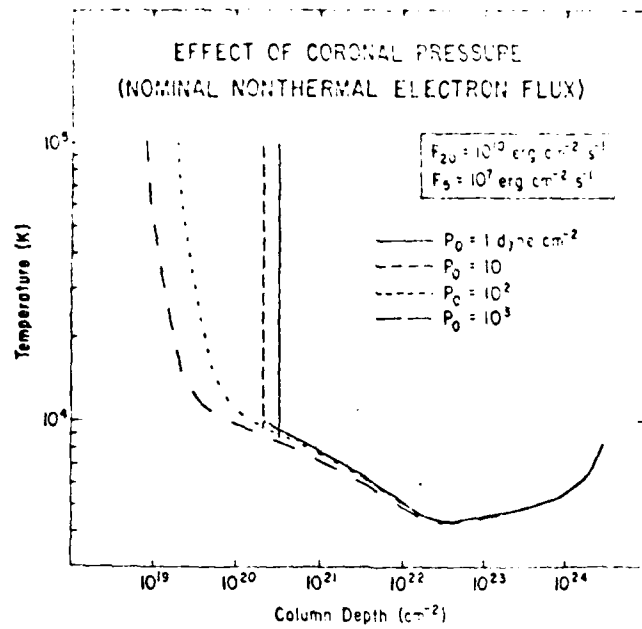


Figure 3

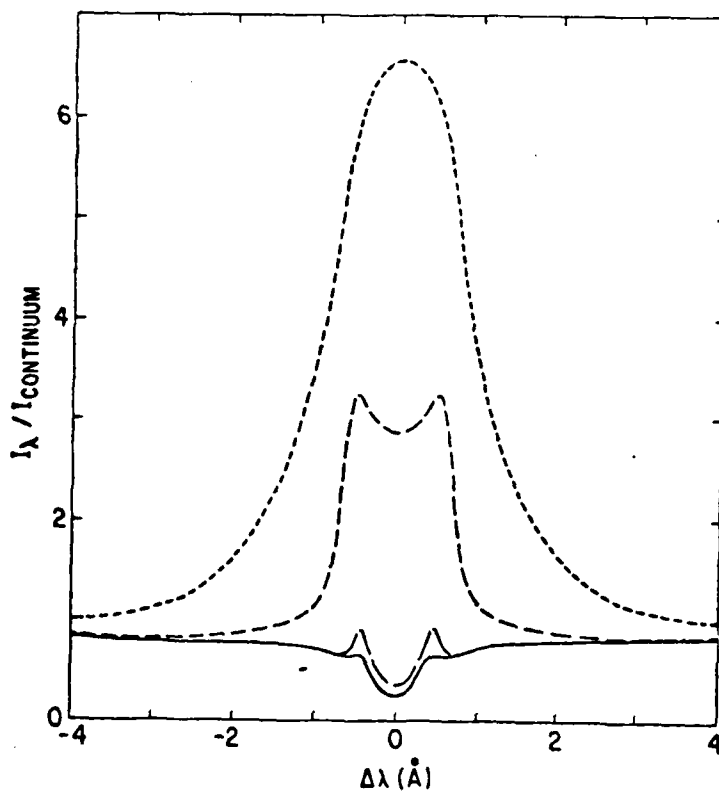
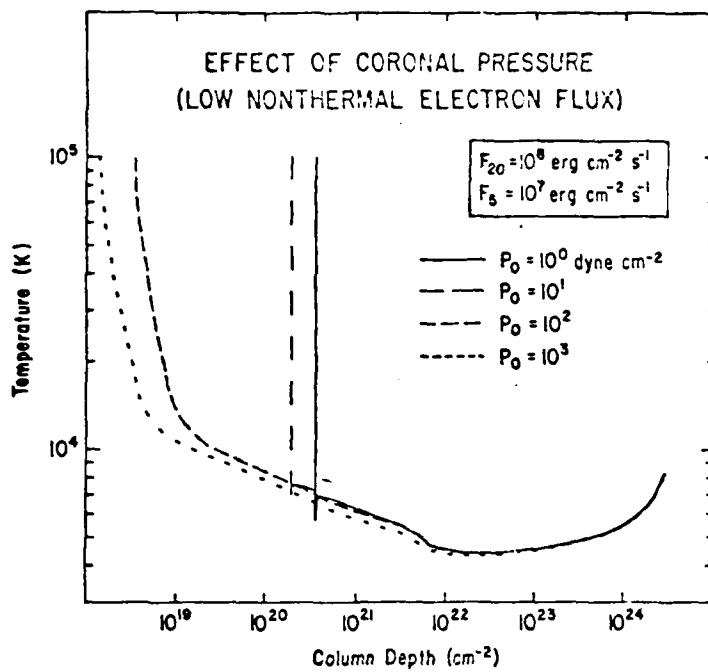


Figure 4

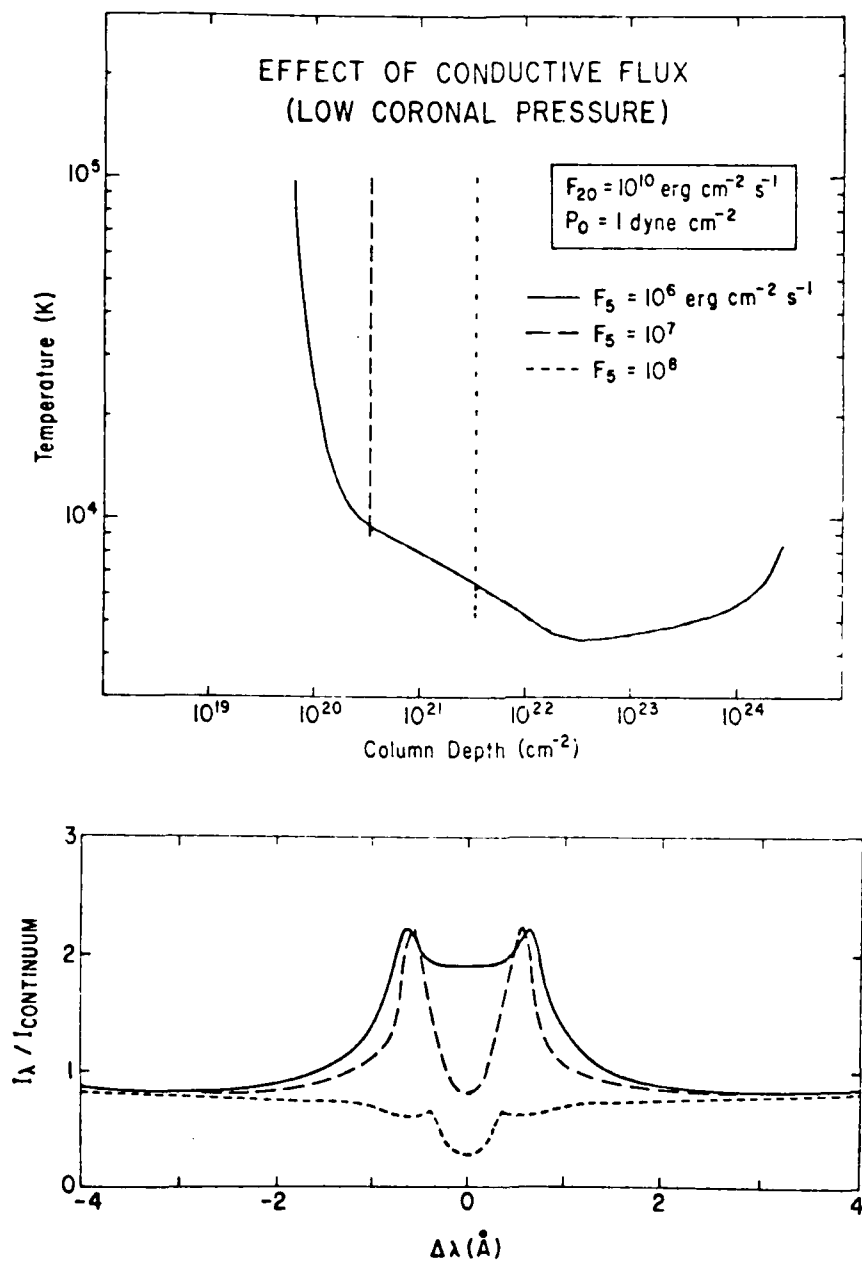


Figure 5

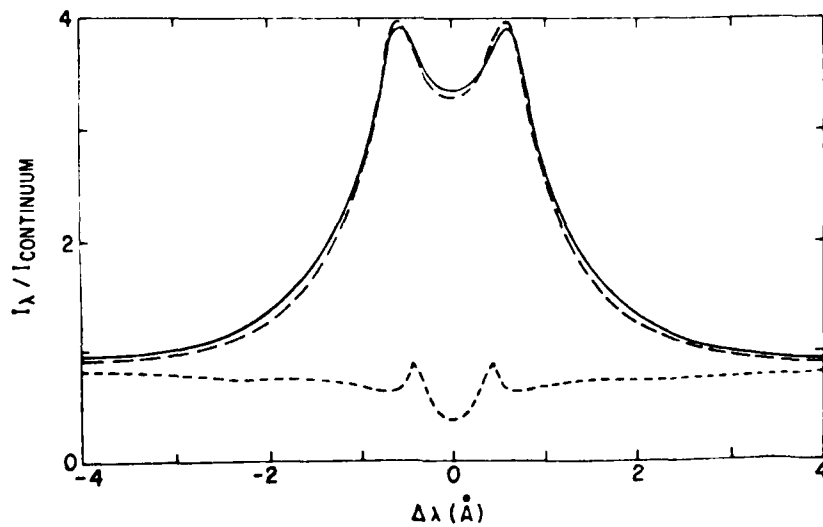
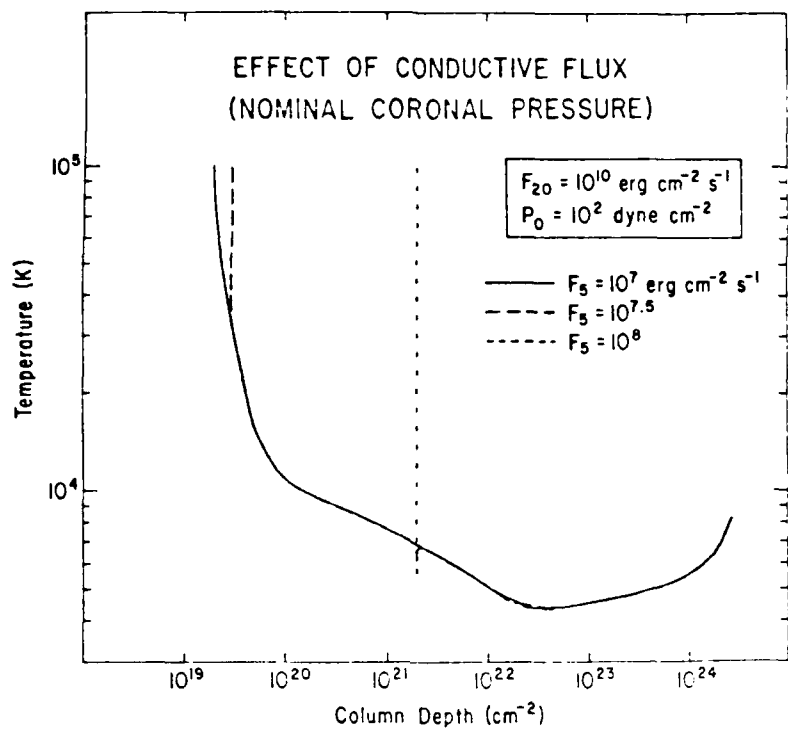


Figure 6

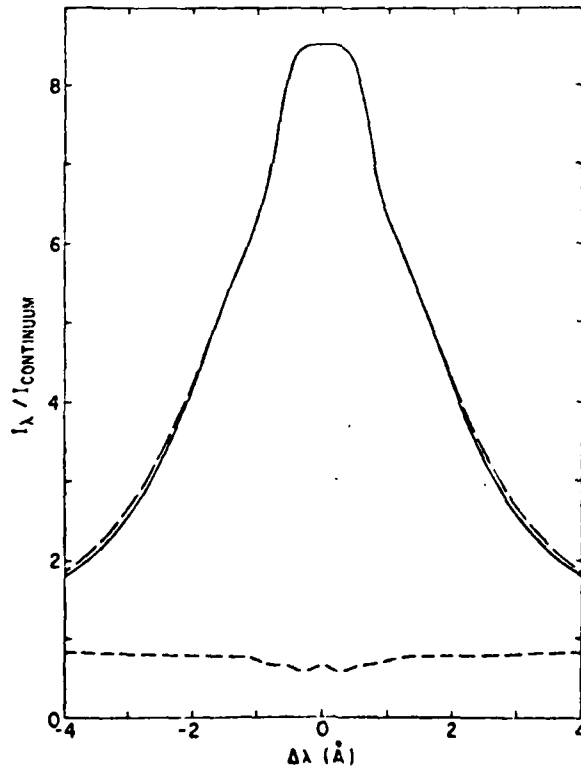
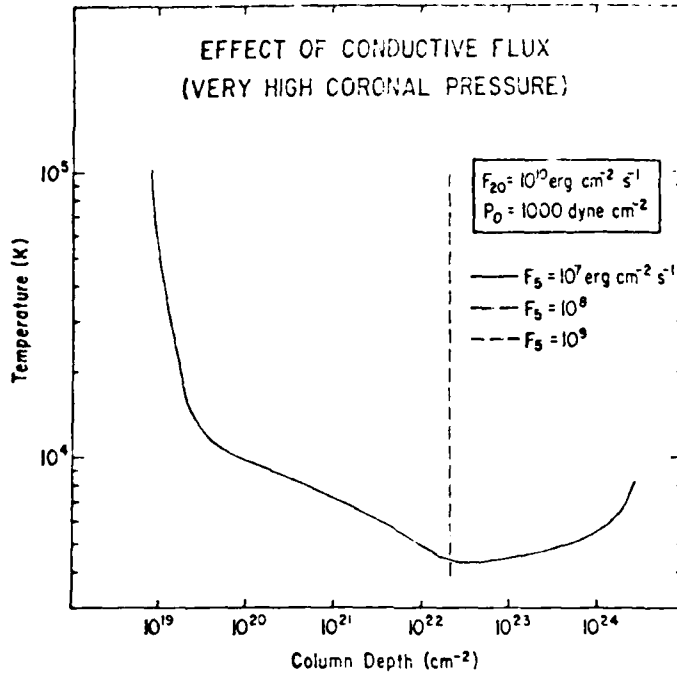


Figure 7

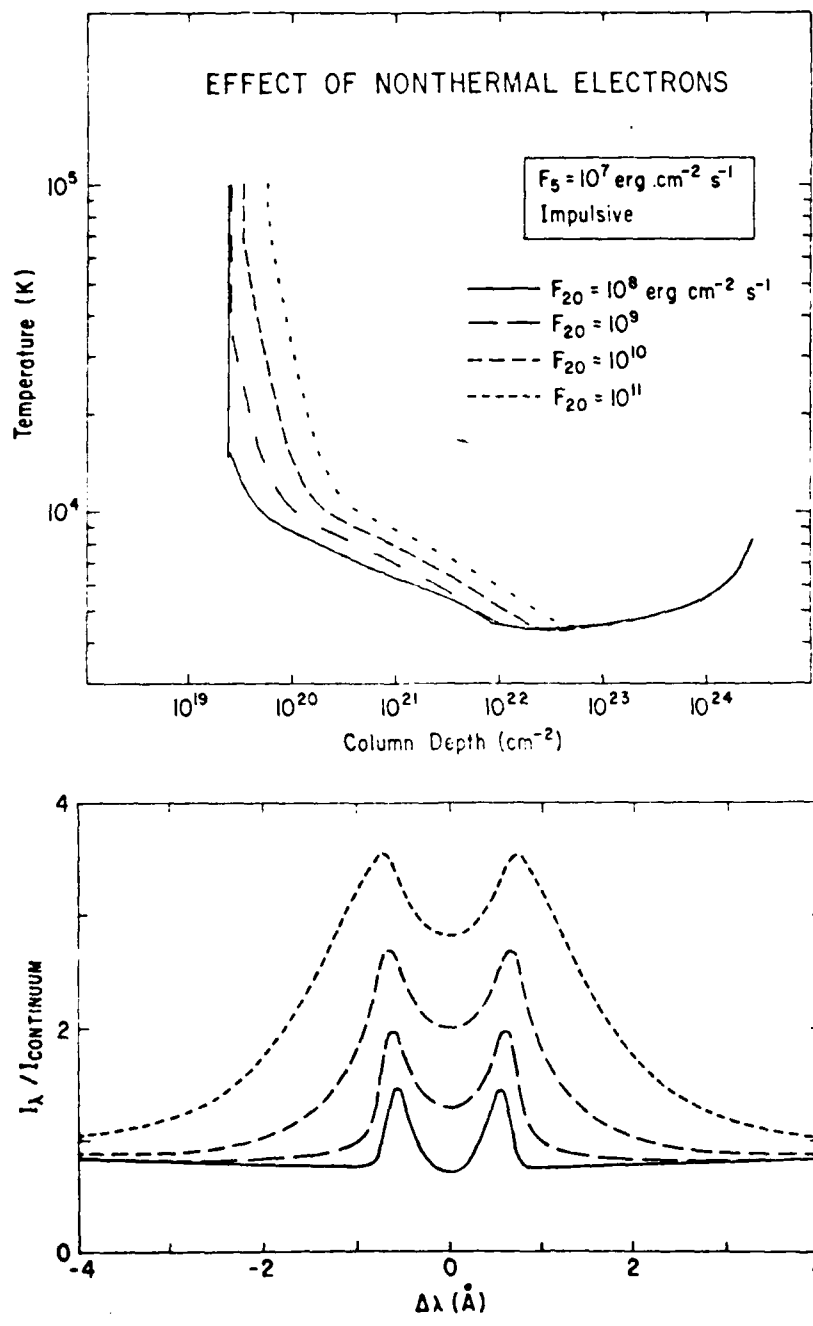


Figure 8

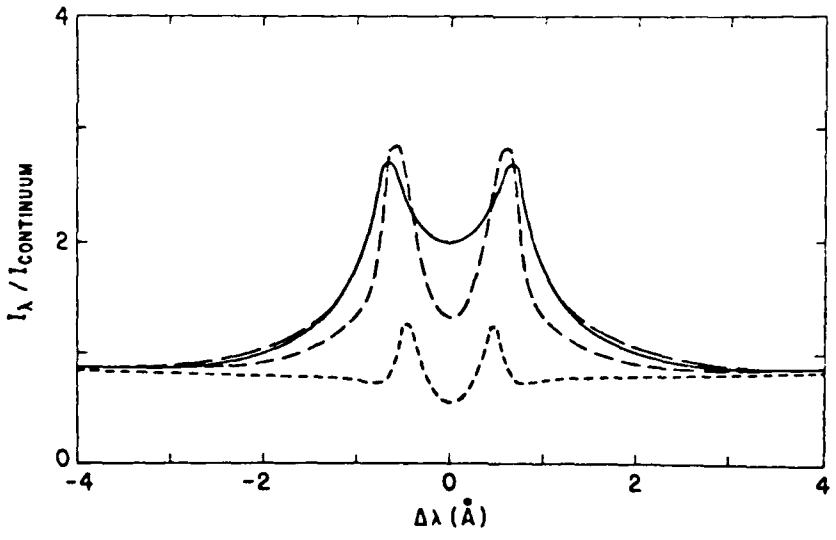
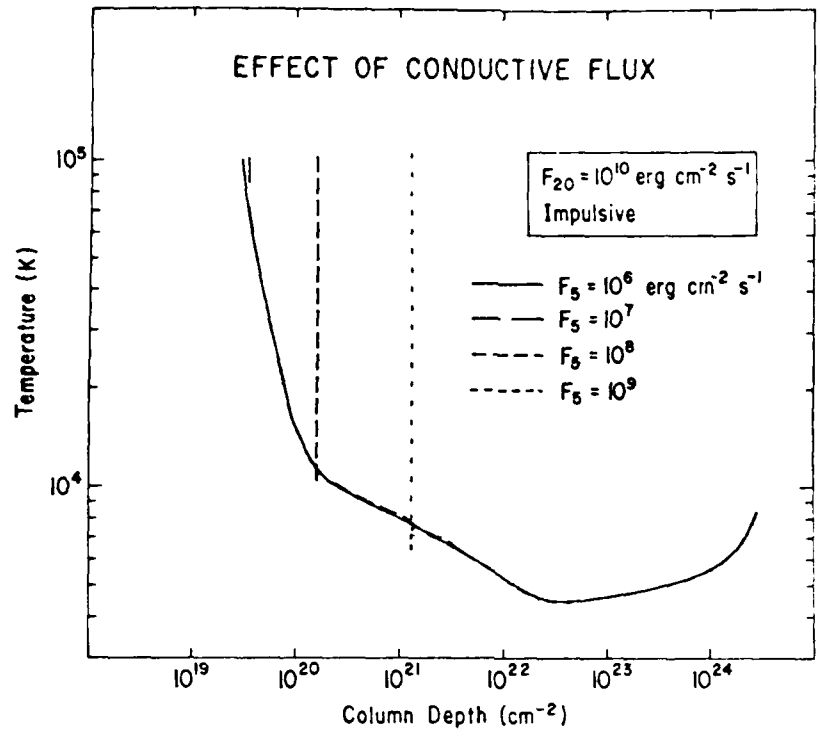


Figure 9

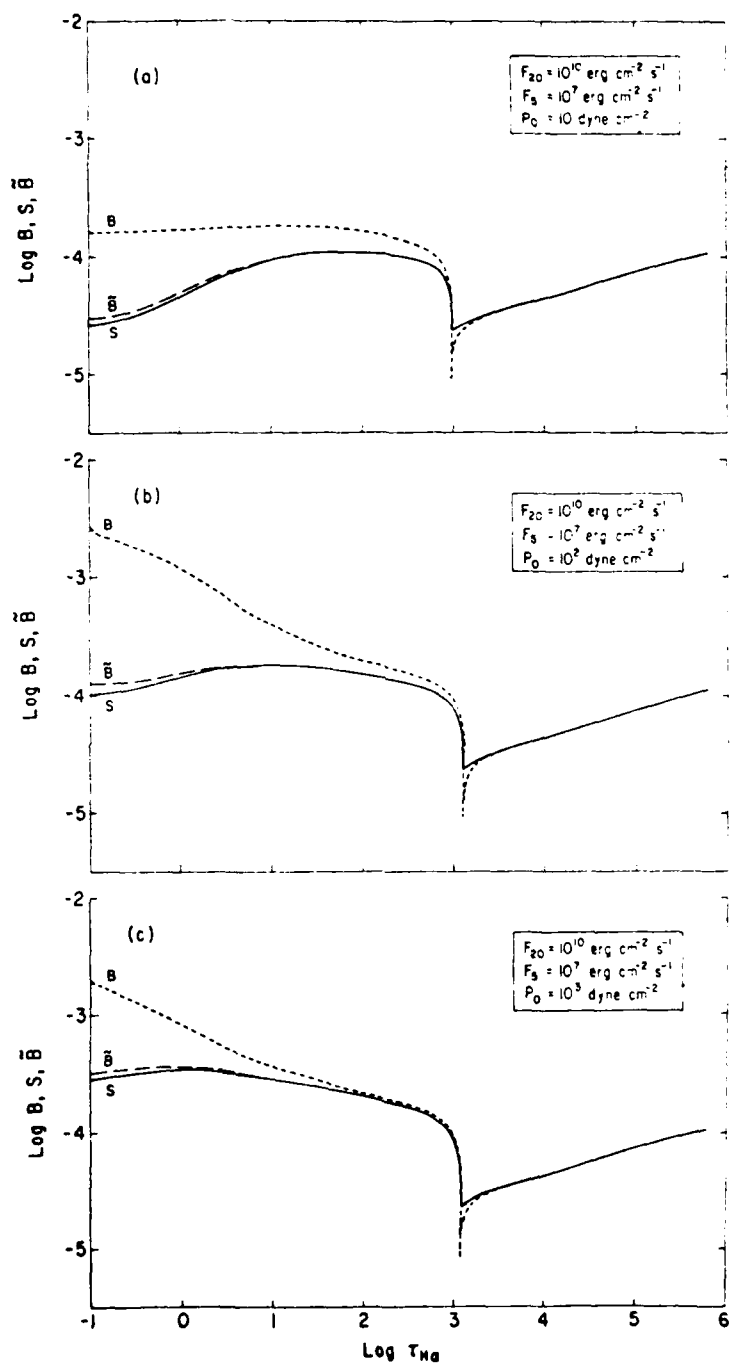


Figure 10

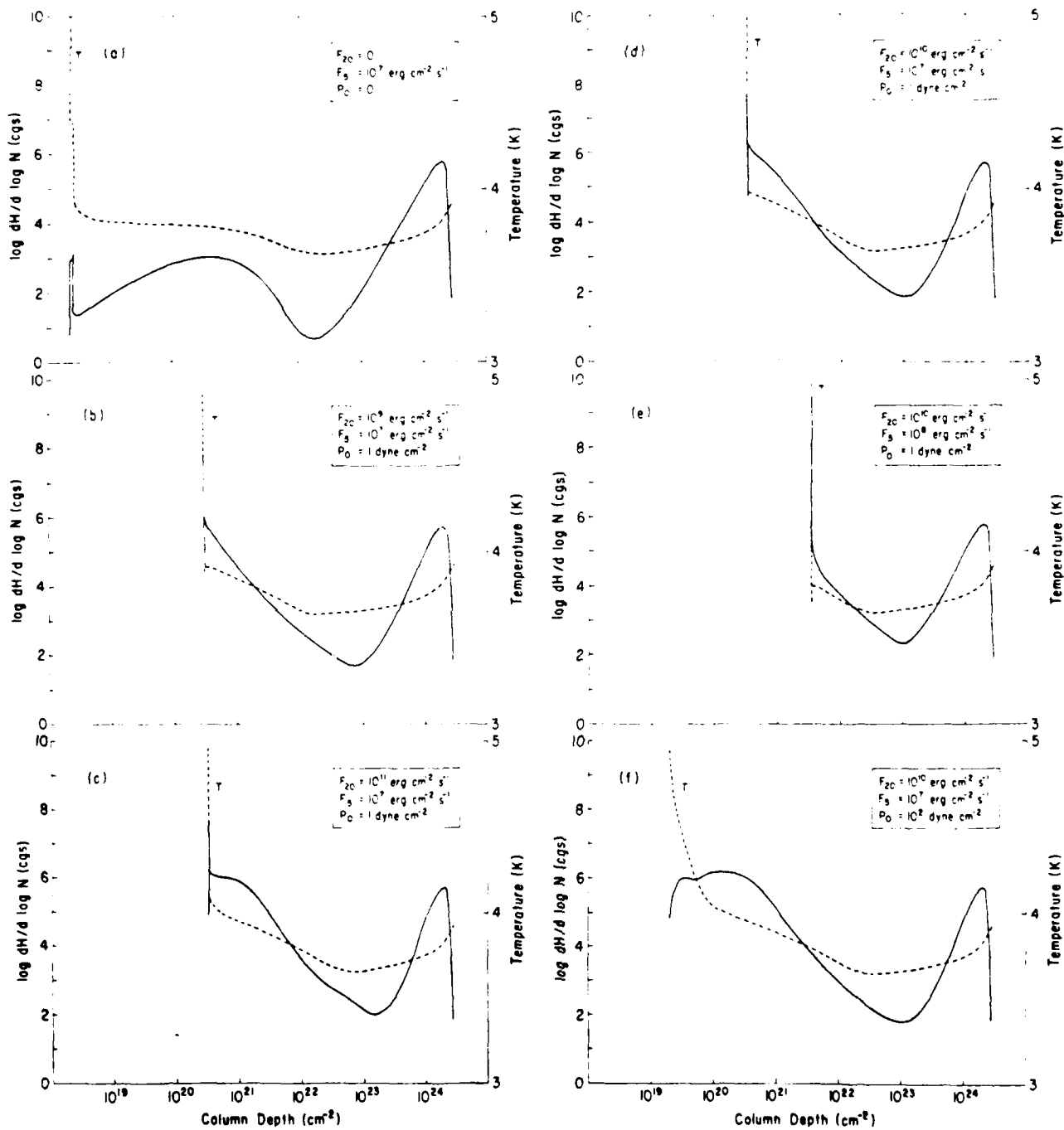


Figure 11

AUTHORS' ADDRESSES

Richard C. Canfield and Todd A. Gunkler

Mail Code C-011

University of California, San Diego

La Jolla, CA 92093

Paul J. Ricchiazzi

Mission Research Corporation

735 State Street

P.O. Drawer 719

Santa Barbara, CA 93102

c) Solar Coronal Loop Magnetohydrodynamic Stability Theory

Magnetic flux tubes, manifested as X-ray emitting loops, are ubiquitous in the solar corona. They are not yet fully understood theoretically, and they are therefore an active area of current solar research. We have carried out a variety of theoretical studies that have contributed to progress in this field.

Results of our solar MHD stability studies include the following:

1. Radiative energy loss affects both the growth rate and stability boundary of ideal-MHD modes.
2. Compressibility of the solar plasma is a stabilizing effect on ideal MHD modes, and the effect comes in through magnetosonic modes.
3. The twist of magnetic field lines (nonpotential) in a cylindrical plasma (flux tube) has a significant effect on the stability of thermal condensation modes.
4. Kink instabilities show magnetic field line-tying (at the feet of coronal loops) effects that depend on whether or not the equilibria are force-free, and on the degree of magnetic shear.
5. The effect of line-tying depends on the radial pressure profile within the cylindrical model of the coronal loop.

MHD STABILITY OF INCOMPRESSIBLE CORONAL LOOPS WITH RADIATIVE ENERGY LOSS

CHANG-HYUK AN

Center for Astrophysics and Space Sciences, University of California, San Diego

Received 1982 March 29, accepted 1982 June 24

ABSTRACT

Previous studies of the magnetohydrodynamic (MHD) stability of solar coronal loops have not taken into account the effects of radiative or conductive energy loss in the energy equation. However, since coronal loops continuously lose energy by radiation and heat conduction, it is important to understand how these energy loss mechanisms affect MHD stability. We investigate the problem assuming that a magnetic loop has cylindrical geometry. As a first step, stability is studied for a localized mode, and the result is applied to a specific equilibrium. We find that the radiative energy loss effect not only changes the growth rate of ideally unstable modes, but also alters the stability boundary predicted by ideal MHD theory.

Subject headings: hydromagnetics — radiative transfer — Sun: corona

I. INTRODUCTION

Numerous observations have shown that the solar corona consists of many loop structures, which are believed to be magnetic loops. The interesting features of these magnetic loops are that they are long lived, and solar flares occur in them in active regions. In recent years many studies have been done to understand their apparent stability. Magnetohydrodynamic (MHD) stability studies have emphasized photospheric line tying and positive pressure profile effects (Foukal 1975) on global MHD modes. Giachetti, Van Hoven, and Chiuderi (1977) and Van Hoven, Chiuderi, and Giachetti (1977) studied MHD stability of a cylindrical loop with a positive pressure gradient (Foukal 1975) using Newcomb's (1960) criterion; Raadu (1972), Hood and Priest (1979), An (1982), and Einaudi and Van Hoven (1981) studied the photospheric field line tying effect using the energy principle of Bernstein *et al.* (1958). All of these studies neglected radiation and heat conduction effects, even though these are the dominant energy dissipation mechanisms. On the other hand, Antiochos (1979), Hood and Priest (1980), Chiuderi, Einaudi, and Torricelli-Ciamponi (1981), McClymont and Canfield (1983), and An *et al.* (1982) studied thermal instability driven by radiative energy loss to understand long-lived nonflare X-ray emission of coronal loops (Vaiana *et al.* 1976). They found that instability is localized near the transition region. In their calculations they did not take into account the magnetic field, except that heat is transmitted along magnetic field lines. Field (1965) studied field effects on the thermal stability of a uniform atmosphere. He found that the effect can enhance or reduce stability, depending on modes considered, as well as the angle between the wave vector and the magnetic field. Chiuderi and Van Hoven (1979) extended the work to study the effect of spatial variation of the background magnetic field on the thermal instability.

It is not yet known how radiation and heat conduction affect the MHD stability of magnetic loops. From recent observations (Van Hoven *et al.* 1980; Harvey 1981; Davis and Webb 1981) it is suggested that thermal instability may be a trigger mechanism for global MHD instabilities. For better understanding of the observational characteristics of solar magnetic loops it may be important to include radiation and heat conduction effects in MHD stability calculations. This is the motivation for the present study.

In this paper we investigate how energy dissipation and redistribution mechanisms affect the MHD stability of a coronal magnetic loop. We assume that the loop has a cylindrical geometry, with physical quantities uniform along the loop, which have only radial dependence. The loop can be subject to MHD as well as thermal instabilities. By including these energy dissipation mechanisms we hope to better understand observational characteristics and to find clues for flare eruptions. As a first step, we study stability for localized modes and apply the result to a specific equilibrium, cool-core loops (Foukal 1975). We find that the radiative energy loss effect not only changes the growth rate of ideally unstable modes, but also alters the stability boundary predicted by ideal MHD theory.

In § II, we describe the basic equations and derive a second-order ordinary differential equation. Stability for localized modes is studied in § III. In § IV we apply the results to cool-core loops, and the conclusion is given in § V.

II. GOVERNING EQUATIONS

In this section we will derive a differential equation for stability of a coronal loop with the following configurations.

I. The loop is assumed to be a circular cylinder with uniform temperature, density, and magnetic field along the loop direction. We will consider only radial dependence of these equilibrium variables.

2. Plasma is confined by a nonpotential magnetic field generated by plasma current. Therefore, magnetic field lines are helically twisted along the loop.

3. Since for coronal temperature $T \approx 10^6$ K, heat conductivity parallel to the magnetic field line is much larger than the perpendicular component (Spitzer 1962), we will neglect the perpendicular heat conductivity in this calculation. In this case, radiative energy loss is balanced by ambient heating for a loop in steady state.

Before perturbation a coronal loop in a steady state is governed by the equations below:

$$\nabla P_0 - J_0 \times B_0 = 0, \tag{1}$$

$$\nabla \times B_0 = J_0, \tag{2}$$

$$H(\rho) - R(\rho, T) = 0. \tag{3}$$

Here P_0, J_0, B_0 are equilibrium pressure, current density, and magnetic field; $H(\rho)$ and $R(\rho, T)$ are ambient heating and radiative energy loss function, respectively. Because T has only radial dependence, the contribution of conduction to energy balance is zero.

Assuming we give a linear perturbation of the form $f_1(r, t) = e^{i\omega t} f_1(r) e^{i(m\theta - kz)}$, the loop is governed by the following equations:

$$\rho_0 \frac{\partial v}{\partial t} = -\nabla P_1 + J_0 \times B_1 + J_1 \times B_0, \tag{4}$$

$$\frac{\partial P_1}{\partial t} = -\gamma P_0 \nabla \cdot v - (\gamma - 1) \left[\left(\frac{\partial R}{\partial T} \right)_\rho T_1 + \left(\frac{\partial R}{\partial \rho} \right)_T \rho_1 + (k \cdot B_0)^2 \frac{\kappa}{B_0^2} T_1 \right] - v \cdot \nabla P_0, \tag{5}$$

$$J_1 = \nabla \times B_1, \tag{6}$$

$$B_1 = \nabla \times (\xi \times B_0), \tag{7}$$

$$\rho_1 = -\xi \cdot \nabla \rho_0 - \rho_0 \nabla \cdot \xi. \tag{8}$$

Here f_0 is an equilibrium and f_1 is a perturbed quantity; ξ is a displacement vector which satisfies $\partial \xi / \partial t = v$; κ is the coefficient of heat conduction parallel to the magnetic field, and γ is the specific heat constant; k is the wave vector, and $k \cdot B_0 = k B_{0z} + m r B_{0\theta}$, where k and m are longitudinal and poloidal wave numbers. In equation (5) we assume that the ambient heating function is not perturbed mainly because we do not know the form of the function.

We simplify the calculation by assuming that plasma is incompressible, i.e., $\nabla \cdot v = 0$. This assumption may weaken the effect of the radiative instability since it disallows the isobaric condensation mode, but the essential features of the radiative energy loss effect will remain.

Using state equation $P_1 = \alpha(T_1 \rho_0 + T_0 \rho_1)$ and equations (5) and (8), we get

$$P_1 = -\frac{\rho_0 \Phi + \omega P'_0}{\omega + \theta} \xi_r, \tag{9}$$

where

$$\theta = \frac{1}{\alpha \rho_0} (\gamma - 1) \left[\left(\frac{\partial R}{\partial T} \right)_\rho + (k \cdot B_0)^2 \frac{\kappa}{B_0^2} \right], \tag{10}$$

$$\Phi = (\gamma - 1) \left[\frac{T_0}{\rho_0} \left(\frac{\partial R}{\partial T} \right)_\rho + \frac{T_0}{\rho_0} (k \cdot B_0)^2 \frac{\kappa}{B_0^2} \right]. \tag{11}$$

Here α is 2 times the Boltzmann's constant, and P'_0 is a derivative of P_0 with r .

From equations (4)-(8) we derive a second-order ordinary differential equation:

$$\left(\chi \frac{B_0^2}{r} F_1 \right)' + \frac{\chi'}{r} \left(\frac{\rho_0 \Phi - P'_0 \theta}{\omega + \theta} \right) F_1 + \chi F_2 = 0, \tag{12}$$

where $\chi = r \xi_r$, and ξ_r is r component of ξ . Here

$$F_1 = \frac{[\rho_0 \omega^2 + (k \cdot B_0)^2]}{[\rho_0 \omega^2 + B_0^2 [(m^2, r^2) + k^2]]}, \quad F_2 = \left[\frac{\rho_0 \Phi - P'_0 \theta}{r(\omega + \theta)} F_1 - H_1 \right]' + H_2, \tag{13}$$

$$H_1 = \frac{2B_{0\theta}}{r\Omega} \left[\frac{mB_0^2}{r^2 \rho_0 \omega^2} (k \cdot B_0) + \frac{B_{0\theta}}{r} \right],$$

$$H_2 = \frac{-[\rho_0 \omega^2 + (k \cdot B_0)^2]}{r} + \frac{2B_{0\theta}}{r\Omega} \left[\left(\frac{B_{0\theta}}{r} \right)' \left(1 + \frac{m^2 B_0^2}{r^2 \rho_0 \omega^2} \right) + \frac{k^2 B_0^2}{r \rho_0 \omega^2} \left(B'_{0\theta} + \frac{B_{0\theta}}{r} \right) + \frac{k}{r \rho_0 \omega^2} \left(\frac{mB_{0z}}{r} - kB_{0\theta} \right) \frac{\rho_0 \Phi - P'_0 \theta}{\omega + \theta} \right]. \tag{14}$$

In order to study stability for various equilibrium loop configurations we have to solve equation (12) numerically. Since the equation is not Hermitian, the eigenfunction and eigenvalue are complex variables. When we solve the equation numerically, we have to decouple the equation into real and imaginary parts and solve them simultaneously for given boundary conditions. Because of this non-Hermitian property it is a difficult task to solve the equation numerically. However, we can solve it analytically for some special case. In the next section we will solve the equation analytically for localized modes and find the radiative energy loss effect on the MHD stability.

III. STABILITY FOR LOCALIZED MODES

For ideal MHD stability, the eigenfunction is localized near a mode rational surface r_s , where $kr_s B_z + mB_\theta = 0$ is satisfied as the poloidal wave number is increased (Goedbloed and Sakanaka 1974; An 1982). We find that the same is true for the case discussed in this study. We will take the limit as k and m go to infinity while keeping a safety factor q finite in order to study the stability of local modes. The safety factor q is defined as

$$q = krB_{0z}/nB_{0\theta}.$$

and n is the number of the wavelength in the cylinder length L . By taking the limit $m \rightarrow \infty$, we will show that the eigenfunction χ of equation (12) is localized near r_s ($kr_s B_z + mB_\theta = 0$) and will derive an equation for the local mode.

If we take the limit $m \rightarrow \infty$, with q and n fixed, equation (12) becomes

$$\left\{ \chi \frac{B_{0z}^2}{B_0^2} \left[\frac{r\rho_0\omega^2}{m^2} + \frac{B_{0\theta}^2}{r} \left(1 - \frac{n}{m}q \right)^2 \right] \right\}' + \chi(D_1 - \chi(D_2 - D_3)) = 0. \quad (15)$$

Here

$$\begin{aligned} D_1 &= \frac{1}{r} \frac{\rho_0 \Phi - P_0 \theta}{\omega + \theta} \frac{B_{0\theta}^2 [1 + (nm)q]^2}{rB_0^2 [1 + (nqB_{0\theta}/mB_{0z})^2]}, \\ D_2 &= \frac{(\rho_0 \Phi - P_0 \theta)}{r(\omega + \theta)} \frac{B_{0\theta}^2 [1 - (nm)q]^2}{B_0^2 [1 + (nqB_{0\theta}/mB_{0z})^2]} - \frac{2B_{0\theta}^2 [1 - (nm)q]}{r^2 [1 - (nqB_{0\theta}/mB_{0z})^2]} \\ &\quad + \frac{2B_{0\theta}}{r[1 + (nqB_{0\theta}/mB_{0z})^2]} \left\{ \left(\frac{B_{0\theta}}{r} \right)' + \left(\frac{nqB_{0\theta}}{mB_{0z}} \right)^2 \frac{1}{r} \left(B_{0\theta} + \frac{B_{0\theta}}{r} \right) + \frac{(nqB_{0\theta}/m)[1 - (nqB_{0\theta}/mB_{0z})^2]}{rB_0^2} \left(\frac{\rho_0 \Phi - P_0 \theta}{\omega + \theta} \right) \right\}, \\ D_3 &= \frac{\rho_0 \omega^2 + (m^2 B_{0\theta}^2 / r^2) [1 + (n/m)q]^2}{r}. \end{aligned} \quad (16)$$

For the limit $m \rightarrow \infty$, D_1 and D_2 stay finite, while D_3 goes to infinity in the region where $1 + (nm)q \gg 1/m$. In this region equation (15) becomes

$$\frac{B_{0\theta}^2}{r^3} \left(1 + \frac{n}{m}q \right)^2 m^2 \chi = 0, \quad (17)$$

and $\chi = 0$ is the solution. On the other hand, in the region where $1 + (nm)q \ll 1/m$ (near $r = r_s$), equation (15) becomes

$$\frac{\partial}{\partial s} \left[\frac{\partial \chi}{\partial s} (C_1 s^2 + x_1^2) \right] + g\chi - \frac{\rho_0 \omega^2}{r_s} \chi - \frac{C_2}{\omega + \theta} \chi = 0. \quad (18)$$

Here

$$\begin{aligned} s &= r - r_s, \quad C_1 = \frac{1}{r} \left(\frac{B_{0\theta} B_{0z}}{B_0} \right)^2 \left(\frac{n}{m}q \right)^2, \quad C_2 = \frac{2B_{0\theta}^2 (\rho_0 \Phi - P_0 \theta)}{r^2 B_0^2} = -\frac{2B_{0\theta}^2}{r^2 B_0^2} (\gamma - 1) \left(\frac{dR}{dr} \right), \\ g &= -2 \left(\frac{B_{0\theta} B_{0z}}{rB_0} \right)^2 \frac{n}{m}q' + \frac{2B_{0\theta} B_{0z}^2}{rB_0^2} \left\{ \left(\frac{B_{0\theta}}{r} \right)' + \frac{B_{0\theta}^2}{rB_{0z}^2} \left(B_{0\theta} + \frac{B_{0\theta}}{r} \right) \right\}, \quad x_1^2 = \frac{rB_{0z}^2 \rho_0 \omega^2}{B_0^2 m^2}. \end{aligned} \quad (19)$$

When we derive equation (18), we expand $[1 + (nm)q]^2$ in Taylor series at r_s such as

$$\left(1 + \frac{n}{m}q \right)^2 = \left(\frac{n}{m}q' \right)^2 (r - r_s)^2$$

for the first term of equation (15). We keep x_1^2 in equation (18), even though x_1^2 goes to zero as $m \rightarrow \infty$. By keeping x_1^2 we can avoid a singularity at $s = 0$ which appears for marginal stability analysis of ideal MHD (Newcomb 1960). From equations (17) and (18) we find that for the limit $m \rightarrow \infty$, χ is localized near a mode rational surface r_s . Since χ is localized at $r = r_s$, equilibrium variables in equation (18) are all calculated at $r = r_s$, and coefficients in equation (19) are all constant. We can solve equation (18) for a given boundary condition. However, if we do not want detailed

information about eigenfunctions but only want to know eigenvalues, we may multiply the equation by χ^* (complex conjugate of χ) and integrate by parts.

The result is

$$\frac{1}{C_1} \left(g - \frac{\rho_0}{r_s} \omega^2 + \frac{C_2}{\omega + \theta} \right) = \frac{\int s^2 |\chi'|^2 ds}{\int |\chi|^2 ds} + \frac{x_1^2 \int |\chi|^2 ds}{C_1 \int |\chi|^2 ds}.$$

Since x_1^2 is infinitesimally small as $m \rightarrow \infty$, we can neglect the last term of the above equation. Using an estimate of integral $\int s^2 |\chi'|^2 ds \geq \frac{1}{4} \int |\chi|^2 ds$, we get

$$g - \frac{\rho_0}{r_s} \omega^2 + \frac{C_2}{\omega + \theta} = \frac{1}{4} \sigma C_1, \quad (20)$$

where $\sigma \geq 1$.

If we exclude $\omega = \theta$ as a root, equation (20) is a cubic equation for ω :

$$\omega^3 + \theta \omega^2 + \omega \frac{r_s}{\rho_0} \left(\frac{\sigma}{4} C_1 - g \right) + \theta \frac{r_s}{\rho_0} \left(\frac{1}{4} \sigma C_1 - g \right) + \frac{C_2 r_s}{\rho_0} = 0. \quad (21)$$

Roots of equation (21) for any equilibrium are not difficult to get, but it is more instructive to study the case in which the ideal MHD growth rate is much bigger than the radiative growth rate. This is true for $T \approx 10^6$ K. In this case we can let $\omega = \omega_0 + \omega_1$ with $\epsilon = \omega_1, \omega_1 \ll 1$. Here ω_0 is the growth rate for ideal MHD, and ω_1 is the contribution due to radiative instability. Since θ is the growth rate of the isochoric mode, $\theta/\omega_0 \approx \epsilon \ll 1$.

The zeroth order in ϵ of equation (21) is

$$\omega_0^3 + \omega_0 \frac{r_s}{\rho_0} \left(\frac{\sigma}{4} C_1 - g \right) = 0,$$

and the roots are

$$\omega_0 = 0, \quad \pm \left[\frac{r_s}{\rho_0} \left(g - \frac{\sigma}{4} C_1 \right) \right]^{1/2}. \quad (22)$$

Here we have to neglect $\omega_0 = 0$ as a solution because this solution implies that a loop is in a marginally stable state for any equilibrium.

If $g - (\sigma/4)C_1 < 0$, the loop is in an ideal MHD stable state, and if $g - (\sigma/4)C_1 > 0$, the loop is in an ideal MHD unstable state. The explicit expression of $g - (\sigma/4)C_1$ is

$$g - \frac{\sigma}{4} C_1 = -\frac{2B_{0\theta}^2}{rB_0^2} P'_0 - \frac{\sigma B_{0\theta}^2 B_{0z}^2}{4rB_0^2} \left(\frac{nq'}{m} \right)^2. \quad (23)$$

Therefore, the ideal MHD stability condition $g - (\sigma/4)C_1 < 0$ turns out to be the Suydam criterion (Suydam 1958) if we let $\sigma = 1$:

$$\frac{r^2}{4} \left(\frac{q'}{q} \right)^2 + \frac{2rP'_0}{B_{0z}^2} > 0. \quad (24)$$

The first-order solution in ϵ of equation (21) is

$$\omega_1 = \frac{C_2}{2[(1/4)C_1 - g]} = -\frac{C_2}{2(\rho_0 r_s) \omega_0^2}. \quad (25)$$

The effect of radiative energy loss on MHD stability is stabilizing or destabilizing, depending on the sign of ω_1 , i.e., stabilizing for $\omega_1 < 0$ and destabilizing for $\omega_1 > 0$. We will study the radiative energy loss effects on the MHD stability for several cases:

Case I: $\omega_0^2 > 0$, i.e., the ideal MHD unstable case. If $C_2 > 0$ (i.e., $dR/dr < 0$), ω_1 is negative, which means the radiative energy loss effect is stabilizing. If $C_2 < 0$ (i.e., $dR/dr > 0$), the effect is destabilizing.

Case II: $\omega_0^2 < 0$, i.e., the ideal MHD stable case. If $C_2 > 0$ ($dR/dr < 0$), the radiative energy loss effect is destabilizing. If $C_2 < 0$, the effect is stabilizing.

Case III: $\omega_0^2 = 0$, i.e., the ideal MHD marginally stable case.

In this last case we cannot use equation (25). From equation (21) we get

$$\omega^3 + \theta \omega^2 + \frac{C_2 r_s}{\rho_0} = 0. \quad (26)$$

The roots of this cubic equation are (Abramowitz and Stegun 1970)

$$z_1 = (s_1 + s_2) - \frac{\theta}{3}, \quad z_2 = -\frac{1}{2}(s_1 + s_2) - \frac{\theta}{3} + \frac{i(3)^{1/2}}{2}(s_1 - s_2), \quad z_3 = -\frac{1}{2}(s_1 + s_2) - \frac{\theta}{3} - \frac{i(3)^{1/2}}{2}(s_1 - s_2). \quad (27)$$

Here

$$s_1 = [r + (q^3 + r^2)^{1/2}]^{1/3}, \quad s_2 = [r - (q^3 + r^2)^{1/2}]^{1/3}, \quad r = -\frac{C_2 r_2}{2\rho_0} - \frac{1}{27}\theta^3, \quad q = -\frac{\theta^2}{9}. \quad (28)$$

Since we consider a loop with $T \leq 10^6$, θ (eq. [10]) is negative near r_3 .

If $dR/dr > 0$, then z_1 is real positive, and z_2, z_3 are complex conjugates. The real part of z_2 and z_3 can be positive or negative depending on the detailed equilibrium. In this case there is at least one unstable mode, even when ideal MHD theory predicts marginal stability. If $dR/dr < 0$, stability is not obvious unless we solve the roots numerically for the given equilibrium.

Case III shows that there are unstable modes even when ideal MHD predicts a marginally stable state. This result indicates that the stability boundary is altered by the inclusion of radiative energy loss. Since we study a mode localized near a mode rational surface where the radial component of the magnetic field is not perturbed, conduction does not play any role in stability for this mode. The results are summarized in Table I.

Next, let us consider how radiation affects the stability for various cases. Note that the local mode treated in this section is an interchange instability driven by a pressure gradient. This mode has analogies to the Rayleigh-Taylor instability driven by a density gradient under a gravitational field. The pressure gradient in the MHD interchange mode has the same effect as the density gradient in the Rayleigh-Taylor mode, and the curvature of the magnetic field line plays the same role as gravitational force (with the opposite sign). We can, therefore, understand how radiation affects MHD interchange modes by analogy.

The Rayleigh-Taylor mode is unstable when the density gradient has a sign opposite to the gravitational force. If plasma displacement in the same direction as the gravitational force is accompanied by a density decrease due to some mechanism (e.g., radiation), then the instability growth rate decreases because the reduced density causes the buoyancy force to be increased. If the density increases, on the other hand, the growth rate will be increased. For the unstable MHD interchange mode, the radiation increases P_1 from that of ideal MHD (see eq. [9]) for positive ξ_r , if $dR/dr > 0$. By analogy to the Rayleigh-Taylor mode, radiation increases the growth rate of the instability. If $dR/dr < 0$, the radiation decreases P_1 from that of ideal MHD, resulting in enhancement of stability. For ideally stable cases, we can use a similar argument to understand the results.

IV. STABILITY FOR A COOL-CORE LOOP

Foukal (1975) observed cool-core loops whose radial pressure gradient is positive. The cool-core loop is especially interesting from the MHD stability viewpoint because the equilibrium satisfies the Suydam stability criterion (1958), i.e., the loop is stable for the local mode by the ideal MHD theory. Since violation of the Suydam criterion implies (Goedbloed and Sakanaka 1974) that the entire infinity of all lower-mode solutions, including $m = 1, n = 0$, is unstable, the cool-core loop has certain advantages for stability over equilibria with a negative pressure gradient. Giachetti, Van Hoven, and Chiuderi (1977) studied local and global ideal MHD stability for cool-core loops and found stability for the short-wavelength mode. Xue and Chen (1980) found that the positive pressure gradient is a necessary requirement for the existence of an equilibrium toroidal loop.

Observations (Foukal 1975) show that pressure has a positive radial gradient, while density is nearly uniform:

$$\frac{dp}{dr} > 0, \quad \frac{dn}{dr} \approx 0. \quad (29)$$

For the radiative energy loss function R , we use

$$R = n^2 \chi T^{-3/2}. \quad (30)$$

TABLE I
RADIATION EFFECTS ON MHD STABILITY

Parameter	Case I $\omega_j^2 > 0$	Case II $\omega_j^2 < 0$	Case III $\omega_j^2 = 0$
$dR/dr < 0$	stabilizing	destabilizing	not obvious
$dR/dr > 0$	destabilizing	stabilizing	destabilizing

and for the ambient heating function H , we use

$$H = nh. \quad (31)$$

Energy equation (3) becomes

$$nh = n^2 \chi T^{-3/2}. \quad (32)$$

If we assume $h \sim T^{-3/2}$, density n is uniform. Since stability depends on the sign of dR/dr , we calculate the term using equation (30):

$$\frac{dR}{dr} = -\frac{3}{2\alpha} n \chi T^{-5/2} \frac{dP}{dr} \sim -\frac{dP}{dr}. \quad (33)$$

For the cool-core loop which is ideal MHD stable we can use the result of case II from the previous section. From equation (33), which shows $dR/dr < 0$, and the result of case II, we find that the radiative energy loss is a destabilizing effect. Because the observations show that the temperature at the core is much lower than 10^6 K, we can expect that the loop is unstable for the local mode even though ideal MHD theory predicts stability.

Before closing this section, we have to mention that local instability of the cool-core loop due to the effect of radiation does not mean that the loop is globally unstable. The observations (Foukal 1975, 1976) show that cool-core loops maintain long-term stability.

The following physical picture of the cool-core loop can be drawn from this study and the observations. The loop is stable for global modes, and therefore maintains its long-lived loop configuration. On the other hand, it is unstable (due to radiation) for the local interchange mode, especially near its cool core. Therefore, there is mixing of materials in the core and in the surrounding hotter region. The mass flow across magnetic field lines due to radiation might be the source of mass flowing continuously down along the cool core, as claimed by Foukal (1976).

V. CONCLUSIONS

We have studied the effect of radiative energy loss on the MHD stability of coronal loops. Because of the effect, the governing differential equation is not Hermitian. This non-Hermitian property of the equation causes mathematical and numerical difficulties. We have attempted to solve the equation analytically for a limiting case where poloidal and longitudinal wavenumbers go to infinity. We have derived results for the stability of localized modes and apply the results to a specific equilibrium, cool-core loops (Foukal 1975). Our result demonstrates that radiative energy loss can enhance or reduce the stability of a loop, depending on the detailed equilibrium profiles. The result also shows that the cool-core loop, which is predicted to be stable for localized modes by ideal MHD theory, can be unstable due to radiation and predicts the mixing of the material between the cool core and the surrounding hotter region. This result supports the claim by Foukal (1976) that the mass flowing down along the cool core is supplied from the surrounding plasma by MHD instability. The effect will be more important for filaments where the temperature is much less than 10^6 K.

We have considered the stability of local modes as a first step in the study of large-scale modes. By solving equation (12) in § II numerically we can see how the stability boundary of the $m = 1$ mode is changed by radiation and heat conduction. For a more complete treatment, we have to discard the assumption about incompressibility of plasma and include the perpendicular component of heat conduction for low-temperature coronal loops.

The author thanks Dr. R. C. Canfield for his valuable discussions and comments during the course of this work. This work is supported by the Air Force Office of Scientific Research, Air Force Systems Command, USAF, under grant AFOSR 82-0092, and by NASA under grant NSG-7406.

REFERENCES

- Abramowitz, M., and Stegun, I. A., eds. 1970. *Handbook of Mathematical Functions* (New York: Dover), p. 17.
- An, C.-H. 1982. *Solar Phys.*, **75**, 19.
- An, C.-H., Canfield, R. C., Fisher, G. H., and McClymont, A. N. 1982. *Ap J.*, in press.
- Antiochos, S. K. 1979. *Ap J. (Letters)*, **232**, L125.
- Bernstein, I. B., Frieman, E. A., Kruskal, M. D., and Kubrud, R. M. 1958. *Proc. Roy. Soc. London*, **4**, **244**, 17.
- Chiuderi, C., Einaudi, G., and Torricelli-Ciamponi, G. 1981. *Astr. Ap.*, **97**, 27.
- Chiuderi, C., and Van Hoven, G. 1979. *Ap J. (Letters)*, **232**, L69.
- Davis, J. M., and Webb, D. F. 1981. *Bull.*, **4.45**, **13**, 821.
- Einaudi, G., and Van Hoven, G. 1981. *Phys. Fluids*, **24**, 1092.
- Field, G. B. 1965. *Ap J.*, **142**, 531.
- Foukal, P. V. 1975. *Solar Phys.*, **43**, 327.
- 1976. *Ap J.*, **210**, 575.
- Giachetti, R., Van Hoven, G., and Chiuderi, C. 1977. *Solar Phys.*, **55**, 371.
- Goedbloed, J. P., and Sakanaka, P. H. 1974. *Phys. Fluids*, **17**, 908.
- Harvey, K. L. 1981. *Bull.*, **4.45**, **13**, 890.
- Hood, A. W., and Priest, E. R. 1979. *Solar Phys.*, **64**, 303.
- 1980. *Astr. Ap.*, **87**, 126.
- McClymont, A. N., and Canfield, R. C. 1983. **266**, in press.

- Newcomb, W. A. 1960, *Ann. Phys.*, **10**, 232.
Raadu, M. A. 1972, *Solar Phys.*, **22**, 425.
Spitzer, L. 1962, *Physics of Fully Ionized Gases* (New York: Interscience), pp. 136-146.
Suydam, B. R. 1958, *IAEA Geneva Conference*, **31**, pp. 157-159.
Vaiana, G. S., Krieger, A. S., Timothy, A. F., and Zombeck, M. V. 1976, *Ap. Space Sci.*, **39**, 75.
Van Hoven, G., Chiuderi, C., and Giachetti, R. 1977, *Ap. J.*, **213**, 869.
Van Hoven, G., et al. 1980, in *Solar Flares* (Boulder: Colorado Associated University Press), pp. 43-46.
Xue, M.-L., and Chen, J. 1980, PFC LA-27-80, MIT Preprint.

CHANG-HYUK AN: Center for Astrophysics and Space Sciences, C-011, University of California, San Diego, La Jolla, CA 92093

MHD STABILITY OF COMPRESSIBLE CORONAL LOOPS WITH RADIATIVE ENERGY LOSS

CHANG-HYUK AN

Center for Astrophysics and Space Sciences, University of California, San Diego

Received 1982 November 1, accepted 1983 June 14

ABSTRACT

We have studied the effect of radiative energy loss on the stability of compressible plasma in coronal loops. By taking the limit as poloidal wavenumber $m \rightarrow \infty$, we derive stability conditions for local modes. We have found that the radiation effect can trigger MHD instabilities of coronal loops which are in ideally marginally stable states.

Compressibility is a stabilizing effect for ideal MHD local modes because the compression of magnetic field lines exerts a restoring force by increasing magnetic pressure. Compression of plasma induces two modes in a radiatively unstable plasma, magnetosonic and condensation modes. Compressibility affects the stability of ideally stable (or unstable) coronal plasmas through magnetosonic modes, which are a stabilizing (destabilizing) effect for ideally stable (unstable) plasmas. For coronal plasmas in ideally marginally stable states, condensation as well as magnetosonic modes can trigger MHD instability. Because of these two modes, the effect of radiation on compressible coronal plasmas is more destabilizing than it is on incompressible plasmas when the plasmas are in ideal MHD unstable or marginally stable states.

Subject headings: hydromagnetics -- plasmas -- Sun: corona

1. INTRODUCTION

In recent years, numerous studies of coronal loop stability have been carried out to understand their stable nature. Two different approaches have been used, magnetohydrodynamic (MHD) and radiative hydrodynamic approaches. MHD stability studies have emphasized the effects of photospheric line tying (Raadu 1972; Hood and Priest 1979; Einaudi and Van Hoven 1981; An 1982) and radial pressure profile (Giachetti, Van Hoven, and Chiuderi 1977; Van Hoven, Chiuderi, and Giachetti 1977) on the ideal MHD stability of loops. For radiative hydrodynamic studies, condensation modes have been studied to understand solar prominences (Field 1965) as well as long-lived coronal loops (Antiochos 1979; Hood and Priest 1980; Chiuderi, Einaudi, and Torricelli-Cramponi 1981; McClymont and Canfield 1983; An *et al.* 1983; Antiochos *et al.* 1984). The previous MHD studies did not take into account radiation and heat conduction, even though these are important energy dissipation mechanisms in coronal loops. Most of the previous studies of thermal stability neglected magnetic field effects other than heat conduction and mass motion along magnetic field lines. Since radiation as well as magnetic fields plays a role in loop stability, it is important to include these effects in MHD as well as thermal stability studies. The effects of magnetic field on thermal stability were studied by Field (1965), Chiuderi and Van Hoven (1979), and Zweibel (1980) for plane-parallel atmospheres. Recently, An (1983, hereafter Paper I) studied the effect of radiative energy loss on MHD stability of loops with cylindrical geometry. In Paper I, we found that radiation not only changes the growth rate, but also alters the stability boundary predicted by ideal MHD theory. We also found that a cool-core loop (Foukal 1975) with a positive pressure gradient, which is stable for ideal MHD interchange modes, can be unstable because of radiation. This result supported the claim by Foukal (1976) that mass flowing down along the cool

core is supplied from surrounding plasma by MHD instabilities.

This study is a continuation of Paper I and includes the effect of plasma compression. Since Paper I did not consider compressibility, magnetosonic and condensation modes were excluded. Noting that compressibility is an expected characteristic of coronal loop plasma, we believe that compressibility will have a significant effect of radiative MHD stability.

This paper is organized as follows. In § II, we describe the basic equations and derive a second-order ordinary differential equation. The effects of compression on localized ideal MHD modes is considered in § III, and the effects of radiative energy loss on the modes are studied in § IV. The conclusion is given in § V.

II. GOVERNING EQUATIONS

In this section we will derive a differential equation for stability of a coronal loop with the following configurations:

1. The loop is assumed to be a circular cylinder with uniform temperature, density, and magnetic field along the loop direction. We will consider only radial dependence of these equilibrium variables.

2. Plasma is confined by a nonpotential magnetic field generated by plasma current. Therefore, magnetic field lines are helically twisted along the loop.

3. We neglect the perpendicular heat conduction. In this case, radiative energy loss is balanced by ambient heating for a loop in a steady state.

Before perturbation, a coronal loop in a steady state is governed by the equations below.

$$\nabla P_0 - \mathbf{J} \times \mathbf{B}_0 = 0, \quad (1)$$

$$\nabla \times \mathbf{B}_0 = \mathbf{J}_0, \quad (2)$$

$$H(\rho, T) - R(\rho, T) = 0 \quad (3)$$

Here, P_0 , J_0 , B_0 are equilibrium pressure, current density, and magnetic field; $H(\rho, T)$ and $R(\rho, T)$ are ambient heating and radiative energy loss function, respectively. Because T has only radial dependence, the contribution of conduction to energy balance is zero.

The linearized dimensionless equations are

$$\frac{\rho_0 \partial v}{\partial t} = -\beta \nabla P_1 + J_0 \times B_1 + J_1 \times B_0, \quad (4)$$

$$\frac{\partial P_1}{\partial t} = -\gamma P_0 \nabla \cdot v - v \cdot \nabla P_0 - \epsilon(\gamma - 1) \left[\frac{3}{2} \left(\frac{\partial R}{\partial T} \right)_\rho T_1 + \frac{3}{2} \left(\frac{\partial R}{\partial \rho} \right)_r \rho_1 + (k \cdot B_0)^2 \frac{K_0}{B_0^2} \frac{t_r}{t_c} (T_1 + T_0 \xi_r) \right], \quad (5)$$

$$J_1 = \nabla \times B_1, \quad (6)$$

$$B_1 = \nabla \times (\xi \times B_0), \quad (7)$$

$$\rho_1 = -\xi \cdot \nabla \rho_0 - \rho_0 \nabla \cdot \xi, \quad (8)$$

$$P_1 = T_1 \rho_0 - T_0 \rho_1. \quad (9)$$

Here P_0 , ρ_0 , T_0 , and B_0 are scaled by standard values of coronal pressure, density, temperature, and magnetic field; and t_0 is scaled by the MHD time scale, $t_0^2 = \rho_0 a^2 / B_0^2$ (a is the radius of a loop). The radiative time scale is $t_r = 3P_0 / 2R$; the conductive time scale is $t_c = a^2 P_0 / k_0 T_0^2$; ϵ is the ratio of MHD and radiative time scales, $\epsilon = (t_0 / t_r)$; and β is the ratio of plasma and magnetic pressure, $\beta = P_0 / B_0^2$; ξ is a displacement vector ($\partial \xi / \partial t = v$); $K_0 = k_0 T_0^2$ is the coefficient of heat conduction parallel to the magnetic field; γ is the specific heat constant; k is the wave vector; and $k \cdot B_0 = k B_{0z} + m r B_{0\theta}$, where k and m are longitudinal and poloidal wavenumbers. In equation (5) we assume that the ambient heating function is not perturbed. In this study, we assume $\nabla \cdot \xi \neq 0$; i.e., plasma is compressible.

A perturbed quantity is expressed as

$$J_1(r, t) = f_1(r) e^{i(m\theta - k z) + \omega t}.$$

Using equations (5), (8), and (9) we can express the perturbed pressure P_1 as

$$P_1 = -(\gamma P_0 \nabla \cdot \xi + P_0 \xi_r) + \epsilon \nabla \cdot \xi \left(\frac{\theta P_0 - \phi \rho_0}{\omega + \epsilon \theta} \right) + \epsilon \xi_r \left[\frac{\theta P_0 - \phi \rho_0 - (k \cdot B_0)^2 (T_0^2 / B_0^2) T_0 (t_r / t_c) (\gamma - 1)}{\omega + \epsilon \theta} \right], \quad (10)$$

Here

$$\theta = (\gamma - 1) \left[\frac{3}{2} \left(\frac{\partial R}{\partial T} \right)_\rho + (k \cdot B_0)^2 \left(\frac{T_0^2}{B_0^2} \right) \frac{t_r}{t_c} \right] \rho_0, \quad (11)$$

$$\phi = T_0 (\gamma - 1) \left[\frac{3}{2} \left(\frac{\partial R}{\partial T} \right)_\rho + (k \cdot B_0)^2 \left(\frac{T_0^2}{B_0^2} \right) \frac{t_r}{t_c} \right] \rho_0.$$

The compression term, $\nabla \cdot \xi$, can be derived using equations (4), (7), and (10).

$$\nabla \cdot \xi = \rho_0 \omega^2 \left[\frac{X F}{r} - X \left(\frac{2k B_{0\theta}}{r^3} \right) (m B_{0z} - k r B_{0r}) \right] \bar{D} - \epsilon (m^2 + k^2 r^2) F \times \left[\phi \rho_0 + (\gamma - 1) \frac{t_r}{t_c} (k \cdot B_0)^2 \frac{T_0^2}{B_0^2} T_0 - \theta P_0 \right] X / r^3 \bar{D} (\omega + \epsilon \theta). \quad (12)$$

Here

$$F = \rho_0 \omega^2 + (k \cdot B_0)^2,$$

$$D = \rho_0 \omega^2 \left[\rho_0 \omega^2 + B_0^2 \left(\frac{m^2}{r^2} - k^2 \right) \right] + \left(\frac{m^2}{r^2} - k^2 \right) \beta P_0 F,$$

$$D_0 = \frac{\beta (\omega \rho_0 - \gamma P_0 \theta) (m^2 r^2 - k^2) F}{\omega - \epsilon \theta},$$

$$\bar{D} = D - D_0. \quad (13)$$

P_0 is the derivative of P_0 with r , ξ_r is the radial component of ξ , $X = r \xi_r$. Using equations (4), (7), (10), and (12), we can derive a second-order differential equation for the study.

$$(Q_1 X Y + (Q_2 - Q_1) X + (G_1 X Y + G_2 X - G_3 X')) = 0. \quad (14)$$

Here

$$Q_1 = F [\rho_0 \omega^2 (\beta P_0 - B_0^2) + \beta P_0 (k \cdot B_0)^2] r D,$$

$$Q_2 = -2 B_{0\theta} \left[\frac{m (k \cdot B_0) (\beta P_0 F + \rho_0 \omega^2 B_0^2)}{r^2} - \frac{B_{0\theta} (\rho_0 \omega^2)^2}{r} \right] r D,$$

$$Q_3 = -\frac{1}{r} F - 2 B_{0\theta} \left(\frac{B_{0\theta}}{r} \right) - \frac{4 k^2 B_{0\theta}^2 [\rho_0 \omega^2 B_0^2 - \beta P_0 (k \cdot B_0)^2]}{r^2 \bar{D}},$$

$$G_0 = \phi \rho_0 + (\gamma - 1) \frac{t_r}{t_c} (k \cdot B_0)^2 \frac{T_0^2}{B_0^2} T_0 - \theta P_0 - \frac{2 k B_{0\theta} \rho_0 \omega^2 (m B_{0z} - k r B_{0\theta}) (\phi \rho_0 - \gamma P_0 \theta)}{r^2 \bar{D}},$$

$$G_1 = \beta (\rho_0 \omega^2)^2 F (\phi \rho_0 - \gamma P_0 \theta) / (\omega + \epsilon \theta) r \bar{D},$$

$$G_2 = \frac{G_0 \beta \rho_0 \omega^2 2 k B_{0\theta} (m B_{0z} r - k B_{0\theta})}{r^2 \bar{D} (\omega + \epsilon \theta)} + \left[\frac{\beta \rho_0 \omega^2 F C}{r \bar{D} (\omega + \epsilon \theta)} \right],$$

$$G_3 = \frac{\beta F [\phi \rho_0 + (\gamma - 1) (t_r / t_c) (k \cdot B_0)^2 (T_0^2 / B_0^2) T_0 - \theta P_0]}{r \bar{D} (\omega + \epsilon \theta)}.$$

Equation (14) consists of two parts, an ideal MHD part (first three terms) and an energy dissipation part (last three terms). The ideal MHD limit (zeroth-order solution) is $\epsilon = 0$; we know that $\epsilon \ll 1$ for coronal loop conditions. As in Paper I, we will study the effect of radiative energy loss, as higher order solutions, on localized interchange modes.

III. THE EFFECT OF COMPRESSIBILITY ON IDEAL MHD LOCAL MODES

We will derive a stability condition for local ideal MHD modes of compressible plasmas as a zeroth-order solution of equation (14). Since radiation effects appear in high-order solutions, and the solutions depend on the zeroth-order solution (see eqs. [23] and [27]), a detailed study of the zeroth-order solution is necessary to understand the radiation effects. The stability condition for local modes, the Suydam condition (Suydam 1958), is derived from marginal stability analysis by excluding the compressibility of plasmas (Newcomb 1960) in minimizing the energy equation (Bernstein *et al.* 1958). The effect of compressibility on ideal MHD modes was studied by Ware (1964) with assumptions that the magnetic shear is negligibly little and $|x'/x| \ll k$. Since he considered various modes ($m \geq 1$), his stability condition is not a Suydam-type local stability condition. By taking the limit as $m \rightarrow \infty$ with kB_z/mB_r fixed, we derive a local stability condition, the Suydam condition for compressible plasmas. A noble aspect of our result over that of Ware (1964) is that our derivation is based strictly on the localization of eigenfunctions near singular surfaces as $m \rightarrow \infty$ (Paper I) rather than any approximations.

Before deriving the stability condition, let us consider how the compression term, $\nabla \cdot \xi$, behaves near and far from a singular surface.

According to equation (12) with $\epsilon = 0$, the compression term, $\nabla \cdot \xi$, is proportional to ω^2 . Therefore, we tend to believe that there is no distinction between compressible and incompressible plasmas for marginal stability because $\nabla \cdot \xi = 0$ for $\omega^2 = 0$. However, we notice that the behavior of $\nabla \cdot \xi$ is different at a mode rational surface r_s when compared with its behavior far from the surface as $\omega^2 \rightarrow 0$. Let us consider the compression term $\nabla \cdot \xi$ at r_s and at a region far from r_s using the explicit expression

$$\begin{aligned} \nabla \cdot \xi &= E_1 \cdot E_2, \\ E_1 &= \rho_0 \omega^2 \left[F \frac{1}{r} (r_s^2 y) - 2kB_{0\theta} \left(\frac{mB_{0z}}{r} - B_{0\theta} \right) \frac{z}{r} \right], \\ E_2 &= \rho_0 \omega^2 \left[\rho_0 \omega^2 + \left(\frac{m^2}{r^2} + k^2 \right) (\beta_i P_0 + B_0^2) \right. \\ &\quad \left. + \left(\frac{m^2}{r^2} + k^2 \right) \beta_i P_0 (k \cdot B_0)^2 \right]. \end{aligned} \quad (15)$$

For $\omega^2 = 0$, $\nabla \cdot \xi = 0$, where $k \cdot B_0 \neq 0$, but $\nabla \cdot \xi$ is not defined at r_s , where $k \cdot B_0 = 0$. If we take a limit as $\omega^2 \rightarrow 0$, $\nabla \cdot \xi$ becomes

$$\nabla \cdot \xi = - \frac{2kB_{0\theta}(mB_{0z} r - kB_{0\theta}) \xi_r}{r(m^2 r^2 + k^2)(\beta_i P_0 + B_0^2)} \quad (16)$$

at r_s . On the other hand, $\nabla \cdot \xi$ becomes zero at $k \cdot B \neq 0$. Equation (16) has two implications. The first is that marginal stability analysis cannot study the effect of compressibility by letting $\omega^2 = 0$ from the beginning. The second is that the effect of compressibility is especially important near the mode rational surface, r_s . From equation (16) we expect that compressibility significantly affects the stability of localized modes.

As found in Paper I, X is zero far from r_s but satisfies the following differential equation near r_s as $m \rightarrow \infty$:

$$[f(r, \omega)X'] - g(r, \omega)X = 0, \quad (17)$$

where

$$\begin{aligned} f(r, \omega) &= \frac{r\rho_0\omega^2}{m^2 A_1} + \frac{(nB_{0\theta} q' m)^2 (r - r_s)^2}{r A_1}, \\ g(r, \omega) &= 2 \left[\frac{B_{0\theta}^2 (1 + nq'm)}{r^2 A_1} \right]' + \frac{A_2}{r}, \\ A_1 &= 1 + (nq'B_{0\theta} m B_{0z})^2, \\ A_2 &= \rho_0 \omega^2 - 2B_{0\theta} \left(\frac{B_{0\theta}}{r} \right)' - \frac{4B_{0\theta}^2}{r^2 B_0^2} + \frac{4B_{0\theta}^2 \beta_i P_0}{r^2 B_0^2 (B_0^2 + \beta_i P_0)}. \end{aligned}$$

After multiplying equation (17) by X and integrating by parts, we can derive the stability condition for localized modes of compressible plasma:

$$\frac{r^2 (q - q')^2}{4} + \frac{2r\beta_i P_0}{B_0^2} + \frac{4B_{0\theta}^2 \beta_i P_0}{B_0^2 (B_0^2 + \beta_i P_0)} > 0. \quad (18)$$

Here $q = krB_{0z} mB_{0\theta}$, and n is the wavenumber in the longitudinal direction. When we derive equation (18), we neglect a term which is proportional to $1/m^2$ as the term goes to zero for $m \rightarrow \infty$. Unlike the Suydam stability criterion (Suydam 1958), equation (18) has an additional stabilizing term, $4B_{0\theta}^2 \beta_i P_0 / [B_0^2 (B_0^2 + \beta_i P_0)]$. We can easily find out the origin of the term by taking a limit as $m \rightarrow \infty$ in equation (16). As $m \rightarrow \infty$, $\nabla \cdot \xi$ becomes

$$\nabla \cdot \xi = 2B_{0\theta}^2 \xi_r [r(\beta_i P_0 + B_0^2)]. \quad (19)$$

Noting that the compression term in equation (5) has $\beta_i P_0$, we can understand that the additional stabilizing term is due to compressibility. Since $\nabla \cdot \xi$ is proportional to ξ_r , $\nabla \cdot \xi$ is finite at r_s but smoothly goes to zero at a region far from r_s . Equation (18) shows that even when there is no shear (i.e., $q' = 0$), the local mode can be stabilized.

IV. LOCAL MODES OF COMPRESSIBLE PLASMA WITH RADIATION

Field (1965) found two modes, magnetosonic and condensation, with wave vector perpendicular to the magnetic field. Since these two modes appear only for compressible plasma, the stability condition for compressible plasma will be different from that derived in Paper I for incompressible plasma.

The stability condition for local modes of compressible plasma can be obtained by studying higher order solutions of equation (14), after taking the limit as $m \rightarrow \infty$, with the same method used in Paper I: multiply equation (14) by X^* (complex conjugate of X) and integrate by parts. After using the relation (Paper I)

$$\int |s^2| dX |ds|^2 ds \geq \frac{1}{2} \int |X|^2 ds$$

and neglecting a term with $1/m^2$, we have

$$\rho_0 \bar{P} \omega^3 r + \epsilon \rho_0 \bar{Q} \omega^2 r + Y \bar{P} \omega + \epsilon (Y \bar{Q} + W) = 0 \quad (20)$$

Here

$$\begin{aligned} \bar{P} &= \rho_0(C_m^2 - C_i^2), \\ \bar{Q} &= \frac{(\gamma - 1)C_i^2}{\gamma} \left[\left(\frac{C_m^2}{C_i^2} + 1 \right) \left(\frac{\partial R}{\partial T} \right)_r - \frac{\rho_0}{T_0} \left(\frac{\partial R}{\partial \rho} \right)_r \right], \\ W &= -\frac{\beta B_{0\theta}^2}{r^2} \left[\frac{4(\gamma - 1)^2 T_0 B_{0\theta}^2 \rho_0 C_m^2 (\partial R / \partial T)_r}{r B_0^2 \bar{P}} + 2(\gamma - 1) \frac{dR}{dr} \right], \\ Y &= \frac{B_{0z}^2 B_{0z}^2 (q^2 - q)}{4r B_0^2} + \frac{2B_{0\theta}^2 \beta P_0}{r^2 B_0^2} + \frac{4B_{0\theta}^2 \beta P_0}{r^3 B_0^2 (B_0^2 + \beta P_0)}. \end{aligned} \quad (21)$$

and

$$\begin{aligned} C_m^2 &= B_0^2 \rho_0, \quad C_i^2 = \beta P_0 \rho_0, \\ \left(\frac{\partial R}{\partial T} \right)_r &= \left(\frac{\partial R}{\partial T} \right)_r - \rho_0 \left(\frac{\partial R}{\partial \rho} \right)_r [T_0(\gamma - 1)]. \end{aligned}$$

The quantity \bar{Q} is proportional to the growth rate of the condensation mode whose wave vector is perpendicular to the magnetic field in a uniform atmosphere (Field 1965). The first term of W is proportional to the growth rate of the magnetosonic mode in a uniform medium (Field 1965), and the other is the same term dR/dr that appeared for incompressible plasma (An 1983). Since $\epsilon \ll 1$ for coronal loop conditions, we can obtain zeroth-, first-, and second-order solutions from equation (20) by expanding ω as

$$\omega = \omega^{(0)} + \epsilon \omega^{(1)} + \epsilon^2 \omega^{(2)} + \dots$$

a zeroth-order solution, $\omega^{(0)}$, is

$$\omega^{(0)2} = -rY\rho_0, \quad (22)$$

and the condition $\omega^{(0)2} < 0$ is a sufficient stability condition for localized modes of compressible plasma, i.e., equation (18).

The first-order solution, $\omega^{(1)}$, is, assuming $\omega^{(0)} \neq 0$,

$$\omega^{(1)} = -rW(2\bar{P}\rho_0\omega^{(0)2}). \quad (23)$$

From equation (23) we can understand how radiation affects the stability of compressible plasma. A difference of stability between incompressible and compressible plasmas is that stability of compressible plasma is affected by the magnetosonic mode as well as the sign of dR/dr . The effect of condensation modes does not appear in the first-order solution. For optically thin radiative energy loss function, $R \sim \rho^2 T^{-n}$, $(\partial R / \partial T)_r$ is positive because $n < 3$ (Hildner 1974). Since $(\partial R / \partial T)_r > 0$ for any temperature profile, the magnetosonic mode is a stabilizing effect for $\omega^{(0)2} < 0$ (i.e., ideal MHD stable) but a destabilizing effect for $\omega^{(0)2} > 0$.

Since $\epsilon \ll 1$ for coronal loop conditions, the radiation effect is insignificant except when the coronal loop is in an ideal MHD marginally stable state ($\omega^{(0)2} = 0$). For quiescent prominences, however, the radiation effect is important because $\epsilon \geq O(10^{-1})$. For example, for a quiescent prominence with $T = 10^4$ K, $n = 10^{16} \text{ m}^{-3}$, $a = 5 \times 10^3$ km, and $B_0 = 8$ gauss, ϵ is estimated as $\epsilon \sim O(10^{-1})$. If the quiescent prominence is ideally unstable ($\omega^{(0)2} > 0$), the radiation effect accelerates MHD instabilities. Since the condensation mode is a second-order effect in ϵ for $\omega^{(0)2} \neq 0$, it is an insignificant effect for the coronal loop condition, but it can be an important effect for quiescent prominences. The second-order solution will be derived later.

If plasmas are in an ideal MHD marginally stable state (i.e., $\omega^{(0)2} = 0$), the radiation effect can trigger MHD instabilities, which might lead to flares, or completely stabilize the instability depending on initial equilibrium. The radiation effect on ideally marginally stable plasma can be studied by letting $\omega^{(0)2} = 0$ (or $Y = 0$) in equation (20). The equation becomes

$$\rho_0 \bar{P} \omega^3 r + \epsilon \rho_0 \bar{Q} \omega^2 r + \epsilon W = 0. \quad (24)$$

The roots of this cubic equation are (Abramowitz and Stegun 1970)

$$\begin{aligned} z_1 &= (s_1 + s_2) - a_2/3, \\ z_2 &= -(s_1 + s_2)/2 - a_2/3 + i\sqrt{3}(s_1 - s_2)/2, \\ z_3 &= -(s_1 + s_2)/2 - a_2/3 - i\sqrt{3}(s_1 - s_2)/2. \end{aligned} \quad (25)$$

Here

$$\begin{aligned} s_1 &= [d - (q^3 - d^2)^{1/2}]^{1/3}, \quad s_2 = [d + (q^3 - d^2)^{1/2}]^{1/3}, \\ d &= -rW(2r\bar{P}) + (\bar{Q}r\bar{P})^2/27, \\ q &= -(\epsilon\bar{Q}r\bar{P})^2/9, \quad a_2 = \epsilon\bar{Q}r\bar{P}. \end{aligned} \quad (26)$$

A marginally stable equilibrium has $dP/dr < 0$ and $dR/dr > 0$ (see eq. [33] of Paper I). For coronal loop conditions (i.e., $T \sim 10^4$ K), $\bar{Q} < 0$, $W < 0$, which results in $d > 0$, $q < 0$, and $a_2 < 0$ in equation (26). Therefore, we can see that $z_1 > 0$. The sign of the real part of z_2 (or z_3) is not easily determined because the first and second terms of z_2 have different signs. We need numerical calculation to determine the signs for a given equilibrium. The solution shows that there is at least one unstable mode in coronal plasmas due to radiation if the plasma is in an ideally marginally stable state. The solution (see z_1 of eq. [25]) also shows that not only magnetosonic but also condensation modes destabilize coronal plasmas in an ideally marginally stable state. By comparison with the results of incompressible plasmas with $\omega^{(0)2} = 0$ (see eq. [27] of Paper I), we find that radiation has more of a destabilizing effect on compressible coronal plasmas. For plasmas of quiescent prominences with $\omega^{(0)2} = 0$, the radiation effect is not as obvious as for coronal plasmas because in quiescent prominences, condensation modes are stabilizing, while magnetosonic modes are destabilizing, effects.

The effects of condensation modes on MHD stability are different depending on ideal MHD stability; when $\omega^{(0)2} \neq 0$, condensation modes affect MHD stability only to second order in ϵ as

$$\omega^{(2)} = -3\omega^{(1)2} 2\omega^{(0)} - 2\omega^{(1)}\bar{Q}(2\bar{P}\omega^{(0)}), \quad (27)$$

while condensation modes are first-order effects for $\omega^{(0)2} = 0$.

The physical interpretation of the effect of radiation on compressible plasma is essentially the same as that in incompressible plasma mentioned in Paper I; i.e., including the compression term in equation (20), radiation affects the perturbed pressure P_1 and then affects the stability of localized modes.

5. CONCLUSION

We have studied the effect of radiation on the local stability of compressible plasma. We have found that compressibility is not important far from a mode rational surface

$r_s(kr_s B_z + mB_\theta = 0)$ but is important near it. We have pointed out that the Suydam stability criterion (Suydam 1958) derived from marginal stability analysis excludes the effects of compressibility by letting $\omega^2 = 0$ (so $\nabla \cdot \xi = 0$) from the beginning. Careful study of the compression term $\nabla \cdot \xi$ reveals that $\nabla \cdot \xi$ is not zero near a mode rational surface as ω^2 approaches zero. Compressibility has a stabilizing effect on ideal MHD local modes because compression of magnetic field lines exerts a restoring force by increasing magnetic pressure. The compressibility induces magnetosonic and condensation modes in a radiatively unstable medium.

If the plasma is in an ideal MHD stable (or unstable) state, the effect of condensation modes on the localized MHD instability is insignificant. However, if the plasma is in an ideally marginally stable state, condensation as well as magnetosonic modes leads to MHD instabilities. Because of these two modes, the effect of radiation on compressible coronal plasma is more destabilizing than on incompressible coronal plasmas for $\omega^{(0)2} \geq 0$. The effect of radiation on MHD stability of solar filaments will be significant because the radiative time scale is nearly the same as the MHD time scale for filament conditions. The results suggest that thermal instabilities might be a triggering mechanism for global MHD instabilities (Harvey 1981; Davis and Webb 1981).

We have studied radiation effects on localized interchange modes in cylindrical plasmas. How does the radiation affect global modes? Any quantitative answer to this question is certainly out of the scope of this paper. However, we can consider two important effects of global modes. First, heat conduction plays a stabilizing role on the global modes. For the local modes, heat conduction does not play any role because heat conduction affects the stability through the term $(\mathbf{k} \cdot \mathbf{B}_0)^2$ (see ψ or ϕ in eq. [11]), which is zero at a mode rational surface, r_s , where the modes are localized. Since global modes are distributed over regions beyond the mode rational surface,

where $\mathbf{k} \cdot \mathbf{B}_0 \neq 0$, heat conduction can be a stabilizing mechanism. The other effect of global modes is that plasma current density can be enhanced in a condensed region. For (ideal MHD) marginally stable plasmas, as thermal instability develops, condensation modes squeeze the plasmas, resulting in enhancement of plasma current density. As plasma current density increases, the plasma can change its state from marginally stable to unstable. We do not know how the two competing effects actually influence the global MHD modes until we solve equation (14) numerically.

Stability for ideal MHD local modes in toroidal plasmas was studied by Mercier (1960) and Greene and Johnson (1962), and the physical meaning of the stability condition is discussed by Shafranov and Yurchenko (1968). While an ideal MHD local stability condition for toroidal plasma can be derived using the energy principle (Bernstein *et al.* 1958), we cannot use the method for local modes of radiative MHD. We can postulate how toroidal effects alter stability by considering equation (11). From this equation we can see that the radiation term depends on local density, temperature, and magnetic field. On the other hand, the heat conduction term depends on the magnitude of $(\mathbf{k} \cdot \mathbf{B}_0)^2$ as well as local plasma quantities. Noting that toroidal plasmas do not have mode rational surfaces for a given longitudinal mode, the heat conduction term may be affected strongly.

For better understanding of the radiation effect on MHD stability of coronal loops, we have to extend our effort to global modes and include toroidicity in the calculations.

The author thanks Dr. R. C. Canfield for his valuable discussions and comments during the course of this work. This work was supported by the Air Force Office of Scientific Research, Air Force Systems Command, USAF, under grant AFOSR 82-0092, and by NASA under grant NSG-7406.

REFERENCES

- Abramowitz, M., and Stegun, I. A. (eds.) 1970, *Handbook of Mathematical Functions* (New York: Dover), p. 17.
 An, C.-H. 1982, *Solar Phys.* **75**, 19.
 ——— 1983, *Ap J.* **264**, 302 (Paper I).
 An, C. H., Canfield, R. C., Fisher, G. H., and McClymont, A. N. 1983, *Ap J.* **267**, 421.
 Antiochos, S. K. 1979, *Ap J. (Letters)*, **232**, L125.
 Antiochos, S. K., Emslie, E. G., Shoub, E. C., and An, C.-H. 1984, *Ap J.* submitted.
 Bernstein, I. B., Frieman, E. A., Kruskal, M. D., and Kulsrud, R. M. 1958, *Proc. Roy. Soc. London*, **4**, 244, 17.
 Chiuderi, C., Einaudi, G., and Torricelli-Ciamponi, G. 1981, *Astr. Ap.* **97**, 27.
 Chiuderi, C., and Van Hoven, G. 1979, *Ap J. (Letters)*, **232**, L69.
 Davis, J. M., and Webb, D. F. 1981, *Bull.* **445**, 13, 821.
 Einaudi, G., and Van Hoven, G. 1981, *Phys. Fluids*, **24**, 1032.
 Field, G. B. 1965, *Ap J.* **142**, 531.
 Foukal, P. V. 1975, *Solar Phys.* **43**, 327.
 Foukal, P. V. 1976, *Ap J.* **210**, 575.
 Giachetti, R., Van Hoven, G., and Chiuderi, C. 1977, *Solar Phys.* **55**, 371.
 Greene, J. M., and Johnson, J. L. 1962, *Phys. Fluids*, **5**, 510.
 Harvey, K. L. 1981, *Bull.* **445**, 13, 890.
 Hildner, E. 1974, *Solar Phys.* **35**, 123.
 Hood, A. W., and Priest, E. R. 1979, *Solar Phys.* **64**, 303.
 ——— 1980, *Astr. Ap.* **87**, 126.
 McClymont, A. N., and Canfield, R. C. 1983, *Ap J.* **265**, 497.
 Mercier, C. 1960, *Nucl. Fusion*, **1**, 47.
 Newcomb, W. A. 1960, *Ann. Phys.* **10**, 232.
 Raadu, M. A. 1972, *Solar Phys.* **22**, 425.
 Shafranov, V. D., and Yurchenko, E. I. 1968, *Sov. Phys.—JETP*, **26**, 682.
 Suydam, B. R. 1958, *I.A.E.A. Geneva Conference*, **31**, 157-159.
 Van Hoven, G., Chiuderi, C., and Giachetti, R. 1977, *Ap J.* **213**, 869.
 Ware, A. A. 1964, *Phys. Rev. Letters*, **12**, 439.
 Zweibel, E. 1980, *Solar Phys.* **66**, 305.

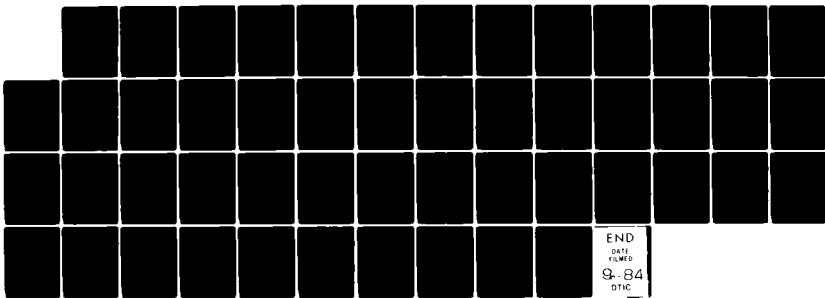
AD-A145 009

STUDIES OF SOLAR FLARES AND CORONAL LOOPS(U) CALIFORNIA
UNIV SAN DIEGO LA JOLLA CENTER FOR ASTROPHYSICS AND
SPACE SCIENCES R C CANFIELD 10 JUL 84 UCSD-SP-84-21
AFOSR-TR-84-0719 AFOSR-82-0092 F/G 3/2

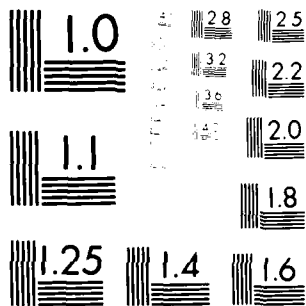
33

NL

UNCLASSIFIED



END
DATE
FILMED
9-84
DTIC



MICROCOPY RESOLUTION TEST CHART
NATIONAL BUREAU OF STANDARDS-1963-A

CONDENSATION MODES IN MAGNETIZED CYLINDRICAL PLASMAS

CHANG-HYUK AN

Center for Astrophysics and Space Sciences, University of California, San Diego

Received 1983 February 11, accepted 1983 July 5

ABSTRACT

We have studied condensation modes of the thermal instability in a cylindrical plasma to understand the formation and stability of solar prominences.

The magnetic field in the cylinder has both potential (longitudinal) and nonpotential (poloidal) components which form helically twisted field lines. We find that the twist of field lines has a significant effect on the stability of condensation modes; these modes are unstable if field lines are nearly straight but become stable as the twist increases. This trend is opposite to that of the ideal magnetohydrodynamic (MHD) modes, which become more stable as the twist decreases. Stability is also strongly affected by magnetic field strength and loop aspect ratio. In a strong magnetic field region, condensation modes are stabilized at a low field line twist. On the other hand, in a weak magnetic region, higher twist is needed for stability. A loop with higher aspect ratio needs higher twist for thermal stability. From the results, we can understand why prominences have long-lived global structures.

We have treated the problem in a fully self-consistent way to derive a second-order ordinary differential equation for radiative magnetohydrodynamic stability. Because the differential equation is not Hermitian, a complete solution has not been attempted. We have made an approximation, by neglecting inertial terms, which is valid for coronal loop conditions and if there is no singular surface in the plasma, and we have derived a simplified differential equation. We have studied stability for the $m = 0, 1,$ and 2 modes numerically for various loop parameters.

Subject headings: hydrodynamics — Sun: corona — Sun: prominences

I. INTRODUCTION

Previous hydrodynamic studies of thermal stability of loops (Antiochos 1979; Habbal and Rosner 1979; Hood and Priest 1980; Chiuderi, Einaudi, and Torricelli-Ciamponi 1981; Craig and McClymont 1981; McClymont and Craig 1981a, b, c; Antiochos *et al.* 1984) neglected MHD effects. It was found that stability can be obtained if thermally stable chromospheric material is included (Craig and McClymont 1981; Peres *et al.* 1982) and if the ambient heating function satisfies certain conditions (McClymont and Craig 1981c). The stabilizing mechanism in the hydrodynamic model is heat conduction parallel to field lines. Since these studies neglect plasma motion perpendicular to magnetic field lines and examine the thermal stability of single field lines, potentially important MHD effects remain to be studied and understood.

The effect of a magnetic field on thermal stability was studied by Field (1965), Nakagawa (1970), and Zweibel (1980) for uniform magnetic field configurations in plane-parallel geometry. Chiuderi and Van Hoven (1979) extended the work of the above authors by considering the effect of magnetic shears in plane-parallel geometry. Noting that observations of active region filaments and prominences (Smith and Smith 1963; Zirin 1966; Gibson 1973; Rust 1972) have shown that they consist of many small-scale individual loops, the stability of cylindrical plasmas should be studied to understand various phenomena of prominences. Since the magnetic field configuration of coronal loops is basically different from that of uniform atmosphere, it is expected that the stability of cylindrical loops will be significantly different from that of plane-parallel plasmas. Recently, cylindrical geometry was

studied by An (1983, 1984) to understand the effects of radiative energy loss on the MHD stability of incompressible and compressible plasmas.

In this paper, we study the effects of magnetic field on condensation modes of a cylinder to answer the following questions. Is the thermal stability of loops in hydrodynamic approaches altered by including the plasma motion perpendicular to field lines? How does the magnetic field affect the condensation modes in loops? Can we understand the formation and stability of prominences with the cylindrical models?

We will present detailed explanations of how a helically twisted magnetic field affects thermal stability, and we will apply the results to prominences in order to understand their formation and stability.

This paper is organized as follows. In § II we present governing equations for radiative magnetohydrodynamic (RMHD) study, and in § III we obtain a model equilibrium. We linearize the governing equations and derive a differential equation for RMHD stability in § IV and study the stability of condensation modes in § V. We discuss the formation and stability of prominences in § VI.

II. GOVERNING EQUATIONS

We make several assumptions for this study: Coronal plasma is compressible and is confined in a rigid straight circular cylinder. Physical quantities are uniform along the loop direction, having only radial variations. The loop has nonpotential as well as potential magnetic field; i.e., field

lines are helically twisted. Heat conduction perpendicular to magnetic field lines is neglected.

We assume plasmas are governed by the following equations:

$$\rho \hat{c} v \hat{c} t - \nabla P - \mathbf{J} \times \mathbf{B} = 0, \quad (1)$$

$$dP/dt = \rho \nabla \cdot \mathbf{v} - (\gamma - 1)$$

$$\times [H - R(\rho, T) + \nabla \cdot \kappa_{\parallel} \mathbf{e}_b \mathbf{e}_b \cdot \nabla T] = 0, \quad (2)$$

$$\hat{c} \rho \hat{c} t + \nabla \cdot (\rho \mathbf{v}) = 0, \quad (3)$$

$$\nabla \times \mathbf{B} - \mathbf{J} = 0, \quad (4)$$

$$\hat{c} \mathbf{B} \hat{c} t + \nabla \times \mathbf{E} = 0, \quad (5)$$

$$\mathbf{E} + \mathbf{v} \times \mathbf{B} = 0, \quad (6)$$

$$P = K \rho T. \quad (7)$$

Here ρ , P , and T are plasma density, pressure, and temperature, and \mathbf{B} , \mathbf{J} , and \mathbf{E} are magnetic field, plasma current density, and electric field; H and $R(\rho, T)$ are ambient heating and radiative energy loss functions; κ_{\parallel} is the heat conductivity parallel to the magnetic field, defined as $\kappa_{\parallel} = k_{\parallel} T^{5/2}$, and k_{\parallel} is a heat conduction constant (Spitzer 1962); $\mathbf{e}_b = \mathbf{B}/|\mathbf{B}|$ is a unit vector parallel to the local magnetic field; γ is the specific heat constant, and K is a gas constant.

III. EQUILIBRIUM OF CYLINDRICAL PLASMA

Before perturbation, a coronal loop is assumed to be governed by the steady state equations below.

$$\beta \nabla P_0 - \mathbf{J}_0 \times \mathbf{B}_0 = 0, \quad (8)$$

$$\nabla \times \mathbf{B}_0 = \mathbf{J}_0, \quad (9)$$

$$H - R(\rho, T) = 0. \quad (10)$$

Here P_0 , \mathbf{J}_0 , \mathbf{B}_0 , ρ , and T are dimensionless equilibrium pressure, current density, magnetic field, plasma density, and temperature scaled by standard coronal values. The quantities H and $R(\rho, T)$ are dimensionless ambient heating and radiative energy loss functions, respectively. Because T has only radial dependence, there is no contribution of heat conduction to the energy equation (eq. [10]). The quantity β is the ratio of plasma to magnetic pressure at the surface of the cylinder, $\beta = P_0/B_0^2$.

We can calculate equilibrium quantities by solving equations (8)-(10). However, since we do not know the functional form of the ambient heating rate H , complete solutions of equilibrium equations are not possible. We solve equations (8) and (9) with a specified plasma current density to obtain plasma pressure $P_0(r)$. In order to calculate the ambient heating rate H , which satisfies steady state energy equation (10), we have to specify $\rho = \rho(r)$. The heating rate calculated from equation (10) with a specified $\rho(r)$ is not a function of ρ and T but a function of r . If we know the functional form of $H = H(\rho, T)$, $\rho(r)$ can be obtained by solving equation (10). We assume that longitudinal current density, longitudinal magnetic field, and plasma density are uniform. Since such profiles produce uniform twisting of field lines, we can simplify the analysis. The justification of uniform plasma density can be found in Foukal (1975), where he found that variation of plasma density along the radial direction is insignificant

compared with the variation of temperature or plasma pressure.

The equilibrium quantities are as follows:

$$B_{0z} = 1, \quad B_{0\theta} = r B_a, \quad P_0 = B_a^2 (1 - r^2) \beta + 1, \quad (11)$$

$$q = -2\pi r B_{0z} L B_{0\theta}, \quad B_a = -2\pi q A.$$

Here A is the aspect ratio, $A = L/a$ (a is a radius of the cylinder cross section). The quantity q stands for the twist of magnetic field lines: $q \gg 1$ means that field lines are nearly straight lines, and $q \ll 1$ implies that field lines are highly twisted. We assume that the radiative energy loss function R is $R = \rho_0^2 T^{-1}$. Coronal temperature, pressure, and loop length are obtained by solving the hydrostatic energy equation. The standard equilibrium studied in this paper has coronal temperature of $T_0 = 2.3 \times 10^6$ K, density $n_0 = 4.4 \times 10^9 \text{ cm}^{-3}$, and length $L = 1.7 \times 10^9$ cm.

IV. LINEARIZED EQUATIONS FOR STABILITY

After giving a linear perturbation, we obtain linearized dimensionless MHD equations:

$$\epsilon \rho_0 \hat{c} v \hat{c} t = -\beta \nabla P_1 - \mathbf{J}_0 \times \mathbf{B}_1 + \mathbf{J}_1 \times \mathbf{B}_0, \quad (12)$$

$$\frac{\hat{c} P_1}{\hat{c} t} = -\gamma P_0 \nabla \cdot \mathbf{v} - (\gamma - 1) \left[\frac{3}{2} \left(\frac{\hat{c} R}{\hat{c} T} \right)_0 T_1 + \frac{3}{2} \left(\frac{\hat{c} R}{\hat{c} \rho} \right)_0 \rho_1 - \frac{t_r}{t_c} \frac{T_1 (k \cdot \mathbf{B}_0)^2 \kappa}{B_0^2} - \frac{t_r}{t_c} \frac{(k \cdot \mathbf{B}_0)^2 \kappa}{B_0^2} T_0 \frac{\hat{c} r}{\hat{c} t} \right] - \mathbf{v} \cdot \nabla P_0, \quad (13)$$

$$\mathbf{J}_1 = \nabla \times \mathbf{B}_1, \quad (14)$$

$$\mathbf{B}_1 = \nabla \times (\xi \times \mathbf{B}_0), \quad (15)$$

$$\rho_1 = -\xi \cdot \nabla \rho_0 - \rho_0 \nabla \cdot \xi, \quad (16)$$

$$P_1 = T_1 \rho_0 + T_0 \rho_1. \quad (17)$$

Here ξ is a plasma displacement vector. $\hat{c} \xi, \hat{c} t = v$; t is scaled by the radiative time scale, $t_r = 3P_0/2R$, in order to study the effect of magnetic field on slow condensation modes. The MHD time scale is $t_M^2 = \rho_0 a^2/B_0^2$, the conductive time scale is $t_c = L^2 P_0/k_0 T_0^2$, and ϵ is the ratio of MHD to radiative time scales, $\epsilon = t_M^2/t_c^2$. In order to define the conductive time scale t_c , we use the expression $k_0 T_0^{5/2}$ for parallel heat conductivity, κ_{\parallel} ; L is a loop length, and k_0 is a heat conduction constant. For derivation of the linearized equation, we assume that the ambient heating rate H is not disturbed by perturbations, because we do not know the functional form of the ambient heating function (Chiuderi and Van Hoven 1979).

If we express a perturbed quantity $f_1(r, t)$ as

$$f_1(r, t) = f_1(r) e^{i(m\theta + kz) e^{i\omega t}},$$

we can derive a second-order differential equation for radiative magnetohydrodynamic (RMHD) stability of compressible plasmas (for a detailed derivation, see An 1984).

$$(Q_1 X') + (Q_2 + Q_3)X + [(G_1 X') + G_2 X + G_3 X] = 0, \quad (18)$$

Here $X = r\zeta_r$, and ζ_r is a radial component of ζ . The coefficients of the differential equation are defined as follows:

$$\begin{aligned}
 Q_1 &= F[\epsilon\rho_0\omega^2(\beta; P_0 + B_0^2) - \beta; P_0(k \cdot B_0)^2] rD, \\
 Q_2 &= -2B_{0\theta} \left[\frac{m(k \cdot B_0)(\beta; P_0 F + \epsilon\rho_0\omega^2 B_0^2)}{r^2} + \frac{B_{0\theta}(\epsilon\rho_0\omega^2)^2}{r} \right] rD, \\
 Q_3 &= - \left[F - 2B_{0\theta} \left(\frac{B_{0\theta}}{r} \right) - \frac{4k^2 B_{0\theta}^2 [\epsilon\rho_0\omega^2 B_0^2 + \beta; P_0(k \cdot B_0)^2]}{r^2 D} \right] r. \quad (19)
 \end{aligned}$$

$$\begin{aligned}
 G_1 &= \left[\phi\omega_0 - \frac{t_r(k \cdot B_0)^2}{t_c B_0^2} T_0^2 (\zeta - 1) T_0 - \theta P_0 \right] \\
 &\quad - \frac{2k B_{0\theta} \epsilon\rho_0\omega^2 (mB_{0z} - krB_{0\theta})(\phi\rho_0 - \zeta P_0 \theta)}{r^2 D}, \\
 G_2 &= \beta(\epsilon\rho_0\omega^2)^2 F(\phi\rho_0 - \zeta P_0 \theta) [(\omega - \theta)r\bar{D}D], \\
 G_3 &= \frac{\bar{G}[\beta(\epsilon\rho_0\omega^2)^2 2k B_{0z}(mB_{0z} - krB_{0\theta}) + \beta(\epsilon\rho_0\omega^2)^2 FG_3]}{r^2 \bar{D}(\omega - \theta)}, \\
 \bar{G}_3 &= \beta F \left[\phi\omega_0 - \frac{t_r(k \cdot B_0)^2}{t_c B_0^2} \right. \\
 &\quad \left. \times T_0^2 (\zeta - 1) T_0 - \theta P_0 \right] r\bar{D}(\omega - \theta). \quad (20)
 \end{aligned}$$

$$\begin{aligned}
 F &= \epsilon\rho_0\omega^2 + (k \cdot B_0)^2, \\
 \theta &= (\zeta - 1) \left[\frac{3}{2} \left(\frac{\bar{r}R}{\bar{c}T} \right)_\theta + (k \cdot B_0)^2 \left(\frac{T_0^2}{B_0^2} \right) \frac{t_r}{t_c} \right] \rho_0, \\
 \phi &= T_0 (\zeta - 1) \left[\frac{3}{2} \left(\frac{\bar{r}R}{\bar{c}T} \right)_\phi + (k \cdot B_0)^2 \left(\frac{T_0^2}{B_0^2} \right) \frac{t_r}{t_c} \right] \rho_0, \\
 D &= \epsilon\rho_0\omega^2 \left[\epsilon\rho_0\omega^2 + B_0^2 \left(\frac{m^2}{r^2} + k^2 \right) \right] + \left(\frac{m^2}{r^2} + k^2 \right) \beta; P_0 F, \\
 D_1 &= \frac{\beta(\phi\rho_0 - \zeta P_0 \theta)(m^2 r^2 + k^2) F}{\omega + \theta}, \\
 \bar{D} &= D + D_1. \quad (21)
 \end{aligned}$$

Note that the energy dissipation term due to radiation is expressed as $3(\partial R/\partial T)_\theta/2$ in θ and $3(\partial R/\partial T)_\phi/2$ in ϕ , and the term due to conduction is expressed as $(k \cdot B_0)^2 \times (T_0^2/B_0^2)(t_r/t_c)$ in θ and ϕ . In the equations, k is a wave vector, and $k \cdot B_0 = kB_{0z} + m rB_{0\theta}$, where k is a longitudinal component of k , and m is a poloidal wavenumber.

For coronal loop conditions, $\epsilon \ll 1$ ($\sim 10^{-8}$). Since other terms in equations (19) are on the order of 1, we can neglect terms which have $\epsilon\rho_0\omega^2$ unless instability growth time is much shorter than the radiative time scale. This approximation has been used by numerous authors for hydrodynamic study of thermal stability. For magnetized cylindrical plasmas, this approximation should be viewed with caution. For example,

let us consider Q_1 in equation (18). Even when $\epsilon\rho_0\omega^2 \ll 1$ is satisfied, we cannot neglect the term near a mode rational surface where $k \cdot B_0 = 0$ because the term with $\epsilon\rho_0\omega^2$ is not smaller than the term with $(k \cdot B_0)^2$ near the surface. In other words, the inertial term is important near the mode rational surfaces. In the following analysis, we neglect $\epsilon\rho_0\omega^2$ terms assuming that the instability growth time is of the same order as the radiative time scale and there are no mode rational surfaces in the plasma. If mode rational surfaces are in plasmas, the plasmas are subject to ideal MHD instabilities, whose time scale is so much shorter than radiative time scales that it is meaningless to consider the slow thermal modes.

If we neglect $\epsilon\rho_0\omega^2$ terms in equation (18), we have

$$\begin{aligned}
 \left(\frac{rX^2}{M} \right)' - X \left[\left(\frac{2mB_{0z}X}{rM} \right) + \frac{1}{r} \left[X^2 - 2B_{0\theta} \left(\frac{B_{0\theta}}{r} \right) - \frac{4k^2 B_{0z}^2}{M} \right] \right. \\
 \left. - \frac{Xr[(3/2)(\zeta - 1)(dR/dr)]}{M(\zeta P_0 \omega + \phi\rho_0)} \right] = 0. \quad (22)
 \end{aligned}$$

Here $X = k \cdot B_0$ and $M = k^2 r^2 + m^2$. We will solve equation (22) numerically to study $m = 0, 1$, and 2 condensation modes.

V. STABILITY

We solve equation (22) numerically for equilibrium calculated in § III. The differential equation is converted to a finite difference equation to find eigenvalues and eigenfunctions of a tridiagonal matrix using standard procedure (Potter 1973). The boundary condition $X = 0$ at $r = 0$ is obtained by solving equation (22) near $r = 0$, and the boundary condition $X = 0$ at $r = 1$ is determined by the assumption that the cylindrical plasma is surrounded by a rigid wall. A more realistic boundary condition at $r = 1$ will be considered in future work. Since equilibrium profiles are uniform along a longitudinal direction, periodic boundary conditions are given at both ends of the cylinder. The effect of finite loop length on stability appears through longitudinal wavenumber and aspect ratio. For a given aspect ratio, shorter longitudinal wavelength enhances conductive stabilizing effect over longer wavelength, and for the given wavelength, shorter aspect ratio induces higher conductive stabilizing effect (see θ and ϕ in eq. [22]).

For ideal MHD study, stability is determined by q , which measures the relative twist of field lines. We also find that stability of thermal modes strongly depends on the twist of field lines. Since the sign of ω_r (the real part of ω) indicates stability, the maximum values of ω_r versus q are plotted in the following figures. Note that $\omega_r > 0$ implies instability.

In Figure 1, we plot the maximum value of ω_r of the $m = 1$ mode versus q for various values of aspect ratio. The assumed magnetic field is 100 gauss and $\beta = 1.75 \times 10^{-3}$. First, the figure shows that stability of condensation modes is strikingly different from that of ideal MHD modes. The $m = 1$ ideal MHD mode becomes unstable as the twist of field lines exceeds a certain value which corresponds to $q < 1$ (Bateman 1978). The stability of condensation modes has the opposite tendency; i.e., they become unstable as the twist of field lines decreases. The result indicates that the $m = 1$ thermal mode is unstable at values of q where the

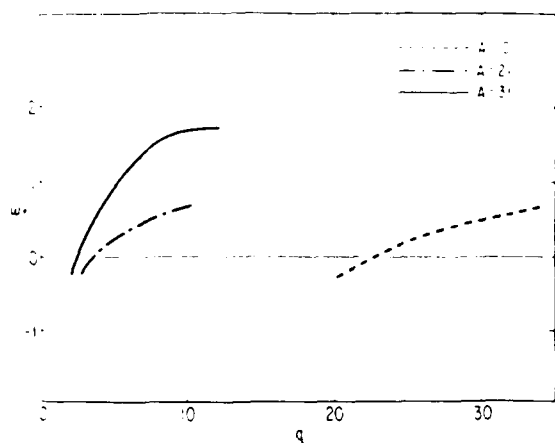


FIG. 1. Growth rates ω_r vs q are plotted for aspect ratios of 10, 21, and 31. Magnetic fields are 100 gauss.

$m = 1$ ideal MHD kink mode is stable. This result may explain why filaments (prominences) have very stable structures.

Figure 1 also shows that aspect ratio is an important parameter which strongly determines the stability. A loop with higher aspect ratio has higher growth rate at a given q and needs greater twisting of field lines to stabilize the mode than does a loop with lower aspect ratio.

Figure 2 demonstrates how the strength of the magnetic field influences stability. The magnetic fields are 50, 100, and 200 gauss, and the aspect ratio is fixed at 10. For a 200 gauss magnetic field, the loop is stabilized for q smaller than 50. On the other hand, for 50 gauss, the loop is stabilized for q smaller than 10. The modes in stronger magnetic fields are stabilized by less twist than in weaker ones. In a region with strong magnetic field, condensation will cease relatively soon after magnetic field lines start to twist from straight potential field lines.

For ideal MHD modes, stabilities of various poloidal modes differ significantly from one another; i.e., the instability region of the $m = 1$ mode is $q \leq 1$, and the region of the $m = 2$

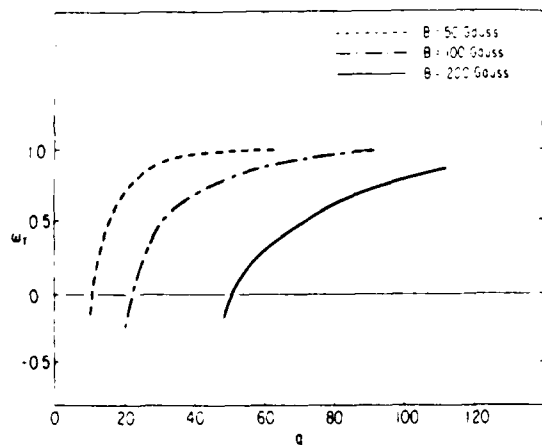


FIG. 2. Growth rates ω_r vs q are plotted for magnetic fields of 50, 100, and 200 gauss. The aspect ratios of the loops are 10.

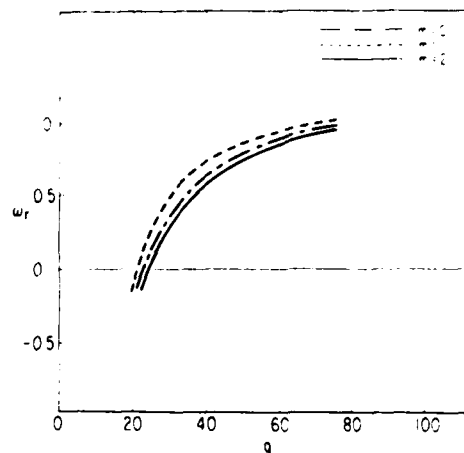


FIG. 3. Stabilities for poloidal modes $m = 0, 1,$ and 2 . The loop has magnetic fields of 100 gauss and aspect ratios of 10.

mode is $q \approx 2$ (Bateman 1978). Figure 3 shows how similar the stabilities of thermal modes are for different poloidal modes. The figure shows no appreciable differences between $m = 0, 1,$ and 2 modes. This result is strikingly different from that of ideal MHD stability.

Let us consider how magnetic fields affect thermal modes in cylindrical plasmas. Unlike the effects of magnetic fields on ideal MHD instabilities, the magnetic fields affect the thermal modes in indirect ways. Magnetic fields affect ideal MHD modes by exerting magnetic tension, building up magnetic pressure, and forming magnetic shear. These effects prevent further plasma displacement after the initial perturbation. On the other hand, magnetic tension and magnetic pressure cannot completely stabilize the thermal instability, even when the magnetic fields are extremely high, because plasma can cool down nearly isochorically (Field 1965). The most effective stabilizing mechanism for the thermal modes is heat conduction. Since we neglect heat conduction perpendicular to the magnetic field, heat conduction cannot have a stabilizing effect on the modes unless field lines bend. Figure 4 shows how the bending of field lines affects thermal modes. In Figures 4a and 4b, temperature varies along the radial direction but is uniform along the z -direction. If field lines are not bent by the perturbation (i.e., $\mathbf{k} \cdot \mathbf{B}_0 = 0$), as shown in Figure 4a, the condensed region cannot receive heat from a higher temperature region because heat cannot be transmitted across the field lines. The only stabilizing effect is magnetic pressure, which cannot stabilize condensation modes; it only reduces the growth rate (Field 1965). If magnetic fields bend (i.e., $\mathbf{k} \cdot \mathbf{B}_0 \neq 0$), as shown in Figure 4b, the condensed lower temperature region, indicated by shading, can receive heat from an unperturbed region along the field lines. For coronal loop conditions, where the conductive time scale is several times lower than the radiative time scale, parallel heat conduction can effectively stabilize the modes. The dependence of stability on $q, A,$ and β can be understood with equation (23) below. Plasma pressure depends on $q, A,$ and β in the following form:

$$P_0(r) = (2\pi q A)^2 (1 - r^2) \beta + 1 \quad (23)$$

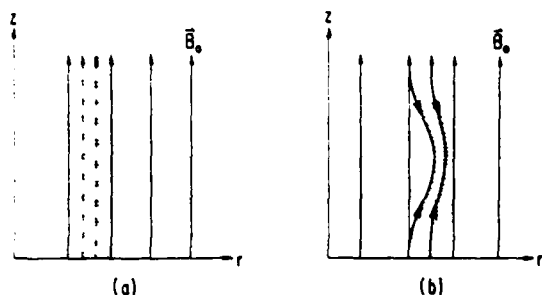


FIG. 4.—(a) Condensation of plasmas perpendicular to field lines ($\lambda = B_z = 0$). Since heat flows only along the field lines, the condensed region cannot receive heat from adjacent regions. (b) The bending of field lines makes it possible for the heat to flow into the condensed region from adjacent regions along field lines. The shaded areas in Figs. 4a and 4b are condensed regions, and the thick arrows in Fig. 4b are heat flows along the field lines.

For given λ and β , plasma pressure increases as q decreases. Since we assume that equilibrium plasma density is uniform, the increase of pressure is associated with the increase of temperature. As temperature increases, the destabilizing effect of radiative energy loss is reduced, while the stabilizing effect of heat conduction is enhanced. That is the reason why thermal modes are stabilized as q decreases. The effect of aspect ratio A on the stability is similar to that of q . For given q and β , a higher aspect ratio means lower pressure and lower temperature, which enhances the destabilizing effect of radiation and reduces the stabilizing effect of heat conduction. Therefore, Figure 1 shows that plasmas become more unstable as A increases. Equation (23) also indicates that for a lower value of β , a certain increase of field twisting causes higher increases of pressure and temperature in the plasma. This is the reason why plasmas in stronger magnetic fields are more stable for a given q -value (see Fig. 2). The insensitivity of the stability to different poloidal modes (Fig. 3) is due to the facts that the major destabilizing mechanism, radiation, is independent of poloidal modes, and the major stabilizing mechanism, heat conduction, weakly depends on poloidal modes (see θ and ϕ in eq. [21]).

VI. DISCUSSION AND CONCLUSION

We have studied the thermal stability of coronal plasmas assuming that the plasmas are confined by magnetic fields, and physical quantities vary only along the radial direction. By discarding a hydrodynamic assumption that plasmas move only along the field lines, we study the MHD effects on condensation modes of cylindrical plasmas. We find that loops can be unstable even when they satisfy the hydrodynamic stability conditions (McClymont and Craig 1981c) unless the twist of field lines exceeds a certain value. Therefore, whenever we discuss the hydrodynamic stability of condensation modes, we have to implicitly assume that the twist of field lines exceeds a certain value.

An interesting result of this study is that the condensation modes are distinguished from ideal MHD kink modes for stability: The $m = 1$ kink mode is unstable for $q < 1$ but becomes stabilized as the twist of field lines decreases ($q > 1$). On the other hand, the $m = 1$ condensation mode is

unstable for $q \gg 1$, at which value the $m = 1$ kink mode is stable, but becomes stabilized as the twist increases. This is important for the understanding of the very stable nature of prominences.

Conceding that detailed observational phenomena cannot be understood with this simple model, we try to understand some of the essential features of the observations qualitatively by dividing field configurations into three types: very low twist ($q \gg 1$), medium twist, and high twist ($q \leq 1$) of field lines. Since condensation modes are unstable for $q \gg 1$, we believe that prominences (or filaments) are formed in this field configuration. Noting that eruptions of prominences are believed to be due to MHD kink instabilities for high twisting of field lines ($q \leq 1$) (Sakurai 1976), we expect that the prominences and filaments are in globally stable configurations; i.e., the prominences (or filaments) are in thermally unstable but MHD stable states. This assertion is supported by numerous observational studies (Rust 1972; Malville 1979; Smith and Smith 1963; Gibson 1973; Zirin 1966; Tandberg-Hanssen 1974) which describe prominences which have materials flowing down continuously along the field lines in stable global configurations. The flows of materials in prominences are interpreted as a result of continuous condensation of surrounding plasmas.

According to Malville (1979), preflare loops do not exhibit the extensive down flows that postflare prominences do. Our interpretation is that loops about to flare have medium twisting of field lines, which results in stability for condensation modes as well as MHD kink modes. On the other hand, since postflare loops lose much of their free magnetic energy to the flare, their field lines are less stressed ($q \gg 1$), and their configurations allow more extensive plasma condensations.

Figure 2 shows how the formation of condensations is affected by the strength of the magnetic field. In a strong magnetic field region, where $B \sim 200$ gauss, condensation will cease before prominences are formed, as the field lines start to twist further by the buildup of nonpotential magnetic field. On the other hand, in a weaker magnetic field region, where $B \sim 50$ gauss, condensation continues until the twisting of field lines increases to a larger degree. During this time, the condensation develops fully to form prominences. From Figure 2 we can predict that prominences and filaments are more likely to form in a weak magnetic field region than in a strong one if the other physical conditions in the regions relevant to the formation of filaments are the same (e.g., existence of neutral lines, etc.).

Flare loops have high twisting of field lines ($q \leq 1$) in strong magnetic field regions, where condensation of the loops is not likely to occur. Erupting filaments also have high twisting of field lines, but they are in weak magnetic field regions, where condensation can occur in relatively highly twisted field configurations.

We have found that the effect of magnetic fields on condensation modes is different from that on MHD kink modes. Magnetic tension and magnetic pressure do not directly affect the condensation modes, unlike the ideal MHD case, but they influence the stability by affecting heat flows along field lines.

The results enhance our understanding of the formation and stability of prominences. Since our model is extremely simplified, any quantitative comparisons between theory and

observations are not appropriate. In the future, we will study thermal modes with nonuniform current density to understand the effect of magnetic shear, and we will abandon the rigid wall boundary condition. It can be expected that studies of more realistic geometries of prominences with longitudinal variations of temperature and density will further enhance our understanding of the physics of prominences.

The author thanks Dr. R. C. Canfield for his valuable discussions and comments during the course of this work. This work was supported by the Air Force Office of Scientific Research, Air Force Systems Command, USAF, under grant AFOSR 82-0092, and by NASA under grant NSG-7406.

REFERENCES

- An, C.-H. 1983, *Ap. J.*, **264**, 302.
 ——— 1984, *Ap. J.*, **276**, 352.
 Antiochos, S. K. 1979, *Ap. J. (Letters)*, **232**, L125.
 Antiochos, S. K., Emslie, E. G., Shoub, E. C., and An, C.-H. 1984, *Ap. J.*, submitted.
 Bateman, G. 1978, *MHD Instabilities* (Cambridge, Mass.: MIT Press).
 Chidemi, C., Einaudi, G., and Torricelli-Ciamponi, G. 1981, *Astr. Ap.*, **97**, 17.
 Chidemi, C., and Van Hoven, G. 1979, *Ap. J. (Letters)*, **232**, L69.
 Craig, I. J. D., and McClymont, A. N. 1981, *Nature*, **294**, 333.
 Field, G. B. 1965, *Ap. J.*, **142**, 531.
 Foukal, P. V. 1975, *Solar Phys.*, **43**, 327.
 Gibson, E. G. 1973, *The Quiet Sun* (Washington: Scientific and Technical Information Office, NASA).
 Hirshel, S. R., and Rosner, R. 1979, *Ap. J.*, **234**, 1113.
 Hood, A. W., and Priest, E. R. 1980, *Astr. Ap.*, **87**, 126.
 Malville, J. M. 1979, in *IAC Colloquium 44, Physics of Solar Prominences*, ed. E. Jensen, P. Maltby, and F. Q. Orrall (Blindern, Institute of Theoretical Astrophysics).
 McClymont, A. N., and Craig, I. J. D. 1981a, *Univ. of Waikato, Math. Res. Rept.*, No. 96.
 ——— 1981b, *Univ. of Waikato, Math. Res. Rept.*, No. 99.
 ——— 1981c, *Univ. of Waikato, Math. Res. Rept.*, No. 100.
 Nakagawa, Y. 1970, *Solar Phys.*, **12**, 419.
 Peres, G., Rosner, R., Serio, S., and Vaiana, G. S. 1982, *Ap. J.*, **252**, 791.
 Potter, D. 1973, *Computational Physics* (New York: Wiley-Interscience), chap. 4.
 Rust, D. M. 1972, *Air Force Survey in Geophysics*, No. 237.
 Sakurai, T. 1976, *Pub. Astr. Soc. Japan*, **28**, 177.
 Smith, H. J., and Smith, E. V. P. 1963, *Solar Flares* (New York: Macmillan).
 Spitzer, L. 1962, *Physics of Fully Ionized Gases* (New York: Interscience), pp. 136-146.
 Tandberg-Hanssen, E. 1974, *Solar Prominences* (Dordrecht: Reidel).
 Zirin, H. 1966, *The Solar Atmosphere* (Waltham, Mass.: Blaisdell).
 Zweibel, E. 1980, *Solar Phys.*, **66**, 305.

CHANG-HYUK AN: Center for Astrophysics and Space Sciences, C-011, University of California, San Diego, La Jolla, CA 92093

COMMENTS ON THE MHD STABILITY OF CORONAL PLASMAS WITH LINE-TYING

CHANG-HYUK AN

Center for Astrophysics and Space Sciences, University of California, San Diego

Received 1983 August 19, accepted 1983 December 8

ABSTRACT

The effect of line-tying in the photosphere on the magnetohydrodynamic (MHD) stability of coronal loops has been investigated by a number of authors. We comment on the various boundary conditions, plasma displacement functions, and other assumptions used by a number of investigators. Our comments lead to three conclusions. First, as a boundary condition for line-tying studies, the plasma at the footpoints of a loop may safely be assumed to be stationary. Second, when a simple perturbed test function is used for the energy principle, the function should be helical in form, because the complete stability of ideal MHD modes obtained in a previous study is due not to line-tying but to the choice of a nonhelical perturbed function. Finally, constraints on the test function (e.g., the component parallel to field lines is zero) should be discarded because they overestimate stability.

We study kink instabilities in cylindrical plasmas on this basis. The results are very different from those of a previous study which used a nonhelical test function, which indicates the importance of a helical test function. We find that the effects of line-tying on force-free equilibria are not the same as on non-force-free equilibria. As the value of the aspect ratio increases, the effect of line-tying becomes less important for force-free equilibria, but more important for non-force-free equilibria. We also find that line-tying is a more stabilizing effect on the equilibria with a higher magnetic shear (or a more peaked radial current profile).

Subject headings: hydromagnetics — instabilities — plasmas — Sun: corona

1. INTRODUCTION

Numerous earlier papers concern the effect of photospheric line-tying on the ideal magnetohydrodynamic (MHD) stability of coronal loops. Most of the authors have used simple test functions in order to represent plasma perturbations satisfying a line-tying boundary condition. Because the simple test functions lack generality and cannot include all displacements, they cannot be used to define both necessary and sufficient stability conditions. Recently, more sophisticated methods have been proposed to evaluate loop stability. Hood and Priest (1981) used a two-dimensional numerical analysis to obtain a necessary and sufficient condition for stability of a force-free loop equilibrium. Their results showed that the method of Hood and Priest (1979) using much simpler test functions gives a good bound on the critical values of the stability parameters. Einaudi and Van Hoven (1981) developed an energy-principle method, in which a general initial perturbation is expressed as a uniformly convergent sum over a complete discrete set of longitudinal mode numbers. With this method, they later defined necessary and sufficient stability conditions for various loop equilibria (Einaudi and Van Hoven 1983). But while these studies have improved on previous work, none allows the addition of nonideal effects (i.e., resistivity, radiation, and heat conduction), because of the extreme complexity of the methods. Use of a simple test function may thus have certain advantages if we wish to study nonideal effects.

Looking at the various ways in which boundary conditions and simple test functions for line-tying have been determined, we note that the results do not coincide. For example, Hood and Priest (1979) used a helical form of displacement function whose amplitude is modulated by the factor $\cos \alpha z$, i.e., $\xi(r) = \xi(r)e^{i(m\theta + kz)} \cos \alpha z$. Here m and k are poloidal and longitudinal mode numbers, respectively, and $\alpha = b\pi/2L$. Here b and L are the radius and the length of the cylinder. The quantity $\alpha (= b\pi/2L)$ is one of many possible choices from $\alpha = (n + \frac{1}{2})b\pi/L$ ($n = 0, 1, 2, \dots$) to satisfy the line-tying boundary condition. The quantity $\alpha = b\pi/2L$ was used by Hood and Priest (1979) to study the least stable case. By applying the energy principle (Bernstein *et al.* 1958), they predicted instability onset for a force-free equilibrium with aspect ratio ($= 2L/b$) larger than 3.3π . On the other hand, Van Hoven, Ma, and Einaudi (1981) obtained complete stability for any equilibrium by using a nonhelical form of test function, $\xi(r) = \xi(r)e^{im\theta} \cos \alpha z$. The two contradictory results demonstrated that the choice of the function is crucial in determining loop stability. Raadu (1972), Hood and Priest (1979), and An (1982, hereafter Paper I) used the helical form of the function, while Van Hoven, Ma, and Einaudi (1981) used the nonhelical form. The study of line-tying has been extended to include resistive instabilities by Mok and Van Hoven (1982), who used the nonhelical test function.

As for boundary conditions, Raadu (1972), Hood and Priest (1979, 1981), and An (Paper I) assumed that plasmas do not move at the footpoints, while Van Hoven, Ma, and Einaudi (1981), Einaudi and Van Hoven (1981, 1983), and Mok and Van Hoven (1982) all assumed that plasma motion perpendicular to the magnetic field would be zero, but that an arbitrary parallel component might exist. The different assumptions yield different results.

Most of the previous works by Hood and Priest (1979, 1981) assumed that there is no plasma motion parallel to magnetic fields. This assumption overestimates stability unless plasma pressure is identically zero.

Since different choices of test functions, boundary conditions, and other assumptions give different results, it is important to discuss how the choices affect the results and to determine which test function and boundary conditions are the most reasonable in

order to evaluate stability properly. These problems should be clarified before we study nonideal effects on the stability of coronal loops.

In this paper, I discuss which boundary conditions and test function for line-tying are more reasonable and how the choices affect the results. I will also present my results for cylindrical plasma stability. Throughout this paper I will use dimensionless equations for convenience.

II. COMMENTS ON THE PREVIOUS STUDIES

a) Boundary Conditions

Why should a line-tying boundary condition be considered in order to study the MHD stability of coronal loops? The tops of coronal loops are occupied by tenuous plasmas of density $n \approx 10^9 \text{ cm}^{-3}$ and have a narrow transition region in the chromosphere where plasma density increases steeply. The loops may extend farther down, to the photosphere, whose density is about 10^{17} cm^{-3} . The huge difference of densities between the coronal and photospheric regions means that the MHD time scales, $(\rho_0 b^2 B_0^2)^{1/2}$, of the two regions are very different: i.e., $\tau_1/\tau_2 \approx 10^{-4}$. Here ρ_0 , b , and B_0 are density, radius of loop cross section, and magnetic field, respectively, and τ_1 and τ_2 are the coronal and photospheric MHD time scales. A perturbation of the loop plasma in the coronal region generates changes on the coronal MHD time scale, while the plasma at the photospheric footpoints undergoes no appreciable change. This is the physical reason to consider the effect of line-tying on MHD stability.

Einaudi and Van Hoven (1981) assumed that at the footpoints motions perpendicular to the magnetic field (ξ_\perp) are zero, but that parallel components of the motions (ξ_\parallel) are arbitrary. This permitted them to neglect the plasma compression term, $\nabla \cdot \xi$, when they minimized the energy integral, δW (Bernstein *et al.* 1958). Their analyses were greatly simplified by the condition $\xi_\parallel = \text{arbitrary}$ at footpoints. The choice of boundary condition was inspired by observations (e.g., Foukal 1976) that showed quasi-steady flows along loops that probably extend down to the footpoints.

A question concerning such plasma flows at the footpoints is whether the flows are induced by perturbations. For an answer to this question, we must recall the assumption that plasmas before perturbation are in an equilibrium state with no motion. The energy-principle method (Bernstein *et al.* 1958) is based on the assumption. Let us consider the parallel component of plasma motion. The perturbed momentum equation parallel to the magnetic field is

$$\omega^2 \rho_0 (\xi \cdot B_0) = -B_0 \cdot \nabla P_1 - B_1 \cdot \nabla P_0. \quad (1)$$

Here, ρ , P , and B are dimensionless density, pressure, and magnetic field, and the subscripts 0 and 1 stand for equilibrium and perturbed quantities, respectively. The quantity ω is the dimensionless growth rate, and ξ is the plasma displacement. The equation shows that parallel motions change on a hydrodynamic time scale, $(\rho_0 L_z^2 P_0)^{1/2}$, not on an MHD time scale. Here L_z is a scale height. If the hydrodynamic time scale at the footpoints, τ_3 , is comparable to the coronal MHD time scale, τ_1 , a perturbation on the coronal time scale would cause substantial parallel motions at the footpoints. In this case, we must treat the observed plasma flows as a boundary condition. But if $\tau_1/\tau_3 \ll 1$, however, parallel motions at the footpoints are negligible on the coronal MHD time scale. Thus we can assume that plasma motion in any direction is zero at the footpoints. If we wish to consider the observed quasi-steady flows (Foukal 1976), we must construct a steady state with a steady flow and study the stability of the steady state. But note that we can no longer use the energy-principle methods of Bernstein *et al.* (1958).

Let us estimate the ratio of the coronal MHD time scale to the photospheric hydrodynamic time scale, τ_1/τ_3 , for a semiempirical equilibrium. We take the VAL model (Vernazza, Avrett, and Loeser 1981) as an example, since it has been used extensively to study both linear (McClymont and Canfield 1983) and nonlinear (An *et al.* 1983) thermal instability. The plasma pressure in the loop at the minimum temperature region is about 10^4 dyn cm^{-2} , and the photospheric scale height, measured from the lower transition region down to the minimum temperature region, is about one-tenth of the loop length. For a magnetic field of 100 gauss, $\tau_1/\tau_3 \approx 10^{-4}$, which is the same as the ratio of coronal to photospheric MHD time scales τ_1/τ_2 . Since we neglect gravity in our calculations, we may not put the footpoints at the minimum temperature region, where gravity is important. We also estimate the time scales at the region with temperature $T = 6.5 \times 10^3 \text{ K}$ and density $n = 8.5 \times 10^{12} \text{ cm}^{-3}$, where the gravitational force is negligible (about 1% of the Lorentz force). The estimated time scales are $\tau_1/\tau_2 \approx 10^{-2}$ and $\tau_1/\tau_3 \approx 10^{-2}$. Thus we may justifiably neglect parallel as well as perpendicular motions at the footpoints.

There are two different ways to represent the absence of motion at footpoints. One is that the plasma displacement $\xi = 0$ (Raadu 1972; Hood and Priest 1979, 1981; Hood, Priest, and Einaudi 1982); the other is that the perturbed magnetic field $B_1 = 0$ (Paper I). Note that the condition $B_1 = 0$ ensures the condition $\xi = 0$, but the reverse is not true (Paper I). Since the condition $B_1 = 0$ implies tighter binding of field lines to the footpoints than the condition $\xi = 0$, $B_1 = 0$ should yield a higher stability boundary. Using $\xi(r) = \xi(r)e^{i(m\theta + kz)}$ $\cos^2 xz$ (An 1982) and $\xi(r) = \xi(r)e^{i(m\theta + kz)}$ $\cos xz$ (Hood and Priest 1979) to represent $B_1 = 0$ and $\xi = 0$ at the footpoints, respectively, we can derive an energy-principle expression

$$\delta W = \delta W_0 + \theta \delta W_1. \quad (2)$$

Here δW_0 is the energy integral without line-tying (Newcomb 1960), and δW_1 is due to line-tying; $\theta = 1$ and $4/3$ for the boundary conditions $\xi = 0$ and $B_1 = 0$, respectively; and δW_1 is identical for the two different boundary conditions. (Paper I). Since $\delta W_1 > 0$, we can see that the condition $B_1 = 0$ gives an insignificantly higher stability than $\xi = 0$.

b) Test Functions for Line-Tying

Which test function [$\xi_1(r) = \xi(r)e^{i(m\theta + kz)}$ $\cos xz$ or $\xi_2(r) = \xi(r)e^{i(m\theta + kz)}$ $\cos xz$] represents a perturbation with line-tying most reasonably, and how does the choice affect the results? Let us first consider the form of the perturbations. The helical form of $\xi_1(r) = \xi(r)e^{i(m\theta + kz)}$ $\cos xz$ is shown in Figure 1a. Line-tying is expressed with $\cos xz$. Since equilibrium magnetic field lines

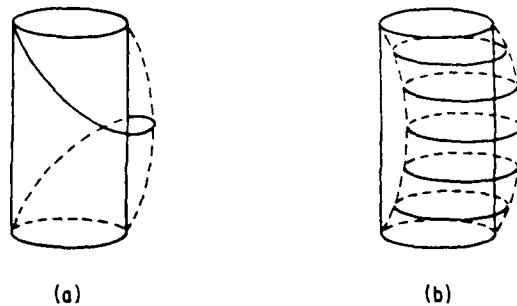


FIG. 1. (a) The form of a helical perturbed displacement function $\xi_1(r) = \xi(r)e^{i(m\theta - kz)}$. (b) The form of a nonhelical perturbed displacement function $\xi_2(r) = \xi(r)e^{-im\theta} \cos kz$.

are helically twisted, the field lines are least disturbed if their helicity is the same as that of the perturbation. The nonhelical form [$\xi_2(r) = \xi(r)e^{-im\theta} \cos kz$] is shown in Figure 1b. Because the perturbation is not helical, it can disturb the field lines greatly no matter what helicity they possess. The disturbance of field lines can induce two competing mechanisms, slow magnetosonic modes which may be destabilizing and magnetic tension which is stabilizing. The following calculation will show that $\xi_2(r)$ results in complete stability, while $\xi_1(r)$ predicts instability for a force-free equilibrium. The result implies that the stabilizing effect of magnetic tension is more significant than the destabilizing effect of the slow magnetosonic mode for kink modes. The effect of choosing the helical $\xi_1(r)$ over the nonhelical $\xi_2(r)$ is easier to understand if we simply note that the nonhelical $\xi_2(r)$ is a special case of the helical $\xi_1(r)$, with $k = 0$.

Consider the force-free equilibrium given by Gold and Hoyle (1960); namely,

$$B_z = 1(1 + r^2), \quad B_\theta = r(1 + r^2). \tag{3}$$

The magnetic fields have a uniform twist and a uniform plasma pressure. Hood and Priest (1979) showed, using $\xi_1(r)$ as the test function, that the equilibrium with pressure $p_0 = 0$ becomes unstable as the aspect ratio $A = 2L/b$ becomes larger than 3.3π . Here L is a half loop length, and b is the radius of a loop cross section. But if we use $\xi_2(r)$, we can show analytically that the equilibrium is completely stable no matter what the aspect ratio is. By letting $k = 0$ in the energy integral of Hood and Priest (1979) for the force-free equilibrium, we obtain a δW for the nonhelical $\xi_2(r)$

$$\delta W = \int dr [f(\xi_r')^2 + g\xi_r'^2]. \tag{4}$$

Here

$$f = (rm^2 B_\theta^2 + x^2 r^3 B_0^2) D, \quad g = (m^2 - 1)x^2 r B_\theta^2 D + 2x^4 r^3 B_z^2 D^2 - 2x^2 r^2 B_z' B_z D, \quad D = m^2 + x^2 r^2, \tag{5}$$

where ξ_r is a radial component of ξ , $x = \pi b 2L$, $B_0^2 = B_z^2 + B_\theta^2$, and B_z' is the derivative of B_z with respect to r . For the force-free equilibrium, $g > 0$ for $m \geq 1$ modes. Since f is always positive, δW is positive for $m \geq 1$ no matter how large the aspect ratio is.

This result contradicts the result of Hood and Priest (1979), who found the instability for $A > 3.3\pi$. The different results are due solely to the different choice of test function. Because Van Hoven, Ma, and Einaudi (1981) used $\xi_2(r)$, the complete stability they obtained is not from line-tying but is owed rather to their choice of test function. The analysis suggests that results obtained using the nonhelical $\xi_2(r)$ do not predict the stability correctly. Mok and Van Hoven (1982) used the nonhelical $\xi_2(r)$ to study the effect of line-tying on resistive instabilities. They concluded that line-tying completely stabilizes $m \geq 1$ resistive modes by noting that $\xi_2(r)$ does not allow mode rational surfaces in the plasma except for the $m = 0$ mode.

c) A Constraint on the Test Function, $\xi \cdot B_0 = 0$

It was assumed that plasma motion parallel to the magnetic field is zero, i.e., $\xi \cdot B_0 = 0$, to simplify the calculations (Hood and Priest 1979) and to obtain a necessary and sufficient stability condition for a force-free equilibrium in the limit $\beta = 0$ (Hood and Priest 1981). The validity of the constraint can be checked by studying a component of the perturbed momentum equation parallel to the magnetic field (eq. [1]). For the left-hand side of equation (1) to be zero, the equilibrium pressure must be identically zero. For force-free equilibria with $p_0 \neq 0$, the constraint $\xi \cdot B_0 = 0$ is not valid; it results in an overestimation of stability.

Since Paper I did not use the constraints that Hood and Priest (1979) used for ξ , comparisons of the results obtained in Paper I with those of Hood and Priest (1979) will give a good indication of how the constraint affects the stability. For comparisons, we have to change 4.3 to 1 in equations (16)–(24) and correct a mistyped term $2x^2 T_s r^3$ to $x^2 T_s r^3$ in equation (18) of Paper I. The number 4.3 came from the use of $B_\theta = 0$ (rather than $\xi_\theta = 0$) as a line-tying boundary condition. The non-force-free equilibrium which Hood and Priest used is

$$B_z = 1, \quad B_\theta = (b 2L)\Phi(0)r(1 + r^2), \quad p_0 = \beta/2 + [(b 2L)\Phi(0)]^2/2(1 + r^2)^2. \tag{6}$$

Here $\Phi(0)$ is a twist of field lines at $r = 0$, defined as $\Phi(r) = 2LB_\theta/b r B_z$, and β is the ratio of plasma to magnetic pressure. Figure 2 shows how the stability boundary is changed by the constraint $\xi \cdot B_0 = 0$. We plot the critical twist $\Phi(0)/2$ versus longitudinal wave vector k for a marginally stable plasma with aspect ratio $A = 2L/b = 10$. Line 1 is the Kruskal-Shafranov limit (Kadomtsev 1966).

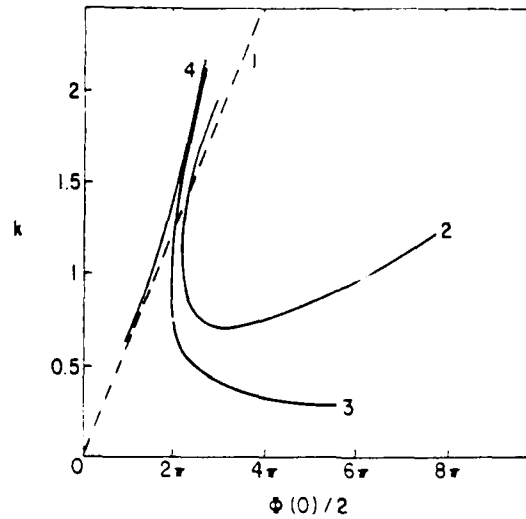


FIG. 2.—Critical twist, $\Phi(0)/2$, vs. longitudinal wavenumber k for $A = 2L/b = 10$. Line 1 is the Kruskal-Shafranov limit, line 2 is the result of Hood and Priest (1979) using the constraint $\xi \cdot B_0 = 0$, line 3 is the result of this paper without the above constraint, and line 4 is the result without line-tying.

line 2 is a result of Hood and Priest (1979) using the constraint above, line 3 is the same result without the constraint (detailed calculation is in the next section), and line 4 is a result without line-tying. The instability region is the right side of each curve. The figure shows how the constraint $\xi \cdot B_0 = 0$ alters stability for various values of k . Note that the effect of the constraint is to raise the stability boundary, and that the effect is significant for low values of k . As the difference between lines 2 and 3 shows, constraint $\xi \cdot B_0 = 0$ yields, for certain values of k , two stability regions for high and low values of $\Phi(0)$; without the constraint, only one stability region exists. The figure demonstrates that the constraint should be discarded for a meaningful study of the line-tying effect. More detailed calculations and comparisons are given in the next section.

III. KINK INSTABILITIES IN CYLINDRICAL PLASMAS

a) A Differential Equation for Stability

In Paper I, we studied the MHD stability of cylindrical plasmas with line-tying using the energy principle (Bernstein *et al.* 1958). The test function $\xi(r) = \xi(r)e^{im\theta + kz} \cos^2 \alpha z$ was used, with $B_z = 0$ at the footpoints. A stability condition for local modes was derived analytically by taking a limit as m goes to infinity. In this section, we will study kink instabilities for various equilibria. A detailed physical explanation for the effect of line-tying will result. For comparison with other work, we will use $\xi = 0$ rather than $B_z = 0$ as the boundary condition. By changing the equations to the dimensionless form, we have

$$\delta W = (\pi/2\alpha) \int [\Omega(\xi_r')^2 + G\xi_r'^2] dr, \quad (7)$$

$$\begin{aligned} \Omega &= [r(mB_\theta + krB_z)^2(1 + S_0) + x^2r^3(B_\theta^2 + B_z^2S_0)]/A_1, \\ G &= r(k \cdot B_0)^2(1 - 1/A_1) + 2\beta p_0 k^2 r^2/A_1 + 2k^2 r(k^2 r^2 B_z^2 - m^2 B_\theta^2)/A_1^2 + 2k^2 r(x^2 T_5 r^3 + x^4 T_3)/A_1^2 \\ &\quad + x^2 T_2 (k^2 r^2 B_z^2 - m^2 B_\theta^2 + x^2 T_5 r^3 + x^4 T_3)/A_1^2 - x^2 (r^2 B_z^2 S) - x^2 T_2 (r^2 B_\theta^2) r^2 A_1 + x^2 B_z^2 (1 + S)r \\ &\quad + (x^2 T_1 + x^4 T_3)/r A_1 - [x^2 (r^3 T_3)' + x^4 T_3']/A_1. \end{aligned} \quad (8)$$

Here

$$\begin{aligned} T_1 &= r^2 B_\theta^2 + r^2 S [m^2 (B_\theta^2 - B_z^2) - 2mkrB_z B_\theta], & T_2 &= r^2 (1 + m^2 S), & T_3 &= -(mr^2 B_z S)^2, \\ T_4 &= B_\theta^2 + S [(B_\theta^2 - B_z^2)m^2 + 2krmB_\theta B_z], & T_5 &= (B_z^2 - B_\theta^2) r - SB_\theta^2 m^2 r, \\ A_1 &= m^2 + k^2 r^2 + x^2 T_2, & S &= \beta/p_0 [(krB_z + mB_\theta)^2 + x^2 r^2 B_z^2], & S_0 &= x^2 r^2 S. \end{aligned} \quad (9)$$

and γ is a specific heat constant. Stability can be studied after obtaining the Euler-Lagrange equation from equation (7):

$$(\Omega \xi_r')' - G \xi_r = 0. \quad (10)$$

We use Newcomb's theorem (Newcomb 1960) to study the stability, as previous authors have done (Chiuderi, Giacchetti, and Van Hoven 1977; Hood and Priest 1979; Ray and Van Hoven 1982); stability is determined by examining whether or not the solution of equation (10) has a zero crossing between $r = 0$ and a radial boundary $r = d$ (Newcomb 1960). The boundary condition for ξ_r at $r = 0$, which is obtained by solving equation (10) near $r = 0$, is

$$\xi_r = 1 \quad \text{for } m = 1, \quad \xi_r = 0 \quad \text{for } m \geq 1.$$

Since equation (10) does not have singularity, we integrate the equation up to $r = d$. For most of our calculations, $d = 8$ is used even though we found that the results are insensitive to the choice of d for $d > 5$.

b) Equilibrium

We have studied the stability of two different equilibria. One is the force-free equilibrium, equations (3), with $p_0 = 0$; the second is the non-force-free equilibrium, equations (6). Both were studied by Hood and Priest (1979). We have already taken these two equilibria to understand how the constraint $\xi \cdot B_0 = 0$ affects the results (§ II). Since the equilibria have current densities distributed uniformly in space, we have constructed two new equilibria with current density localized within a cylinder of radius $r = 1$, namely,

$$j_z = j_0(1 - r^2)^l \quad \text{for } r \leq 1, \quad j_z = 0 \quad \text{for } r > 1, \quad B_z = 1. \quad (11)$$

The equilibrium has a current density localized at $r \leq 1$ and becomes smoothly zero for $r \geq 1$. The current channel is embedded in current-free ambient plasma with $\beta = 2 \times 10^{-3}$. We took two different current densities, $l = 1$ and $l = 2$, to learn how different current-density profiles (or magnetic shears) affect loop stability with line-tying. Note that the current-density profile with $l = 1$ is broader than that with $l = 2$, and that $l = 2$ has a higher magnetic shear than $l = 1$.

c) Results

First, let us consider the force-free equilibrium, equation (2). Since equations (8) and (9) are identical to equations (2.5) and (2.6) of Hood and Priest (1979) for this equilibrium, we can use the result shown in Figure 2 of Hood and Priest (1979) without repeating the calculation. The figure shows that plasmas without line-tying are unstable for $0 \leq k \leq 1$ for any aspect ratio. Line-tying completely stabilizes plasmas of aspect ratio $4 = 2L/h < 3.3\pi$. As the aspect ratio increases, however, the effect of line-tying becomes negligible.

For the non-force-free equilibria, we need to understand how the pressure gradient affects stability. As an example, we take the equilibrium presented in equations (6) and compare our results with those of Hood and Priest (1979). Figures 2 and 3 show the critical twist $\Phi(0)/2$ versus longitudinal wave vector k for aspect ratios of $4 = 10$ and $4 = 20$, respectively. The number in each curve of Figure 3 has the same meaning as in Figure 2. As we pointed out in § II, the constraint $\xi \cdot B_z = 0$ strongly affects the stability of k -axis modes, and the effect is more significant at the lower aspect ratio. It is also shown that stability without line-tying (line 4) departs significantly from the Kruskal-Shafranov limit as k increases. A comparison of line 3 with line 4 reveals that line-tying has a significant stabilizing effect for low- k modes, but insignificant for higher- k modes. The two figures do not show any destabilizing effect of line-tying as the aspect ratio increases, in contrast to the force-free equilibrium studied above. In fact, as the ratio increases, line-tying has a more stabilizing effect, even though the magnetic tension owing to line-tying decreases.

In Figure 4, we plot a critical twist yielding marginal stability for various aspect ratios. The critical twist increases with aspect ratio. The figure demonstrates that line-tying is more stabilizing at higher aspect ratios.

Since changes in the plasma current-density profile drive instabilities, different current-density profiles should result in differing stability. In Figure 5 we present the stability of the equilibrium shown in equations (11) for $l = 1$ and $l = 2$. The figure shows that line-tying has a more stabilizing effect on more peaked current-density profiles.

d) Interpretation

We have found that line-tying has a significant stabilizing effect at small longitudinal wavenumber k , but the effect becomes insignificant as k increases for a given aspect ratio. As the aspect ratio increases, line-tying becomes more stabilizing for equilibria with a pressure gradient, but less stabilizing for force-free equilibria. The stability of force-free equilibria with and without line-tying is indistinguishable at extremely high aspect ratio. In this section, we provide the physical explanation for these results.

First, why does the effect of line-tying become negligible as k increases? The contribution of line-tying to stability is expressed in terms proportional to x^2 or x^4 in equations (8) and (9); x^2 is a small quantity ($x^2 \ll 1$) for the usual coronal loop condition. For example, for a loop with $h/L = 0.1$, x^2 is less than 0.04. Because x^2 is so small, any terms which have x^2 or x^4 can be negligible.

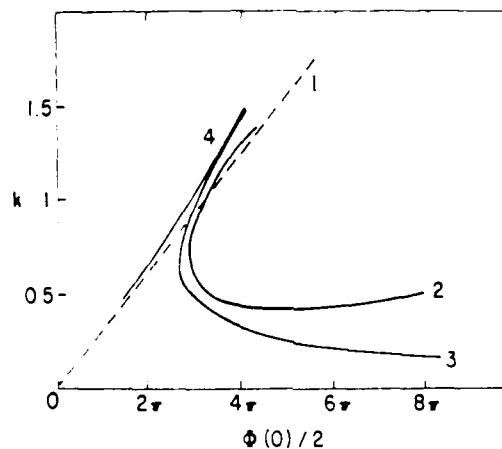
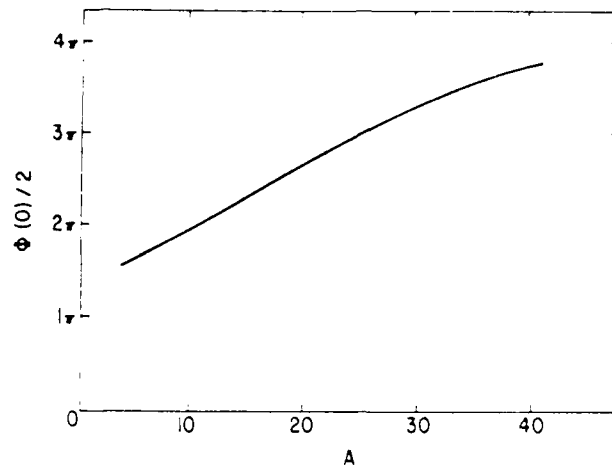


FIG. 3.—Critical twist vs. longitudinal wavenumber k for $4 = 20$.

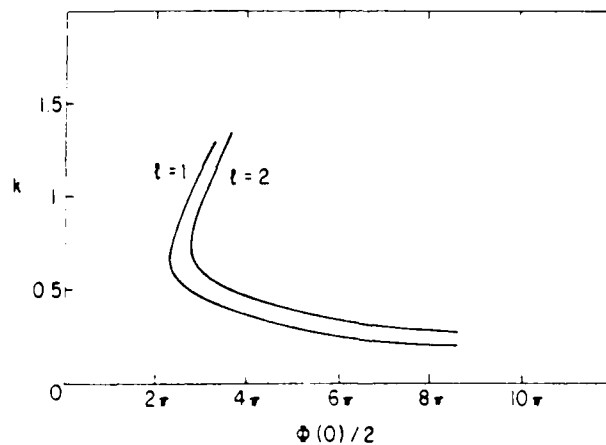
FIG. 4—Critical twist vs. aspect ratio A .

However, terms which have $x^2 S$ are not negligibly small for some cases, even when $x^2 \rightarrow 0$. From equations (9) we have

$$x^2 S = x^2 \beta_0 p_0 [r^2 (\mathbf{k} \cdot \mathbf{B}_0)^2 + x^2 r^2 B_z^2]. \quad (12)$$

At a mode rational surface, where $krB_z + mB_\theta = 0$, $x^2 S = \beta_0 p_0 r^2 B_z^2$, which is not negligible even when $x^2 \rightarrow 0$. From this mathematical behavior of $x^2 S$ we concluded quickly in Paper I that line-tying was important only near a mode rational surface. However, we find that the conclusion is true only for large values of k for a non-force-free equilibrium. This equilibrium, equations (6), has $B_z = x\Phi(0)r/(1-r^2) = xB_z(r)$, $k = 4\pi n$ (n is a longitudinal wavenumber), and $(krB_z + mB_\theta)^2 = x^2(4\pi n + mB_\theta)^2$. For large values of k (or n), $(krB_z + mB_\theta)^2$ is large; in other words, $x^2 S$ is small, except near a mode rational surface, where line-tying will be important. On the other hand, since $(krB_z + mB_\theta)^2$ is small ($\sim x^2$) for small values of k even far from a mode rational surface, line-tying can also be an important stabilizing mechanism far from a mode rational surface. Figures 2 and 3 show that the critical twists $\Phi(0)$ with and without line-tying approach each other for higher k but significantly depart from each other for low k . The physical explanation is that magnetic fields are bent so severely by a perturbation with a short longitudinal wavelength (large k) that the bending caused by line-tying does not make a significant contribution to the magnetic tension. On the other hand, for a perturbation with a long wavelength, the bending of field lines by line-tying makes an important contribution to the magnetic tension.

How does the pressure gradient affect the stability of plasmas with line-tying? It does not directly affect kink instabilities, because the driving force of the instability is plasma current, not pressure (Bateman 1978). Rather, it affects the stability indirectly, by influencing the magnetic field profiles. If the plasma has a pressure gradient, B_θ depends on the aspect ratio as well as the field twist, $\Phi(0)$, as we can see in equations (6). The quantity B_θ decreases as aspect ratio increases for a given $\Phi(0)$, resulting in decrease of the plasma current density (the driving force of kink modes). In equation (8) we note that as $x \rightarrow 0$, stabilizing terms (magnetic tension) decrease with x^2 (even at mode rational surfaces), but driving terms decrease with x^4 . Therefore, as the aspect ratio increases ($x \rightarrow 0$), line-tying is more stabilizing. The stabilizing force increases compared with the destabilizing force. On the other hand, for a

FIG. 5—Critical twist vs. longitudinal wavenumber k for equilibria with longitudinal current density $j_z = j_0(1-r^2)^2$ and $A = 20$.

force-free equilibrium, since B_z is independent of aspect ratio (see eqs [3]), the plasma current density does not change while the stabilizing effect of line-tying ($\sim \alpha^2$) decreases as $\alpha \rightarrow 0$. If the aspect ratio increases sufficiently ($\alpha^2 \approx 0$), the stability of the plasma with line-tying becomes indistinguishable from that without.

IV. CONCLUSION

We have discussed several studies of the MHD stability of coronal loops with line-tying, concentrating on boundary conditions, test functions, and other assumptions commonly used, and we have reached the following conclusions:

1. A reasonable boundary condition for line-tying is to assume that plasmas do not move in any direction at the footpoints of a loop.

2. When a simple test function is used for the energy principle (Bernstein *et al.* 1958), the function should be helical in form, i.e., $\xi(r) = \xi_0(r)e^{im\theta - kz}f(z)$, with $f(z) = 0$ at the footpoints.

3. The constraint on ξ , $\xi \cdot \mathbf{B}_0 = 0$, should be discarded because it overestimates stability when $\beta \neq 0$.

We have compared the stability of cylindrical plasmas on this basis with the results of Hood and Priest (1979) and Van Hoven, Ma, and Einaudi (1981). We have found qualitative agreement with Hood and Priest (1979) although their results predict a higher stability boundary. The very different results of Van Hoven, Ma, and Einaudi (1981) appear to underline the importance of choosing a helical test function. Our previous assertion (Paper I) that line-tying is an insignificant effect for a loop with a high aspect ratio is true only for high values of the longitudinal wave vector k and only for force-free equilibria. The effects of line-tying on force-free equilibria are not the same as on non-force-free equilibria. As aspect ratio increases, the effect of line-tying becomes negligible for force-free equilibria, but it becomes more important for non-force-free equilibria. We have provided detailed explanations of why line-tying has different effects on the force-free and non-force-free equilibria.

Even though the simple helical test function does not give sufficient and necessary stability conditions, it has a certain advantage over more sophisticated methods, i.e., Einaudi and Van Hoven (1981, 1983) and Hood and Priest (1981). With the method of Hood and Priest (1981) we cannot study the stability of non-force-free equilibria because their assumption $\xi \cdot \mathbf{B}_0 = 0$ is not valid for $\nabla p_z \neq 0$. The method of Einaudi and Van Hoven (1981) is so complicated that nonideal effects cannot be included in the calculation. That is why Mok and Van Hoven (1982) used a simple test function to study the effect of line-tying on resistive modes. Because they did not use a helical test function, their results could not properly predict the stability of resistive modes. The ideal MHD stability of coronal arcades with line-tying was studied by various authors, who found that line-tying completely stabilizes kink modes. Most of these studies, too, used the constraint $\xi \cdot \mathbf{B}_0 = 0$ or nonhelical test functions, and their results overestimated the stability. We believe that further careful studies are needed, using helical perturbed functions, to understand the effect of line-tying on nonideal MHD modes as well as on the stability of coronal arcades.

The author thanks Dr. R. C. Canfield for valuable discussions and comments during the course of this work. This work was supported by the Air Force Office of Scientific Research, Air Force Systems Command, USAF, under grant AFOSR 82-0092, and by NASA under grant NSG-7406.

REFERENCES

- An, C.-H. 1982, *Solar Phys.*, **75**, 19 (Paper I).
 An, C.-H., Canfield, R. C., Fisher, G. H., and McClymont, A. N. 1983, *Ap J.*, **267**, 421.
 Bateman, G. 1978, *MHD Instabilities* (Cambridge: MIT Press).
 Bernstein, I. B., Frieman, E. A., Kruskal, M. D., and Kulsrud, R. M. 1958, *Proc Roy Soc Lond. A*, **244**, 17.
 Chiuderi, C., Giacchetti, R., and Van Hoven, G. 1977, *Solar Phys.*, **54**, 107.
 Einaudi, G., and Van Hoven, G. 1981, *Phys. Fluids*, **24**, 1092.
 ——— 1983, University of California, Irvine Tech. Rept. #83-26.
 Frukst, P. V. 1976, *Ap J.*, **210**, 575.
 Gold, T., and Hoyle, F. 1960, *M.N.R.A.S.*, **120**, 89.
 Hood, A. W., and Priest, E. R. 1979, *Solar Phys.*, **64**, 303.
 ——— 1981, *Geophys. Ap. Fluid Dyn.*, **17**, 197.
 Hood, A. W., Priest, E. R., and Einaudi, G. 1982, *Geophys. Ap. Fluid Dyn.*, **10**, 247.
 Kadomtsev, B. B. 1966, *Rev. Plasma Phys.*, **2**, 153.
 McClymont, A. N., and Canfield, R. C. 1983, *Ap J.*, **265**, 497.
 Mok, Y., and Van Hoven, G. 1982, *Phys. Fluids*, **25**, 636.
 Newcomb, W. A. 1960, *Ann. Phys.*, **10**, 232.
 Raadu, M. A. 1972, *Solar Phys.*, **22**, 425.
 Ray, A., and Van Hoven, G. 1982, *Solar Phys.*, **79**, 353.
 Van Hoven, G., Ma, S. S., and Einaudi, G. 1981, *Astr. Ap.*, **97**, 232.
 Vernazza, J. E., Avrett, E. H., and Loeser, R. 1981, *Ap J. Suppl.*, **45**, 619.

CHANG-HYUK AN: Center for Astrophysics and Space Sciences, C-011, University of California, San Diego, La Jolla, CA 92093

The Effect of Line-Tying on the Radiative MHD Stability
of Coronal Plasmas with Radial Pressure Profile

by

Chang-Hyuk An

Center for Astrophysics and Space Sciences, C-011
University of California, San Diego

Received: 1983 November 16

Subject Readings:

ABSTRACT

We have studied the effects of photospheric line-tying on the localized radiative magnetohydrodynamic (MHD) modes of compressible coronal plasmas. We used a simple trial function to represent the effect of line tying.

We have found that the effect of line-tying on radiative MHD stability varies, depending on the radial pressure profile; line-tying completely stabilizes both ideal and radiative MHD modes for plasmas with a negative pressure gradient. For plasmas with a positive pressure gradient (e.g., cool-core loops), which are in ideal-MHD stable state, radiation can initiate MHD instabilities near the center of the cool-core loop. In the surrounding hot region, however, line-tying completely stabilizes the plasmas. It also has stabilizing effects on the magnetosonic and condensation modes; bent field lines allow heat flows into or out of the condensed (compressed) region.

Subject Headings: hydrodynamics - plasmas - Sun: corona

I. INTRODUCTION

Since coronal plasmas are strongly coupled with magnetic fields, the plasmas are subject to MHD as well as radiative instabilities. A number of investigators have studied the MHD effect on the thermal instabilities to understand the formation of solar filaments in a plane-parallel geometry (Field, 1965; Nakagawa, 1970; Chiuderi and Van Hoven, 1979). Because loop structures are basic magnetic field configurations in the solar atmosphere, study of the stability in cylindrical geometry is preferable. In previous papers, the radiation effects on local MHD modes of incompressible (An, 1983a) and compressible (An, 1984a, hereafter Paper I) cylindrical plasmas were investigated, and the magnetic field effect on condensation modes was also studied (An, 1984b). Since cylindrical geometry is closer to the real solar loop geometry, these studies enhanced our understanding of observational results.

However, these and earlier studies have not taken into account the photospheric boundary, in which plasmas are essentially motionless on the coronal MHD time scale. The effects of photospheric line-tying on ideal MHD stability have been studied by numerous authors (Raadu, 1972; Hood and Priest, 1979, 1980, 1981; Einaudi and Van Hoven, 1981; Van Hoven, Ma, and Einaudi, 1981; An, 1982; Migliuolo and Cargill, 1983). All found

that line-tying has a stabilizing effect on ideal MHD modes. Magnetic tension is the most important stabilizing mechanism arising from line-tying.

How does line-tying affect radiation and heat conduction? We may certainly expect that its effects on energy dissipation mechanisms will not be the same as on ideal MHD modes—magnetic tension does not affect the energy dissipation directly. This study is a continuation of the attempt made in An (1983b) and Paper I, to study the true role of photospheric line-tying in compressible radiative plasmas. In Paper I, we found that radiative and compressible plasmas have magnetosonic and condensation modes that affect the MHD local interchange modes. Radiation can initiate MHD instabilities in plasmas that are in marginally stable ideal-MHD states. Cool-core loops (Foukal 1975) with positive pressure gradient everywhere in the loops, which are stable to local interchange modes, are also destabilized by radiation (An 1983a). According to recent theoretical studies of loop equilibria, the cool-core plasma is a natural consequence of force and energy balance (Xue and Chen, 1980; Einaudi, Torricelli-Ciamponi, and Chiuderi, 1983). In other words, the cool core is not a result of dynamical evolution, but a condition of loop equilibrium. If a cool-core is a general phenomenon in solar loops, as observed by Foukal (1975) and predicted by the theoretical studies, the radial pressure profile should be taken

into account in the stability calculation.

In this paper, we will try to derive the basic physics underlying the effect of line-tying on radiative modes and to study how different radial pressure profiles influence the effect of line-tying on radiative MHD stability.

II. GOVERNING EQUATIONS

We make several assumptions for this study. Coronal plasmas are represented as compressible cylindrical plasmas of circular cross section, with helically twisted magnetic fields. Heat conduction across the magnetic field is neglected. The ambient heating is assumed constant over time. Physical quantities are uniform along the loop direction and have only radial variations. This assumption does not represent the photospheric boundary where variations of temperature and density from coronal values are significant. As a realistic treatment of the photospheric boundary would require solution of two 2-D second-order partial differential equations, we assume an idealized boundary condition, discussed in Section III below, to simplify the calculation.

(a) Time-Dependent Equations

The equations that describe the MHD properties of the loop plasma under the above assumptions are

$$\rho \frac{\partial \vec{v}}{\partial t} = - \nabla P + \vec{j} \times \vec{B} \quad (1)$$

$$\frac{dP}{dt} = - \gamma P \nabla \cdot \vec{v} + (\gamma - 1) [H - R(\rho, T) + \nabla \cdot \kappa_{\parallel} \vec{e}_b \vec{e}_b \cdot \nabla T] \quad (2)$$

$$\frac{\partial \rho}{\partial t} + \nabla \cdot (\rho \vec{v}) = 0 \quad (3)$$

$$\nabla \times \vec{B} = \vec{j} \quad (4)$$

$$\frac{\partial \vec{B}}{\partial t} = - \nabla \times \vec{E} \quad (5)$$

$$\vec{E} + \vec{v} \times \vec{B} = 0 \quad (6)$$

$$P = K \rho T \quad (7)$$

Here ρ , P , and T are plasma density, pressure, and temperature, and \vec{B} , \vec{j} , and \vec{E} are magnetic field, plasma current density, and electric field, respectively. H and $R(\rho, T)$ are ambient heating and radiative energy loss functions. The quantity κ_{\parallel} is the heat conductivity parallel to the magnetic field, defined as $\kappa_{\parallel} = \kappa_0 T^{5/2}$ where κ_0 is a heat conduction constant (Spitzer, 1962). The quantity $\vec{e}_b = \vec{B}/|B|$ is a unit vector parallel to the local magnetic field; γ is the specific heat constant; and K is the gas constant.

(b) Steady States

An equilibrium for a cylindrical plasma can be obtained by solving the dimensionless static steady-state equations below:

$$\beta \nabla P_0 = \vec{j}_0 \times \vec{B}_0 \quad (8)$$

$$\nabla \times \vec{B}_0 = \vec{j}_0 \quad (9)$$

$$H - R(\rho, T) = 0 \quad (10)$$

Subscript 0 signifies the equilibrium quantity and β is the ratio of plasma to magnetic pressure at a standard point, $\beta = P_0/B_0^2$. Because T has only radial dependence, heat conduction does not contribute to the steady state energy balance, Eq. (10). As discussed in Paper I, we obtain equilibria assuming that density is uniform along the radial direction. This assumption is supported by Foukal (1975), who observed that radial density variation is insignificant compared with the temperature variation. We assume that the radiative energy loss function $R(\rho, T)$ has a functional form as $R(\rho, T) \sim \rho^2/T$ for $T > 10^5$ k. We do not attempt to solve Eq. (10), because we do not know the functional form of the ambient heating rate H . Rather, we calculate H as a function of radius from Eqs. (8) and (9).

In An (1983a) we found that the effect of radiation on MHD

stability varies, depending on the pressure profile. We expect a similar effect of the pressure profile on line-tied radiative MHD modes. We therefore construct two different equilibria. One has a negative pressure gradient (i.e., the pressure is greatest along the axis of the cylinder and decreases outward), which is unstable to local interchange modes, and the other has a positive pressure gradient, which is similar to that of cool-core loops (Poukal, 1975). The profiles of the two equilibria are as follows:

Equilibrium I (negative radial pressure gradient)

$$\begin{aligned}
 B_z &= 1 \\
 B_\theta &= \frac{\pi}{Aq_0} (r^3 - 2r) \\
 P &= P_0 - \left(\frac{\pi}{Aq_0}\right)^2 \left(\frac{2}{3}r^6 - 3r^4 + 4r^2\right)/3 \\
 P_0 &= 1 + \frac{5}{3} \left(\frac{\pi}{Aq_0}\right)^2 /3
 \end{aligned} \tag{11}$$

Equilibrium II (positive radial pressure gradient)

$$\begin{aligned}
 B_z &= 2-r^2, \quad B_\theta = -r/3 \\
 P &= 1 + \left[\frac{17}{9}r^2 - \frac{r^4}{2}\right]/6
 \end{aligned} \tag{12}$$

Here the boundary of the loop is $r = 1$, A is the aspect ratio, defined as $A = L/a$ (a and L are the radius of a cross section and

the cylinder length, respectively), and q_0 is the safety factor q at $r = 0$, defined as $q = -2\pi r B_z / LB_\theta$.

III. DERIVATION OF A DIFFERENTIAL EQUATION FOR STABILITY

The linearized, dimensionless Eqs. (1) through (7) are

$$\rho_0 \frac{\partial \vec{v}}{\partial t} = -\beta \nabla p_1 + \vec{j}_0 \times \vec{B}_1 + \vec{j}_1 \times \vec{B}_0 \quad (13)$$

$$\begin{aligned} \frac{\partial p_1}{\partial t} = & -\gamma p_0 \nabla \cdot \vec{v} - \vec{v} \cdot \nabla p_0 - \epsilon (\gamma - 1) \left\{ \frac{3}{2} \left(\frac{\partial R}{\partial T} \right) T_1 + \frac{3}{2} \left(\frac{\partial R}{\partial \rho} \right) T_0 \rho_1 \right\} \\ & + (\gamma - 1) \left[\vec{\tau} \cdot \kappa_0 \frac{\vec{e}_b}{|\vec{B}_0|} \cdot \vec{e}_b \cdot \nabla T_1 + \vec{\tau} \cdot \kappa_0 \frac{\vec{e}_b}{|\vec{B}_0|} \cdot \nabla T_0 \right] \end{aligned} \quad (14)$$

$$\vec{j}_1 = \nabla \times \vec{B}_1 \quad (15)$$

$$\vec{B}_1 = \nabla \times (\vec{\xi} \times \vec{B}_0) \quad (16)$$

$$\rho_1 = -\vec{\xi} \cdot \nabla \rho_0 - \rho_0 \nabla \cdot \vec{\xi} \quad (17)$$

$$p_1 = T_1 \rho_0 + T_0 \rho_1 \quad (18)$$

Here subscripts 0 and 1 stand for equilibrium and perturbed quantities, respectively. Time t is scaled by the MHD time scale $t_M = (\rho_0 a^2 / B_0^2)^{1/2}$. The radiative time scale is $t_r = 3P_0 / 2R$; the conductive time scale is $t_c = L^2 P_0 / \kappa_0 T_0^{7/2}$; and ϵ is the ratio of

MHD and radiative time scales, $\epsilon = t_M/t_r$. The quantity $\vec{\xi}$ is a plasma displacement vector ($\partial \vec{\xi} / \partial t = \vec{v}$), \vec{k} is the wave vector, and $\vec{k} \cdot \vec{B}_0 = k B_z + (m/r) B_\theta$, where k and m are longitudinal and poloidal wavenumber. In Eq. (14), we assume that ambient heating is not perturbed.

In order to impose a line-tying boundary condition, we assume that the plasma displacement function $\vec{\xi}$ is

$$\vec{\xi}(\vec{r}, t) = \vec{\xi}(r) e^{i(m\theta + kz) + \alpha t} \cos \alpha z \quad (19)$$

Here $\alpha = \pi a/2L$ and $\cos \alpha z$, which is zero at the footpoints, represents line-tying. There are several other choices of $\vec{\xi}(\vec{r})$ for line-tying; the effects of different choices on the results were discussed in detail by An (1983b). Equation (19) represents a helical perturbation, which least perturbs a magnetic field line if the helicity of the field line is the same as that of the perturbation. Note that the trial function does not predict a sufficient and necessary stability condition. The most general form of $\vec{\xi}$ for line tying can be expressed as a Fourier series in the z -direction (Einaudi and Van Hoven 1981; Hood and Priest 1981), which gives the lowest bound for stability. However, the general form does not allow the addition of heat conduction and radiation because of the extreme complexity of the calculation; couplings between all the longitudinal harmonics will frustrate the analyses.

By substituting Eq. (19) in Eq. (14) and using Eqs. (17) and (18), we can derive a perturbed pressure with a form $P_1 = C_1(r) \cos \alpha z + C_2(r) \sin \alpha z$. In this form, P_1 is never zero at the footpoints. For ideal MHD studies, both $C_1(r)$ and $C_2(r)$ are included in the calculation (An, 1982). But adding radiation effects with the additional term $C_2(r)$ makes the calculation hopelessly complicated. For simplicity we therefore assume that P_1 is zero at the footpoints, i.e., P_1 is

$$P_1 = P_1(r) e^{i(m\theta + kz)} \cos \alpha z \quad (20)$$

This simple form allows us to understand the basic physics without making the mathematics overcomplicated. Neglecting the $\sin \alpha z$ term in Eq. (20) can be justified if we restrict the study to high aspect ratio loops (i.e. $\alpha \ll 1$) because the term, which comes from $\partial \xi / \partial z$, is proportional to α . Equations (19) and (20) imply that plasma velocity and perturbed pressure are both zero at the footpoints. In a hydrodynamic study of thermal stability, Antiochos (1979) used the same boundary condition to discard the symmetric modes as unphysical. Recently, Antiochos et al. (1982) found that Eqs. (19) and (20) correspond to the boundary condition for antisymmetric modes and Eq. (19) alone corresponds to symmetric modes with a rigid wall boundary. Hydrodynamic

stabilities for the two different boundary conditions are different. For a detailed discussion of the boundary condition and stability, see Antiochos et al. (1982) and McClymont and Craig (1982,a,b,c).

By substituting $\vec{\xi}$ from Eq. (19) and P_1 from Eq. (20) in the linearized Eqs. (13) - (18), we can derive a differential equation for stability. We do not consider $\sin \alpha z$ terms by restricting the problem to high aspect ratio loops. For a general expression of $\vec{\xi}$ used by previous authors (e.g. Einaudi and Van Hoven 1981; Hood, Priest, and Einaudi 1982), the sine, cosine, and their cross terms might all be important for determining the stability. After a lengthy calculation, we have

$$P_1 = W_1 + W_2 \quad (21)$$

$$\begin{aligned} \nabla \cdot \vec{\xi} = & A_3 P_1 + \frac{\chi F}{r\Omega} + \frac{(\vec{k} \cdot \vec{B}_0) \partial P_0 / K}{r\Omega^2} \\ & + \frac{\chi}{\Omega} \left[\frac{(k^2 + \frac{m^2}{r^2}) \partial P_0}{r} + \frac{2kB_\theta}{r^2} (kB_\theta - \frac{mB_z}{r}) \right] \end{aligned} \quad (22)$$

$$\begin{aligned} \frac{\rho_0 \omega^2}{r} \chi = & -q_1 + \chi \left[2 \left(\frac{B_\theta}{r} \right)^2 + \frac{2kB_\theta}{r\Omega} (kB_\theta - \frac{mB_z}{r}) w_3 \right] \\ & + \chi \left[\frac{2B_\theta}{r} \left(\frac{B_\theta}{r} \right) + \frac{2kB_\theta}{r\Omega} (kB_\theta - \frac{mB_z}{r}) w_4 \right. \\ & \left. + \frac{(2kB_\theta)^2 B_0^2}{r^2 \Omega} - \frac{\{(\vec{k} \cdot \vec{B}_0)^2 + \alpha^2 B_z^2\}}{r} \right] \end{aligned} \quad (23)$$

$$q_1 = \lambda \frac{W_3 F}{\Omega} + \chi \left[\frac{\partial W_4 F}{\Omega} + \frac{2B_0^2}{r^2} - \frac{2kB_z B_0^2}{r^2} \left(kB_z - \frac{mB_z}{r} \right) \right] \quad (24)$$

Here

$$\chi = r \xi_r \quad (25)$$

$$K = k^2 + \frac{m^2}{r^2} + \alpha^2 \quad (26)$$

$$\Omega = \rho_0 \omega^2 + B_0^2 K \quad (27)$$

$$A = \frac{1}{\rho_0 \omega^2} \left[\frac{\rho_0 \omega^2 \left(\frac{m^2}{r^2} + k^2 \right) + K (\vec{k} \cdot \vec{B}_0)^2}{\Omega} \right] \quad (28)$$

$$F = \rho_0 \omega^2 + (\vec{k} \cdot \vec{B}_0)^2 + \alpha^2 B_0^2 \quad (29)$$

$$\theta = \frac{(\gamma-1)}{\rho_0} \left[\left(\frac{\partial R}{\partial T} \right)_\rho + \frac{T_0^{5/2}}{B_0^2} \frac{t_r}{t_c} \{ (\vec{k} \cdot \vec{B}_0)^2 + \alpha^2 B_z^2 \} \right] \quad (30)$$

$$\dot{\theta} = \frac{(\gamma-1) T_0}{\rho_0} \left[\left(\frac{\partial R}{\partial T} \right)_P + \frac{T_0^{5/2}}{B_0^2} \frac{t_r}{t_c} \{ (\vec{k} \cdot \vec{B}_0)^2 + \alpha^2 B_z^2 \} \right] \quad (31)$$

$$\bar{\theta} = \theta + \alpha^2 \frac{8T_0^{5/2} (\gamma-1) 2T_0 B_z (\vec{k} \cdot \vec{B}_0)}{B_0^2 \rho_0 \omega^2} \frac{t_r}{t_c} \left\{ \frac{k \rho_0 \omega^2 + (\vec{k} \cdot \vec{B}_0) B_z K}{\Omega} \right\} \quad (32)$$

$$W_1 = \left(W_3 + \frac{B_0^2}{r} \right) / \beta \quad (33)$$

$$W_2 = W_4 - P_0' / r \quad (34)$$

$$W_3 = - [\omega + \epsilon \bar{\theta} + A B (\epsilon \phi_0 + \gamma P_0 \omega)]^{-1} \left[\frac{T_0^{5/2}}{B_0^2} \frac{(\gamma-1) 2 T_0 B_z^2 (\vec{k} \cdot \vec{B}_0)^2 \alpha^2 \epsilon \epsilon}{r B_0^2} \right. \\ \left. + \frac{B_0^2 (\omega + \epsilon \theta)}{r} + \frac{(\phi_0 \epsilon + \gamma P_0 \omega)}{r B_0^2} B [c_0 \omega^2 + (\vec{k} \cdot \vec{B}_0)^2] \right] \quad (35)$$

$$W_4 = - [\omega + \epsilon \bar{\theta} + A B (\epsilon \phi_0 + \gamma P_0 \omega)]^{-1} \left[\epsilon \frac{\phi_0' - P_0' \theta}{r} \right. \\ \left. + \epsilon \frac{(\gamma-1) T_0^{5/2} T_0'}{r B_0^2} [(\vec{k} \cdot \vec{B}_0)^2 + \alpha^2 B_z^2] \right. \\ \left. + \epsilon \frac{T_0^{5/2} (\gamma-1) 2 T_0 B_z^2 \alpha^2 (\vec{k} \cdot \vec{B}_0)^2}{r B_0^2} \frac{2 k B_z^2}{r} \right. \\ \left. + \frac{(\phi_0 \epsilon + \gamma P_0 \omega) 2 k B_z^2 (k B_z^2 - \frac{m B}{r})}{r} \right] \quad (36)$$

Here χ' is a derivative of χ with r . Eqs. (26)-(29) represent terms for ideal MHD and Eqs. (30)-(32) are due to radiation and heat conduction. Eqs. (33)-(36) show how perturbed pressure is affected by the energy dissipations and line-tying. The effect of line-tying appears in different forms in Eqs. (26)-(29) and (30)-(32). Line-tying enhances magnetic tension in the ideal MHD terms in Eqs. (26)-(29), but affects heat conduction in the energy dissipation term of Eqs. (30)-(32). Note that at a mode rational surface heat conduction plays a role only for line-tied plasmas.

IV. LOCAL INTERCHANGE MODES

We now derive the stability condition for local interchange modes to study how line-tying affects them. The method is the same as in An (1983a). A second-order ordinary

differential equation is derived from Eqs. (23) and (24). As m and k go to infinity while keeping q finite in the differential equation, eigenfunctions are localized near a mode rational surface r_s ($kr_s B_z + mB_\theta = 0$) (An 1983a) and the pressure gradient becomes the dominant driving force over plasma current for instability (Dobrott *et al.* 1977). Since radiation and heat conduction affect directly plasma pressure [see Eq. (14)], we expect that the effect of the energy dissipations on the local modes (driven by pressure gradient) will be significant. After taking the limit as $m \rightarrow \infty$, the second order differential equation becomes, at a region far from a mode rational surface r_s ,

$$\chi \frac{B_\theta^2}{r^3} (1 - nq)^2 = 0 \quad (37)$$

here n is a longitudinal mode number and q is a safety factor defined below Eq. (12). The solution of the equation is $\chi = 0$. Near $r = r_s$, the differential equation becomes

$$\begin{aligned} \frac{\rho_o \omega^2}{r} \chi = & \left[\chi \left\{ \frac{(\rho_o \omega^2 + \alpha^2 B_o^2) r B_z^2}{m^2 B_o^2} + \frac{B_e^2 B_z^2}{r B_o^2} \left(\frac{q'}{q} \right)^2 (r - r_s)^2 \right\} \right]' \\ & + \chi \left[- \frac{2B_\theta^2}{r^2 B_o^2} \beta P_o' - \frac{\alpha^2 B_z^2}{r} - \frac{2B_\theta^2 \beta}{r} \left\{ \epsilon \frac{\phi \rho_o' - P_o' \theta}{r} \right. \right. \\ & \left. \left. + \frac{\epsilon(\gamma-1) \kappa_o T_o^{5/2} T_o' \alpha^2 B_z^2}{r B_o^2} + \frac{(\phi \rho_o \epsilon + \gamma P_o \omega)}{r^2} \frac{2B_\theta^2}{B_o^2} \right\} / G \right] \end{aligned} \quad (38)$$

where

$$G = \omega(B_0^2 + \beta\gamma P_0) + \epsilon(B_0^2\theta + \phi\rho_0\beta)$$

Eqs. (37) and (38) show that χ is localized near $r = r_s$ as $m \rightarrow \infty$.

We can derive a dispersion relation for local modes by multiplying Eq. (38) by χ^* (complex conjugate of χ) and integrate by parts.

$$\frac{c_0 \bar{P}}{r} \chi'^2 + \epsilon \frac{c_0 \bar{Q}}{r} \chi'^2 + Y \bar{P} \chi + \epsilon(Y \bar{Q} + W) \chi = 0 \quad (39)$$

When we derive Eq. (39) we use $\int s^2 |\chi'|^2 ds \geq 1/4 \int |\chi|^2 ds$ and neglect a term with $1/m^2$.

Here

$$\bar{P} = c_0(C_m^2 + C_s^2) \quad (40)$$

$$\bar{Q} = \frac{(\gamma-1)C_s^2}{\gamma} \left[\left(\frac{C_m^2 \gamma}{C_s^2} + 1 \right) \left(\frac{\partial R}{\partial T} \right) - \frac{c_0}{T_0} \left(\frac{\partial R}{\partial z} \right) \right] + (\gamma-1) \left[C_m^2 + \frac{C_s^2}{\gamma} \right] \frac{T_0^{5/2}}{B_0^2} \frac{t_r}{z} \frac{t_c}{t} \quad (41)$$

$$Y = \frac{1}{4} \frac{B_0^2 B_z^2}{r B_0^2} \left(\frac{q'}{q} \right)^2 + \frac{2B_0^2 \beta P_0'}{r^2 B_0^2} + \frac{\alpha^2 B_z^2}{r} + \frac{4B_0^4 \beta \gamma P_0}{r^3 B_0^2 (B_0^2 + \beta \gamma P_0)} \quad (42)$$

$$\begin{aligned}
 W = & -\frac{2B_0^2}{r^2} (\gamma-1) \delta \frac{dR}{dr} - \frac{C_s^2 C_m (\gamma-1)^2}{\gamma} \frac{4\alpha \mu B_0^2}{Pr^3 B_0^2} \left[\left(\frac{\partial R}{\partial T} \right)_S \right. \\
 & \left. + \frac{T^{5/2}}{B_0^2} \alpha^2 B_z^2 \frac{t_r}{t_c} \right]
 \end{aligned} \quad (43)$$

and

$$\begin{aligned}
 C_s^2 &= \beta \gamma P_0 / \rho_0, \quad C_m^2 = B_0^2 / \rho_0 \\
 \left(\frac{\partial R}{\partial T} \right)_S &= \left(\frac{\partial R}{\partial T} \right)_V + \frac{\rho_0}{(\gamma-1) T_0} \left(\frac{\partial R}{\partial \sigma} \right)_T
 \end{aligned} \quad (44)$$

The coefficients of Eq. (39) are evaluated at a mode rational surface $r_s (kr_s B_z + mB_\theta = 0)$. The quantity Y represents the stability condition for local ideal MHD modes, and Q and W are due to radiation and heat conduction. The effects of line-tying appear as magnetic tension in Y and as heat conduction in Q and W . In Paper I, we found that heat conduction does not influence the stability of the localized modes when no line-tying is considered. Since $Q > 0$ is a stability condition for condensation modes in uniform plasmas whose wave vector is perpendicular to the magnetic field (Field, 1965), line-tying may be seen as a stabilizing mechanism for the condensation modes. It also stabilizes the magnetosonic modes represented by the terms within brackets in W of Eq. (43).

There are sound physical explanations for the effect of

line-tying on the magnetosonic and condensation modes. As plasmas are condensed (or compressed), so are the anchored field lines. Plasma motions across the field lines bend the lines, as shown in Fig. 1. In condensation, line tying connects the cool-condensed central region to unperturbed boundaries, results in heat conduction from the boundaries into the condensed region along the field lines (Fig. 1a). On the other hand, in adiabatic compression (magnetosonic modes), heat will be conducted out of the hot compressed region (Fig. 1b). The heat flows stabilize the two modes and can do so only because of line-tying. Without line-tying, the field lines are not bent by the perpendicular motion, and heat cannot flow into or out of the condensed or compressed region (Fig. 1c).

Next, we may see how line-tying affects the local MHD modes. As discussed in Paper I, we can derive zero- and first-order solutions of Eq. (39), noting that $\epsilon \sim 10^{-4}$ for coronal loops and $\epsilon \sim 10^{-1}$ for quiescent prominences. The growth rate ω can be expanded with respect to ϵ as

$$\omega = \omega_0 + \epsilon \omega_1 + \epsilon^2 \omega_2 + \dots \quad (45)$$

The zero-order solution ω_0 (ideal MHD) is

$$\omega_0^2 = - \frac{rY}{\rho_0} \quad (46)$$

and $Y > 0$ is the condition for stability. [Note that we use $e^{\omega t}$ rather than $e^{i\omega t}$ for time dependence of perturbed quantities, see Eq. (19)]. A difference between stability conditions with and without line-tying is the third term in Eq. (42), $(\alpha^2 B_z^2/r)$, which represents magnetic tension due to line-tying. For Equilibrium I, [$P_0' < 0$, Eq. (11)], $\alpha^2 B_z^2/r$ is larger than the P_0' term in Y because $B_z \sim O(1)$, $B_\theta \sim O(\alpha)$, and $\beta P_0' \sim O(\alpha^2)$. Line-tying completely stabilizes the local modes for this equilibrium.

The first-order solution, when $\omega_0^2 \neq 0$, is

$$\omega_1 = - \frac{rW}{2\bar{P}_0 \omega_0^2} \quad (47)$$

For $\omega_0^2 = 0$, we have to solve the equation

$$\frac{\rho_0 \bar{P}}{r} \omega^3 + \frac{\epsilon \rho_0 \bar{Q}}{r} \omega^2 + \epsilon W = 0 \quad (48)$$

The solution is given in Eq. (25) of Paper I, where we find that at least one unstable mode exists in coronal plasmas without line-tying.

In order to understand the effect of the radial pressure gradient, it is necessary to numerically evaluate ω_0 and ω_1 . For plasmas in ideal MHD stable states, ω_0 is imaginary [see Eq. (31)]

and the sign of ω_1 determines the stability. When plasmas are ideal MHD unstable (i.e., $\omega_0 > 0$) the sign of ω_1 does not influence the stability because $\epsilon \ll 1$. Let us consider the stability of Equilibrium I, Eq. (11), and then Equilibrium II, Eq. (12).

For Equilibrium I ($P_0' < 0$), a numerical evaluation of Y [in ideal MHD stability, Eq. (31)] with and without line-tying is given in Fig. 2. The figure shows that plasmas without line-tying are unstable for $r \leq 0.35$ and marginally stable at $r \approx 0.36$. Radiation can induce MHD instabilities in the marginally stable region (Paper I). When line-tying is included, the plasmas are completely stabilized ($\omega_0^2 < 0$). Noting that $W < 0$ for $P_0' < 0$, radiation cannot induce MHD instabilities in plasmas anchored by line-tying [see Eq. (47)].

For Equilibrium II ($P_0' > 0$), whose pressure profile is similar to that of cool-core loops, the equilibrium is ideally stable ($\omega_0^2 < 0$) with or without line-tying [see Eqs. (42) and (46)]. From Eq. (47), for $\omega_0^2 < 0$, $W > 0$ ($W < 0$) implies instability (stability). Figure 3 shows the numerical estimate of W . For the estimation, we assumed that the temperature at $r = 0$ is $T = 1.5 \times 10^5 \text{K}$, density $n = 1 \times 10^9 / \text{cm}^3$, magnetic field $B_z = 10 \text{G}$, and aspect ratio $A = 10$. The stability of equilibria similar to Equilibrium II ($P_0' > 0$) was studied for the incompressible case

in An (1983a). It was found that radiation destabilizes the incompressible plasmas with $P_0' > 0$ which is in the ideal MHD stable state. In Paper I we considered the effect of compressibility on radiative MHD modes. The study showed that compressibility is a stabilizing effect for cool-core loops but did not mention how important the effect is. Is the compressibility able to stabilize the radiative MHD modes? The numerical estimate (Fig. 3) shows that compressibility does not alter the result of An (1983a); radiation can destabilize the compressible cool-core loops without line tying. The result suggests that radiative plasmas can flow across magnetic field lines, as claimed by Foukal (1976). When line-tying is included, however, heat conduction plays a stabilizing role. Near the cool-core region ($r \leq 0.2$), where heat conduction is negligible, the stability with or without line-tying is nearly the same. However, for $r \geq 0.3$, where heat conduction becomes important, stabilities for the two cases are significantly different. Line-tying stabilizes the modes for $r \geq 0.3$. The figure thus implies that plasmas can flow across the field lines near the cool core but that line-tying prohibits such flow in the surrounding hot region.

V. CONCLUSIONS

We have studied the effects of photospheric line-tying on the local interchange modes of compressible cylindrical plasmas in which energy is dissipated by heat conduction and radiation. By taking the limit as $m \rightarrow \infty$, the modes are localized near a mode rational surface r_s ($kr_s B_z + mB_\theta = 0$). Noting that the ratio of MHD and radiative time scales $\epsilon \ll 1$ for coronal loops, we obtain the zero- (ideal MHD) and first-order (with radiation) solution of ϵ by expanding the eigenvalue with respect to ϵ . The effect of line-tying appears as a magnetic tension for the zero-order mode and completely stabilizes it. For the first-order mode, if the lines are tied, heat conduction occurs along bent field lines when plasmas move across the field lines. Without line-tying, heat conduction plays no role in the first-order solution.

The effects of line-tying on stability differ for various radial pressure profiles; for equilibria with $P_0' < 0$, since the first-order mode is stable and line-tying completely stabilizes zero-order modes, radiation has an insignificant effect on the stability, i.e., it does not alter ideal MHD stability. On the other hand, for equilibria with $P_0' > 0$ ($T_0' > 0$), as in cool-core loops, radiation has a significant effect on the stability. It destabilizes plasmas in an ideal-MHD stable state. Compressibility, which is stabilizing for $P_0' > 0$ (Paper 1), does

not alter the result. Line-tying here reduces the destabilizing effect of radiation by generating heat conduction. The numerical estimate of the stability of a first-order state in a cool loop shows that plasma near the cool core is unstable owing to radiation, i.e., the line-tying effect is insignificant in this region. On the other hand, the plasma in the surrounding hot region is stabilized by heat conduction: line-tying has an important stabilizing effect on the hot region. The result suggests that plasma mixing across the field lines occurs mainly near the cool-core region, while the surrounding hot region undergoes no appreciable MHD activity. If plasmas flow down along the loop, as suggested by Poukal (1976), the flow might be concentrated near the cool core.

Thus we see that radiation is an important mechanism for initiating MHD instabilities in loops with positive radial pressure gradient that are in an ideal-MHD stable state. If so, radiation and radial pressure profile must be taken into account in determining loop stability.

By neglecting the $\sin \alpha z$ term in P_1 , as is done in Eq. (20) to simplify the calculation, we render the line-tying boundary condition essentially the same as the boundary for antisymmetric modes in hydrodynamic thermal stability studies (Antiochos et al., 1982). The constraint on P_1 may overdetermine the stability,

but the essential effect of line-tying on radiative as well as ideal MHD modes will be the same as without the constraint.

We have studied the radiative MHD modes in cylindrical plasmas analytically by utilizing the fact that the modes are localized near a singular surface as $m \rightarrow \infty$. A question arises concerning the applicability of the results to finite m modes. How large should m be for the results to be valid in good approximation? Since $m > 2$ modes are localized near a singular surface (An 1982) the results might be applicable for all $m > 2$. Furthermore, noting that the major destabilizing mechanism, radiation, is independent of m [see Eq's (30) and (31)], we may expect that the dependence of the radiative modes on the poloidal mode number m is not significant. The precise limit of m can be obtained only by solving Eq's (23) and (24) numerically.

In this study, we have considered the photospheric boundary in the stability calculation. Since our model is greatly simplified, we do not attempt to compare our results with observations. Rather we have put more emphasis on understanding the basic physics governing the effects of line-tying and radiation on MHD stability. Future work should include the variation of physical quantities along the loop direction and take into account more realistic loop geometry and boundary conditions.

ACKNOWLEDGMENTS

The author thanks Dr. R.C. Canfield for valuable comments during the course of this work. This work was supported by the Air Force Office of Scientific Research, Air Force Systems Command, USAF, under grant number APOSR 82-0092, and by NASA under grant number NSG-7406.

REFERENCES

- An, C.-H., 1982, *Solar Phys.* 76, 19.
- _____ 1983a, *Ap. J.* 264, 302.
- _____ 1983b, UCSD Research Report SP-83-21, *Ap. J.* accepted
for publication.
- _____ 1984a, *Ap. J.* 276, 352, Paper I.
- _____ 1984b, *Ap. J.* 276, 755.
- Antiochos, S.K., 1979, *Ap. J. Lett.* 232, L-125.
- Antiochos, S.K., Emslie, A.G., Shoub, E.C., and An, C.-H., 1982,
Stanford University SUIPR Report No. 931.
- Chiuderi, C., and Van Hoven, G., 1979, *Ap. J. Lett.* 232, L-69.
- Dobrott, D., Nelson, D.B., Greene, J.M., Glasser, A.H., Chance,
M.S., and Frieman, E.A., 1977, *Phys. Rev. Lett.* 39, 943.
- Einaudi, G., and Van Hoven, G., 1981, *Phys. Fluids* 24, 1092.
- Einaudi, G., Torricelli-Ciamponi, G., and Chiuderi, C., 1983,
submitted to *Solar Phys.*.
- Field, G.B., 1965, *Ap. J.* 142, 531.
- Foukal, P.V., 1975, *Solar Phys.* 43, 327.
- _____, 1976, *Ap. J.* 210, 575.
- Hood, A.W., and Priest, E.R., 1979, *Solar Phys.* 64, 303.
- _____, 1980, *Solar Phys.* 64, 113.
- _____, 1981, *Geophys. Astrophys. Fluid Dyn.* 17, 197.
- Hood, A.W., Priest, E.R., and Einaudi, G., 1982, *Geophys. Astrophys.*
Fluid Dyn. 10, 247.

- McClymont, A.N., and Craig, I.J.D., 1982a, *Astr. Ap.* (submitted).
- _____, 1982b, *Astr. Ap.* (submitted).
- _____, 1982c, *Astr. Ap.* (submitted).
- Nakagawa, Y., 1970, *Solar Phys.* 12, 419.
- Raadu, M.A., 1972, *Solar Phys.* 22, 425.
- Spitzer, L., 1962, *Physics of Fully Ionized Gases* (New York: Interscience), pp 136-146.
- Van Hoven, G., Ma, S.S., and Einaudi, G., 1981, *Astron. Ap.* 97, 232.
- Xue, M.-L., and Chen, J., 1980, PFC/LA-27-80, MIT Preprint.

FIGURE CAPTIONS

Figure 1: Magnetic field lines after plasma condensation (or compression). Because of line-tying, field lines bend for plasma motions perpendicular to field lines: (a) when plasma is condensed, heat flows along the field lines into the condensed region; (b) when adiabatically compressed, heat flows out of the compressed region; and (c) without line-tying, the field lines do not bend for the perpendicular motion. No heat flows into (out of) the condensed (compressed) region because heat conduction perpendicular to field lines is neglected.

Figure 2. Numerical estimation of the ideal MHD local mode stability condition Y ; $Y > 0$ implies stability. The left vertical axis is for $\alpha = 0$, and the right is for $\alpha \neq 0$. The abscissa is radial distance from the center of a unit cylinder cross section.

Figure 3. Numerical estimation of first-order stability (the effect of radiation and heat conduction) condition W ; $W > 0$ implies instability owing to energy dissipation.

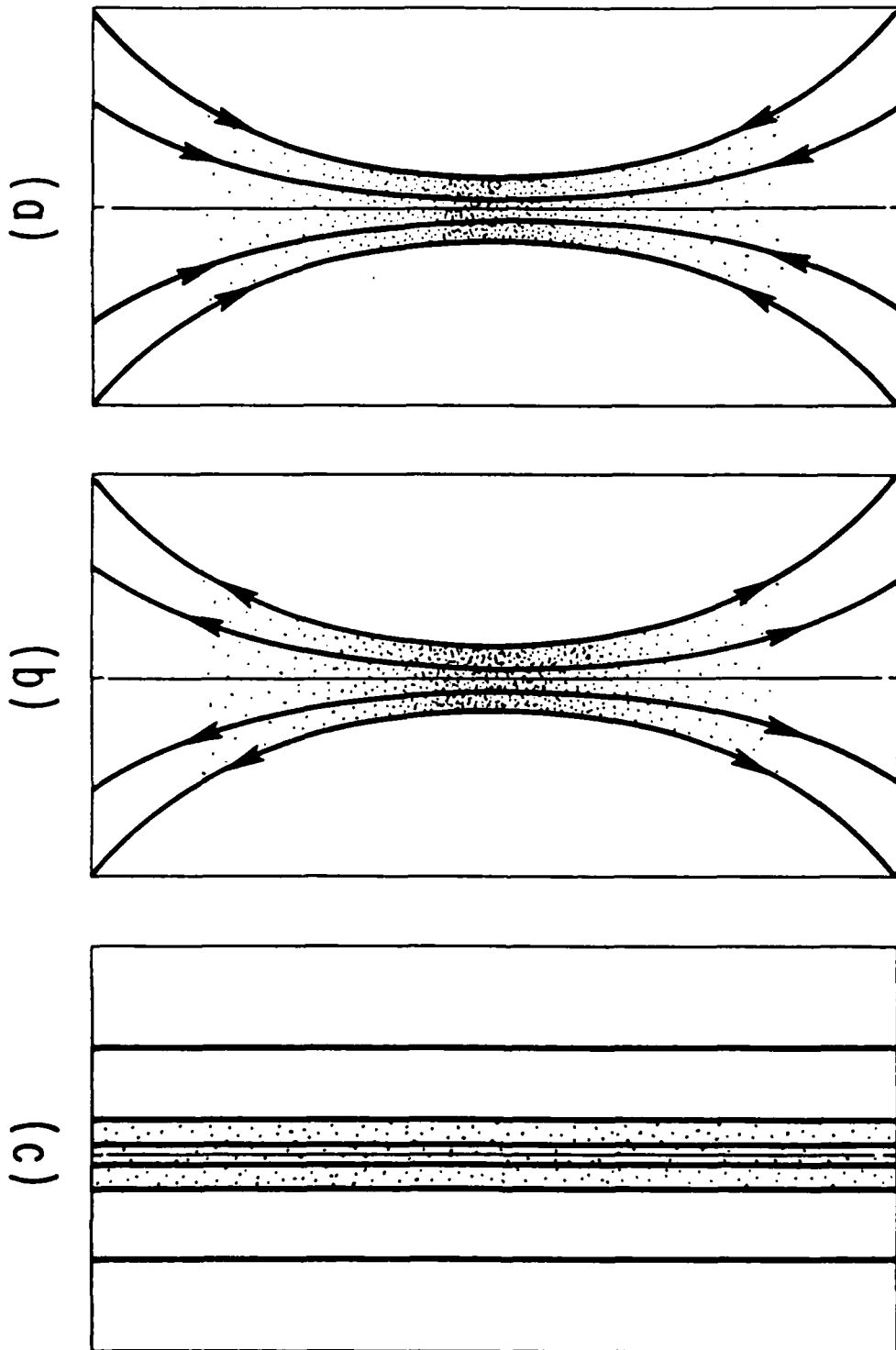


Figure 1.

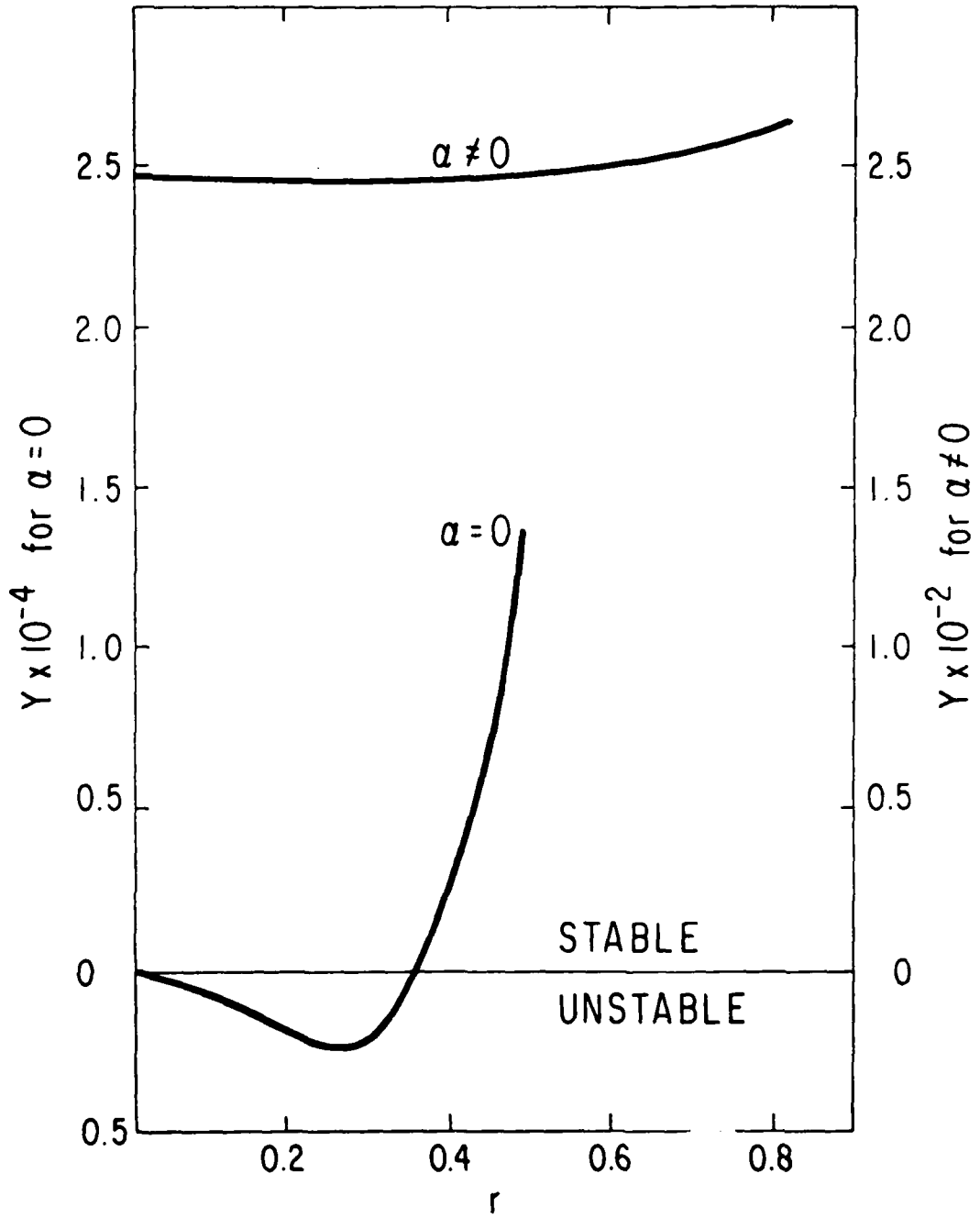


Figure 2.

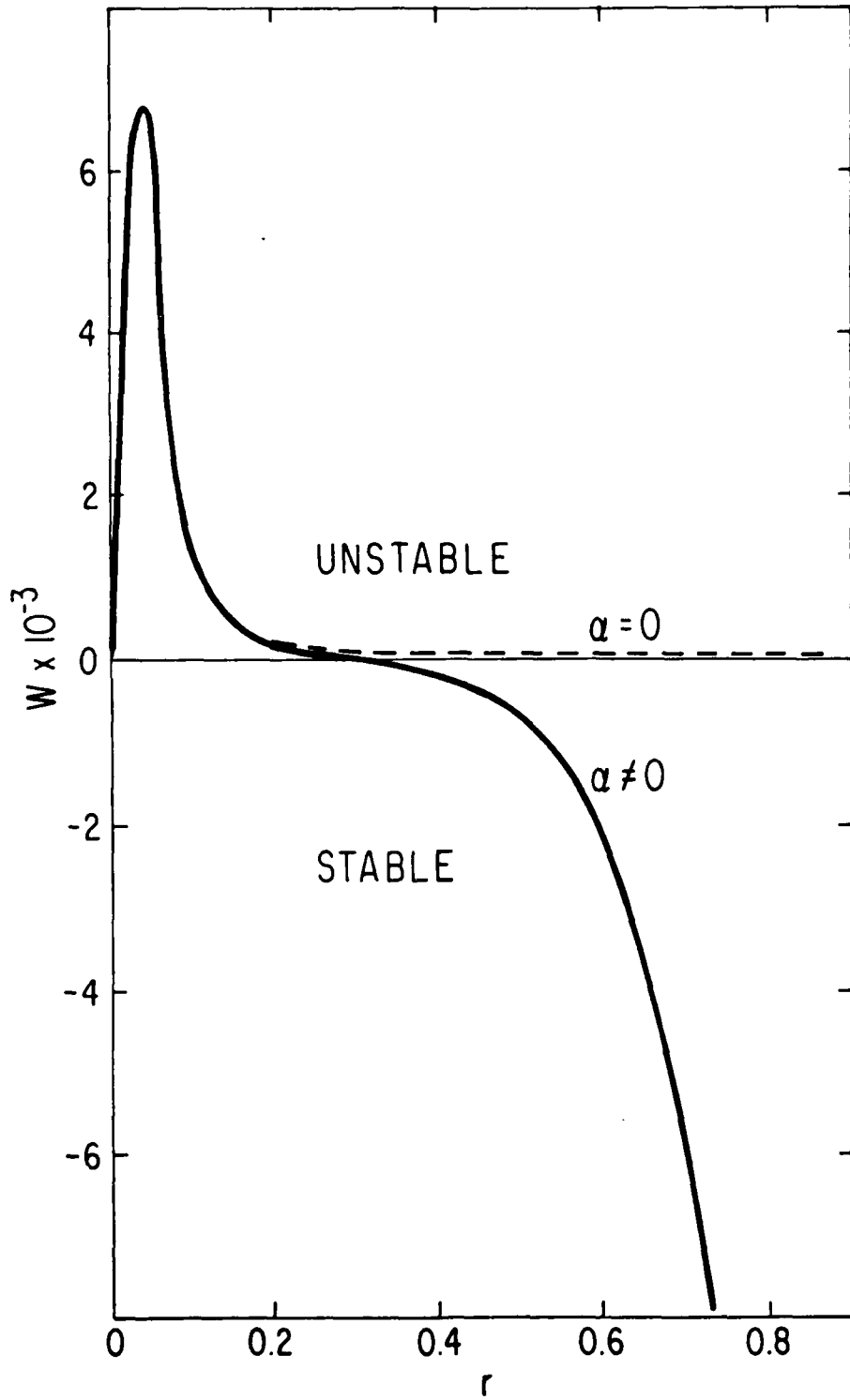


Figure 3.

Chang-Hyuk An

Center for Astrophysics and Space Sciences, C-011

University of California, San Diego

La Jolla, California 92093

III. PROFESSIONAL PERSONNEL

Richard C. Canfield
Research Physicist
Principal Investigator

Alexander N. McClymont
Assistant Research Physicist

Chang-Hyuk An
Postgraduate Research Physicist

Todd A. Gunkler
Research Assistant

IV. PUBLICATIONS

An, Chang-Hyuk 1983; *Ap. J.*, 264, 302, "MHD Stability of Incompressible Coronal Loops with Radiative Energy Loss."

Ricchiuzzi, P. J., and Canfield, R. C. 1983; *Ap. J.*, 272, 739, "A Static Model of Chromospheric Heating in Solar Flares."

Canfield, R. C., McClymont, A. N., and Puetter, R. C. 1984; in *Methods of Radiative Transfer*, (ed. W. Kalkofen, Cambridge University Press) p. 101, "Probabilistic Radiative Transfer."

An, Chang-Hyuk 1984; *Ap. J.*, 276, 352, "MHD Stability of Compressible Coronal Loops with Radiative Energy Loss."

An, Chang-Hyuk 1984; *Ap. J.*, 276, 755, "Condensation Modes in Magnetized Cylindrical Plasmas."

An, Chang-Hyuk 1984; *Ap. J.*, 281, 419, "Comments on the MHD Stability of Coronal Plasmas with Line Tying."

Canfield, R. C., Gunkler, T. A., and Ricchiuzzi, P. J. 1984; *Ap. J.* (in press), "The $H\alpha$ Spectral Signatures of Solar Flare Nonthermal Electrons, Conductive Flux, and Coronal Pressure."

An, Chang-Hyuk 1984; *Ap. J.* (in press), "The Effect of Line-Tying on the Radiative MHD Stability of Coronal Plasmas with Radial Pressure Profile."

V. SPOKEN PAPERS

"A Static Model of Chromospheric Heating in Solar Flares", R. C. Canfield and P. J. Ricchiazzi, American Astronomical Society, Boston, 9 January 1983.

"Condensation Modes in Magnetized Coronal Loops", C.-H. An, American Astronomical Society, Boston, 9 January 1983.

"The H α Spectral Signature of Several Flare Processes", T. A. Gunkler, R. C. Canfield and P. J. Ricchiazzi, American Astronomical Society, St. Paul, 19 June 1983.

"MHD Stability of Coronal Loops with Radiative Energy Loss", C.-H. An, American Astronomical Society, Solar Physics Division, St. Paul, 19 June 1983.

"Chromospheric Evaporation in Flare Loops Heated Impulsively by Nonthermal Electrons", G. H. Fisher, R. C. Canfield and A. N. McClymont, American Astronomical Society, Solar Physics Division, St. Paul, 19 June 1983.

"Emission from Flare Loops Heated Impulsively by Nonthermal Electrons", R. C. Canfield, G. H. Fisher and A. N. McClymont, American Astronomical Society, Solar Physics Division, St. Paul, 19 June 1983.

"Maximum Upward Velocities of Chromospheric Evaporation in Flares", G. H. Fisher, R. C. Canfield and A. N. McClymont, American Astronomical Society, Las Vegas, 8 January 1984.

"Theoretical H α Signatures of Impulsive Flare Heating by Energetic Nonthermal Electrons and Thermal Conduction", R. C. Canfield, T. A. Gunkler and P. J. Ricchiazzi, American Astronomical Society, Las Vegas, 8 January 1984.

"A Consistent Picture of Coronal and Chromospheric Processes in a Well-Observed Flare", T. A. Gunkler, R. C. Canfield, L. W. Acton and A. L. Kiplinger, American Astronomical Society, Las Vegas, 8 January 1984.

"MHD Stability of Line-Tied Coronal Loops with Radiative Energy Loss", C.-H. An, American Astronomical Society, Las Vegas, 8 January 1984.

"Nonthermal Lyman α Emission by 3 keV-300 MeV Protons", C.-R. Chang and R. C. Canfield, American Astronomical Society, Baltimore, 10 June 1984.

"Chromospheric Evaporation in Flares Due to Heating by Nonthermal Electrons", G. H. Fisher, R. C. Canfield and A. N. McClymont, American Astronomical Society, Baltimore, 10 June 1984.

"Electron Beam Heating During A Well-Observed Compact Flare", R. C. Canfield and T. A. Gunkler, American Astronomical Society, Baltimore, 10 June 1984.

VI. CONSULTATIVE AND ADVISORY FUNCTIONS

Space Science Board, National Academy of Sciences, Cape Canaveral, FL, 18-20 February 1982, R. C. Canfield.

Space Science Board, National Academy of Sciences, Washington, D.C. 29-30 April 1982, R. C. Canfield.

Committee on Solar and Space Physics, Space Science Board, National Academy of Sciences, Snowmass, CO, 12-13 July 1982, R. C. Canfield.

Space Science Board, National Academy of Sciences, Snowmass, CO, 26-30 July 1982, R. C. Canfield.

Space Science Board, National Academy of Sciences, Washington, D.C., 4-6 November 1982, R. C. Canfield.

Solar Interior Dynamics Mission Working Group, Pasadena, CA, 17-19 January 1983, R. C. Canfield.

Space Science Board, National Academy of Sciences, Houston, TX, 10-12 February 1983, R. C. Canfield.

Space Science Board, National Academy of Sciences, Greenbelt, MD, 28-29 April 1983, R. C. Canfield.

Space Science Board, National Academy of Sciences, Washington, D.C., 11 August 1983, R. C. Canfield.